STRUCTURAL BEHAVIOUR OF
HIGH STRENGTH S690 COLD-FORMED SQUARE HOLLOW SECTIONS
UNDER COMPRESSION

MENG XIAO

PhD

The Hong Kong Polytechnic University

2021

The Hong Kong Polytechnic University
Department of Civil and Environmental Engineering

Structural Behaviour of High Strength S690 Cold-Formed Square Hollow Sections under Compression

Meng Xiao

A thesis submitted in partial fulfilment of the requirements for the degree of Doctor of Philosophy

March 2021

CERTIFICATE OF ORIGINALITY

I hereby declare that this thesis is my own work and that, to the best of my knowledge and belief, it reproduces no material previously published or written, nor material that has been accepted for the award of any other degree or diploma, except where due acknowledgement has been made in the text.

________________________________ (Singed)

MENG XIAO (Name of student)

ABSTRACT

Motivation

Compared with normal strength steels, high strength steels have remarkable advantages in construction, due to their high resistances per unit weight of the materials. Structural hollow sections have been widely applied in steel construction all over the world because of their high resistances against instability and their highly desirable architectural appearance. In general, fabrication of hot-finished structural hollow sections always requires a huge amount of initial capital investment, and it is only financially viable to produce many thousand tons of standard sections. In recent years, cold-formed square hollow sections (CFSHS) become very popular because of their low set-up costs even to produce several hundred tons of non-standard sections. These CFSHS are readily fabricated with a combination of transverse bending and longitudinal welding in many modern fabricators. It should be noted that these two fabrication processes will impose significant effects onto the structural performance of these sections which are very different to those of hot-finished structural hollow sections. Currently, applications of high strength steel CFSHS are rather limited due to a lack of understanding on their structural behaviour as well as a lack of effective design rules.

Objectives and Scope of Work

In order to exploit effective use of S690 CFSHS in construction, a comprehensive experimental-numerical incorporated investigation is conducted to examine structural behaviour of these CFSHS under compression. Effects of fabrication processes, namely, i) transverse bending, and ii) longitudinal welding, onto the structural behaviour of these sections are also examined. New understandings and insights on effective use of these S690 CFSHS are thus generated, and applicability of the current design rules to these sections is verified according to these new findings and data.

- **Task 1: Experimental and numerical investigation into plastic strains and residual stresses in S690 CFSHS**

  To examine mechanical properties of the S690 CFSHS due to i) transverse bending, and ii) longitudinal welding.

- **Task 2: Full scale structural tests on stocky and slender columns with S690 CFSHS under compression**

  To examine section and member resistances of the S690 CFSHS under compression, including i) stocky columns under concentric compression, ii) stocky columns under eccentric compression, and iii) slender columns under concentric compression.

- **Task 3: Numerical modelling on stocky and slender columns with S690 CFSHS under compression**

  To calibrate numerical models against the test data and to conduct parametric studies with the validated models for design development.

It should be noted that two series of CFSHS, namely, i) Series SA, and ii) Series SB, are examined in the present project, and they are manufactured with components of different sizes and shapes.

Research Methodology

The research takes the following forms of investigation:

- **Task 1: Experimental and numerical investigation into plastic strains and residual stresses in S690 CFSHS**

  In order to determine mechanical properties in the round corners of the S690 CFSHS, a total of 7 flat coupons extracted from the S690 steel plates and 19 flat and curved coupons extracted from the S690 CFSHS were tested under tension. Complementary numerical models as well as analytical solutions were also developed. These two methods were developed to predict the residual stresses as well as the strength enhancements at these corner regions of the S690 CFSHS with a high degree of accuracy.

  Moreover, the residual stresses in the S690 CFSHS due to i) transverse bending, and ii) longitudinal welding were measured with the sectioning method. It should be noted that both the cold-bending and the welding processes were examined in detail, and key parameters on these two manufacturing processes were recorded. Based on specific heat transfer coefficients and codified thermal properties, sequentially-coupled thermomechanical analyses on these CFSHS were conducted with ABAQUS to predict accurately the residual stresses in these sections.

- **Task 2: Full scale structural tests on stocky and slender columns with S690 CFSHS under compression**

  A total of 38 columns of S690 CFSHS were tested under compression, including i) 8 stocky columns under concentric compression, ii) 6 stocky columns under eccentric compression, and iii) 24 slender columns under concentric compression. Execution of these tests provided a detailed examination on their load-deformation characteristics, in particular, both the section and the member resistances, for calibration of numerical models, and for verification of design rules.

- **Task 3: Numerical modelling on stocky and slender columns with S690 CFSHS under compression**

  Advanced numerical models of both stocky and slender columns of these S690 CFSHS were established and validated against the test data obtained in Task 2. A set of parametric studies were then conducted to develop a database on the member resistances of these S690 CFSHS. Both the design rules for section classification and the design rules for member resistances given in EN 1993-1-1 were verified to be applicable to these S690 CFSHS according to both test and numerical results.

Key Findings and Their Research Significance

Major academic merits of this research study are:

- This is the first research which systematically investigates residual stresses in S690 CFSHS induced by transverse bending and longitudinal welding. An experimental-numerical incorporated investigation is carried out to predict the residual stresses and the strength enhancements at the corner regions of these CFSHS.

- Generalized numerical models are developed, which can be directly employed to predict the residual stress distributions of the S690 CFSHS with various combinations of transverse bending and longitudinal welding.

- Structural performance of stocky and slender columns of the CFSHS is examined under compression, and hence, both the section and the member resistances of these columns are obtained as definitive test data for reference.

- Modifications to the current design rules of section classification given in EN 1993-1-1 are proposed to enable an effective prediction for their section resistances.

- Current design rules in EN 1993-1-1 are shown to be very conservative in predicting member resistances of slender columns with S690 CFSHS. After calibrating against both test and numerical data, it is proposed to adopt a smaller imperfection factor, when compared with the current value, to achieve an improved design for the members with S690 CFSHS under axial buckling.

Consequently, this study generates new test and numerical data on the structural behaviour of the S690 CFSHS under compression, and the current design rules are confirmed to predict safe section and member resistances of these columns in many cases. Minor modifications to these design rules are also provided to improve their structural efficiency. As a result, engineers are encouraged to take good advantages of HSS CFSHS to use them in construction projects.

LIST OF PUBLICATIONS

Journal Papers (published):

[1] Ho, H. C., Guo, Y. B., **Xiao, M.**, Xiao, T. Y., Jin, H., Yam, M. C. H., Chung, K. F., & Elghazouli, A. Y. (2021). Structural response of high strength S690 welded sections under cyclic loading conditions. Journal of Constructional Steel Research, 182, 106696.

[2] Ho, H. C., **Xiao, M.**, Hu, Y. F., Guo, Y. B., Chung, K. F., Yam, M. C. H., & Nethercot, D. A. (2020). Determination of a Full Range Constitutive Model for High Strength S690 Steels. Journal of Constructional Steel Research, 174, 106275.

[3] Chung, K. F., Ho, H. C., Hu, Y. F., Wang, K., Liu, X., **Xiao, M.**, & Nethercot, D. A. (2020). Experimental Evidence on Structural Adequacy of High Strength S690 Steel Welded Joints with Different Heat Input Energy. Engineering Structures, 204, 110051.

[4] Ho, H. C., Chung, K. F., Liu, X., **Xiao, M.**, & Nethercot, D. A. (2019). Modelling Tensile Tests on High Strength S690 Steel Materials undergoing Large Deformations. Engineering Structures, 192, 305-322.

[5] Liu, X., Chung, K. F., Ho, H. C., **Xiao, M.**, Hou, Z. X., & Nethercot, D. A. (2018). Mechanical Behavior of High Strength S690-QT Steel Welded Sections with Various Heat Input Energy. Engineering Structures, 175, 245-256.

[6] Ho, H. C., Liu, X., Chung, K. F., Elghazouli, A. Y., & **Xiao, M.** (2018). Hysteretic Behaviour of High Strength S690 Steel Materials under Low Cycle High Strain Tests. Engineering Structures, 165, 222-236.

Conference Papers (published):

[1] **Xiao, M.**, & Chung, K. F. (2019). Structural Behaviour of High Strength S690 Cold-formed Structural Hollow Sections under Compression. The 16th East Asia-Pacific Conference on Structural Engineering and Construction (EASEC-16). Brisbane, Australia.

[2] Guo, Y. B., Ho, H. C., **Xiao, M.**, Liu, X., & Chung, K. F. (2019). Structural Responses of High Strength S690 Welded Sections under Different Cyclic Actions. The 16th East Asia-Pacific Conference on Structural Engineering and Construction (EASEC-16). Brisbane, Australia.

[3] **Xiao, M.**, Hu, Y. F., & Chung, K. F. (2019). Numerical Study into Residual Stresses and Axial Buckling of Q460 High Strength Steel Welded Box-sections. The 12th Pacific Structural Steel Conference (PSSC2019). Tokyo, Japan.

[4] Guo, Y. B., **Xiao, M.**, Liu, X., Ho, H. C., & Chung, K. F. (2019). Hysteretic Behaviour of S355 and S690 Steels under Cyclic Tests with Constant and Varying Strain Amplitudes. The 12th Pacific Structural Steel Conference (PSSC2019). Tokyo, Japan.

[5] Ho, H. C., Chung, K. F., **Xiao, M.**, Yan, M. C. H., & Nethercot, D. A. (2018). True Stress-strain Characteristics of High Strength S690 Steels. International Conference on Engineering Research and Practice for Steel Construction 2018 (ICSC2018). Hong Kong SAR, China.

[6] Ho, H. C., **Xiao, M.**, Liu, X., & Chung, K. F. (2017). Tensile Tests on High Strength Steel Materials Using High Precision Measurements. The 15th East Asia-Pacific Conference on Structural Engineering and Construction (EASEC-15). Xi'an, China.

[7] Ho, H. C., Liu, X, **Xiao, M.**, & Chung, K. F. (2016). Experimental Investigation into Hysteretic Behaviour of High Strength S690 Steel under Different Targeted Strains. Eighth International Conference on Steel and Aluminium Structures. Hong Kong SAR, China.

[8] Chung, K. F., Ho, H. C., Liu, X., & **Xiao, M.** (2016). Low Cycle High Strain Cyclic Tests on Steel Coupons of High Strength S690 Steel Welded Sections. Eighth International Conference on Steel and Aluminium Structures. Hong Kong SAR, China.

Journal Papers (in progress):

[1] **Xiao, M.**, Hu, Y. F., & Chung. K. F. (2021). Mechanical Properties of Round Corners of High Strength S690 Steels due to Cold-bending. (under preparation)

[2] **Xiao, M.**, Chung, K. F, & Zhu, M. F. (2021). Structural Behaviour of S690 CFSHS Stocky Columns under Compression. (under preparation)

[3] **Xiao, M.**, Chung, K. F & Shen, M. H. (2022). Experimental-Numerical Investigation into S690 CFSHS Slender Columns under Compression. (under preparation)

[4] **Xiao, M.**, Chung, K. F., & Jin, H. (2022). Measurements and Simulation of Residual Stresses of S690 CFSHS. (under preparation)

[5] **Xiao, M.**, Chung, K. F., & Ho, H. C. (2023). Parametric Studies into S690 CFSHS Slender Columns under Compression. (under preparation)

ACKNOWLEDGEMENTS

Throughout the writing of this Thesis, I have received many supports and assistances from various people who enabled this project to be possible. I would first like to express my sincere gratitude to my research supervisor, Prof. K. F. CHUNG, for providing me with helpful supervision and enthusiastic encouragement to this project. This fifty-four-month research journey guided by him is vital in inspiring me to think outside the box, from multiple perspectives to form a comprehensive and objective critique.

The financial supports from the Research Committee and the Chinese National Engineering Research Centre for Steel Construction (Hong Kong Branch) of The Hong Kong Polytechnic University are acknowledged. Great thanks are given to both Dr. H. C. HO and Ms. Catherine E. NG, for their advices and assistances in keeping my research progress on schedule. In addition, the instruction given by Dr. T. M. CHAN is also acknowledged, for his help in designing my test programmes.

Sincere thanks also go to the technicians of CEE, Mr. M. C. NG, Mr. K. H. WONG, Mr. Y. H. YIU and Mr. K. L. CHEUNG, and the technician of BRE, Mr. C. F. WONG, for their supports in offering me the resources in carrying out the experiments in the laboratories.

My grateful thanks are extended to the members in our research group, for their collaborative efforts to my experimental and numerical investigations. Advices given by my colleagues and seniors Prof. Fei XU, Dr. Minhui SHEN, Dr. Xiao LIU, Dr. Kai WANG, Dr. Yifei HU, Dr. Tianyu MA, Dr. Han FANG, Dr. Huiyong BAN, Dr. Dan GAN, Dr. Xuanding WANG, Dr. Cheng CHEN, Ms. Wei FENG, Mr. Hao JIANG and Mr. Qi YIN have been a great help to my research project. Assistances provided by Ms. Yibin GUO, Ms. Mengfei ZHU, Mr. Hao JIN and Mr. Wei CHEN are also greatly appreciated.

The presence of my friends from PolyU makes me always feel encouraged and brave when facing any difficulty. My grateful thanks go to Dr. Junbo CHEN, Dr. Jiongyi ZHU, Dr. Yuze ZHANG, Dr. Bo LU, Dr. Xu XU, Dr. Xiaoyi LAN, Dr. Feng TIAN, Dr. Wanmai YUAN, Dr. Tianxi CHI, Dr. Xiao LI, Dr. Linhao ZHANG, Ms. Zhihang XUE, Ms. Qi YUAN, Ms. Shiyao WANG, Ms. Qianru DU, Ms. Qin WANG, Ms. Qingyang ZHAO, Ms. Qiuhan MENG, Ms. Yaohan LI, Ms. Xuemei LIN, Mr. Haixin LIU, Mr. Zhuozhi ZHANG, Mr. Lei HUANG, Mr. Keyue CHEN, Mr. Hui ZENG and Mr. Jiahao HUANG, for their pleasant company over the past years.

Finally, I wish to thank my parents for their continuous support and love throughout my research study.

TABLE OF CONTENTS

LIST OF FIGURES

LIST OF TABLES

CHAPTER 1: INTRODUCTION

1.1 Research Background

High strength steels (HSS) are structural steels with their yield strengths equal to or larger than 460 N/mm^2 (see Fig. 1.1), and they have excellent mechanical properties for engineering applications in bridges and buildings. HSS are often considered to be superior to those of normal strength steels (NSS) because of their high yield strengths due to different chemical compositions, delivery conditions and heat treatments during their manufacturing processes. Hence, HSS can provide an efficient solution to structural design by reducing both material cost and fabrication work, when compared with those of NSS. Owing to their high mechanical resistances, they have been widely used in heavily loaded columns in bridges and buildings.

Structural hollow sections have been widely applied in steel construction all over the world, owing to their high resistances against torsion and their desirable architectural appearance. Typical profiles of structural hollow sections are shown in Fig. 1.2, including square hollow sections (SHS), rectangular hollow sections (RHS) and circular hollow sections (CHS). Hot-finishing and cold-forming are two commonly used methods to produce these structural hollow sections. Cold-formed sections are fabricated through either roll-forming or press-braking at ambient temperatures. However, the fabrication processes, the set-up and the environments for hot-finished sections are rather complicated as a series of rolling operations must be done at elevated temperatures. Hence, fabrication of hot-finished structural hollow sections always requires a huge amount of initial capital investment, and it is financially viable only if many million tons of standard sections are produced. As these two kinds of sections are fabricated with different processes, both the material properties and the structural performance of cold-formed sections vary a lot from those of hot-finished sections. It is normally considered that hot-finished sections have a high degree of uniformity in residual stresses, small geometric imperfections and high section and member resistances, when compared with those of cold-formed sections. In terms of deformation capacities, cold-formed sections exhibited lower ductility when compared with those of hot-finished, and this is due to plastic deformations at the corner regions induced during fabrication.

With development of HSS, there has been an increasing number of studies to investigate the benefits of using HSS in both cold-formed sections and hot-finished sections, respectively. However, for cold-formed hollow sections made of HSS, there was a lack of relevant test data as only roll-formed sections in small dimensions formed with thin steel plates were tested so far. This is because the roll-forming method is suitable for manufacturing a large quantity of cold-formed products in identical sizes while the press-braking method is suitable for producing specially designed sections with customized shapes and dimensions. Hence, to achieve an efficient design of cold-formed sections made of HSS, more practical cold-formed sections with press-braking should be tested to provide test data. CFSHS in various sizes are considered to be readily produced through a combination of press-braking and welding in many modern fabricators. Owing to their mechanical properties of HSS, effects of the fabrication process onto HSS CFSHS may vary significantly from those of NSS. In general, current applications of HSS CFSHS are still rather limited due to a lack of comprehensive understanding on their structural behaviour as well as a lack of effective design rules.

In order to promote effective use of high strength S690 steels in construction and to develop a thorough understanding on the structural behaviour of HSS CFSHS, it is therefore proposed to carry out an experimental-numerical incorporated investigation to address the following issues:

i) Plastic strains and residual stresses in S690 CFSHS

During the fabrication process of CFSHS, both transverse bending and longitudinal welding are very important because both the plastic strains and the residual stresses induced by transverse bending and longitudinal welding will significantly affect the structural performance of CFSHS under various loading cases. Cold-working effects are usually quantified by carrying out monotonic tensile tests on curved coupons extracted from the corner regions, and residual stresses are usually measured with physical measurement techniques, such as the sectioning method.

Numerical methods are able to simulate both transverse bending and longitudinal welding of CFSHS, and thus, to accurately predict the plastic strains and the residual stresses in CFSHS with reduced efforts of laboratory works. In consequence, those numerically generated strains and stresses can be incorporated into structural models for detailed structural analyses.

ii) Structural behaviour of S690 both stocky and slender CFSHS columns under compression

Applications of HSS CFSHS are rather limited due to a lack of understanding on their structural behaviour as well as a lack of effective design rules. Although some experimental studies on columns with HSS CFSHS were reported in the literature, most of those cold-formed sections were roll-formed, and few of them were fabricated with press-braking, so their sectional dimensions were normally small. Therefore, it is recommended to carry out full scale tests on both stocky and slender S690 CFSHS columns under compression, and to examine the structural behaviour of different types of CFSHS.

iii) Structural design for S690 CFSHS columns under compression

It is commonly considered that the member resistances predicted by EN 1993-1-1 are conservative. As a result, the current design rules may not be able to fully utilize the high resistances of HSS CFSHS, and thus, they should be improved with evidence acquired from experimental and numerical investigations. After calibrating against the test data, the validated numerical models are employed to perform a parametric study to provide complementary data. Hence, the existing design rules for HSS CFSHS columns under compression will be improved.

1.2 Objectives and Scope of Work

In order to exploit effective use of S690 CFSHS in construction, a comprehensive experimental-numerical incorporated investigation is conducted to examine the structural behaviour of these CFSHS under compression. Effects of fabrication processes, namely, i) transverse bending, and ii) longitudinal welding, onto the structural behaviour of these sections are also examined. New understandings and insights on effective use of these S690 CFSHS are thus generated, and applicability of the current design rules to these sections is verified according to these new findings and data.

- **Task 1: Experimental and numerical investigation into plastic strains and residual stresses in S690 CFSHS**

  To examine mechanical properties of the S690 CFSHS due to i) transverse bending, and ii) longitudinal welding.

- **Task 2: Full scale structural tests on stocky and slender columns with S690 CFSHS under compression**

  To examine section and member resistances of the S690 CFSHS under compression, including i) stocky columns under concentric compression, ii) stocky columns under eccentric compression, and iii) slender columns under concentric compression.

- **Task 3: Numerical modelling on stocky and slender columns with S690 CFSHS under compression**

  To calibrate numerical models against the test data; and to conduct parametric studies with the validated models for design development.

It should be noted that two series of CFSHS, namely, i) Series SA, and ii) Series SB, are examined in the present project, and they are manufactured with components of different sizes and shapes.

1.3 Research Methodology

The research takes the following forms of investigation:

- **Task 1: Experimental and numerical investigation into plastic strains and residual stresses in S690 CFSHS**

  In order to determine mechanical properties in the round corners of the S690 CFSHS, a total of 7 flat coupons extracted from the S690 steel plates and 19 flat and curved coupons extracted from the S690 CFSHS were tested under tension. Complementary numerical models as well as analytical solutions were also developed. These two methods were developed to predict the residual stresses as well as the strength enhancements at these corner regions of the S690 CFSHS with a high degree of accuracy.

  Moreover, the residual stresses in the S690 CFSHS due to i) transverse bending, and ii) longitudinal welding were measured with the sectioning method. It should be noted that both the cold-bending and the welding processes were examined in detail, and key parameters on these two manufacturing processes were recorded. Based on specific heat transfer coefficients and codified thermal properties, sequentially-coupled thermomechanical analyses on these CFSHS were conducted with ABAQUS to predict accurately the residual stresses in these sections.

- **Task 2: Full scale structural tests on stocky and slender columns with S690 CFSHS under compression**

  A total of 38 columns of S690 CFSHS were tested under compression, including i) 8 stocky columns under concentric compression, ii) 6 stocky columns under eccentric compression, and iii) 24 slender columns under concentric compression. Execution of these tests provided a detailed examination on their load-deformation characteristics, in particular, both the section and the member resistances, for calibration of numerical models, and verification of design rules.

- **Task 3: Numerical modelling on stocky and slender columns with S690 CFSHS under compression**

  Advanced numerical models of both stocky and slender columns of these S690 CFSHS were established and validated against the test data obtained in Task 2. A set of parametric studies were then conducted to develop a database on the member resistances of these S690 CFSHS. Both the design rules for section classification and the design rules for member resistances given in EN 1993-1-1 were verified to be applicable to these S690 CFSHS according to both test and numerical results.

1.4 Research Significance

Major academic merits of this research study are:

- This is the first research which systematically investigates residual stresses in S690 CFSHS induced by both transverse bending and longitudinal welding. An experimental-numerical incorporated investigation is carried out to predict the residual stresses and the strength enhancements at the corner regions of these CFSHS.

- Generalized numerical models are developed, which can be directly employed to predict the residual stress distributions of the S690 CFSHS with various combinations of transverse bending and longitudinal welding.

- Structural performance of both the stocky and the slender columns of the S690 CFSHS is examined under compression, and hence, both the section and the member resistances of these columns are obtained as definitive test data for reference.

- Modifications to the current design rules of section classification given in EN 1993-1-1 are proposed to enable effective prediction for their section resistances.

- Current design rules in EN 1993-1-1 are shown to be very conservative in predicting member resistances of slender columns with S690 CFSHS. After calibrating against both test and numerical data, it is proposed to adopt a smaller imperfection factor, when compared with the current value, to achieve an improved design for the members with S690 CFSHS under axial buckling.

Consequently, this study generates new test and numerical data on the structural behaviour of the S690 CFSHS under compression, and the current design rules are confirmed to predict safe section and member resistances of these columns in many cases. Minor modifications to these design rules are also provided to improve their structural efficiency. As a result, engineers are encouraged to take good advantages of HSS CFSHS to use them in construction projects.

1.5 Outline of the Thesis

This Thesis consists of eight Chapters listed as follows:

- **CHAPTER 1: INTRODUCTION**

  This Chapter presents an overview of this research project. The research background, the scope of work, the research methodology, the research significance, and the outline of the Thesis are presented with an overall perspective.

- **CHAPTER 2: LITERATURE REVIEW**

  This Chapter presents a comprehensive literature review on the key studies of HSS CFSHS, including their manufacturing techniques, project applications, experimental investigations, numerical investigations and existing design rules.

- **CHAPTER 3: MATERIAL PROPERTIES, FABRICATION PROCESSES AND RESIDUAL STRESS MEASUREMENTS OF S690 CFSHS**

  This Chapter presents fundamental studies that constitute the basis of the Thesis. Standard tensile coupon tests are carried out to obtain the stress-strain characteristics of the S690 parent plates. The technical details for fabricating S690 CFSHS are also fully presented and discussed, including the R_{in}/t ratios at the corner regions and the welding parameters employed in GMAW. Moreover, the residual stresses in four CFSHS fabricated with different processes measured with the sectioning methods are presented.

- **CHAPTER 4: EXPERIMENTAL INVESTIGATIONS INTO S690 CFSHS COLUMNS**

  This Chapter presents an experimental investigation into section and member resistances of S690 CFSHS under compression. A total of 38 stocky and slender columns are successfully tested under compression. The measured section and member resistances of the columns are compared with their design resistances predicted by EN 1993-1-1. Modifications to the current design rules of section classification are proposed to enable an effective prediction for their section resistances.

- **CHAPTER 5: COLD-BENDING EFFECTS OF S690 CFSHS**

  This Chapter presents an experimental-numerical-analytical investigation into cold-bending effects of CFSHS. A total of 19 flat and curved coupons are tested under uniaxial tension to obtain their stress-strain characteristics. Both 2D and 3D numerical models are established with ABAQUS, to simulate transverse bending in forming round corners of these CFSHS. An integration method is proposed to predict stress-strain characteristics of the corner regions under transverse bending, and this method is also developed into a hand calculation method. Hence, the predictions on strength enhancements at the corner regions are achieved efficiently.

- **CHAPTER 6: THERMOMECHANICAL ANALYSES FOR S690 CFSHS**

  This Chapter presents a theoretical-numerical investigation into the temperatures and the residual stresses of four S690 CFSHS due to welding. The residual stresses are successfully predicted by the validated sequentially-coupled thermomechanical analyses implemented with ABAQUS. Simplified residual stress patterns are proposed and verified, and these patterns are readily adopted for subsequent structural analyses.

- **CHAPTER 7: NUMERICAL INVESTIGATION INTO S690 CFSHS COLUMNS**

  This Chapter presents a numerical investigation into the structural performance of S690 CFSHS columns under compression. A total of 30 numerical models are established and successfully validated against the test data. Extra 52 finite element analyses are performed based on the validated numerical models. Minor modifications are proposed according to a direct comparison among the test data, and the test results of the parametric studies and the design rules to improve the design of S690 CFSHS columns under axial buckling given in EN 1993-1-1.

- **CHAPTER 8: CONCLUSIONS AND FUTURE WORK**

  This Chapter presents the conclusions of this project and the recommendations for the future work into HSS CFSHS.

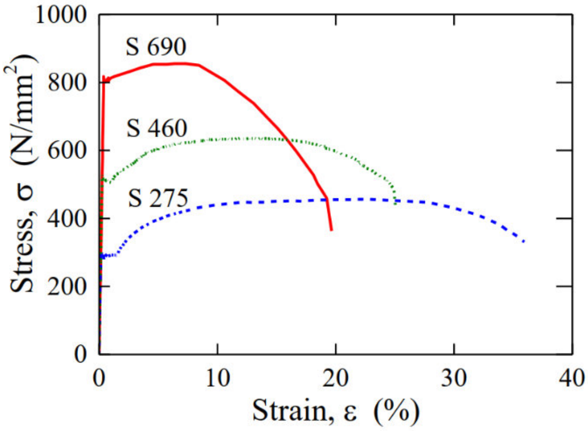

Fig. 1.1 Stress-strain curves for various steel materials

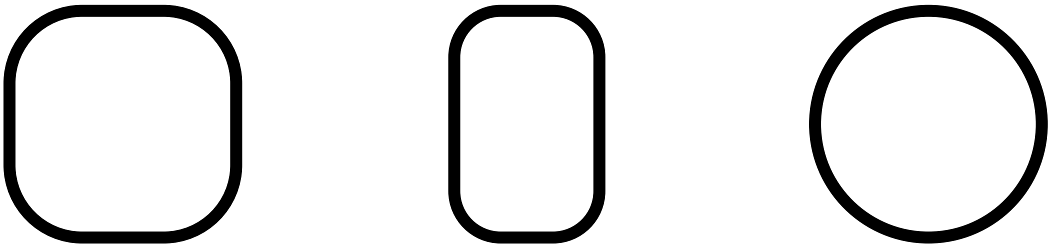

a) SHS b) RHS c) CHS

Fig. 1.2 Typical profiles of structural hollow sections

CHAPTER 2: LITERATURE REVIEW

2.1 Introduction

This Chapter presented a comprehensive literature review on a number of key references on high strength steel (HSS) cold-formed square hollow sections (CFSHS), and a comparison on research backgrounds, project applications, experimental investigations, numerical investigations, and existing design rules given in Eurocode 3 is reported.

Compared with normal strength steels (NSS), HSS have remarkable advantages in construction, due to their excellent mechanical properties, especially, high strength-to-self-weight ratios. Owing to low costs and large resistances per unit weight, HSS can achieve an efficient design for modern structures, and thus, they have already been used in construction of a number of bridges and buildings around the world.

Nowadays, even only CFSHS become very popular in construction because of their low set-up costs in producing several hundred tons of non-standard sections. These CFSHS are readily fabricated with a combination of transverse bending and longitudinal welding in many modern fabricators. Owing to the key features of HSS, the fabrication process of HSS CFSHS may be very different from that of NSS tubular sections. Of the whole fabrication process, cold-forming and welding are regarded as two important procedures, and the technical parameters employed in both processes for HSS CFSHS were reviewed.

Residual stresses induced during fabrication of CFSHS are a critical issue that should be considered carefully, as these affect significantly section and member behaviour. It is important to identify, and thus, quantify the residual stresses induced by transverse bending and longitudinal welding. The commonly used methods for residual stress measurements were reviewed, and by using these measurement techniques, many experimental investigations were carried out on various welded sections made of HSS, as reported in the literature.

With development of advanced finite element analyses, numerical methods had been successfully developed to simulate transverse bending and longitudinal welding of CFSHS. These numerical methods were able to accurately predict the plastic strains and the residual stresses induced during fabrication, and thus, to determine the strains and the stresses in CFSHS with reduced efforts of laboratory works. In consequence, those strains and stresses generated with numerical predictions are incorporated into subsequent structural analyses.

Currently, the applications of HSS CFSHS are rather limited due to a lack of understanding on their structural behaviour as well as a lack of effective design rules. Although some experimental studies on columns with HSS CFSHS were found in the literature, most of the cold-formed sections were roll-formed, and only few were shaped with press-braking. Hence, the range of their sectional dimensions were normally limited. Besides, after reviewing the current design rules, the member resistances predicted by EN 1993-1 were found to be fairly conservative. As a result, the current design rules may fail to fully utilize the high resistances of these HSS CFSHS, and thus, they should be improved according to scientific evidence and test results obtained from experimental investigations.

In summary, only few references were available in the literature, and there was a lack of technical information for improving the design of S690 CFSHS. Therefore, it is proposed to carry out an experimental-numerical-theoretical investigation into high strength S690 CFSHS to improve structural efficiency of the existing design method. It is expected that the current research study can develop an efficient solution to improve the design of HSS CFSHS, and thus, to promote effective uses of these structural sections in construction.

2.2 High Strength Steels

High strength steels (HSS) are structural steels with their yield strengths not less than 460 N/mm^2, performing satisfactory ductility for either conventional plastic design or novel performance-based design in bridges and buildings (Ban and Shi 2017). The mechanical properties of high strength steels (HSS) are superior to those of normal strength steels (NSS) due to different chemical compositions, delivery conditions and heat treatments in their manufacturing processes. The most remarkable advantage of HSS lies in their high resistances per unit weight. By taking good use of this merit, the materials can provide an efficient solution to structural design by reducing both material cost and fabrication work, when compared with those with NSS.

2.2.1 Material properties

a) Chemical compositions

Chemical compositions constitute the basis of steel materials, and a slight change in chemical elements may significantly affect mechanical properties of the steels, such as strength, hardness, ductility, toughness, weldability and corrosion resistances. Many chemical elements are generally considered to be favourable to various mechanical properties. For example, Manganese (Mn) and Nickel (Ni) increase strength; and Vanadium (V) and Chromium (Cr) increase hardness. However, some chemical elements, such as Phosphorus (P), Sulphur (S) and Nitrogen (N), may adversely influence their mechanical properties, mainly ductility and toughness. Hence, the amount of these elements should be controlled precisely during production. EN 10025-2 (CEN 2019a) and EN 10025-6 (CEN 2019c) propose the requirements on chemical compositions for NSS and HSS, respectively, and the corresponding requirements on two typical steel products, namely, S355J0 and S690QL1, are summarized in Table 2.1.

b) Mechanical properties

Standard tensile tests are carried out on steel coupons to determine key mechanical properties of the steel materials, including Young's modulus, yield strength, tensile strength as well as strains corresponding to these strengths and elongation limit. The testing standard given in EN ISO 6892-1 (CEN 2019g) applies for not only NSS but also HSS, and the steel coupons are extracted from base plates or sections according to specific geometrical dimensions.

Fig. 2.1 shows typical engineering stress-strain curves of various steels obtained from standard tensile tests. Obviously, these four grades of steels have consistent initial Young's moduli in their elastic ranges, but they exhibit different hardening behaviour after on-set of yielding. HSS usually have a very short or even no yielding plateau after reaching their proportional limits. It is found that the strain hardening, which is normally quantified with the strength ratio f_u/f_y, i.e. the ratio of the tensile to the yield strengths, decreases as the steel grade increases. Degradation in hardening may result in a low ductility, as commonly exhibited by HSS. Moreover, the overall elongations of HSS are smaller, when compared with those of NSS.

EN 1993-1-1 (CEN 2014) proposes various requirements on both strength and ductility for NSS, as summarized in Table 2.2. However, as HSS are expected to have reduced ductility, EN 1993-1-12 (CEN 2007) proposes some less stringent requirements for HSS, and they are also summarized in Table 2.2.

c) Hysteretic performance under low-cycle high-strain loading

In addition to have high strength-to-self-weight ratios, HSS are also considered to exhibit excellent hysteretic performance under cyclic loading according to some recent experimental studies (Ho et al. 2018, Guo et al. 2020). The results of cyclic tests under low-cycle high-strain actions demonstrated that the deformation characteristics of high strength S690 steels were superior to those of normal strength S355 steels, in terms of hysteretic performance, and thus, HSS should be further explored to be used in the seismic design of modern building structures.

d) Reduced mechanical properties in HAZ

Heat affected zones (HAZ) in welded sections always exhibit certain reduction in mechanical properties, when compared with those of the steel plates or the weld metal. The reductions in both strength and ductility of S690 welded sections were examined in monotonic tensile tests on cylindrical coupons of the welded section which were composed of steel plates, weld metal and HAZ (Liu et al. 2018). This experimental investigation reported that fracture only occurred in the HAZ in almost all the coupons, and the reductions in both strength and ductility in these welded sections became more sever when the heat energy input was increased.

2.2.2 Delivery conditions

Heat treatments are always involved in steel production which determine the delivery conditions of the steel products. Nowadays, QT, i.e. Quenching-and-Tempering, and TMCP, i.e. Thermal-Mechanically-Controlled-Processing, are two widely used heat treatments for manufacturing HSS plates.

QT is a two-stage heat treatment process, which is commonly used for producing low alloy high strength steels (Willms 2009):

- Stage i) - Quenching: a steel plate is heated to approximately 900 °C, which is a temperature above ferrite-austenite transformation. And then, the plate is cooled down under large quantity of high-pressure water to the ambient temperature within a few seconds.
- Stage ii) - Tempering: the quenched steel plate is heated up again to approximately 600 °C, so that the steel plates are rolled under controlled temperatures and forces to gain desired material properties. Toughness and ductility of the steel plates are greatly improved during this tempering process.

TMCP allows microstructural evaluation with rolling and phase transformation control of materials at lower temperatures, when compared with QT. This process requires only small quantities of alloying elements to manage conflicting requirements of strength, toughness and weldability through grain refinement.

It should be noted that QT has been widely used in producing steel plates with a large range of yield strengths, from 235 up to 960 N/mm^2 as shown in EN 10025-6 (CEN 2019c). However, the applications of TMCP in HSS are relatively limited, it is used in producing steel plates with yield strengths merely ranging from 235 to 500 N/mm^2, as shown in EN 10025-4 (CEN 2019b). The technical details of TMCP were systematically reviewed by Nishioka and Ichikawa (2012). Owing to its merits over the conventional heat treatment processes, the on-going developments of TMCP has a great commercial potential to meet the ever-increasing demands of steel products.

2.2.3 Use of HSS in construction projects

HSS have been used as constructional materials in structures all over the world, owing to their remarkable advantages as demonstrated in previous Sections. These high-performance materials meet the requirements on strength and toughness for bridges, and they were employed in several bridges over the past three decades globally (see Fig. 2.2), such as a) Tokyo Gate Bridge in Tokyo, built in 1989 (f_y = 500 to 700 N/mm^2), b) a hybrid bridge in Mittådalen, built in 1995 (f_y = 690 N/mm^2), c) Rhine Bridge in Düsseldorf-Ilverich, built in 2002 (f_y = 460 N/mm^2), and d) Millau Bridge in Millau-Creissels (f_y = 460 N/mm^2), built in 2004.

HSS were also employed in many commercial buildings in the past decade (see Fig. 2.3), including a) Shenzhen Bay Sports Centre in Shenzhen, built in 2010 (f_y = 460 N/mm^2), b) CCTV Headquarters in Beijing, built in 2012 (f_y = 460 N/mm^2), c) SNU Kwanjeong Library in Seoul, built in 2015 (f_y = 800 N/mm^2), and d) Lotte World Tower in Seoul, built in 2016 (f_y = 800 N/mm^2).

Hence, the HSS with yield strengths ranging from 460 up to 800 N/mm^2 have been successfully used in many bridges and buildings in the past decades. These applications prove that HSS, the renewable and high-performance construction materials, have a great potential to be further promoted as they provide an efficient solution to reduce material usage, construction costs and carbon footprint.

2.3 Cold-Formed Square Hollow Sections

2.3.1 Fabrication of CFSHS

a) Cold-forming

- Roll-forming and press-braking

CFSHS are cold-formed sections which are fabricated through either roll-forming or press-braking at ambient temperatures, and then they are welded up to achieve the sections. The roll-forming method is normally achieved with a numerically-controlled production line consisting of specially-designed rollers. ERW, i.e. electric resistance welding, is then performed on the roll-formed shapes, to form the sections. Fig. 2.4 shows two typical roll-forming processes, namely a) direct forming and b) continuous forming, illustrating how to manufacture a CFSHS from a steel plate. The press-braking method imposes a three-point bending force onto a steel plate, shaping it to reach a target corner angle. During this bending process, the plate lays on the die, and then it is pushed downwards and deformed plastically by a punch which moves downwards vertically. After the plate is formed into the target shape, the punch is then removed. Springback always takes place in these bent angles so that the sections of these shapes are slightly modified (see Fig. 2.5).

It should be noted that the roll-forming method is suitable for manufacturing a large quantity of cold-formed products in identical sizes while the press-braking method is suitable for producing specially designed sections with customized shapes and dimensions.

- R_{in}/t ratio

The ratio of inner corner radius to plate thickness, i.e. R_{in}/t ratio, is a very important parameter for CFSHS, especially for HSS plates with limited capacities of plastic deformations. The R_{in}/t ratio is normally regarded as an indicator of quantifying cold-working effects at the corner regions, and a small ratio represents large plastic deformations existing at the corner regions. EN 10219-2 (CEN 2019d) recommends the R_{in}/t ratios for press-braked sections made of NSS as shown in Table 2.3. However, an HSS plate usually has a weaker bendability due to its lower capacity of plastic deformations, when compared with that of an NSS plate. Therefore, special attention should be paid when fabricating hollow sections made of HSS as those established bending requirements for NSS are found not to be applicable to HSS.

Although no supplementary specification is found on the R_{in}/t ratios for press-braked sections made of HSS, some engineering manuals recommended certain ranges of these ratios for HSS, to avoid cracking or waviness on the outer surface of the corner regions. SSAB, an international steel product manufacturer, proposed the lower limits of R_{in}/t ratios for various types of HSS with yield strengths up to 1300 N/mm^2. Strenx 700 steel is a HSS with its yield strength over 700 N/mm^2 while Strenx 960 steel is another HSS with its yield strength over 960 N/mm^2 (SSAB 2017). As shown in Table 2.4, larger R_{in}/t ratios are proposed for steels with higher yield strengths and thicker plates. A detailed discussion on the R_{in}/t ratios of the high strength S690 steels is presented in Chapter 3.

b) Welding

Welding is of vital importance to the structural performance of steel sections. It is appropriate to review carefully relevant specifications and manuals to guarantee welding quality, and thus, adopt proper welding parameters for good quality of steelwork fabrication.

General recommendations for welding are given in EN 1011-1 (CEN 2009a), EN ISO 13916 (CEN 2017) and EN ISO 17662 (CEN 2016), where the detailed requirements on welding procedure, heat energy input and post-welding treatment are specified. For fabrication of structural sections made of HSS, gas metal arch welding (GMAW) and submerged arc welding (SAW) are two commonly adopted welding methods. Normally, GMAW is imposed to plates with thickness not larger than 10 mm, while SAW is employed for the thicker plates. Since all the S690 plates investigated in this project are thinner than 10 mm, only the specifications regarding GMAW are reviewed. The technical details for GMAW are specified in EN 1011-2 (CEN 2001), EN ISO 14175 (CEN 2008) and EN ISO 15609-2 (CEN 2019f).

- Welding electrode for GMAW

The welding electrodes used for HSS should have sufficient yield strength, f_y, tensile strength f_u, and elongation limit, ε_L, so that they can match those of the HSS and thus, avoid any failure before yielding of the parent metal. T Union GM 110 and GM 120 are two electrodes used in GMAW for high strength S690 and S960 steels, respectively. The key mechanical properties given in the product specifications of these two electrodes are listed in Table 2.5. It should be noted that "M21" is a mixture of shielding gases composed of 15 ~ 25 % CO_2 and 75 ~ 85 % Ar, according to the specification for GMAW given in EN ISO 14175 (CEN 2008). As shown in the table, by using "M21" as shielding gases, higher strengths can be guaranteed though there is a slight decrease in the elongation limit, when compared with those using CO_2 as a shielding gas. Also, according to the test results of standard tensile tests reported in the literature, the measured yield strengths of many S690 steels were found to exceed 720 N/mm^2, and some even larger than 770 N/mm^2 (Ho et al. 2020). Therefore, it is reasonable to adopt GMAW for welding S690 sections using the GM 110 electrode, and shielded with a gas mixture of "M21".

- Preheating temperature and interpass temperature

In order to avoid potential hydrogen cracking during welding, the surface temperatures of steel plates before imposing a welding pass should be well controlled. Hence, the temperature before the first and the subsequent welding passes should be monitored. The specification ISO 13916 (CEN 2017) gives both the requirements and the calculation methods on these temperatures. The steel manufacturer SSAB (2010) proposed the requirements on both the preheating temperatures and the interpass temperatures for various types of steels. For those steels with yield strengths over 700 N/mm^2, there is not any specific requirement on these temperatures, and all the welding passes can be completed at ambient temperatures. However, the preheating temperatures and the interpass temperatures are normally recommended in the welding of HSS. A detailed discussion on the preheating temperature and the interpass temperature of high strength S690 steels investigated in this project is presented in Chapter 3.

2.3.2 Measurements of residual stresses in welded sections

Residual stresses are inevitably induced by transverse bending and welding during fabrication. Existing of residual stresses in steel members may adversely influence their overall structural performance under various loading conditions. Therefore, it is important to measure the residual stress distributions with suitable instrumentation, and thus, to assess how these residual stresses affect the structural behaviour of the members.

a) Measurement methods

The methods for measuring residual stresses are generally categorized into three groups: the destructive methods, the semi-destructive methods and the non-destructive methods. (Withers and Bhadeshia 2001, Rossini et al. 2012).

Both the destructive and the semi-destructive methods are dependent on inferring original stresses from displacements incurred by completely or partially relieving stresses through removing materials. These methods rely on the deformations upon removal of the materials from the specimens, which are caused by the releases of the residual stresses. The sectioning method and the hole-drilling method are the representative ones of the destructive method and the semi-destructive method, respectively.

The non-destructive methods bring no damage to a specimen throughout measurement, and these methods normally measure physical parameters related to stresses, such as positions of diffraction peaks. The neutron diffraction method is a representative one, which measures the difference in lattice spacing between a stressed specimen and a stress-free reference specimen, thus, to determine the residual stresses.

b) Recent studies on measurements of residual stresses in HSS welded sections

Typical residual stress patterns are proposed by ECCS (1986), and these patterns are commonly used in numerical modelling for various NSS sections (see Fig. 2.6). However, these typical residual stresses may fail to be applicable to the residual stresses existing in a HSS welded section. Hence, in order to predict appropriate structural behaviour of HSS welded sections numerically, it is necessary to measure the residual stresses in these sections by using various measurement methods. As reported in the literature, the residual stresses in HSS welded sections have been measured by many researchers over the past few years. Table 2.6 summarizes the representative experimental investigations into HSS welded sections conducted over the past decade, covering various steel grades with yield strengths ranging from 420 up to 1100 N/mm^2. Among these investigations, the residual stresses in many types of HSS welded sections were examined, including angles, plate-to-plate joints, T-joints, H-sections, I-sections, box-sections, CFCHS, CFRHS (roll-formed) and CFSHS (roll-formed).

As shown in the table, in addition to typical destructive and semi-destructive measurement techniques, namely the sectioning method and the hole-drilling method, employed by the researchers, the non-destructive technology, namely the neutron diffraction method, was also employed to measure the residual stresses of box-sections with yield strength over 690 N/mm^2 (Khan et al. 2016). It should be noted that normally only the residual stresses on the surfaces of specimens were measured by the conventional methods, but this cutting-edge measurement technique can also properly determine residual stresses throughout the plate thickness.

It was found that the residual stresses in HSS welded sections were normally less severe than those in the similar NSS sections as reported in the literature. Large and highly localized tensile residual stresses were induced in the vicinity of the welding seams after welding due to quick solidification of the welding electrode during cooling down. Also, the tension zones in the HSS sections were significantly smaller in area, when compared with those of NSS sections due to their increased yield strengths. However, only few investigations into HSS CFSHS fabricated with press-braking were found in the literature.

2.3.3 Structural performance of cold-formed sections and hot-finished sections

Structural hollow sections have been widely applied in steel construction all over the world, owing to their high resistances against torsion and their desirable architectural appearance. Among many types of structural hollow sections, hot-finished sections and cold-formed sections are the most popular ones.

As introduced previously, cold-formed sections are commonly fabricated at ambient temperatures by either roll-forming or press-braking. However, the fabrication processes, the set-up and the environments for hot-finished sections are rather complicated as a series of operations must be done at elevated temperatures. It is normally considered that hot-finished sections have a high degree of uniformity in material properties, small geometric imperfections and good section and member resistances, when compared with those in cold-formed sections. However, the fabrication of hot-finished structural hollow sections always requires a huge amount of initial capital investment, and it is only financially viable to produce many million tons of standard sections.

The design resistances given in EN 1993-1-1 (CEN 2014) for columns with cold-formed structural hollow sections under axial buckling are different a lot from those for hot-finished sections because large geometric imperfections are induced into columns during cold-forming. Therefore, the design curves "a_0" or "a" with small imperfection factors, i.e. $\alpha = 0.13$ or 0.21, are adopted for hot-finished sections, while the design curve "c" with a large imperfection factor, i.e. $\alpha = 0.49$, is adopted for cold-formed sections.

The comparison between these two types of steel sections has been a major interest of research in the international community of steel research (Gardner et al. 2010, Quach and Young 2015, Zhang et al. 2016, Yun et al. 2020). It was reported in the literature that the mechanical properties (see Fig. 2.7), the geometric imperfections and the residual stresses (see Fig. 2.8) of cold-formed sections varied a lot from those of hot-finished sections, as these two kinds of sections were fabricated with totally different processes. The previous experimental investigations showed that the cold-formed sections exhibited larger strength but smaller ductility than hot-finished sections at the corner regions of the sections. This was due to the plastic deformations at the corner regions induced during fabrication. Fig. 2.9 shows that the stress-strain curve of a curved coupon extracted from the corner region of a CFSHS is different from that of a flat coupon extracted from the flat portion (Huang and Young 2014). It was found that the curved coupon has larger tensile strength but smaller elongation limit than the flat one. However, uniform mechanical properties were always found throughout the hot-finished sections.

With the development of HSS, there has been an increasing number of studies to investigate the benefits of using HSS in cold-formed sections and hot-finished sections, respectively (Wang et al. 2016, Wang et al. 2017, Meng et al. 2020a). It was reported in the literature that almost all the columns made of HSS, whatever the fabrication processes, had similar buckling behaviour to those made of NSS, as they were shown to be readily designed with the existing design rules for columns under axial buckling. However, for cold-formed hollow sections made of HSS, there was a lack of a suitable database as only roll-formed sections in small dimensions formed with thin steel plates were tested so far. Hence, to achieve an efficient design of cold-formed sections made of HSS, more full-scale cold-formed sections should be tested to provide test data. Besides, it is considered that more unfavoured structural features may be found in those cold-formed sections fabricated with press-braking, when compared with those fabricated with roll-forming. This is because concentrated plastic strains and residual stresses were induced into the corner regions by press-braking (Tong et al. 2012), and such non-uniform distributions of mechanical properties may adversely affect the load-deformation behaviour of these sections. For press-braked CFSHS made of HSS, this unfavoured effect may be further magnified because the mechanical properties of HSS at the corner regions are more sensitive to the initial plastic deformations induced by press-braking, when compared with NSS.

2.4 Simulation of Fabrication Processes for Cold-Formed Square Hollow Sections

2.4.1 Simulation of cold-forming

As introduced in Section 2.3.1, rolling-forming and press-braking are both commonly used fabrication techniques to produce cold-formed sections. Through the use of finite element modelling, both fabrication processes can be simulated numerically. Hence, both the plastic strains and the residual stresses in these sections are readily assessed.

It was reported in the literature that Rossi et al. (2013) carried out a numerical study into roll-forming of thin-walled HSS open sections, to evaluate strength enhancement in their corner regions. Recently, Han et al. (2020) developed advanced 3D numerical models to simulate the roll-forming processes by using ABAQUS/Explicit, and the study had successfully predicted the plastic strains and the residual stresses in CFSHS fabricated with continuous roll-forming and direct roll-forming, respectively.

A numerical study into press-braking in HSS plates was carried out by Quach et al. (2006). The proposed 2D numerical models established with plane strain elements were successfully calibrated against the measurements (Weng and Peköz 1990, Weng and White 1990). Vorkov et al. (2017) further investigated the effects of punch sizes with 2D press-braking models, and suggestions were proposed for bendability of steel plates bent with various punch sizes and corner angles. Recently, Mutafi et al. (2019) developed 3D press-braked bending models, which showed a good agreement with both measured and numerical results. Besides, another recent study developed 3D numerical models which simulated press-braking and welding simultaneously. The models were able to predict distributions of both the plastic strains and the residual stresses of CFSHS columns with a good agreement with measured data (Yao et al. 2019).

2.4.2 Coupled thermomechanical analyses for welding

Over the past few decades, a number of heat source models were developed by many researchers to simulate heat transfer during welding. Coupled thermomechanical analyses were employed to predict the temperature histories and the residual stresses with the use of a double-ellipsoidal heat source model (see Fig. 2.10) proposed by Goldak et al. (1984). Nguyen et al. (1999) proved applicability of this model in a semi-infinite body, but this was only correct when the front and the rear ellipsoids were equal. The model was further developed by Fachinotti et al. (2011) to achieve improved accuracy, and the newly proposed analytical solution was shown to be applicable to the problem of unsteady thermal conduction in a semi-infinite medium.

However, improvement on accuracy of heat source model was found to have only minor improvement on predictions of residual stresses. In general, the researchers in the community of structural steel design tended to employ the original double-ellipsoidal model, i.e. the simple one proposed in 1984, for the analyses of residual stresses. As reported in the literature, the tool has been successfully implemented for various numerical investigations into the residual stresses of HSS welded sections. Lee et al. (2012b and 2014b) employed the heat source model to simulate the residual stresses in HSS plate-to-plate joints. The numerical models were well validated, and they were shown to be able to predict accurate results of the residual stresses under the given conditions of welding. The same heat source model was also employed by Jiang et al. (2017). Numerical predictions were successfully achieved in HSS box sections with two different commercial packages of finite element analyses.

Further numerical investigations into the residual stresses in HSS welded sections were conducted by Liu and Chung (2018). The validated thermomechanical models were well calibrated against the measurements obtained with the hole-drilling method, and the models were capable of accurately predicting the temperature histories as well as the residual stresses in S690 H- and I-sections. Recently, the validated models were further employed to carry out a parametric study, comparing the effects of the steel grades, the welding passes and the heat input energy (Liu et al. 2019). It was found that the residual stresses in S690 H-sections were less pronounced than those in S355 H-sections, and the effects induced by welding passes with different heat input energy were also well demonstrated. Another recent study reported that a sequentially-coupled thermomechanical model was able to incorporate the cold-bending effects into the finite element models (Hu et al. 2020). The residual stresses in S690 cold-formed circular hollow sections (CFCHS) were precisely predicted by a 2D three-roller bending model and also a 3D thermomechanical model. The numerical methods developed in this study proposed an efficient solution to the residual stresses of many types of cold-formed welded sections made of HSS, including circular hollow sections (CHS), rectangular hollow sections (RHS), square hollow sections (SHS), and even polygonal hollow sections.

2.5 Previous Experimental Investigations into Columns with High Strength Steels under Compression

Recently, many experimental investigations were carried out to investigate the structural behaviour of columns with HSS under compression, covering a wide range of steel grades with yield strengths from 420 to 1100 N/mm^2. These investigations were categorized into six groups according to their section types: (1) press-braked channels (Wang et al. 2019, Wang et al. 2020a, Wang et al. 2020b, Zhang et al. 2020a, Zhang et al. 2020b), (2) built-up sections (Ban et al. 2012, Ban et al. 2013, Wang et al. 2014, Shi et al. 2015, Li et al. 2016, Ma et al. 2018), (3) CHS, i.e. circular hollow sections (Pournara et al. 2017, Chen et al. 2020, Meng and Gardner 2020b), (4) HFSHS, i.e. hot-finished square hollow sections (Gkantou et al. 2017a, Gkantou et al. 2017b, Yun et al. 2020), (5) CFSHS, i.e. cold-formed square hollow sections (Ma et al. 2017, Somodi and Kövesdi 2017, Wang et al. 2017, Ma et al. 2019, Meng and Gardner 2020a), and (6) OctHS, i.e. octagonal hollow sections (Fang et al. 2019, Chen et al. 2020, Fang et al. 2020).

Among all these section types, the studies on HSS CFSHS in the literature are considered to be directly relevant to this study. These studies are summarized in Table 2.7, with various details in their test programmes, including the steel grades, the fabrication processes of the sections, the cross-sectional dimensions and the loading cases. It should be noted that, under the row of "Type of test", "stocky-N" denotes those tests of stocky columns under concentric compression; "stocky-N+M" denotes those tests of stocky columns under eccentric compression; and "slender-N" denotes those tests of slender columns under concentric compression. It is summarized that the structural behaviour of HSS CFSHS were sufficient for the uses in engineering project, as reported in the literature.

Similar to many other column tests with HSS reported in the literature, these column tests with HSS CFSHS also covered a wide range of yield strengths from 420 to 1100 N/mm^2. It should be noted that all these cold-formed sections were fabricated with thin plates with their thicknesses up to 8 mm. Also, as limited by the small plate thicknesses, the cross-sectional dimensions were designed to be small in order to avoid any slender parts of the sections. Such a design of CFSHS were attributed to the fact that all those HSS CFSHS were roll-formed, and the manufacturing set-up was readily modified to produce hollow sections of small dimensions. As introduced previously, with press-braking and welding, CFSHS can be manufactured into sections with customized shapes, sectional dimensions and corner radii.

2.6 Existing Design Rules for S690 CFSHS given in EN 1993-1

Eurocode 3 provides technical recommendations for design of buildings and civil engineering works in steels. It works with the principles and the requirements for safety and serviceability of structures given in EN 1990 – Basis of structural design. Eurocode 3 is concerned with requirements for resistance, serviceability, durability and fire resistance of steel structures (CEN 2005). EN 1993-1 consists of a total of 12 parts, among which three parts are related to the design of S690 CFSHS, and they are briefly introduced as follows:

- EN 1993-1-1 gives basic design rules for steel structures with steel grades from S235 to S460 and material thickness $t \geq 3$ mm. It also gives supplementary provisions for structural design of steel buildings (CEN 2014).

- EN 1993-1-5 gives design requirements of stiffened and unstiffened plates which are subjected to in-plane forces (CEN 2019e).

- EN 1993-1-12 gives design rules that can be used in conjunction with other parts of EN 1993-1 to enable structural to be design with steel grades greater than S460 up to S700 (CEN 2007).

The design rules and the corresponding calculation formulae given in these codes of practice are described in following Sections.

2.6.1 Section classification

Clause 5.5 of EN 1993-1-1 gives a general rule of classifying sections into four classes. The role of section classification is to identify the extent to which the resistance and the rotation capacity of a section is limited by its local buckling resistance. Fig. 2.11 given in EN 1993-1-1 defines the compression parts in various sections under compression, and the dimensions of those parts classifying the sections into Class 1 to 4.

In general, all sections with Classes 1, 2 and 3 can mobilize their yield strengths, but differ in developing the plastic resistances and the rotation capacities of their sections. Therefore, sections with Classes 1 to 3 are generally used for structural design with full development on their elastic or plastic resistances. However, the structural behaviour of a Class 4 section is different from these three, in which local buckling occurs before attainment of the yield strength in one or more parts of the section. Hence, reduced sectional properties should be considered in calculation when designing a Class 4 section, so that a safety design by partially utilizing the resistance of the section is achieved. For a Class 4 CFSHS, its effective area and effective elastic modulus are calculated in accordance with the design rules given in Clause 4.3 of EN 1993-1-5. By adopting the effective sectional properties, the section resistance of a Class 4 CFSHS is calculated, and thus, readily used into the design formulae.

2.6.2 Stocky columns under concentric compression

Clause 6.2.4 of EN 1993-1-1 gives the design rules for sections under concentric compression.

$$\frac{N_{Ed}}{N_{c,Rd}} \leq 1.0 \qquad \text{Eq. (2.1)}$$

$$N_{c,Rd} = \frac{A\, f_y}{\gamma_{M0}} \qquad \text{for Class 1, 2 or 3 section} \qquad \text{Eq. (2.2)}$$

$$N_{c,Rd} = \frac{A_{eff}\, f_y}{\gamma_{M0}} \qquad \text{for Class 4 section} \qquad \text{Eq. (2.3)}$$

where

N_{Ed} is the design normal force;

$N_{c,Rd}$ is the design resistance to normal forces of the section for uniform compression;

f_y is the yield strength;

A is the cross-sectional area, for Class 1, 2 or 3 section;

A_{eff} is the effective cross-sectional area, for Class 4 section; and

γ_{M0} is the partial factor for resistance of section whatever the class is, taken to be 1.00.

2.6.3 Stocky columns under eccentric compression

Clause 6.2.9 of EN 1993-1-1 gives the design rules for sections under eccentric compression.

a) For Class 1 or 2 section

$$M_{Ed} \le M_{N,Rd} \qquad \text{Eq. (2.4)}$$

$$M_{N,y,Rd} = M_{pl,y,Rd}\,(1-n)/(1-0.5a_w) \quad \text{but } M_{N,y,Rd} \le M_{pl,y,Rd} \qquad \text{Eq. (2.5)}$$

where

M_{Ed} is the design bending moment;

$M_{N,Rd}$ is the design plastic moment resistance reduced due to the axial force N_{Ed};

$M_{N,y,Rd}$ is the design plastic moment resistance about y-axis reduced due to the axial force N_{Ed} ;

$M_{pl,y,Rd}$ is the design plastic moment resistance about y-axis;

$n = N_{Ed}/N_{pl,Rd}$; and

$a_w = (A - 2bt)/A$, but $a_w \le 0.5$ for hollow sections.

b) For Class 3 section

$$\sigma_{x,Ed} \le \frac{f_y}{\gamma_{M0}} \qquad \text{Eq. (2.6)}$$

where

$\sigma_{x,Ed}$ is the design value of the local longitudinal stress due to moment and axial force.

c) For Class 4 section

$$\frac{N_{Ed}}{A_{eff}\, f_y \,/\, \gamma_{M0}} + \frac{M_{y,Ed} + \, N_{Ed}\, e_{Ny}}{W_{eff,y,min}\, f_y \,/\, \gamma_{M0}} \leq 1 \qquad \text{Eq. (2.7)}$$

where

$W_{eff,y,min}$ is the effective section elastic modulus when subjected to moment about y-axis; and

e_{Ny} is the shift of the y-axis when the section is subjected to compression only.

2.6.4 Slender columns under concentric compression

Clause 6.3 of EN 1993-1-1 gives the design rules for sections under concentric compression.

$$\frac{N_{Ed}}{N_{b,Rd}} \leq 1.0 \qquad \text{Eq. (2.8)}$$

$$N_{b,Rd} = \frac{\chi\, A\, f_y}{\gamma_{M1}} \quad \text{for Class 1, 2 or 3 section} \qquad \text{Eq. (2.9)}$$

$$N_{b,Rd} = \frac{\chi\, A_{eff}\, f_y}{\gamma_{M1}} \quad \text{for Class 4 section} \qquad \text{Eq. (2.10)}$$

$$\chi = \frac{1}{\Phi + \sqrt{\Phi^2 - \bar{\lambda}^2}} \quad \text{but } \chi \leq 1.0 \qquad \text{Eq. (2.11)}$$

$$\Phi = 0.5[1 + \alpha(\bar{\lambda} - 0.2) + \bar{\lambda}^2] \qquad \text{Eq. (2.12)}$$

$$\bar{\lambda} = \sqrt{\frac{A\, f_y}{N_{cr}}} \quad \text{for Class 1, 2 or 3 section} \qquad \text{Eq. (2.13)}$$

$$\bar{\lambda} = \sqrt{\frac{A_{eff}\, f_y}{N_{cr}}} \quad \text{for Class 4 section} \qquad \text{Eq. (2.14)}$$

where

γ_{M1} is the partial factor for resistance of members to instability assessed by member checks;

α is the imperfection factor. Fig. 2.12 shows five design curves for members under axial buckling, and each curve represents an imperfection factor used in calculating χ. For CFSHS, the design curve "c" is adopted, i.e. α is taken to be 0.49; and

N_{cr} is the elastic critical force.

2.6.5 Supplementary to high strength steel

Clause 2.1 of EN 1993-1-12 gives additional notes to Clause 3.2.2 of EN 1993-1-1, proposing lower requirements on strength and ductility for steels with grades greater than S460, but up to S700. Details of these requirements are presented in Table 2.2.

Besides, EN 1993-1-12 does not propose any additional note to the section classification, the design of members under compression, and the design of plated elements for HSS. Therefore, those design rules in EN 1993-1-1 and EN 1993-1-5 described in the last few sections are applicable to steels with grades greater than S460, but up to S700 without any additional restrictions.

2.7 Summary

After reviewing the literature on HSS CFSHS, it is found that there is a lack of study into the structural performance of S690 CFSHS with press-braking so far. Also, the existing design rules for CFSHS is considered to be fairly conservative, and thus, may fail to fully utilize the member resistances under various loading conditions. Hence, it is proposed to examine the structural performance of these CFSHS under compression by carrying out experimental and numerical investigations. After enlarging the database of S690 CFSHS, the design rules for this type of sections are considered to be improved with sufficient scientific evidence.

Besides, the effects induced by the fabrication processes in S690 CFSHS, namely, transverse bending and longitudinal welding, also should be examined. It is highly desirable to evaluate the plastic strains and the residual stresses due to these fabrication processes, by using the measurement techniques and the numerical methods as reported in the literature. The stress-strain characteristics generated by the validated numerical models are readily incorporated into structural analyses, to improve the numerical predictions with a high level of accuracy.

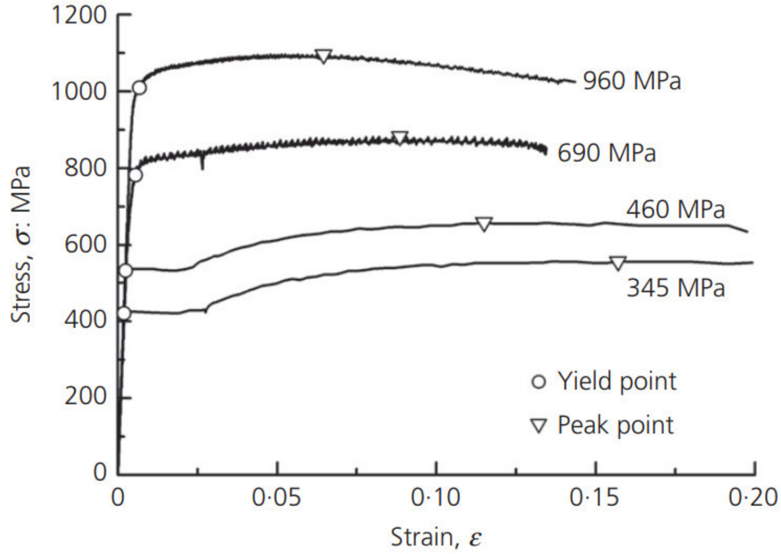

Fig. 2.1 Typical engineering stress-strain curves of steels with various grades (Ban and Shi 2017)

a) Tokyo Gate Bridge,
Tokyo, 1989

b) a hybrid bridge,
Mittådalen, 1995

c) Rhine Bridge,
Düsseldorf-Ilverich, 2002

d) Millau Bridge,
Millau-Creissels, 2004

Fig. 2.2 Bridges built with high strength steels

a) Shenzhen Bay Sports Centre,
Shenzhen, 2010

b) CCTV Headquarters,
Beijing, 2012

c) SNU Kwanjeong Library,
Seoul, 2015

d) Lotte World Tower,
Seoul, 2016

Fig. 2.3 Buildings built with high strength steels

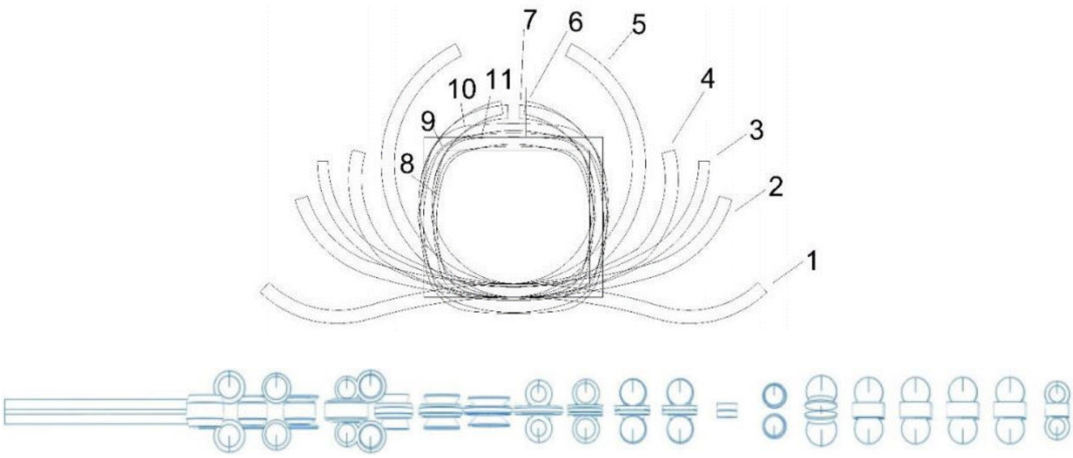

a) indirect forming

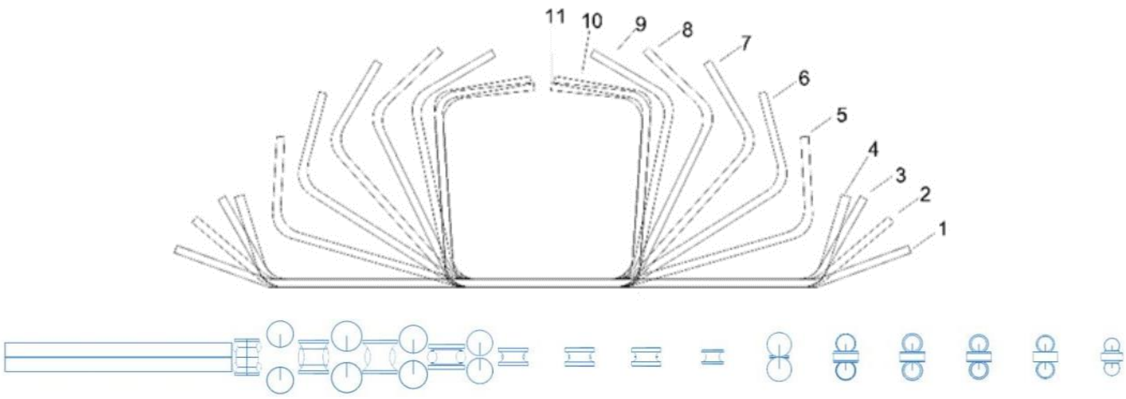

b) direct forming

Fig. 2.4 Sketches of roll-forming (Han et al. 2020)

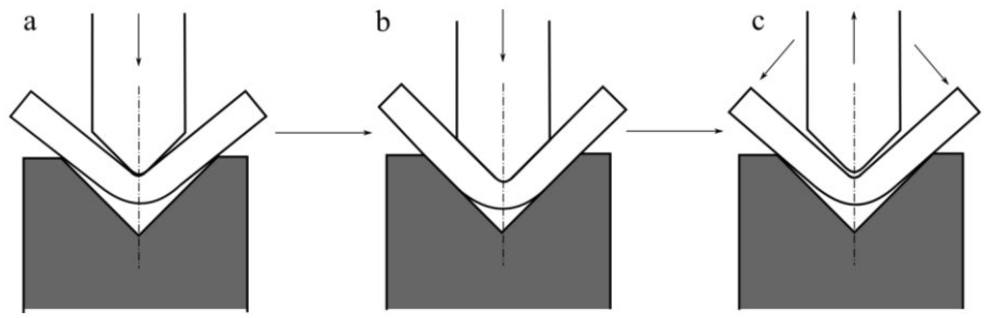

a) moves downwards b) contact c) springback

Fig. 2.5 Sketches of press-braking (Vorkov 2019)

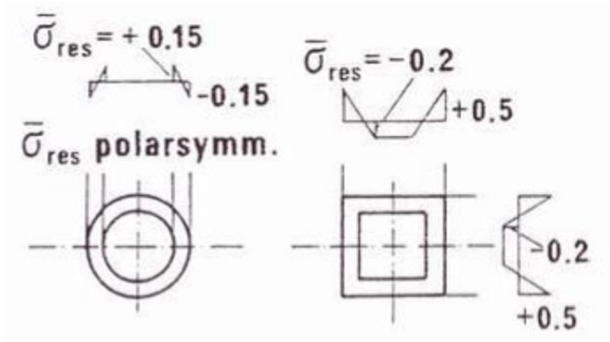

a) tube

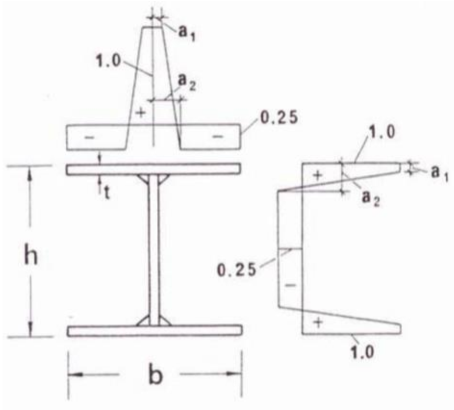

b) welded I-section

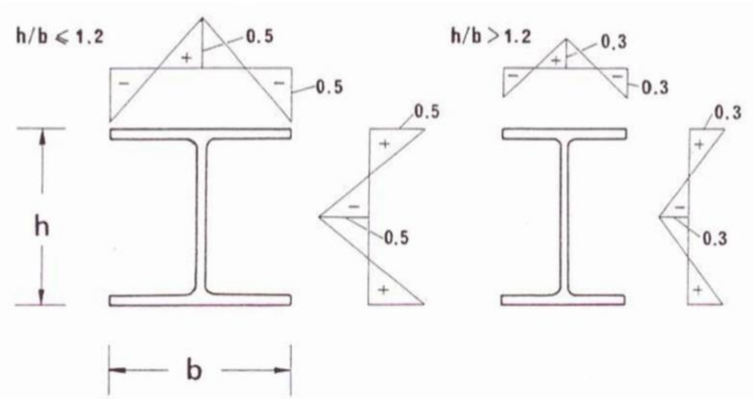

c) rolled I-section

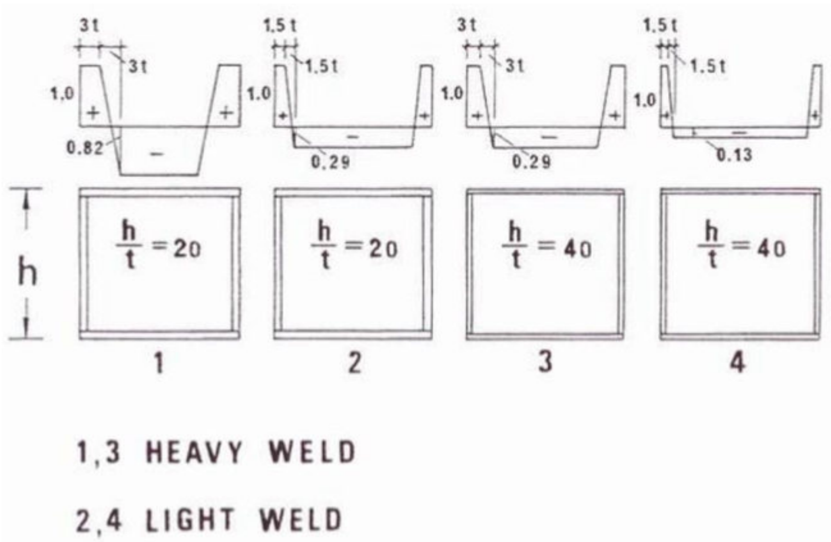

d) welded box-section

Fig. 2.6 Typical residual stress patterns due to welding (ECCS 1986)

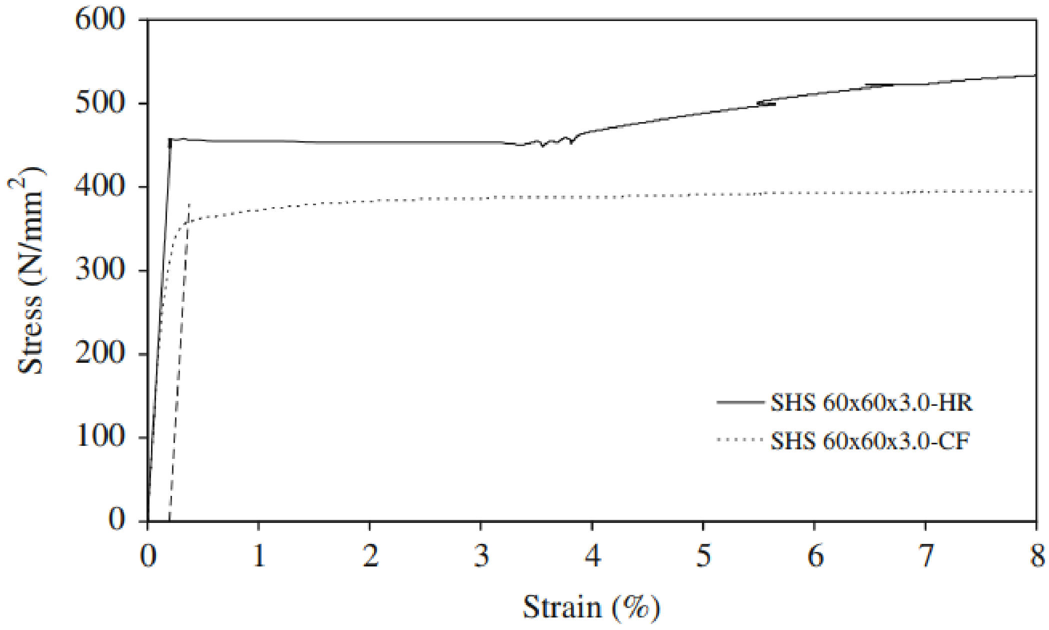

Fig. 2.7 Typical stress-strain curves of coupons extracted from hot-finished and cold-formed steel sections (Gardner et al. 2010)

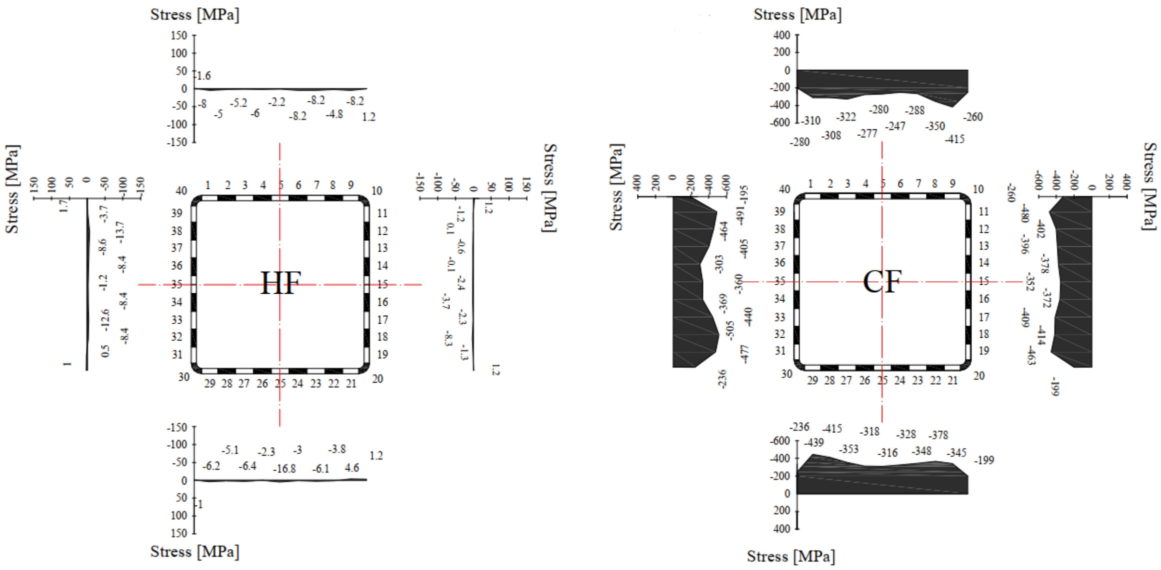

a) Hot-finished section b) Cold-formed section

Fig. 2.8 Typical membrane residual stresses in hot-finished and cold-formed steel sections (Nseir 2015)

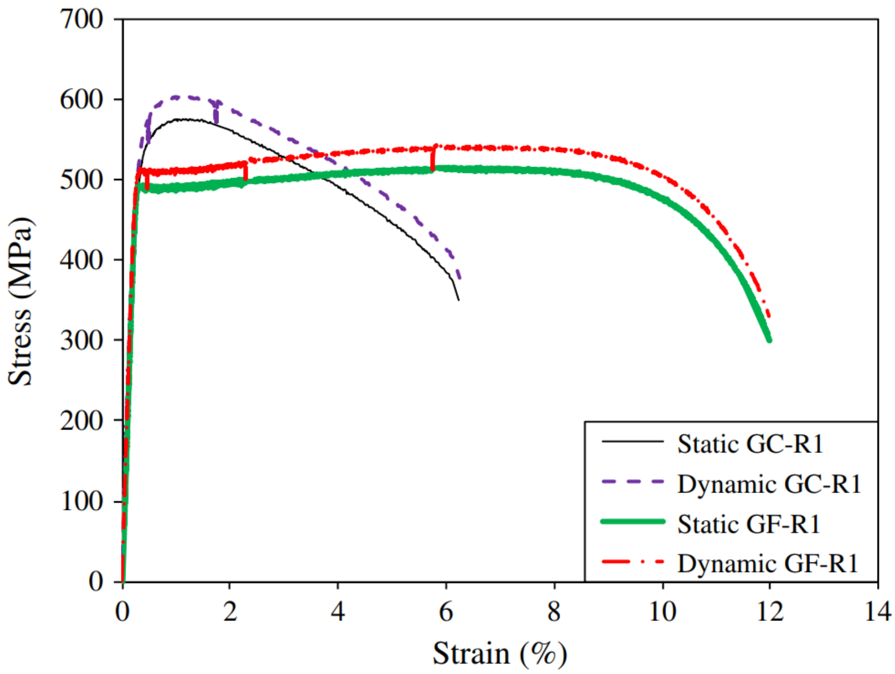

Fig. 2.9 Strength enhancement due to transverse bending (Huang and Young 2014)

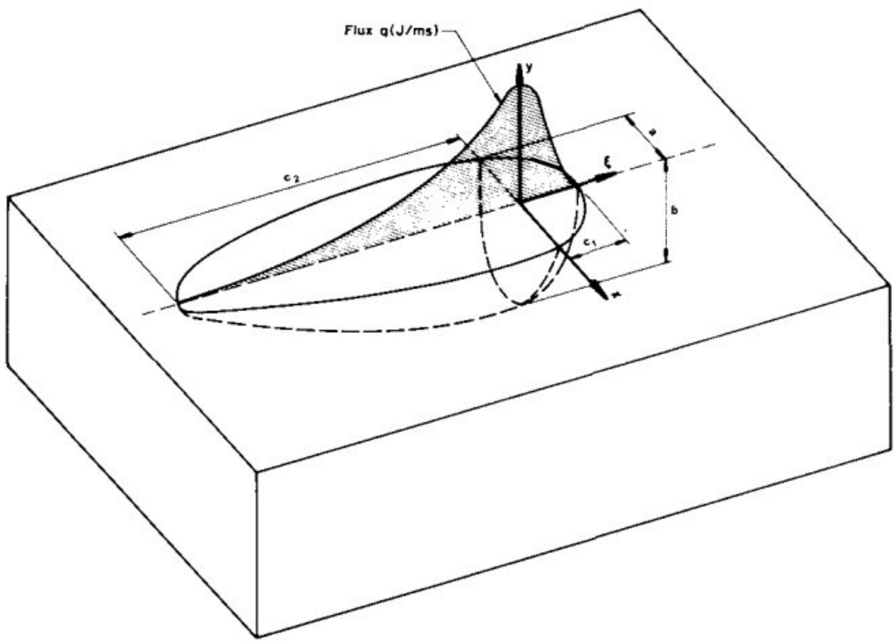

Fig. 2.10 Double-ellipsoidal heat source model (Goldak et al. 1984)

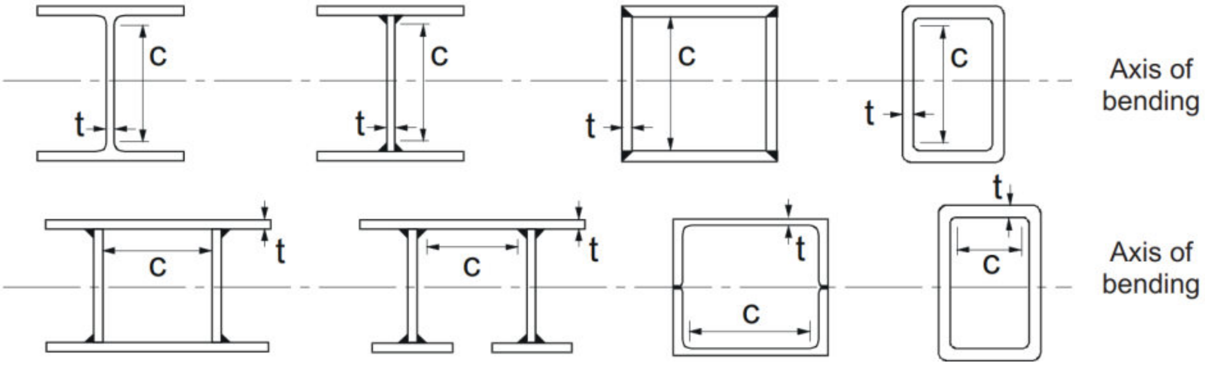

Fig. 2.11 Section classification for compression parts in various sections (CEN 2014)

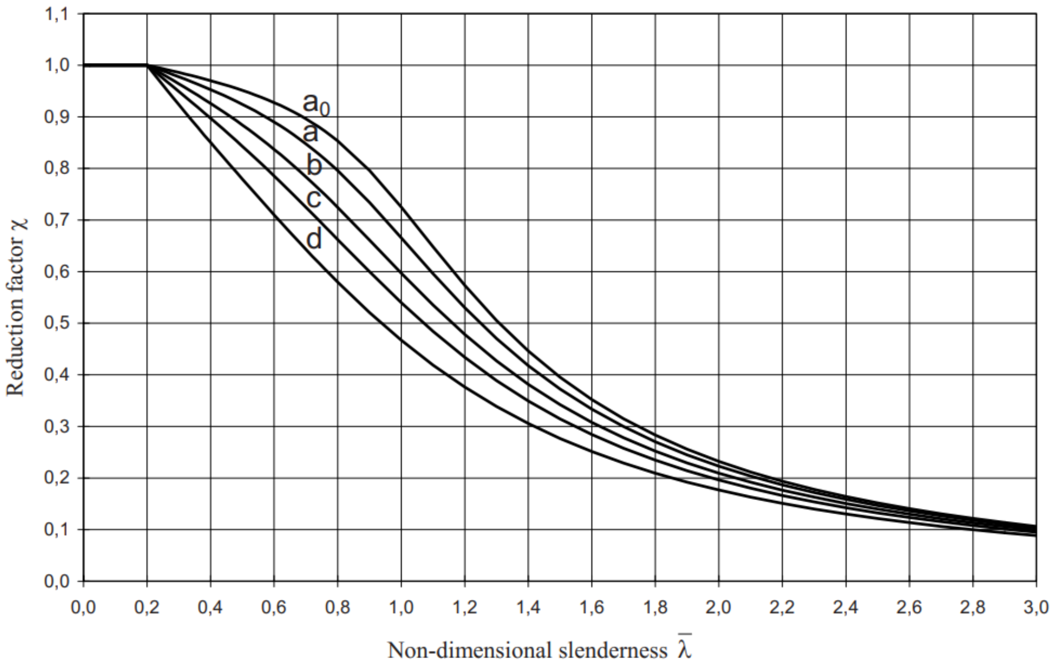

Fig. 2.12 Design curves for members under axial buckling (CEN 2014)

Table 2.1 Requirements on chemical compositions for typical steel products

Specification	Chemical composition (wt %)										
	C	Si	Mn	P	S	Nb	Ti	Cr	Mo	B	CEV
S355J0 (EN 10025-2)	0.23	0.60	1.70	0.040	0.040	--	--	--	--	--	0.45
S690QL1 (EN 10025-6)	0.22	0.86	1.80	0.025	0.012	0.070	0.070	1.60	0.74	0.0060	0.65

Table 2.2 Requirements on mechanical properties of steels given in EN 1993-1

Standard	Steel grade	f_u / f_y	Elongation limit, ε_L	Tensile strain, ε_u
EN 1993-1-1	Smaller than or equal to S460	1.10	≥ 15 %	≥ $15f_y/E$
EN 1993-1-12	Greater than S460, but up to S700	1.05	≥ 10 %	≥ $15f_y/E$

Table 2.3 Tolerances on R_{in}/t ratios given in EN 10219-2

Thickness, t (mm)	R_{in} / t
t < 6	1.6 ~ 2.4
6 < t ≤ 10	2.0 ~ 3.0
10 < t	2.4 ~ 3.6

Table 2.4 Tolerances on R_{in}/t ratios proposed by SSAB

Steel grade	Thickness, t (mm)	R_{in} / t
Strenx 700	t < 15	≥ 2.0
	15 ≤ t	≥ 2.5
Strenx 960	t < 20	≥ 3.0
	20 ≤ t	≥ 3.5

Table 2.5 Key mechanical properties of electrodes T Union GM 110 and GM 120

Electrode	Shielding gas or gas mixture	f_y (N/mm^2)	f_u (N/mm^2)	ε_L (%)
GM 110	M21	≥ 790	≥ 880	≥ 16
	CO_2	≥ 720	≥ 770	≥ 17
GM 120	M21	≥ 890	≥ 940	≥ 15

Table 2.6 Recent studies on measurements of residual stresses in high strength steel welded sections

No.	Literature	f_y (N/mm^2)	Type of welded sections	Measurement method
1	Ban et al. (2012b)	420	angle	sectioning
2	Lee et al. (2012a)	690	plate-to-plate joint	hole-drilling
3	Wang et al. (2012)	460	box section	sectioning
4	Ban et al. (2013b)	460	box section	sectioning
5	Ban et al. (2013c)	460	I-section	sectioning
6	Lee et al. (2014a)	690	T-joint	hole-drilling
7	Li et al. (2015)	690	box and H-section	sectioning
8	Ma et al. (2015)	460, 700 and 1100	CFCHS, CFRHS (roll-formed) and CFSHS (roll-formed)	sectioning
9	Khan et al. (2016)	690	box section	neutron diffraction
10	Yang et al. (2017)	690	box section	hole-drilling and sectioning
11	Somodi and Kövesdi (2017b)	420 to 960	CFSHS (roll-formed)	sectioning
12	Somodi and Kövesdi (2018)	235 to 960	box section	sectioning
13	Liu and Chung (2018)	690	H-section	hole-drilling
14	Chen and Chan (2020)	460, 690 and 960	CFCHS	sectioning
15	Hu et al. (2020)	690	CFCHS	sectioning

Table 2.7 Recent studies on high strength steel CFSHS columns under compression

No.	Literature	f_y (N/mm^2)	Fabrication of section	Section B x H x t	R_{in}/t	Type of test
1	Ma et al. (2017)	700, 900 and 1100	roll-formed SHS	80x80x4 to 140x140x6	1.3 ~ 1.5	(a) stocky-N
2	Somodi and Kövesdi (2017)	420 ~ 960	roll-formed SHS	100x100x3 to 150x150x8	1.1 ~ 1.7	(c) slender-N
3	Wang et al. (2017)	500, 700 and 960	roll-formed SHS	100x100x4 to 150x150x7	0.9 ~ 1.6	(a) stocky-N
4	Ma et al. (2019)	700, 900 and 1100	roll-formed SHS	80x80x4 to 140x140x6	1.3 ~ 1.5	(b) stocky-N+M
5	Meng and Gardner (2020a)	690 and 770	roll-formed SHS	100x100x4 and 120x120x6.3	1.5 ~ 2.0	(a) stocky-N, and (c) slender-N

Note:
“N” denotes axial compression; and
“M” denotes bending moment.

CHAPTER 3: MATERIAL PROPERTIES, FABRICATION PROCESSES AND RESIDUAL STRESS MEASUREMENTS OF S690 CFSHS

3.1 Introduction

This Chapter presented fundamental studies that constitute the basis of the Thesis. In this project, cold-formed square hollow sections (CFSHS) were manufactured for various forms of experimental investigations, including residual stress measurements, curved coupon tests, stocky column tests and slender column tests. All these CFSHS were made of high strength S690 steel plates from the same batch. To determine the mechanical properties of those S690 steel plates, standard tensile coupons extracted from 6 and 10 mm thick plates were tested. By converting the engineering stress-strain curves into the true stress-strain curves, the constitutive models of the S690 steels were proposed, which were used to evaluate section resistances and member resistances of these S690 CFSHS in subsequent chapters.

Technical details in fabricating CFSHS were fully discussed. After considering appearance of these sections and deformation capacities of these S690 steels, the inner radius R_{in} at 3.0t was selected for all corners. Besides, the welding parameters were also presented, including arrangement of welding passes, heat input energy, preheat temperatures and composition of shielding gases.

Moreover, the residual stresses in four CFSHS fabricated with different processes were measured with the sectioning method. In subsequent chapters, all of these fabrication processes were simulated numerically, and a comparison on residual stresses was made between the measurements and the numerical results.

3.2 Material Properties of S690 Steels

3.2.1 Test programme, set-up and procedures

Since all the cold-formed square hollow sections (CFSHS) investigated in this project were made of 6 and 10 mm thick high strength S690 steel plates from the same batch, key material properties of these steel plates were determined for subsequent analyses. The chemical compositions of the 6 and the 10 mm thick plates are summarized in Table 3.1. It is found that the steel plates are able to satisfy all the requirements on the maximum chemical compositions given in EN 10025-6 (CEN 2019c). To determine the mechanical properties of these steel plates, a total of seven standard tensile coupons were tested. The geometric dimensions of these coupons were designed in accordance with EN ISO 6892-1 (CEN 2019g). As illustrated in Fig. 3.1 a), two series of rectangular-shaped coupons are adopted, and the gauge lengths of these two series of coupons are both 50.00 mm, where Series R06 consists of three coupons extracted from a 6 mm thick plate, and Series R10 consists of four coupons extracted from a 10 mm thick plate. The test set-up is illustrated in Fig. 3.1 b), including a tensile machine, a digital camera, a control panel, an extensometer and a coupon. An advanced servo-hydraulic fatigue testing system – Instron 8803 is employed to apply static monotonic tensile force onto the coupons. The digital camera mounted in front of the testing system is employed to obtain instantaneous dimensions of the coupons throughout the tests, and the method is introduced in detail in Section 3.2.3.

During the tests, the straining rates are precisely controlled with an extensometer Instron 2630-112. Technical specifications of the extensometer are listed as follows:

Gauge length:	50.00 mm ± 0.25 mm
Travel range:	-2.50 mm (in compression) to +25.00 mm (in tension)
Strain range:	-5 % to +50 %

It is required that a very slow straining rate should be maintained throughout testing, i.e. from loading initiation to failure of the coupon. It should be noted that the straining rates employed in the present project are slower than those recommended in EN ISO 6892, such that consistent mechanical properties are obtained from the coupons extracted from the same plate. Prior to yielding, the coupon is loaded with a tension force under a constant straining rate at 0.05 %/min, and this allows plotting of a stable stress-strain curve within the elastic range to determine the Young's Modulus accurately. After yielding, the straining rate is increased up to 0.50 %/min, to readily obtain the full-range stress-strain curve of the coupon until failure.

3.2.2 Test results

Key mechanical properties of these coupon tests are summarized in Table 3.2, and the results are directly compared with the requirements given in EN 1993-1-12 (CEN 2007). It is summarized in Table 3.2 that all the mechanical properties, including Young's modulus E, yield strength f_y, tensile strength f_u, elongation limit ε_L and tensile strength-to-yield strength ratio f_u/f_y, meet the requirements.

All measured stress-strain curves of the coupons and their deformed shapes at failure are shown in Figs. 3.2 a) and b), and it should be noted that very little variation in the engineering stress-strain properties (such as strength, hardening and ductility) is found among the same series of tests. Hence, the mechanical properties of this batch of S690 steel plates are highly consistent. By comparing these two series of tests, some minor differences are found. As shown in Fig. 3.2 a), no yielding plateau is found in the coupons extracted from the 6 mm thick plate, though there is significant hardening. However, as shown in Fig. 3.2 b), all the coupons extracted from the 10 mm thick plate exhibit a sharp yielding point, and a yielding plateau with at about 1.5% strain.

3.2.3 True stress-strain properties and constitutive models

3.2.3.1 True stress-true strain curves

The purpose of carrying out standard tensile tests is to determine the mechanical properties of the S690 steels used for fabricating CFSHS, and thus the section resistances and the member resistances are readily predicted. Moreover, accuracy of nonlinear finite element analyses highly relies on the constitutive models of the steels. In some cases, engineering stress-strain curves may be simply incorporated into finite element analyses to generate numerical results with good precision, but accuracy of this simplification depends on the extent of deformation. In particular, when the steel undergoes a very plastic deformation after yielding up to 5%, the engineering stress-strain curve fail to properly describe its structural behaviour. To solve this problem, an incorporation of true stress-strain curves allows for the use of the post-necking deformation characteristics, thus enabling precise simulation in the nonlinear finite element analyses.

The key mechanical properties of engineering stress-strain curves have been well demonstrated as above-mentioned in Section 3.2.2. The transformation from engineering stress-strain curves to true stress-strain curves employs an integration method (Bridgman 1952, Ling 1996), and they are given in:

$$\varepsilon_t = \ln (1+\varepsilon_e) \qquad \text{Eq. (3.1)}$$

$$\sigma_t = \sigma_e (1+\varepsilon_e) \qquad \text{Eq. (3.2)}$$

where

ε_e is the engineering strain;

ε_t is the true strain;

σ_e is the engineering stress; and

σ_t is the true stress.

It should be noted that the application of Eqs. (3.1) and (3.2) is limited with some assumptions. This set of transformation formulae are only applicable when the steel undergoes small deformations, i.e. smaller than 5%. After the on-set of necking, the plastic deformation along the coupon is no longer uniform across its cross-section, so that another set of formulae Eqs. (3.3) and (3.4) should be used to reflect the true stress-strain characteristics beyond necking (Bridgman 1952, Ling 1996):

$$\varepsilon_t = \ln (A_0 / A_i) \qquad \text{Eq. (3.3)}$$

$$\sigma_t = N_i / A_i \qquad \text{Eq. (3.4)}$$

where

A_0 is the original cross-sectional area;

A_i is the measured instantaneous cross-sectional area at the location where necking occurs; and

N_i is the applied load corresponding to A_i.

Throughout the tensile coupon tests, the instantaneous cross-sectional dimensions at the critical location were recorded at small time intervals. High-resolution photos were captured during the test at an interval of 30 seconds, taken with a high-quality digital camera mounted in front of the coupon (see Fig. 3.1). After substituting the measured instantaneous cross-sectional areas and the applied loads into two sets of transformation formulae, the true stress-strain curves of the standard coupon tests are readily generated. Figs. 3.3 a) and b) show typical comparisons between the engineering stress-strain curves and true stress-strain curves for coupons R06 and R10, respectively. Obviously, the true stress-strain properties provide more data describing the stress-strain relationships at large deformations, and there is no significant difference in these two coupons. It should be noted that these true stress-strain curves are fitted among discrete data, and these curves may be directly incorporated into finite element models as the constitutive models of the S690 steels.

3.2.3.2 Proposed constitutive models of S690 steels

As the integrated true stress-true strain curves have incorporated the post-necking stress-strain behaviour, this constitutive model is readily employed in a finite element model that can properly reflect structural behaviour of S690 steels at large deformations. However, it is rather time-consuming and impractical to transform massive test results from engineering stress-strain curves to true stress-strain curves in accordance with the image processing method. Therefore, it is highly desirable to develop alternative constitutive models with a balance of high efficiency and high accuracy. Hence, the constitutive models of S690 steels with different levels of simplicity are presented, to deal with various problems depending on their complexity.

Three commonly used simplified constitutive models (see Fig. 3.4) have been developed to describe the stress-strain curves prior to the on-set of necking over the past few decades. These simplified models have good performances on modelling the structural behaviour of members made of normal strength steels. According to these poly-linear constitutive models, two simplified constitutive models for hot-rolled steels have been developed by Yun and Gardener (2017), making good predictions to the pre-necking stress-strain relationships covering a large range of steel grades from S355 to S960. However, as discussed before, the major weakness of those abovementioned simplified models is that they fail to predict the post-necking stress-strain behaviour accordingly at large deformations.

In the present project, two kinds of constitutive models considering both pre-necking and post-necking stress-strain relationships of S690 steel plates are proposed, which are also named as full-range constitutive models, for S690 steels. One of them has been fully discussed in the previous sections, and this model allows transformation from the engineering stress-strain curve of a tensile coupon using the integration method and the image processing method. Another full-range model is a simplified version developed from the former one, which is a stepwise function consisting of only five poly-lines as defined in Eq. (3.5) (Ho et al. 2020). Compared with the former one, this simplified model is readily established. By incorporating this model into numerical analyses, it is shown that the results match very well with the test results of many standard tensile coupons. The effectiveness of the constitutive proposed models with different levels of simplicity are compared and evaluated with numerical analyses in subsequent chapters.

$$\sigma_{nt}(\varepsilon) \begin{cases} \sigma_{nt} = \varepsilon_{nt} & \text{for} \quad \varepsilon_{nt} \leq 1 \\ \sigma_{nt} = 1.0 + 0.003\,(\varepsilon_{nt} - 1) & \text{for} \quad 1 < \varepsilon_{nt} \leq 6 \\ \sigma_{nt} = 0.91 + 0.0212\,\varepsilon_{nt} - 0.000625\,\varepsilon_{nt}^2 & \text{for} \quad 6 < \varepsilon_{nt} \leq 18 \\ \sigma_{nt} = 1.09 + 0.0012\,(\varepsilon_{nt} - 18) & \text{for} \quad 18 < \varepsilon_{nt} \leq 80 \\ \sigma_{nt} = 1.165 + 0.0011\,(\varepsilon_{nt} - 80) & \text{for} \quad 80 < \varepsilon_{nt} \leq 330 \end{cases} \qquad \text{Eq. (3.5)}$$

where

ε_{nt} is the normalized true strain, $\varepsilon_{nt} = \varepsilon_t \cdot E/f_y$; and

σ_{nt} is the normalized true stress, $\sigma_{nt} = \sigma_t/f_y$.

3.3 Fabrication Processes of S690 CFSHS

3.3.1 Fabrication processes

Two different series of cold-formed square hollow sections (CFSHS) are under investigation, and they are regarded Series SA and SB. These two series of sections are identical in their nominal cross-sectional dimensions, but they are fabricated with different combinations of transverse bending and longitudinal welding, as shown in Fig. 3.5. For those sections of Series SA, two welds are made onto a pair of identical cold-bent C-shaped channels. For those sections of Series SB, a U-shaped channel is cold-bent, and then welded onto a flat plate at both edges. The key differences between these two series of sections are: i) Series SA sections are bi-axially symmetrical while Series SB sections are uni-axially symmetrical; and ii) Series SA sections have four cold-bent corners together with two butt-welded side joints while Series SB sections have only two cold-bent corners together with two butt-welded corner joints.

Fig. 3.6 illustrates the typical fabrication process of a CFSHS. It is shown in Fig. 3.6 a) that a cold-bent channel is cold-bent with a press-braking machine. Two punches with inner radii R_{in} of 18 and 30 mm are employed for the transverse bending of the 6 mm and the 10 mm thick plates, respectively. Therefore, all cold-bent sections are fabricated with an inner radius R_{in} of 3.0t, and an outer radius R_{out} of 4.0t, as shown in Fig. 3.6 b). After completing the transverse bending, these sections are welded with multiple-pass longitudinal welding. Fig. 3.6 c) shows the process of gas metal arch welding (GMAW) with shielding gases as a mixture of 15% CO_2 and 85% Ar, according to EN ISO 14175 (CEN 2008). Six thermocouples are placed onto the surface of a CFSHS to record the temperature history in the vicinity the weld seam during welding. Technical parameters of both transverse bending and longitudinal welding are presented in detail in the following sections.

3.3.2 Transverse bending

When designing a CFSHS, the range of R/t ratios should be discussed in detail as this ratio plays an important role in not only fabrication quality but also section classification. On one hand, if R/t ratio increases, the flat part of CFSHS takes up a reduced portion while the corner part takes up more. An extreme case is that a square hollow section with its maximum R/t ratio may turn itself into a circular hollow section. On the other hand, R/t ratio should not be very small because reducing R/t ratios will amplify plastic deformations within the cold-bent corners. If R/t ratio is so small that its plastic deformation exceeds the plastic deformation limit of the steel, undesirable features such as waving and cracking may occur on both surfaces of the corners after cold-bending. In EN 10219-2 (CEN 2019d), various ratios of the inner corner radius to the plate thickness, R_{in}/t, are proposed for normal strength steels with different plate thickness. For plates with a thickness from 6 to 10 mm, $1.0 \leq R_{in}/t \leq 2.0$ is recommended. However, these ratios should not be directly adopted to a cold-bent section made of S690 steels, because a reduced deformation limit is generally expected for in high strength steels. Fig. 3.7 shows cracking along the bending axis of a S690 steel plate with small R/t ratios. Figs. 3.7 b) and c) show the cracked outer surfaces of the corner with R_{in}/t equalling to 1.5 and 1.0, respectively. An experimental-numerical incorporated investigation on bendability of 6 to 10 mm thick S960 steel plates proposed minimum requirements on the R_{in}/t ratios (Arola et al. 2015). It was proposed that, to avoid surface cracking, the minimum R_{in}/t should be limited to 3.5; to avoid waving on surface, the minimum R_{in}/t should be limited to 3.0. Therefore, R_{in}/t = 3.0 for 6 and 10 mm thick S690 steel plates is adopted in this project.

3.3.3 Longitudinal welding

In order to control quality of welding, the arrangement of welding passes, linear heat input energy, preheating temperatures and interpass temperatures should be properly designed in accordance with various relevant codes of practice and professional manuals.

a) Welding passes

A total of four kinds of multi-pass gas metal arc welding (GMAW) are adopted in this project, and they are applicable to the welds at two different locations on 6 and 10 mm thick plates. Both the sequences and the locations of these welding passes are illustrated in Fig. 3.8. Ceramic backings were attached onto the bottom surfaces prior to welding. These four kinds of welding all start with a backing weld, i.e. the first welding pass, sequentially overlaid with the next one or two welding passes, depending on the plate thickness. Due to a small volume of the backing weld, both the voltage and the current of the first pass are smaller than those of the subsequent passes. It should be noted that the linear heat input energy, q, is a controlling parameter that always significantly affect the mechanical properties of fabricated sections. The linear heat input energy, q, is defined as follows:

$$q = \eta \cdot U \cdot I / v \qquad \text{Eq. (3.6)}$$

where

q is the linear heat input energy (kJ/mm);

η is the efficiency of welding, normally taken 0.80 ~ 0.90 for GMAW;

U is the voltage (V);

I is the current (A); and

v is the speed of welding (mm/s).

It is reported in the literature (Liu et al. 2018) that high heat energy input of GMAW will induce changes to the microstructures of the heat-affected zones in a welded sections S690 steels, thus reducing the mechanical properties of the welded sections. For 16 mm thick S690 steel plates, insignificant degradation in the mechanical properties of these welded sections was found when q does not exceed 1.5 kJ/mm. Therefore, it is proposed to adopt q = 1.5 kJ/mm as an upper limit for GMAW in the present project.

b) Preheating temperature and interpass temperature

Hydrogen cracking may occur during welding, and it has adverse influence on the as-welded sections. An effective means to avoid hydrogen cracking is to apply preheating to the section to delay cooling of the welded sections, and thereby promote hydrogen effusion to a large extent in a short time after welding. For multi-pass welding, it is possible to start welding without preheating if sufficiently high interpass temperatures are reached and maintained with a suitable welding sequence, as given in EN 1011-2 (CEN 2001).

- Preheating temperature, T_p

The minimum preheating temperatures are calculated with Eq. (3.7)

$$T_p = 697CET + 160\tanh(t/35) + 62HD^{0.35} + (53CET-32)q-328 \qquad \text{Eq. (3.7)}$$

where

CET is the carbon equivalent value (%) defined in Eq. (3.8);

t is the plate thickness (mm);

HD is the hydrogen content (ml/100g), and it is equal to be 4 here; and

q is the linear heat input energy (kJ/mm), and it is taken to be1.5 here.

$$\mathrm{CET} = \mathrm{C} + \frac{\mathrm{Mn} + \mathrm{Mo}}{10} + \frac{\mathrm{Cr} + \mathrm{Cu}}{20} + \frac{\mathrm{Ni}}{40}\ (\%) \qquad \text{Eq. (3.8)}$$

After substituting the values into the carbon equivalent value CET and the minimum preheating temperatures T_p for 6 and 10 mm thick plates are presented in Table 3.3. Since preheating temperatures of both the plates are smaller than the room temperature of 23℃, it is not necessary to preheat the plates prior to welding.

- Interpass temperature, T_i

Since preheating is optional for the welded sections in this project, sufficiently high interpass temperatures should be maintained between welding passes. It is found that the mechanical properties and the thermal hydrogen effusion properties of the S690 steels are very similar to those of Weldox 700 steels, so the interpass temperatures in this project are determined by referring to the Welding Handbook - Hadox and Weldox (SSAB 2010). Although it is recommended that the minimum interpass temperatures for both plates are under the room temperature at about 23 °C, an interpass temperature, T_i = 100 °C is still adopted for all welds in this project, to further delay the cooling and promote the hydrogen effusion to a large extent after welding.

3.4 Residual Stress Measurements of S690 CFSHS

Residual stresses are measured with various methods as introduced in the literature review. Determination on residual stress distributions of a welded section or a structural member under a specific fabrication process allows a good understanding onto their structural performances. In this project, the sectioning method is employed to measure the residual stress distributions of the S690 CFSHS fabricated with different combinations of transverse bending and longitudinal welding.

3.4.1 Research programme

A total of four sections are investigated in this project. Table 3.4 presents the overall programme, demonstrating various fabrication processes of these sections and experimental measurements onto them. Two welded sections (Sections SA and SB) and two sections without welding (Sections SA-nw and SB-nw) are investigated, so that the residual stresses induced with transverse bending and longitudinal welding are decoupled, and thus evaluated independently. The nominal cross-sectional dimensions of these four sections are shown in Fig. 3.9.

It should be noted that the residual stress distributions along the length of the specimens are not perfectly uniform. Unstable welding parameters are often found at both the start of and the end of welding, and this disturbance may result in untypical residual stress distributions at these locations. To avoid such an end effect, all specimens are designed to be 760 mm long, and only the residual stresses at the mid-span are measured. As shown in Fig. 3.10, 250 mm portions are cut off from both ends, and the central 260 mm portions are used for residual stress measurements. Therefore, the measured residual stresses at the mid-span of the specimens are regarded typical patterns of these sections fabricated with transverse bending and longitudinal welding.

Details of transverse bending and longitudinal welding are discussed in Section 3.3, including R/t ratios at corner region, interpass temperatures and shielding gases. The sketches of the three-pass GMAW in Sections SA and SB are shown in Fig. 3.8. Also, to avoid significant degradation of the mechanical properties in the vicinity of the heat affected zones of the welded sections, the linear heat input energy are controlled not to exceed 1.5 kJ/mm, and specific welding parameters of each welding pass for Sections SA and SB are recorded, as summarized in Table 3.5.

3.3.3 Residual stresses measured with the sectioning method

3.3.3.1 Test programme

The residual stress measurements of four sections were achieved with the sectioning method. To measure the residual stresses of these sections, they were cut into a total of 99 strips, with strain gauges attached onto both the outer and the inner surfaces at the mid-length of each strip. The width of a strip ranges from 7.0 to 15.0 mm. It should be noted that only a quarter or a half of the section is adopted to be measured because of symmetry of the residual stress distributions in these four sections. Detailed arrangements of the strips are shown in Fig. 3.11. For Sections SA and SB, due to large residual stress gradients in the vicinity of the welds, the strips become increasingly narrow as approaching the weld. For the other two sections without welding, i.e. Sections SA-nw and SB-nw, the arrangements of the strips are kept in line with those with welding.

3.3.3.2 Test set-ups and procedures

A wire cutting machine is employed to cut the sections into strips. As shown in Fig. 3.12, the strain gauges are covered by a waterproof tape before cutting, and a coolant is also applied during cutting to minimize any heat generated. The deformed strips cut from Sections SA-nw and SA are shown in Fig. 3.12.

3.3.3.3 Test results

a) residual strains

Strain readings on both the outer surfaces and the inner surfaces of each strip were recorded before as well as after cutting, respectively. The residual strains on both surfaces are calculated using the following formulae:

$$\varepsilon_o = \varepsilon_{o,1} - \varepsilon_{o,2} \qquad \text{Eq. (3.9)}$$

$$\varepsilon_i = \varepsilon_{i,1} - \varepsilon_{i,2} \qquad \text{Eq. (3.10)}$$

where

ε_o is the residual strain on the outer surface;

$\varepsilon_{o,1}$ is the strain on the outer surface before cutting;

$\varepsilon_{o,2}$ is the strain on the outer surface after cutting;

ε_i is the residual strain on the inner surface;

$\varepsilon_{i,1}$ is the strain on the inner surface before cutting; and

$\varepsilon_{i,2}$ is the strain on the inner surface after cutting.

Therefore, the distributions of the residual strains on both surfaces are readily obtained. As shown in Fig. 3.13, the diamond-shaped data (in red lines) represent the residual strains on the outer surfaces, and the cross-shaped data (in blue lines) represent the residual strains on the inner surfaces. In all these four sections, Points 7 to 12 represent the data at the corner regions with inner radii R_{in} = 3t and outer radii R_{out} = 4t.

Sections SA-nw and SB-nw exhibit consistent residual strain distributions in their corner regions, because these two sections are cold-bent using the same punch with identical bending parameters. At these corner regions, their residual strains on the outer surfaces are in tension at +0.14 % in average while the residual strains on inner surfaces are in compression at -0.12 % in average. For those points located away from the corner regions, they are considered to have very small residual strains, i.e. smaller than ±0.01 %. However, it should be noted that the residual strains at Points 15 to 18 in Section SA-nw and those at Points 18 to 27 in Section SB-nw were inevitably induced by flame cutting. The residual strains at Points 1 to 6 in Section SA-nw and those at Points 1 to 6 in Section SB-nw are considered to properly reflect the distributions of residual strains in the cold-bent sections without welding.

To determine how the residual strains are changed by welding, a comparison is made between the sections without welding and those with welding. For Section SA, as a significant heat energy is induced during welding, tensile strains are generated locally at Points 17 to 19 on both surfaces. By comparing the residual strains in Sections SA-nw and SA, it is found that the welding has only minor effects onto the residual strains at the corner regions. This is probably because the welding is located away from the corner regions, and the concentrated tensile strains induced during welding can only influence very small region in the vicinity of the welds. Similar results are also found in the residual strain distributions of Sections SB-nw and SB.

b) residual stresses

The relationship between the residual stresses and the residual strains is described by the Hook's as follows:

$$\sigma_o = -E \cdot \varepsilon_o \qquad \text{Eq. (3.11)}$$

$$\sigma_i = -E \cdot \varepsilon_i \qquad \text{Eq. (3.12)}$$

where

E is the measured Young's Modulus of the steel;

σ_o is the residual stress on the outer surface; and

σ_i is the residual stress on the inner surface.

Since the residual stresses are calculated with the Hook's Law through a linear transformation from the residual strains, the distributions of the residual stresses are identical to those of the residual strains. In subsequent chapters, the residual strains of these four sections induced by both transverse bending and longitudinal welding are simulated with advanced finite element modelling. The numerical results are directly compared with the measurements shown in Fig. 3.13.

3.5 Conclusions

This Chapter presents details of material properties, fabrication processes and residual stress measurements of the S690 CFSHS. These technical works are considered to constitute a solid foundation of the project, providing important data for effective uses of S690 CFSHS.

- An experimental investigation into S690 standard tensile coupons is presented. It is found that the key mechanical properties of the S690 steels comply well with the requirements of EN 1993-1-12 and EN 10025-6. The measured strengths of the S690 steels are used for predicting section and member resistances of the S690 CFSHS columns prior to testing. Besides, the constitutive models of the S690 steels are also developed according to the test results, and these material models are incorporated into various finite element models for subsequent analyses.

- The fabrication processes, namely, both transverse bending and longitudinal welding, are described in detail. These fabrication processes are simulated numerically to determine residual stresses of S690 CFSHS induced with transverse bending and longitudinal welding.

- The residual stresses of the S690 CFSHS measured with the sectioning method are demonstrated. These measurements are compared with the numerical results of various thermomechanical models in subsequent chapters.

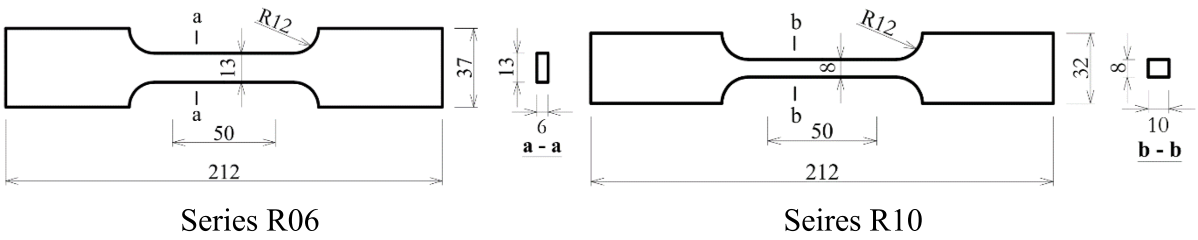

a) Geometry of standard tensile coupons

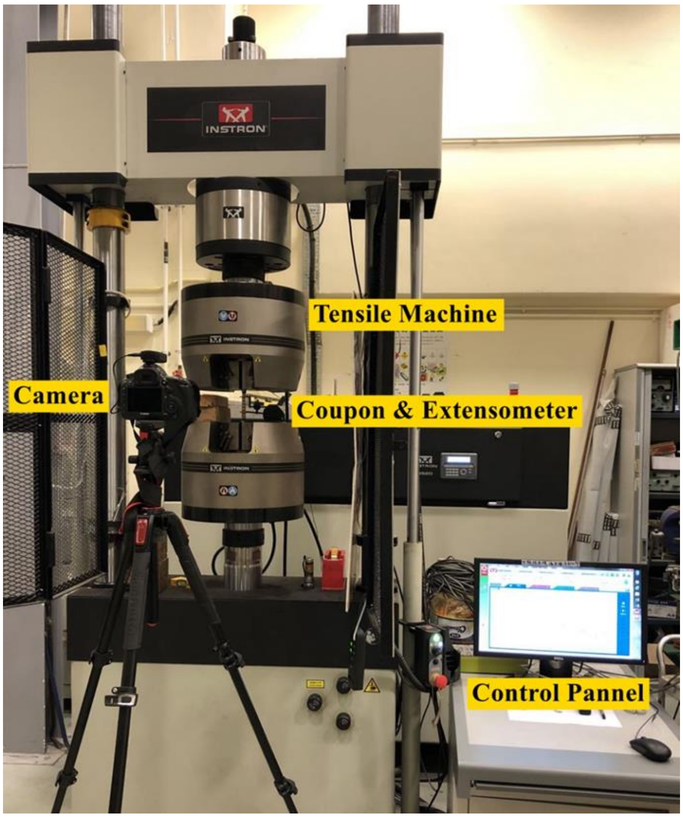

b) Test set-up

Fig. 3.1 Standard tensile coupon test of S690 steel plates

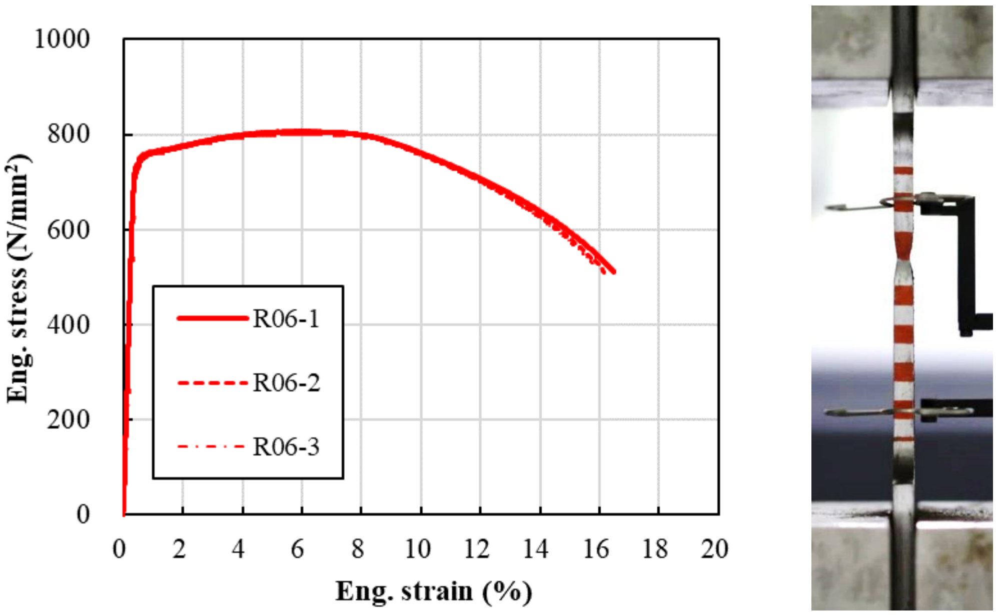

a) Series R06

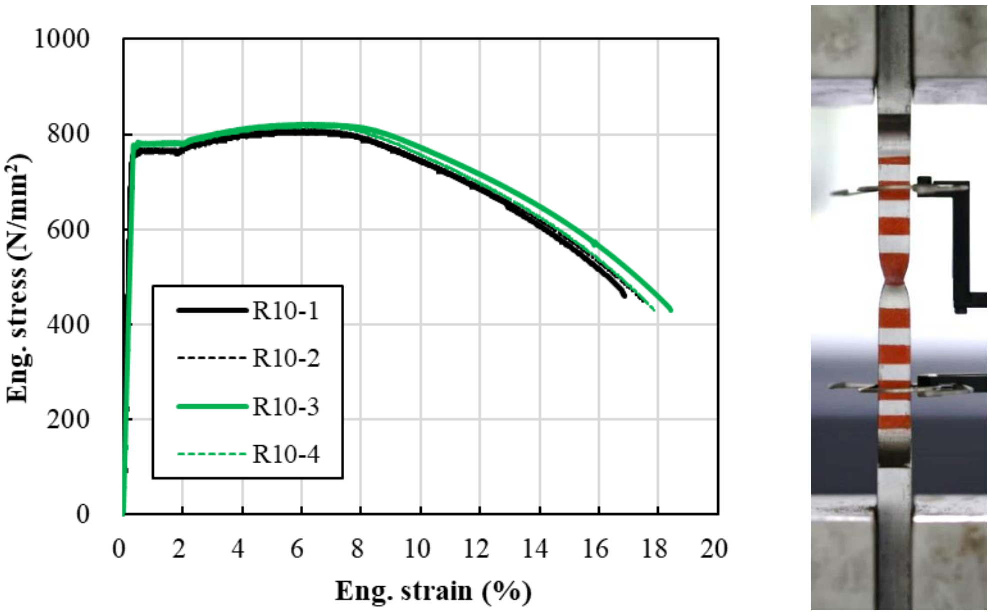

b) Series R10

Fig. 3.2 Engineering stress-strain curves of S690 steel plates

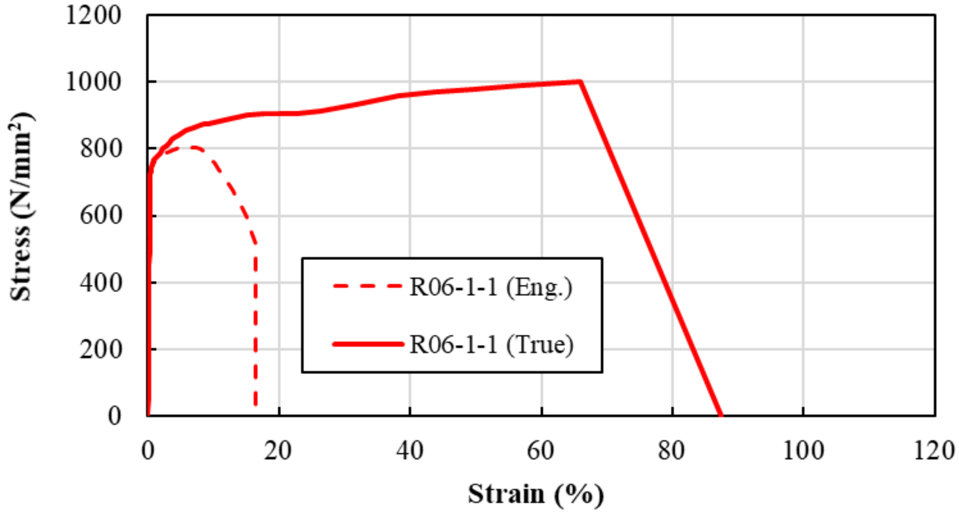

a) Test R06-1-1

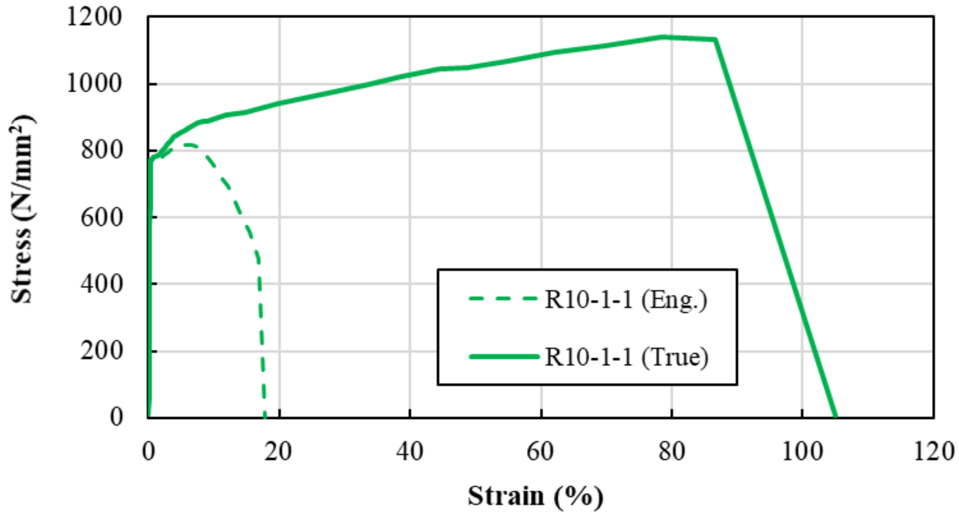

b) Test R10-1-1

Fig. 3.3 Stress-strain curves: engineering properties vs. true properties

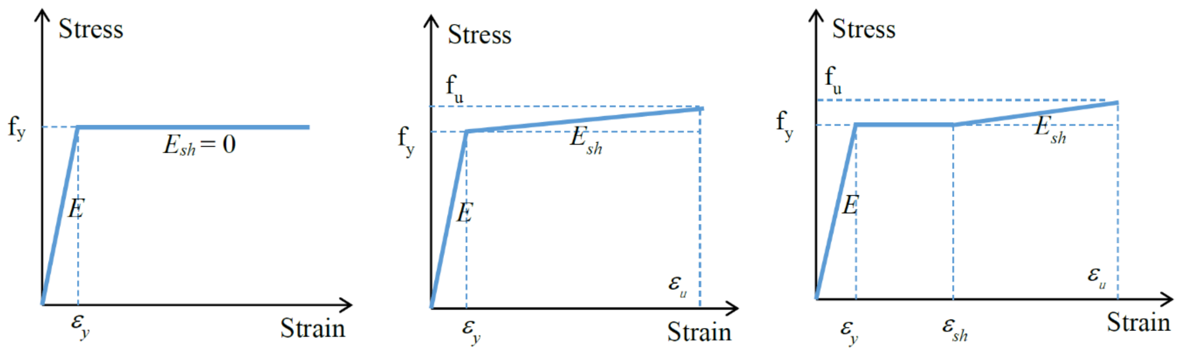

a) elastic-perfectly plastic model

b) elastic-linearly hardening model

c) tri-linear model

Fig. 3.4 Simplified constitutive models for normal strength steels

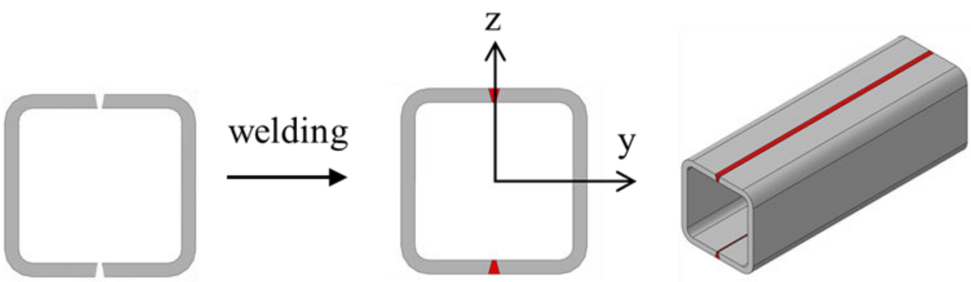

a) Series SA

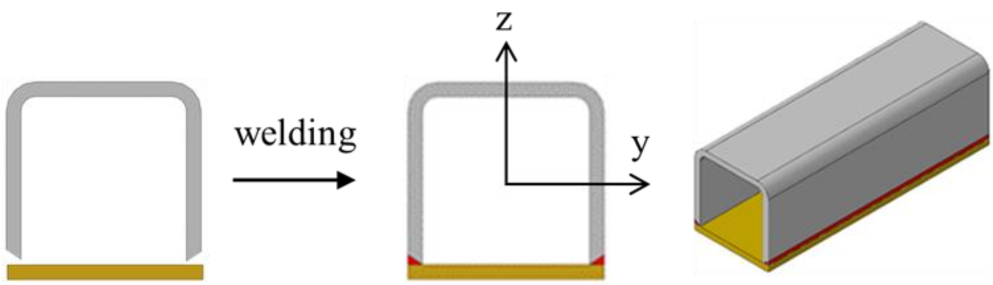

b) Series SB

Fig. 3.5 Fabrication processes of CFSHS

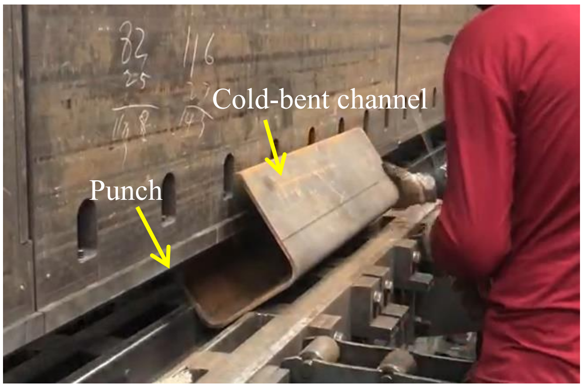

a) Transverse bending with a press-braked bending process

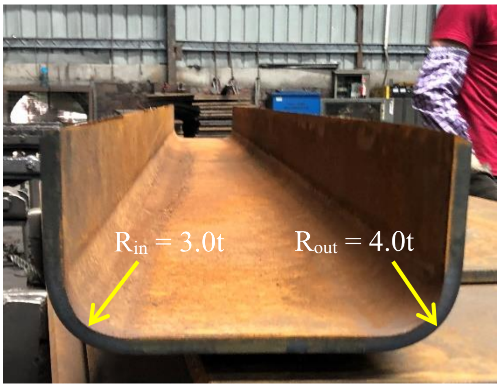

b) A channel after transverse bending and springback

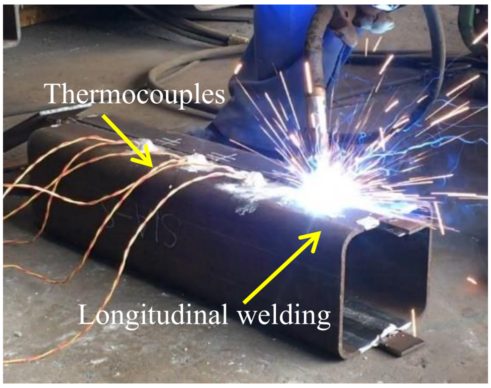

c) Longitudinal welding after transverse bending

Fig. 3.6 Transverse bending and longitudinal welding of CFSHS

a) Cracking along the cold-bent specimen

b) Outer surface of a 6 mm thick specimen

c) Outer surface of a 10 mm thick specimen

Fig. 3.7 Cracked surfaces after bending with a small R/t ratio

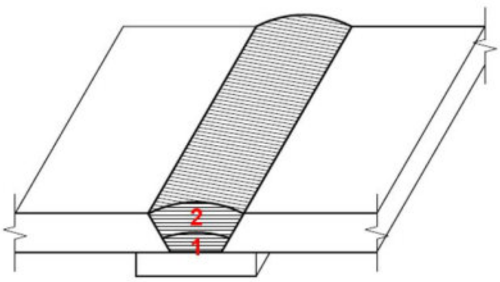

a) 6 mm thick plate, weld at middle

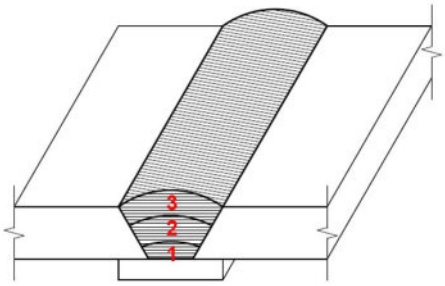

b) 10 mm thick plate, weld at middle

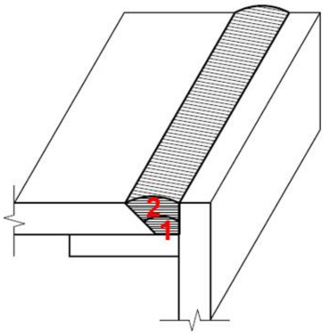

c) 6 mm thick plate, weld at corner

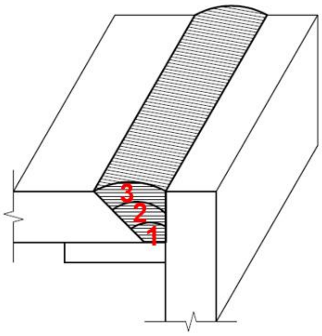

d) 10 mm thick plate, weld at corner

Fig. 3.8 Sketches of multi-pass GMAW in four CFSHS

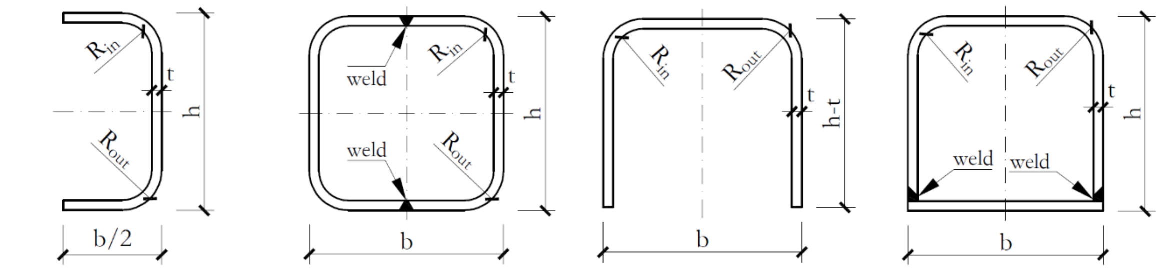

Section SA-nw **Section SA** **Section SB-nw** **Section SB**

b	=	200	mm
h	=	200	mm
t	=	10	mm
R_{in}	=	30	mm
R_{out}	=	40	mm

Fig. 3.9 Cross-sectional dimensions of CFSHS for residual stress measurements

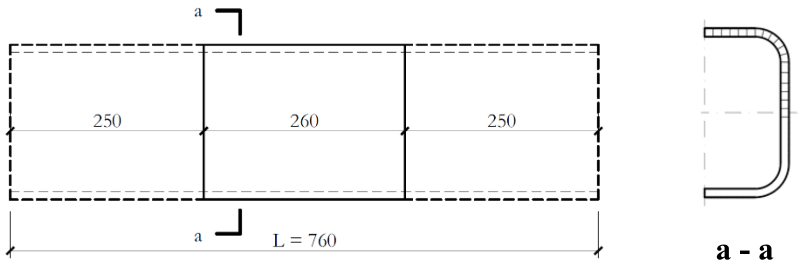

a) Section SA-nw

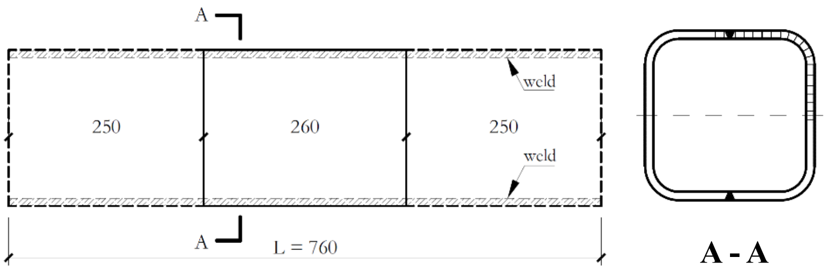

b) Section SA

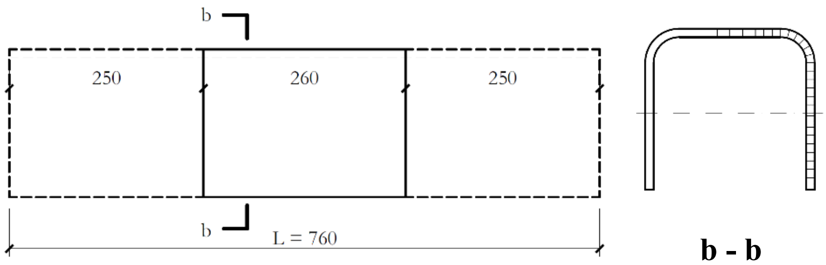

c) Section SB-nw

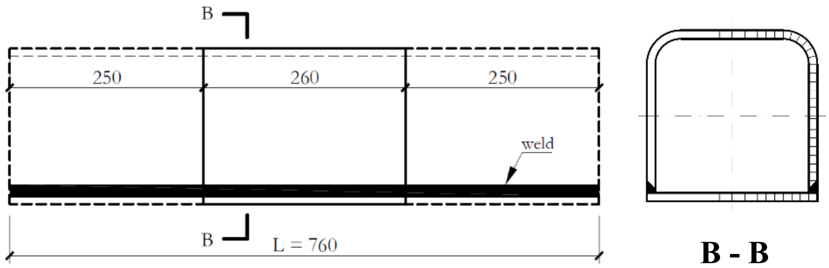

d) Section SB

Fig. 3.10 Cutting of CFSHS for residual stress measurements

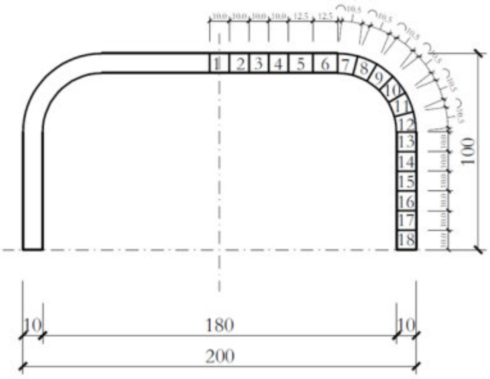

a) Section SA-nw

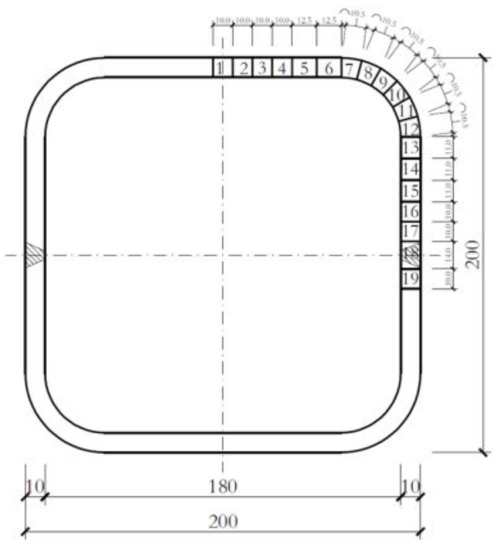

b) Section SA

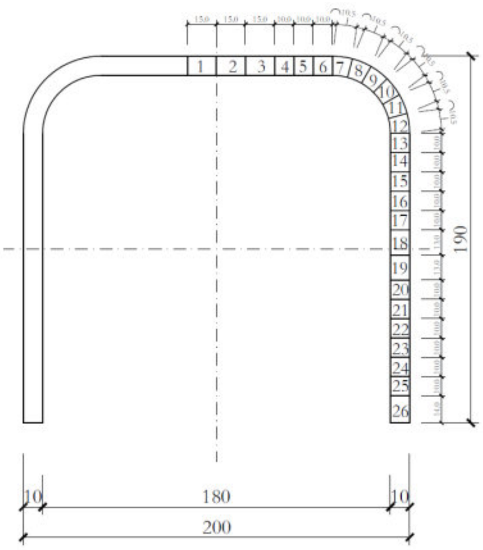

c) Section SB-nw

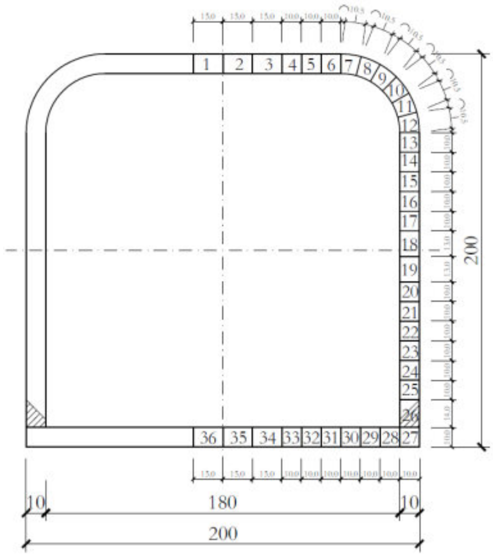

d) Section SB

Fig. 3.11 Arrangements of strips for the sectioning method

a) Section SA-nw

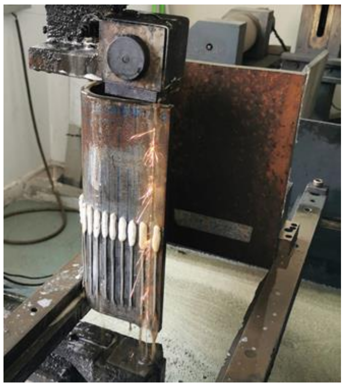

b) Wire cutting of Section SA

c) Section SA

d) Deformed strips cut from Section SA-nw

e) Deformed strips cut from Section SA

Fig. 3.12 Procedures of the sectioning method

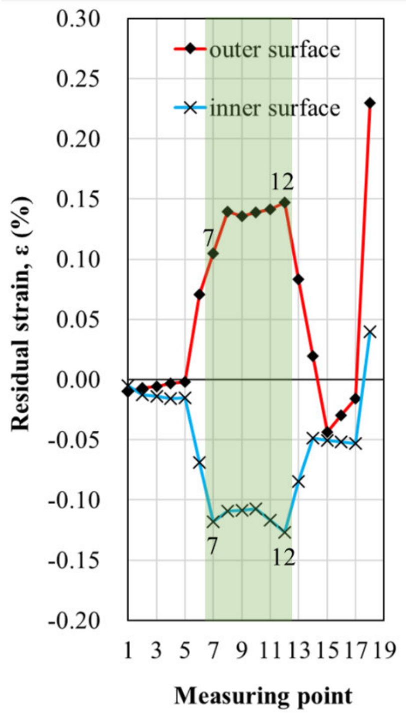

Section SA-nw

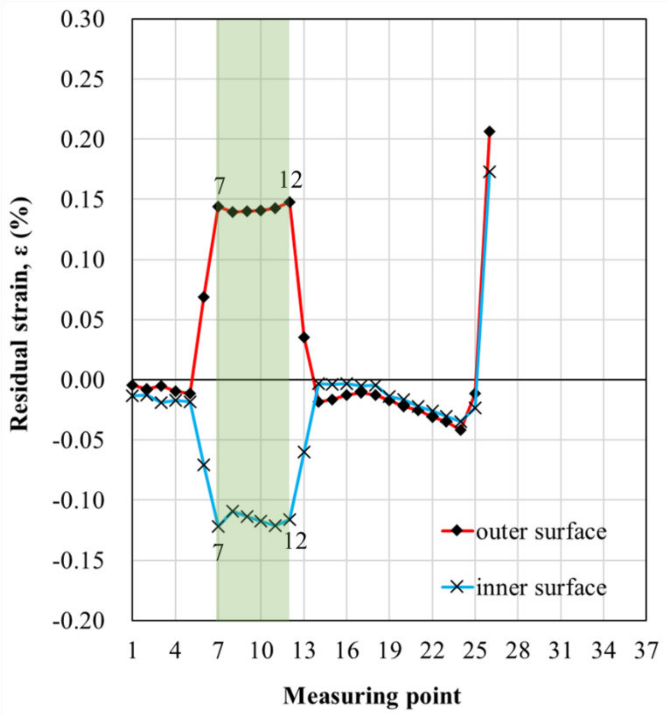

Section SB-nw

a) Transverse bending only

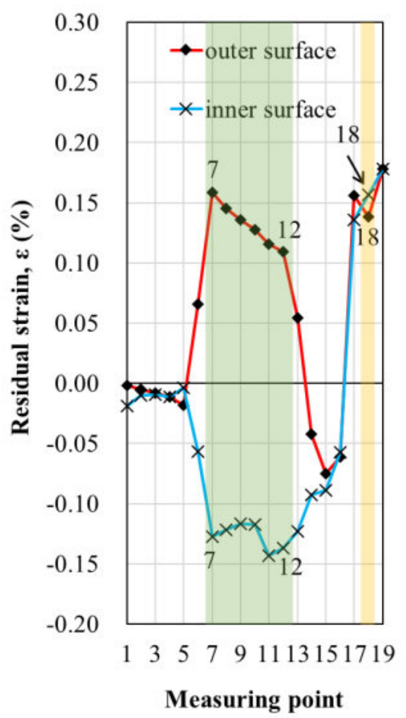

Section SA

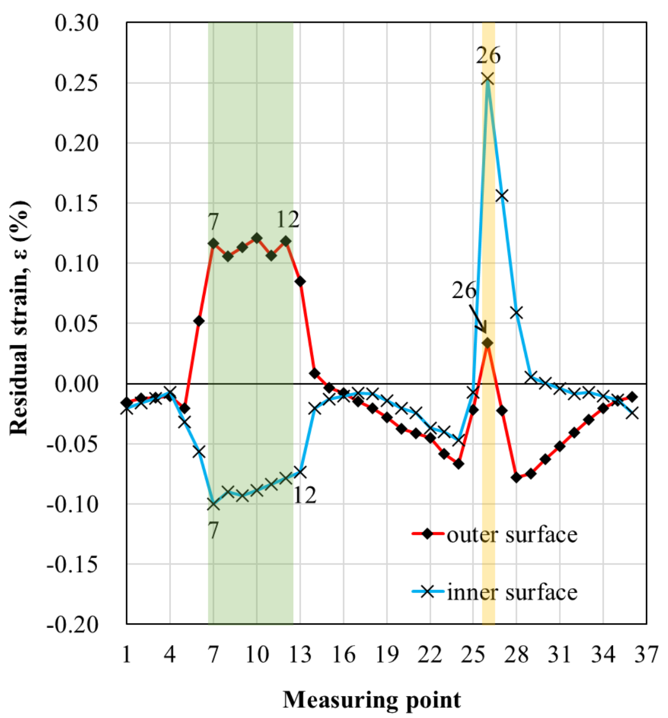

Section SB

b) Transverse bending and longitudinal welding

Fig. 3.13 Measured surface residual strains of four CFSHS

Table 3.1 Chemical compositions of S690 steel plates

Steel plate or specification	Chemical composition (wt %)										
	C	Si	Mn	P	S	Nb	Ti	Cr	Mo	B	CEV
6 mm plate	0.14	0.27	1.40	0.019	0.001	0.024	0.013	0.26	0.14	0.0015	0.46
10 mm plate	0.14	0.26	1.41	0.012	0.001	0.025	0.014	0.26	0.15	0.0015	0.46
EN 10025-6 (upper limit)	0.22	0.86	1.80	0.025	0.012	0.070	0.070	1.60	0.74	0.0060	0.65

Table 3.2 Key mechanical properties of S690 steel plates

Steel plate or specification	E (kN/mm^2)	f_y (N/mm^2)	f_u (N/mm^2)	ε_L (%)	f_u/f_y (/)
6 mm plate	215	733	808	15.9	1.10
10 mm plate	223	754	804	17.5	1.07
EN 1993-1-12 (lower limit)	--	690	--	10.0	1.05

Table 3.3 Calculation of preheating temperatures

Steel plate	Chemical composition (wt %)							T_p (℃)
	C	Mn	Mo	Cr	Cu	Ni	CET	
6 mm plate	0.14	1.40	0.14	0.26	0.00	0.00	0.307	-9.7
10 mm plate	0.14	1.41	0.15	0.26	0.01	0.01	0.310	9.7

Table 3.4 Research programme and scope of work

Section	Fabrication processes		Experimental measurements	
	transverse bending	longitudinal welding	welding parameters	residual stresses
(1) SA-nw	Y	--	--	Y
(2) SA	Y	Y	Y	Y
(3) SB-nw	Y	--	--	Y
(4) SB	Y	Y	Y	Y

Table 3.5 Welding parameters for Sections SA and SB

Section	Weld pass	Current, I (A)	Voltage, U (V)	Welding speed, v (mm/s)	Welding efficiency, η (/)	Line heat input energy, q (kJ/mm)
(2) SA	1	145 ~ 155	20.4	2.09	0.80	1.13 ~ 1.21
	2	200 ~ 210	23.0	4.11	0.80	0.90 ~ 0.94
	3	185 ~ 195	23.1	2.86	0.80	1.20 ~ 1.26
(4) SB	1	160 ~ 170	20.2	2.81	0.80	0.92 ~ 0.98
	2	200 ~ 210	22.6	3.80	0.80	0.95 ~ 1.00
	3	190 ~ 200	22.8	3.35	0.80	1.03 ~ 1.09

Note: line heat input energy, $q = \eta IU/v$.

CHAPTER 4: EXPERIMENTAL INVESTIGATIONS INTO S690 CFSHS COLUMNS

4.1 Introduction

This Chapter presented an experimental investigation into section and member resistances of S690 cold-formed square hollow sections (CFSHS) under compression. A total of 12 CFSHS fabricated with different combinations of transverse bending and longitudinal welding were investigated. To examine structural behaviour of these sections, a test programme consisting of 38 S690 CFSHS column tests was conducted under three loading conditions, including 8 stocky columns under concentric compression, 6 stocky columns under eccentric compression, and 24 slender columns under concentric compression. Measured section resistances of the stocky columns were compared with design resistances predicted to EN 1993-1-1. It was found that the existing section classification failed to identify strength mobilization of these sections. Therefore, a modified rule of section classification was proposed after calibration against the measured section resistances. Moreover, the measured member resistances of the slender columns were compared with the resistances predicted by EN 1993-1-1. It was found that the existing design curve was very conservative for the slender columns. Therefore, it was proposed to adopt a reduced imperfection factor for the design of column buckling, and hence, a higher design curve was recommended to be used.

4.2 Section Classification

A total of 12 S690 CFSHS are investigated (see Figs. 4.1 and 4.2), and these sections were categorized into two series according to their fabrication processes, i.e. Series SA and SB. These two series of sections were identical in their nominal cross-sectional dimensions, but they were fabricated with different combinations of transverse bending and longitudinal welding, as illustrated in Fig. 4.3. Details of these two fabrication techniques were presented in Chapter 3.

For structural design of CFSHS against concentric compression and eccentric compression, the rules of section classification given in EN 1993-1-1 (CEN 2014) were widely accepted. When designing sections made of normal strength steels with a yield strength smaller than 460 N/mm^2, the codified method could precisely predict the resistances of the sections under various actions. Since only high strength S690 steels are investigated in the present project, the classes of these sections categorized with the existing rules might not be able to identify their strength mobilization and ductility. It was proposed to apply the existing rules for section classification preliminarily, and applicability of the rules for high strength steel was then verified with test results. In EN 1993-1-1, the compression part with the largest width-to-thickness ratio, $c/t/\varepsilon$, was selected from a section, and its $c/t/\varepsilon$ ratio defined the section classification:

Class 1:		$c/t/\varepsilon$	≤ 33	Eq. (4.1a)
Class 2:	$33 <$	$c/t/\varepsilon$	≤ 38	Eq. (4.1b)
Class 3:	$38 <$	$c/t/\varepsilon$	≤ 42	Eq. (4.1c)
Class 4:		$c/t/\varepsilon$	> 42	Eq. (4.1d)

where

c is the width or the depth of a part in a section for section classification;

t is the thickness of a part in a section for section classification; and

ε is the factor depending on f_y, $\varepsilon = \sqrt{235/f_y}$.

By substituting nominal dimensions into the equations above, the c/t/ε ratios and the sections classifications of a total of 12 CFSHS investigated in the present project were calculated and summarized in Table 4.1. It was found that eight out of the 12 sections were categorized into Class 1 or 2, which meant these sections were capable of attaining their full plastic resistances of the gross sections. However, Sections S2A and S2B were classified as Class 4 sections, which indicated elastic local plate buckling probably occurred under concentric compression or eccentric compression, thus preventing these sections from attaining the elastic resistances of their gross sections. In a Class 4 section, slender parts were regarded as non-effective zones that could not develop their full section resistance under compression. Therefore, when calculating the section resistances, the widths of the non-effective zones were partially included in accordance with EN 1993-1-5 (CEN 2019e). Fig. 4.4 a) illustrates non-effective zones of both series of sections under compression, while Fig. 4.4 b) illustrates non-effective zones of both series of sections under bending. It should be noted that the width of the non-effective zone at the web, $b_{non\text{-}eff,w}$, and that at the flange, $b_{non\text{-}eff,f}$, under bending should be calculated with different methods due to different stress distributions across the sections. In the present project, there were three different loading cases, and they were: i) stocky columns under concentric compression, ii) stocky columns under concentric compression, and iii) slender columns under concentric compression.

For case i), the non-effective widths, $b_{non-eff}$, are shown in Fig. 4.4 a), and their effective areas, A_{eff}, are readily calculated. For case ii), the non-effective widths, $b_{non-eff}$, are shown in Figs. 4.4 a) and b), and their effective areas, A_{eff}, and effective moduli, $W_{eff,z}$, are then calculated, respectively. For case iii), only the non-effective widths, $b_{non-eff}$, shown in Fig. 4.4 a) are considered, because only the gross section is considered when calculating N_{cr} (EN 1993-1-1). A_{eff} are obtained readily with the calculation process demonstrated in EN 1993-1-5. When calculating $W_{eff,z}$, the section should be broken down into the web and the flanges. The slenderness limit for the web is so large that the full web is normally regarded to be effective. Besides, the non-effective area in each flange under compression is calculated readily. The non-effective area in each flange, the neutral axis is shifted from z-axis to z'-axis by Δ_y, as shown in Fig. 4.5. Consequently, the normal stresses across the section re-distribute under bending about the z'-axis in an asymmetrical pattern. $W_{eff,z}$ is calculated using the following formula:

$$W_{eff,z} = I_{z'}/(0.5B + \Delta_y) \qquad \text{Eq. (4.2)}$$

where

$I_{z'}$ is the second moment of area about the z'-axis, considering the presence of the non-effective area in the flange under compression.

Although $I_{z'}$ and Δ_y can be obtained with an analytical solution, the calculation processes are redundant and time-consuming. An alternative solution to determine these two values is to draw the non-effective section using the software AutoCAD, and both $I_{z'}$ and Δ_y are evaluated readily after the section profile is sketched successfully. The section properties of two Class 4 sections, Sections S2A and S2B, are summarized in Table 4.2 where these two sections have identical reduction ratios of areas and section moduli.

4.3 S690 CFSHS Stocky Columns under Concentric Compression

4.3.1 Test programme

To examine section resistances under compression, a total of eight S690 CFSHS stocky columns are tested. The test programme of these stocky columns is summarized in Table 4.3. In order to avoid occurrence of overall buckling, all the columns are designed to be very short, i.e. the member length is assigned to be three times of the section depth or width, i.e. L_m = 3H or 3B. As shown in Table 4.3, the non-dimensional slenderness of each of the stocky columns is calculated, and their small slenderness ratios indicate that these columns are stocky enough, thus preventing them from overall buckling under compression. It should be noted that the measured dimensions of these stocky columns given in Table 4.3 vary slightly from the nominal dimensions presented in Table 4.1. These errors were inevitably induced during plate cutting, transverse bending and longitudinal welding, and they are unlikely to lead to a change in section classification. Compared with the nominal section classes summarized in Table 4.1, minor differences are found in Table 4.3. In short, most sections have the same classes as their nominal sections do, but only S1A-S and S3B-S changes their sections just from Class 1 to 2, due to slight increases of $c/t/\varepsilon$.

4.3.2 Test set-up and procedures

Fig. 4.6 shows the testing system together with a stocky column under compression. A force is applied using the 1000 tons Hydraulic Servo Control Testing System. Each end of the stocky column is welded with a 20 mm thick S355 bearing plate to ensure consistent axial shortening under compression.

To capture axial deformations over the member length, strain gauges (SGs) and linear variable displacement transducers (LVDTs) are installed. Figs. 4.7 a) and b) illustrate the arrangements of the instrumentations for stocky columns of Series SA-S and SB-S under compression. Up to eight strain gauges are mounted onto the outer surface at the mid-height of stocky column, while four LVDTs are attached on the bearing plates of the stocky columns. Average values of these four measurements are taken as the measured axial shortening.

During the test, the actuator will exert an axial load under a controlled manner at various cross-sections onto the column.

The testing procedure of a compression test consists of three phases with different loading (or displacement) as follows: including preloading, loading and unloading.

- Phase 1: Preloading. The testing system applies a compression force onto the column at a rate of 300 kN/min up to 30 % of the design resistance of the section, $N_{c,Rd}$, and then the applied load is reduced to zero. Such a preloading process is repeated for three times, to minimize any initial bedding of the column.

- Phase 2: Loading. The testing system applies a compressive displacement onto the column at a rate of 0.3 ~ 0.5 mm/min, with the applied load increased from zero to the maximum applied load, $N_{c,Et}$. After the peak load is reached, the applied load starts to drop. When the load drops down to 75 % of $N_{c,Et}$, the applied load is held for one minute.

- Phase 3: Unloading. After one minute, unloading begins, and the applied load is reduced at a rate of 600 kN till zero.

Their loading rates are controlled to be very slow, so that dynamic effects are avoided throughout testing.

4.3.3 Test results

All the tests have been conducted successfully. Except for those columns with Class 4 sections, namely, Sections S2A and S2B, all the stocky columns with Classes 1, 2 and 3 sections are shown to be able to mobilize readily the full resistances of their cross-sections and measured maximum applied loads, $N_{c,Et}$, should be larger than design resistances of the sections, $N_{c,Rd}$. The test results of eight stocky columns are summarized in Table 4.4, showing that Class 4 Sections S2A and S2B achieve only about 82 % of their design resistances of the gross sections. For all the other sections, the measured section resistances are all larger than their gross design resistances. For those Class 4 sections, effective areas, A_{eff}, are calculated and substituted into $N_{c,Rd}$. It is found that Sections S2A and S2B both exceed their design resistances of the effective sections.

Since the key research interest of this project is structural performances of those sections with different fabrication processes, the structural behaviours exhibited by these two series of sections are described and compared in detail. Typical deformed shapes after testing of Sections S3A and S3B are illustrated in Fig. 4.8. These two sections are shown to have failed in an identical deformed shape under almost the same equal section resistances. It is apparent that significant localized plate deformations occur at the mid-height of both columns. However, due to the presence of cold-bending effects at the corner regions, the deformation capacity of a cold-bent channel (in Section S3A) should behave differently from that of a flat plate (in Section S3B) under compression. More details are found by comparing these two counterparts. It should be noted that smaller localized deformation is borne by the flat plate of Section S3B. By contrast, the corresponding flat parts in Section S3A are relatively short, as they are restrained by cold-bent corners with a large R/t ratio. Consequently, such flat parts in Section S3A tend to mobilize a large plastic deformation when compared with that in Section S3B, resulting in more significant plastic deformation occurred in this portion after testing. Therefore, it is considered that a large ductility is exhibited in Section S3A, when compared with that in Section S3B.

As mentioned above, these two series of sections behave differently in local buckling, and this difference is further quantified with the measured strains of these sections. It is shown in Fig. 4.9 that the local buckling occurred after the peak loading is attained, but larger deformations are undertaken by Section S3A than Section S3B, as most strain gauges in Section S3A go beyond 3.0 %, while none of those is larger than 1.5 % in Section S3B. To be more specific, SG-2 and SG-4 in Section S3A represent the deformation behaviour of the flat part restrained by two cold-bent corners, while SG-3 of Section S3B represents the deformation behaviour of the flat plate restrained by two welds. The portions restrained by cold-bent corners in S3A exbibit larger deformation capacity than its counterpart restrained by welds in S3B. The similar failure modes and the consistent localized strain patterns were also found in the other six sections. It is summarized that both series of sections can achieve their section resistances to the equal degree, but larger plastic deformations are mobilized by Series SA sections than Series SB sections. It is considered that Series SA sections perform better ductility under compression.

Applied load-axial shortening curves of all the stocky columns are plotted in Fig. 4.10, where N is the applied load and Δ_x is the average axial shortening of four LVDTs. To have direct comparison on the load-deformation relationships among these eight columns, the effects of different sectional dimensions are eliminated. Therefore, it is proposed to normalize the applied loads and the axial shortenings with the gross cross-sectional areas, A_g, the yield strengths, f_y, and the yield strains, ε_y. Fig. 4.11 shows the relationships between the normalized resistances, $N/(A_g \cdot f_y)$, against the normalized strains, $\varepsilon/\varepsilon_y$. It is shown that Sections S3A and S3B have not only exceeded their design section resistances, but they also exhibit a high degree of ductility. However, Sections S2A and S2B fail to reach the design resistances of their gross sections because they are Class 4 sections, and hence, parts of the gross area should be defined as non-effective so that they do not resist any compression. For Sections S1A, S4A, S1B and S4B, their measured section resistances just exceed their design section resistances with a limited degree of ductility. Although some of these four sections are regarded as Class 1 or 2 according to the existing rules of section classification given in EN 1993-1-1, it is more reasonable to categorize some of them into Class 3 due to their low degree of ductility, and modifications to the existing rules are discussed in Section 4.3.4.

4.3.4 Comparison with EN 1993-1

In accordance with EN 1993-1-1, the compression part with the largest width-to-thickness ratio c/t, of a section is critical for section classification. As each side of Series SA sections has two cold-bent corners with very large corner radii, the calculated width of the critical part, c, is relatively short, i.e. $c = B - 2R_{out}$ or $H - 2R_{out}$, whichever is larger, and this critical part results in a non-conservative design of section resistance under compression. As presented in Table 4.4, the test results show a conflict with the section classification according to the current rules. To be more specific, although a Class 1 section, Section S3A, has utilized its section plastic resistance with a large amount of ductility, another Class 1 section, Section S4A, only attains its section elastic resistance with a limited degree of ductility. A similar conflict is found in the Class 2 section, Section S1A, as it fails to exhibit sufficient ductility after its section elastic resistance is attained. For Series SB sections, their critical parts are all located at the welded plates without cold-bent corners or with only one cold-bent corner i.e. $c = B - 2t$ or $H - t - R_{out}$, whichever is large, so that their critical parts are longer than those of Series SA. The Class 2 section, Section S3B, mobilizes its section plastic resistance with a good ductility; the Class 3 sections, Sections S1B and S4B, utilize their section elastic resistances with a limited ductility; and the Class 4 section, Section S2B, fails to attain its full resistance of the gross section.

However, the c-value for CFSHS is defined in a different way in EN 1993-1-5, where R_{out} is replaced with 1.5t no matter how large the corner radius is. This replacement enables a conservative design of section resistance, because the value of R_{out} at 1.5t is smaller than the minimum outer corner radius R_{out}, which should be larger than 1.6t as given in EN 10219-2 (CEN 2019d). Therefore, the c-value of a Series SA section is replaced with c' = B - 3t or H - 3t, and the c-value of a Series SB section is replaced with c' = B - 2t or H - 2.5t. It is proposed to calculate the c-values with the modified definitions, since EN 1993-1-5 is the code specially used for the design of steel plated elements. Consequently, the values of c'/t/ε of these eight sections are calculated and summarized in Table 4.5. Since some of the sections are modified to Class 4 sections, their effective areas, A_{eff}, and their design section resistances, $N_{c,Rd}$, are re-calculated correspondingly. It is found that these sections of modified classes match well with the anticipated mobilization in both strength and ductility.

4.3.5 Summary

An experimental investigation into a total of eight S690 cold-formed square hollow section (CFSHS) stocky columns under compression is presented.

- Except for those columns with Class 4 sections, all stocky columns with Classes 1, 2 and 3 sections are shown to have mobilized their full resistances of the gross sections. For those Class 4 sections, by considering local buckling in their plated elements, they are shown to have attained their design resistances of the effective sections.

- Both series of sections have achieved their section resistances, but larger plastic deformations are mobilized in Series SA when compared with those in Series SB. It is shown that Series SA sections exhibit an improved ductility under compression.

- It is proposed to adopt modified c-values for section classification to EN 1993-1-1. All those sections of modified classes are shown to match well with the anticipated mobilization in both strength and ductility.

4.4 S690 CFSHS Stocky Columns under Eccentric Compression

4.4.1 Test programme

To examine section resistances under eccentric compression, a total of six S690 CFSHS stocky columns are tested. Measured dimensions of these specimens are summarized in Table 4.6. The nominal sectional dimensions of the stocky columns in this programme are kept consistent with those under compression. It should be noted that both columns with Sections S1A and S1B are excluded from this test programme, because these columns are designed to be short to avoid member buckling. After a preliminary calculation on the dimensions of all these columns, it is found that the sizes for S1A-E and S1B-E fail to match the test set-up and the slenderness limit at the same time, so these two columns are not included in this test programme. Besides, although slight changes are found between nominal dimensions and measured dimensions, the section classification of all the sections keep identical to the nominal ones.

4.4.2 Test set-up and procedures

Fig. 4.12 shows the testing system together with a stocky column under eccentric compression. A compression force with an eccentricity of 100 mm is applied with the 1000 tons Hydraulic Servo Control Testing System. Each end of the stocky column is welded with a 20 mm thick S355 bearing plate with dimensions of 490 x 490 mm to ensure consistent rotations under bending. In order to ensure eccentric loading onto the column ends and to allow for free rotations in the plane about z-axis, a pin support is provided to each end plate of each end of the column with six 10.9 M22 bolts. The effectively length, L_{eff}, of the column is defined as the vertical distance from the centre of one pin to that of another.

The instrumentation for Series SA-E and SB-E are illustrated in Figs. 4.13 a) and b), respectively. Up to eight strain gauges are mounted onto the outer surface of the mid-height of the stocky columns. A total of nine LVDTs are used for measuring axial and horizontal displacements during the test. Eight of them are installed vertically onto the end plates to measure the axial displacements, i.e. four onto each end plate. And the ninth one is installed horizontally at the mid-height of the column to measure its horizontal displacements.

The testing procedure of this test programme follows with those introduced in Section 4.1.2, and the same loading procedure is employed.

4.4.3 Test results

All the tests have been conducted successfully. Except for those columns with Class 4 sections, i.e. Sections S2A and S2B, all stocky columns with Classes 1, 2 and 3 sections are shown to be able to mobilize their resistances of the gross sections. The combined effects of the measured maximum applied loads, $N_{c,Et}$, and the measured maximum bending moments, M_{Et}, are shown to be larger than the design resistances of the gross sections, i.e. $N_{c,Rd}$ and $M_{c,z,Rd}$. The test results of the six stocky columns are summarized in Table 4.7. Hence, the measured section resistances of these sections are shown to be larger than their respective design resistances of the gross sections. However, for those Class 4 sections, the effective areas, A_{eff}, and the effective moduli, $W_{eff,z}$, are calculated and adopted in determining both $N_{c,Rd}$ and $M_{c,z,Rd}$, respectively. It is found that both Sections S2A and S2B exceed the design resistances of their effective sections.

Deformation capacities of sections with the two different fabrication processes, i.e. Series SA and SB, are described and compared. Fig. 4.14 shows typical deformed shapes after testing of Sections S3A and S3B. Their deformed shapes are very similar, regardless of the heights where local buckling occurs. To be more specific, the deformations of each plate are quantified by the applied load-strain curves shown in Fig. 4.15. It is found that the load-strain curves of Section S3A are identical to those of Section S3B. However, their post-buckling behaviour cannot be fully determined from the load-strain curves. This is because the strain gauges were mounted at the mid-height of the columns, but the local failures occurred away from the mid-height. More details will be found by comparing the deformed shapes after testing as shown in Fig. 4.14. Under the similar level of eccentric compression, the flat part in S3A undergoes larger plastic deformation than its counterpart in S3B, and it is considered that more plastic deformations are mobilized in S3A. Moreover, similar comparisons are made between S2A and S2B as well as between S4A and S4B, respectively. All Series SA sections are found to exhibit larger post-buckling deformations than Series SB sections. In summary, when local buckling occurs under combined compression and bending, better ductility is performed by Series SA sections than Series SB sections, which keeps in line with the findings demonstrated in Section 4.3.3.

The applied load-displacement curves of the six tests are shown in Fig. 4.16, where the load-displacement relationships are considered to be consistent between those Series SA and SB sections having the same nominal dimensions. As the measured dimensions of these sections are slightly different from their nominal dimensions, it is proposed to normalize the applied load-axial shortening curves with the gross cross-sectional areas, A_g, the yield strengths, f_y, and the yield strains, ε_y. Therefore, direct comparison is made by the normalized load-strain curves as shown in Fig. 4.17. No significant difference is found between the sections with the two different fabrication processes, though Section S3A is able to resist a larger compression force than Section S3B. Four tests with Class 1 or 3 sections have successfully attained their section resistances while an early failure within the elastic stage of both Sections S2A and S2B are expected as they are merely Class 4 sections. These test results are further discussed in Section 4.4.4 to evaluate the interaction design curves given in EN 1993-1-1.

4.4.4 Comparison with EN 1993-1

The design methods on section resistances under combined compression and bending are given in EN 1993-1-1, among which three methods are presented for sections with i) Class 1 or 2 sections, ii) Class 3 sections, and iii) Class 4 sections. Since the present test programme consists of sections with Classes 1, 3 and 4, the test results are compared with various design rules as shown in Fig. 4.18. In Fig. 4.18 a), where the straight lines represent the envelope for elastic resistances of Class 3 sections under combined compression and bending, and the test data of all the six tests are plotted with $N_{c,Et}/(A_g \cdot f_y)$ and $M_{Et}/M_{el,z,Rd}$,where $M_{el,z,Rd} = W_{el,z} \cdot f_y$. It is found that four tests with Classes 1, 2 and 3 sections attain the elastic resistances of their gross sections. However, the other two tests with Class 4 sections fail before mobilizing their elastic resistances of their gross sections, and they do not satisfy the design requirement.

To evaluate plastic resistances of the sections under combined compression and bending, Sections S3A, S4A and S3B are further compared with the design method for Class 1 or 2 sections. Both the design curve and the test data are plotted onto the same graph in Fig. 4.18 b). The design curve is transformed from a straight line into a bi-linear curve, consisting of a "plateau" and a straight line. The length of the "plateau", n_c, i.e. the critical value of $N_{c,Et}/N_{c,Rd}$, is calculated in accordance with EN 1993-1-1. It should be noted that n_c-values of these four tests are very close to one another, as ranging merely from 0.22 to 0.23. As a larger n_c always represents a large safety margin, n_c is taken as 0.23 on a basis of conservative design. For the test data plotted in the graph, $M_{Et}/M_{el,z,Rd}$ is replaced with $M_{Et}/M_{N,z,Rd}$, where $M_{N,z,Rd}$ is the plastic moment resistance of the section, $M_{pl,z,Rd}$, i.e. $W_{pl,z} \cdot f_y$, in the linear segment, making all the four data being shifted downward, when compared with those in Fig. 4.18 a). Both Sections S3A and S3B are still located above the design curve, i.e. they attain not only their elastic resistances of the sections, but also their plastic resistances. However, Section S4A fails to meet the design requirement for Class 1 or 2 sections, which shows a conflict with the section classification of section of EN 1993-1-1.

As presented in Section 4.3.4, the modified c-values may be adopted to classify the sections under compression to proper section classifications that match well with the observed mobilization in strength and ductility. By replacing R_{out} with 1.5t, the values of c'/t/ε of six sections are calculated, and they are summarized in Table 4.8. A change of section classification is found in Sections S4A (from Class 1 to 3 section), Section S3B (from Class 1 to 2 section) and Section S4B (from Class 3 to 4 section). It should be noted that the change in Section S4A is considered the most critical. Besides, Section S4B is modified to Class 4 section, and its effective area, A_{eff}, and its effective modulus, $W_{eff,z}$, are calculated. Hence, Section S4A is excluded from the comparison with the design curve for Class 1 or 2 sections shown in Fig. 4.18 b). However, this section is able to attain the elastic resistance of the section as shown in Fig. 4.18 a). It is concluded that, by adopting the modified c-values for section classification, all these sections with Classes 1, 2 and 3 fulfil the design requirements given in EN 1993-1-1.

4.4.5 Summary

An experimental investigation into a total of six S690 CFSHS stocky columns of cold-formed square hollow sections under eccentric compression is presented. It should be noted that:

- Except for those columns with Class 4 sections, all stocky columns with Classes 1, 2 and 3 sections are able to mobilize the full resistances of their gross sections. For those Class 4 sections, considering local buckling in their plated elements, they have attained their design resistances of the effective sections.

- Both Series SA and SB sections are shown to be able to achieve their section resistances while large plastic deformations are shown in Series SA sections, when compared with those of Series SB sections. It is considered that Series SA sections exhibit a large ductility under combined compression and bending.

- It is proposed to adopt the modified c-values for the section classification given in EN 1993-1-1. Consequently, all the sections with the modified classes are shown to able to fulfil the design requirements given in EN 1993-1-1.

4.5 S690 CFSHS Slender Columns under Concentric Compression

4.5.1 Test programme

To examine member resistances of these S690 CFSHS under concentric compression, a total of 24 slender columns are tested. The nominal sectional dimensions of these slender columns are kept being the same as those stocky columns in Sections 4.3 and 4.4. Similarly, compared with the nominal sectional dimensions, small differences are found in the measured dimensions of these sections due to fabrication errors, as shown in Fig. 4.9. However, these differences in the sectional dimensions lead to some changes onto the section classification of sections, making only few sections to be changed from Class 1 to 2 sections. Besides, in order to capture overall failure of the columns, each column is designed to be slender enough, with a member length larger than eight times of the section depth or width, i.e. L_m > 8B or 8H. Considering the dimensions of the loading attachments and the pin supports at both ends, the effective length, L_{eff}, and hence, the non-slenderness ratio, $\bar{\lambda}$, of each column are calculated. In order to allow for an effective examination on member buckling of columns under compression, their non-dimensional slenderness ratios are designed to range from 0.3 to 1.4, as presented in Table 4.9. It should be noted that, in this test programme, two member lengths are designed for each section, which are designed with "P" and "Q".

4.5.2 Test set-up and procedures

Fig. 4.19 shows the testing system together with a slender column under concentric compression. The concentric compression force is applied with the 1000 tons Hydraulic Servo Control Testing System. Each end of the slender column is welded with a 20 mm thick S355 bearing plate with dimensions of 490 x 490 mm to ensure consistent axial shortening under compression. In order to deliver a concentric force onto the column and to allow for free rotation in the plane about the z-axis, a pair of pinned supports are attached onto the end plates each with six 10.9 M22 bolts. The effective length, L_{eff}, of the column is defined as the vertical distance from the centre of one pin to that of another.

The instrumentation for Series SA-P/Q and SB-P/Q are illustrated in Figs. 4.20 a) and b), respectively. Four strain gauges are mounted onto the outer surface at the mid-height of the slender column to determine their axial strains. A total of 11 LVDTs are used to measure axial and horizontal displacements during testing. It should be noted that eight of them are installed vertically onto the end plates to measure the axial displacements. Moreover, three of them are installed horizontally at the mid-height of the column, to measure the horizontal displacements along the y-axis while the horizontal displacement along the z-axis is measured with a LVDT.

The testing procedure of this test programme follows with those introduced in detail in Section 4.3.2, and the same loading procedure is employed.

4.5.3 Test results

All the tests have been conducted successfully. Table 4.10 summarizes the test results of all the 24 slender columns under concentric compression. The measured maximum applied loads, $N_{b,Et}$, of all the tests are presented. The design section resistances of the sections, $N_{c,Rd}$, and the design member resistances of the columns, $N_{b,Rd}$, are also presented in Table 4.10. It should be noted that $N_{b,Rd}$ is calculated with the buckling curve "c" with an imperfection factor, $\alpha = 0.49$ according to EN 1993-1-1 for axial buckling design of the slender columns. As presented in the table, the ratios $\frac{N_{b,Et}}{N_{b,Rd}}$ of all the slender columns with Classes 1, 2 and 3 sections are larger than 1.0, indicating that the resistances predicted by curve "c" are too conservative for these S690 CFSHS. For those columns with Class 4 sections, the effective areas, A_{eff}, are calculated and substituted into $N_{c,Rd}$. It is found that the ratios $\frac{N_{b,Et}}{N_{b,Rd}}$ of the four columns with Sections S2A and S2B all exceed 1.0.

The failure modes of all the 24 slender columns are shown in Fig. 4.21, and it is evident that many of them fail in overall buckling. Fig. 4.22 shows the deformed shapes of Tests S3A-Q and S3B-Q i) at the initial stage, ii) at the peak load, and iii) at the critical failure, respectively. These may be considered as typical deformed shapes in overall buckling failure of these S690 CFSHS.

The load-deformation curves are employed to demonstrate the structural behaviour of slender columns under compression. The applied load-axial shortening curves of all the columns increase linearly initially, but suddenly they drop sharply after the peak loads are reached. Moreover, in all cases, the columns fail with overall buckling, and they deflect laterally once the axial loads are applied. Their load-deflection curves then increase linearly, followed with a gradual decrease after the failure mode is attained. Fig. 4.23 illustrates the typical relationships of the applied loads against the displacements of Tests S3A-Q and S3B-Q. As shown in Fig. 4.23 a), significant decreases are found in both the load-displacement curves after the peak loads are reached. It should be noted that, in the same graph, the lateral deflection increases quicker than the axial shortening after the peak load is reached. This indicates that an obvious overall buckling has occurred. Similar trends are also evident in the applied load-displacement curves shown in Fig. 4.23 b), and this signifies that these two series of sections exhibit very similar buckling behaviour under compression.

Fig. 4.24 illustrates typical load-strain curves of Tests S3A-Q and S3B-Q. In each graph, it is shown that four load-strain curves coincide with each other initially, indicating that the column is under a uniform compression at the elastic stage. As the applied load increases, and the strains go beyond f_y/E, these curves gradually depart from one another, indicating overall buckling initiates after yielding. The description on the load-displacement relationships adopt to both graphs in Fig. 4.24, which indicates that structural behaviour without significant difference is performed by these two series of sections. Moreover, the consistent results are demonstrated by the other 22 tests.

4.5.4 Comparison with EN 1993-1

As demonstrated by the test results, the measured member resistances of many of the slender columns exceed the design member resistances, $N_{b,Rd}$, predicted with the buckling curve "c". This means that the current design rule givin in EN 1993-1-1 is too conservative to design these slender columns of CFSHS by directly adopting the existing design rules given in EN 1993-1-1. Figs. 4.25 and 4.26 illustrate the differences in the member resistances between the slender columns with Series SA and SB sections. Obviously, the slender columns with Series SB sections have larger reduction factors, $\chi = \frac{N_{b,Et}}{N_{c,Rd}}$, than those with Series SA sections. Based on a direct comparison between the measured and the design resistances predicted by various buckling curves "a_0" to "d" with different imperfection factors, α, it is reasonable to propose the use of a reduced value for the imperfection factor, α, for slender columns of both Series SA and SB sections.

As previously discussed in Section 4.3.4, the modified c-values should be adopted to classify these S690 CFSHS under compression into the proper classes that match well with their section strength mobilization and ductility. The same modification is adopted for the design of slender columns. By replacing R_{out} with 1.5t, the values of c'/t/ε of all the 24 sections are calculated and summarized in Table 4.11. It is shown that the changes of classification are not only extensive but also significant. Changes in section classes are found in ten sections, among which six sections are degraded to Class 4. Their effective areas, A_{eff}, design section resistances, $N_{c,Rd}$, non-dimensional slenderness ratios, $\bar{\lambda}$, and design member resistances, $N_{b,Rd}$, have been calculated correspondingly. Obviously, the modified c-values reduce $N_{c,Rd}$ of all Class 4 sections, thus increasing the non-slenderness ratios and decreasing the ratios $N_{b,Et}/N_{c,Rd}$. Moreover, the averaged $N_{b,Et}/N_{b,Rd}$ has been increased from 1.35 (see Table 4.10) to 1.36 (see Table 4.11), showing the that using this modification may further increase safety margin for member resistances under axial buckling, but their resistances have already underestimated based on the design curve "c". It is therefore recommended that the modified c-values should not be adopted for the design of slender columns.

4.5.5 Summary

An experimental investigation into a total of 24 S690 slender columns of cold-formed square hollow sections under concentric compression is presented. It should be noted that:

- Except for those columns with Class 4 sections, all stocky columns with Classes 1, 2 and 3 sections are shown to mobilize their member resistances. For those Class 4 sections, by adopting A_{eff} to determine $N_{c,Rd}$, they are shown to have attained their member resistances.

- Based on a direct comparison between the measured and the design resistances of these slender columns, it is proposed to improve the design method such that a higher curve with a smaller imperfection factor should be used.

- It is recommended that the modified c-values should not be adopted for the design of slender columns.

4.6 Conclusions

A total of 12 S690 CFSHS are examined in this Chapter. An experimental investigation into the structural behaviour of a total of 38 S690 CFSHS column tests is presented, including 8 stocky columns under compression, 6 stocky under combined compression and bending, and 24 slender columns under compression.

- In general, all stocky columns with Classes 1, 2 and 3 sections have mobilized their full resistance of the gross section under compression, except Sections S2A and S2B which are Class 4 sections. Consistent findings are also demonstrated by these stocky columns under combined compression and bending. Besides, it is proposed to adopt modified c-values to classify the section classes for the design of S690 CFSHS stocky columns under compression and under combined compression and bending. Consequently, all these sections with modified classes fulfil the design requirements of EN 1993-1-1.

- Similarly, all slender columns with Classes 1, 2 and 3 sections are able to mobilize their member resistances under compression, except for Test S2B-P with Class 4 section. Based on a direct comparison between the measured and the design resistances predicted by the method given in EN 1993-1-1, it is proposed to improve the design method such that a higher curve with a smaller imperfection factor should be used.

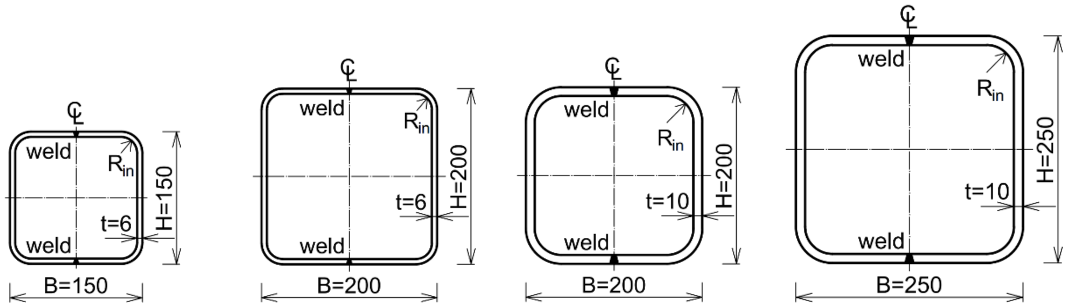

a) Section S1A Class 2 | b) Section S2A Class 4 | c) Section S3A Class 1 | d) Section S4A Class 1

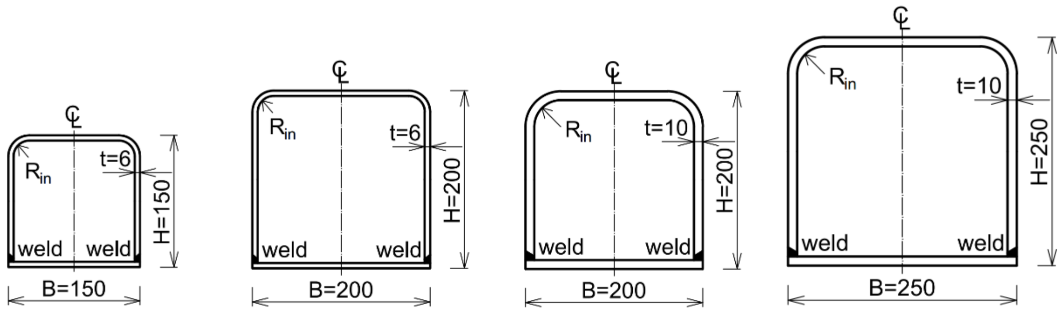

e) Section S1B Class 3 | f) Section S2B Class 4 | g) Section S3B Class 1 | h) Section S4B Class 3

Fig. 4.1 Nominal dimensions of sections with section classification under compression to EN 1993-1-1: Sections S1 to S4

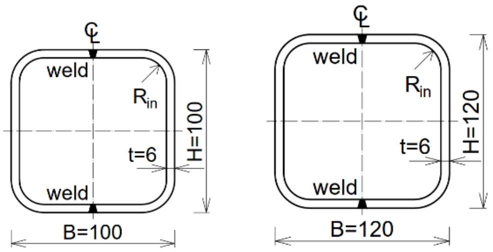

a) Section S5A Class 1 | b) Section S6A Class 1

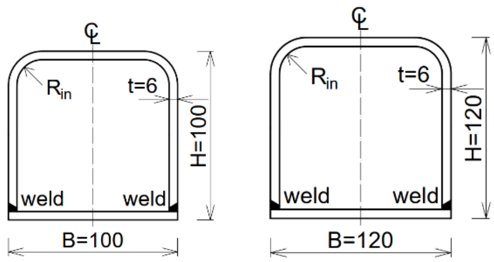

c) Section S5B Class 1 | d) Section S6B Class 1

Fig. 4.2 Nominal dimensions of sections with section classification under compression to EN 1993-1-1: Sections S5 and S6

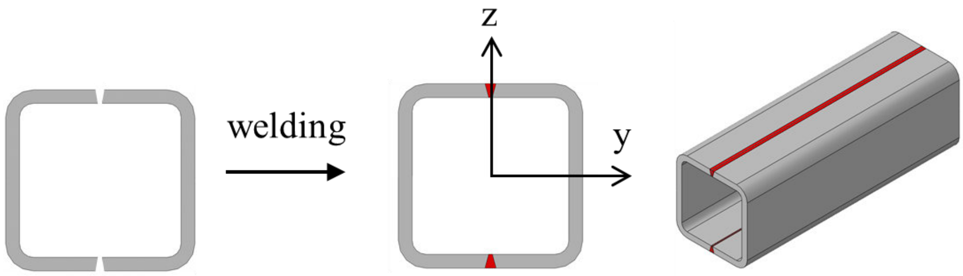

a) Series SA

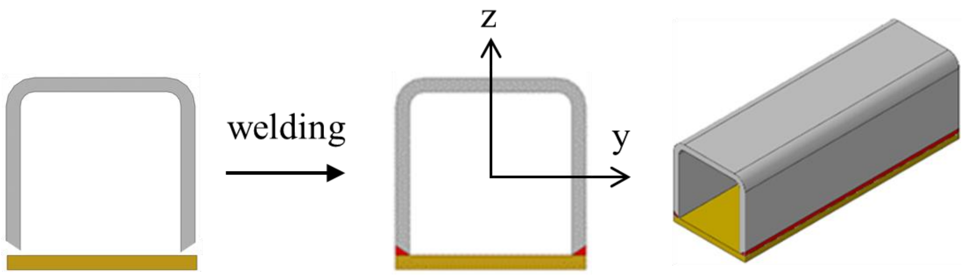

b) Series SB

Fig. 4.3 Fabrication processes of CFSHS

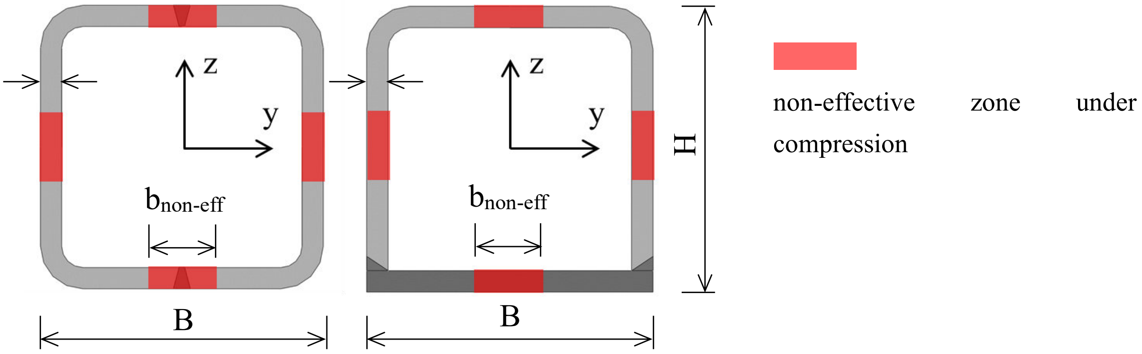

a) under compression

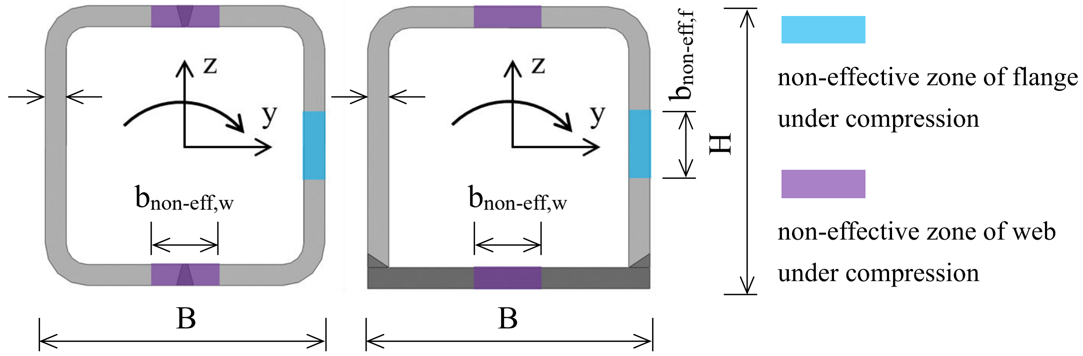

b) under bending

Fig. 4.4 Non-effective zones in Class 4 sections

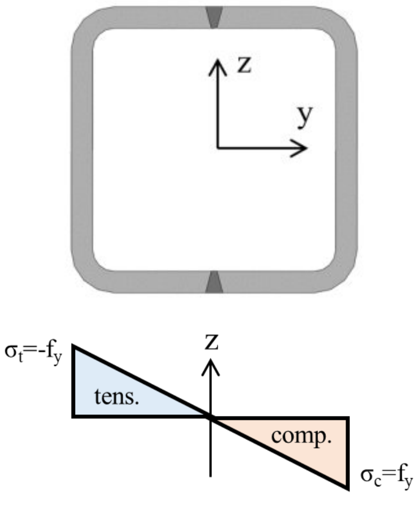

a) stress distribution of gross section

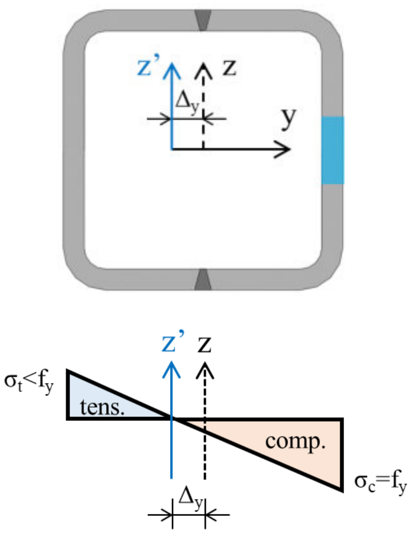

b) stress distribution of effective section

Fig. 4.5 Stress distributions in Class 4 sections under bending

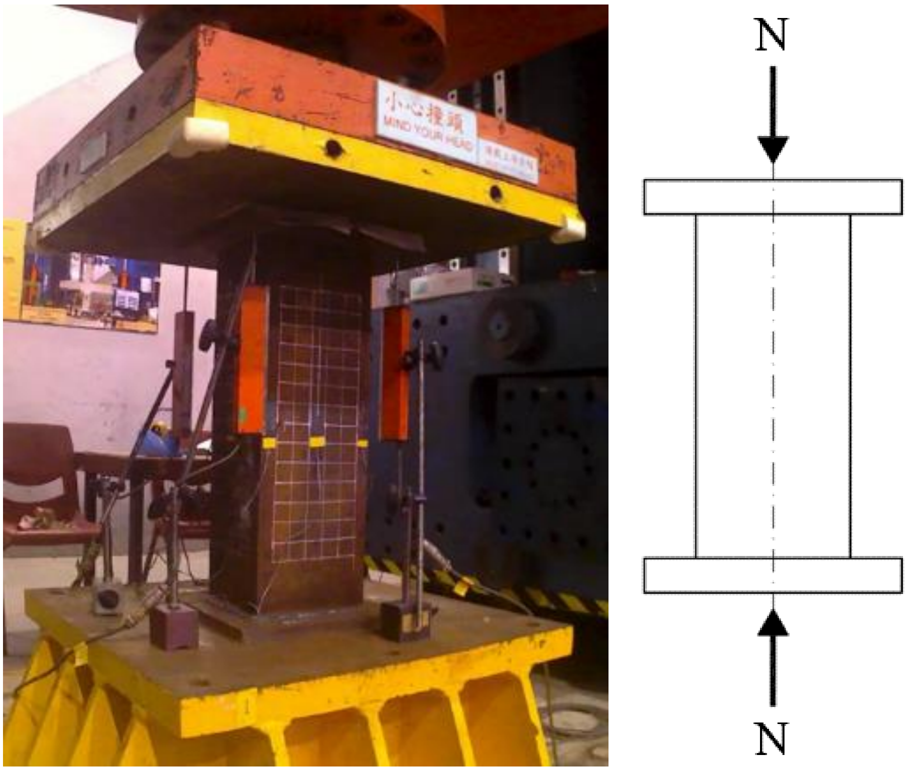

Fig. 4.6 Test set-up for stocky columns under concentric compression

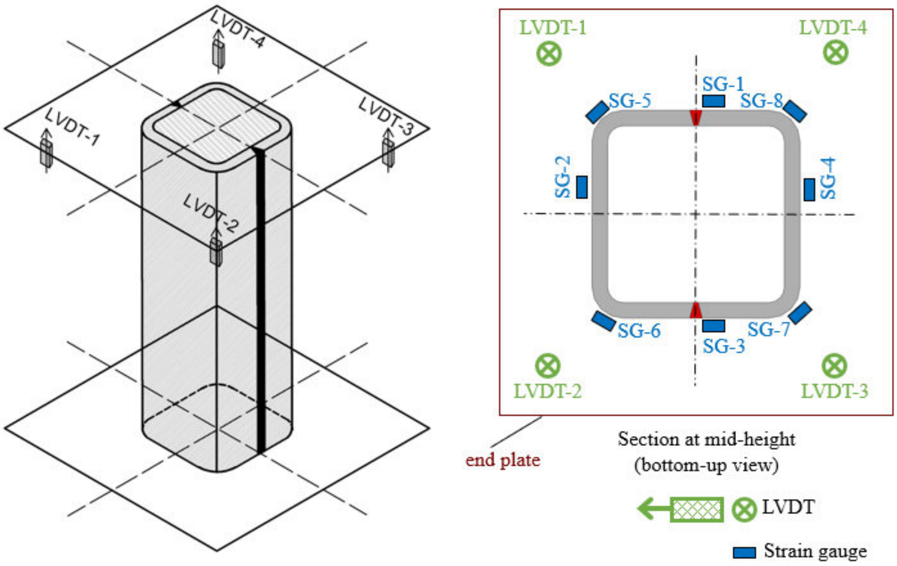

a) Series SA-S

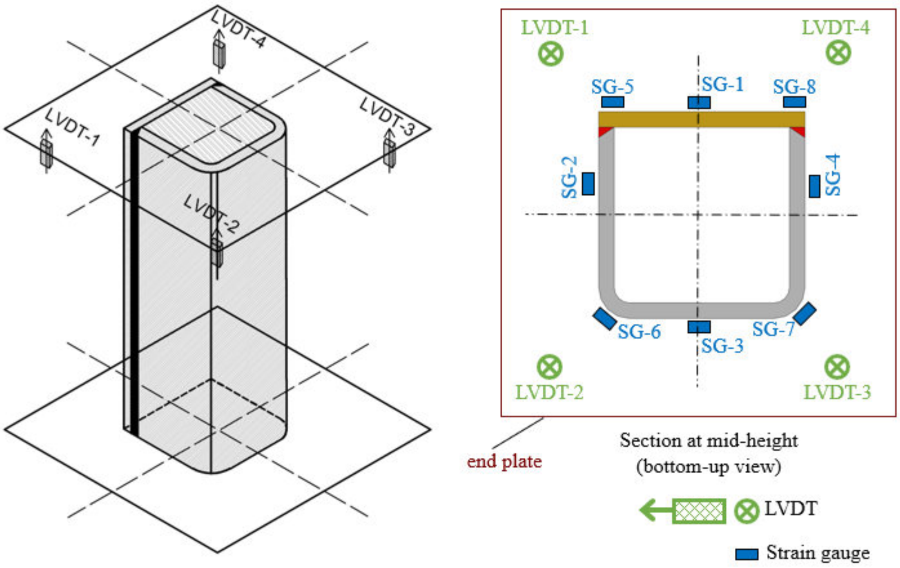

b) Series SB-S

Fig. 4.7 Instrumentation for stocky columns under concentric compression

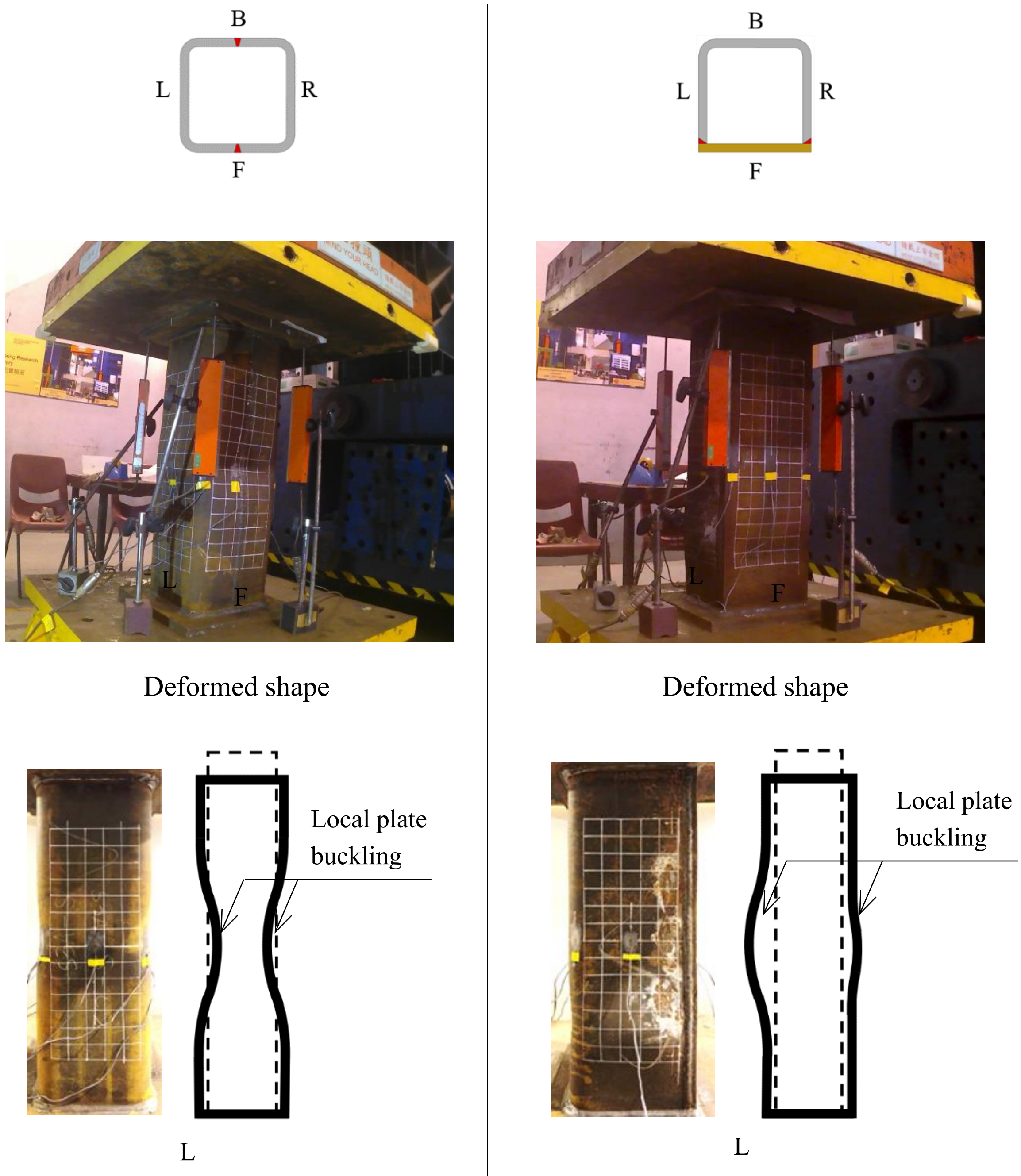

a) Test S3A-S b) Test S3B-S

Fig. 4.8 Typical failure modes of stocky columns under concentric compression: Tests S3A-S and S3B-S

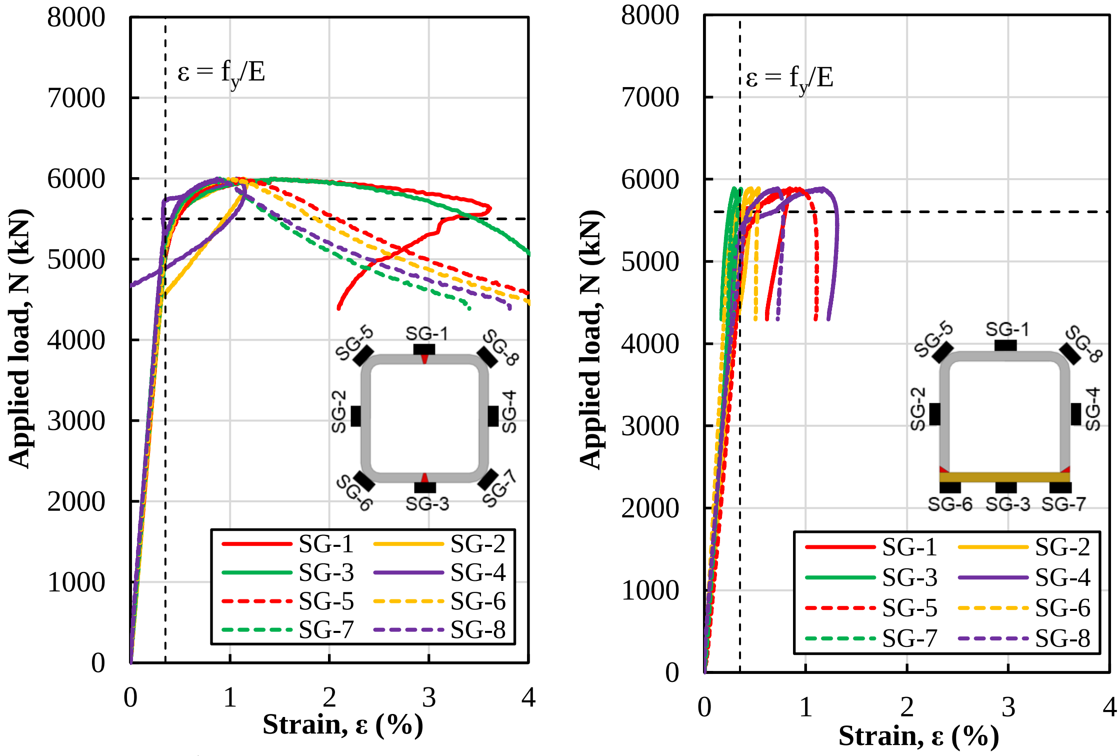

a) Test S3A-S

b) Test S3B-S

Fig. 4.9 Typical applied load-strain curves of stocky columns under concentric compression: Tests S3A-S and S3B-S

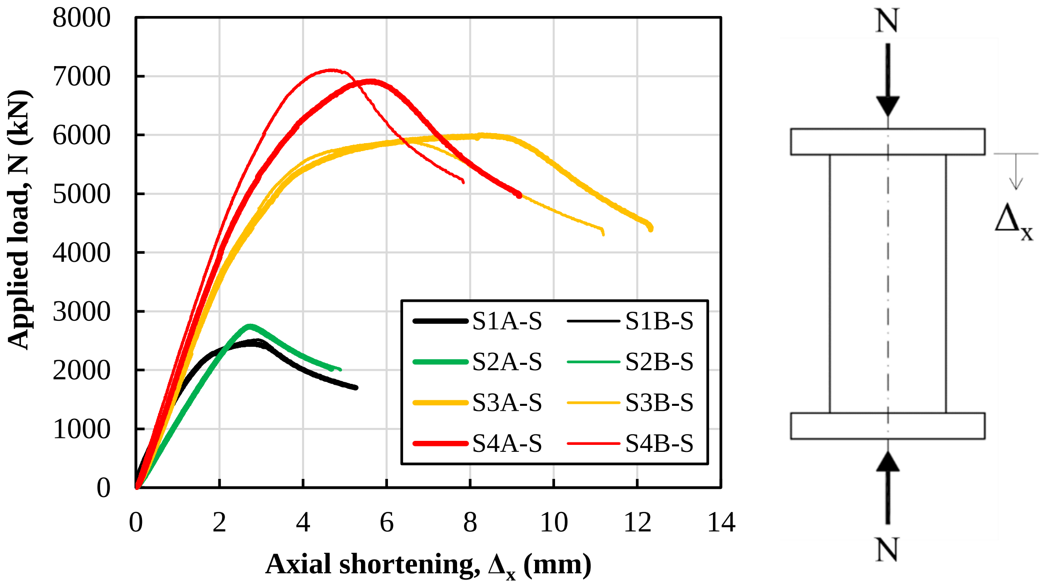

Fig. 4.10 Applied load-axial shortening curves of stocky columns under concentric compression

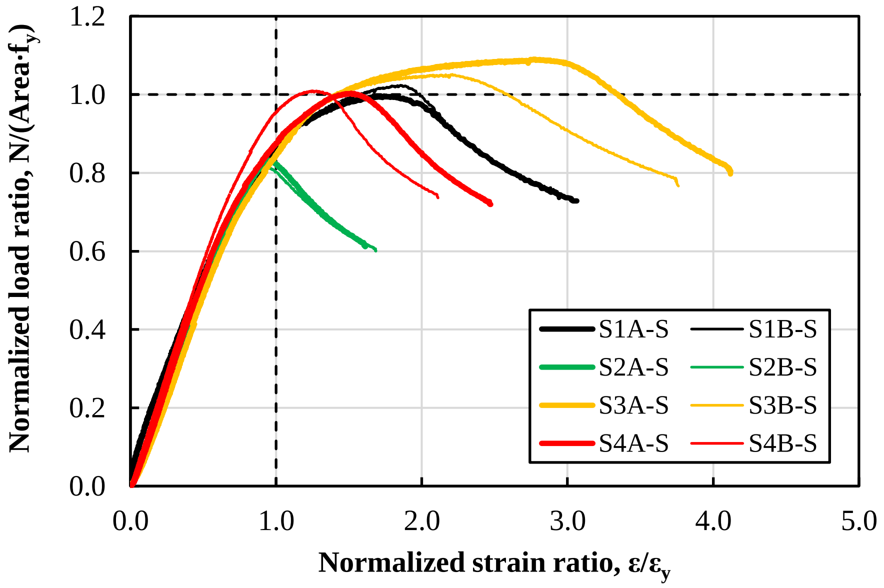

Fig. 4.11 Normalized load-strain curves of stocky columns under concentric compression

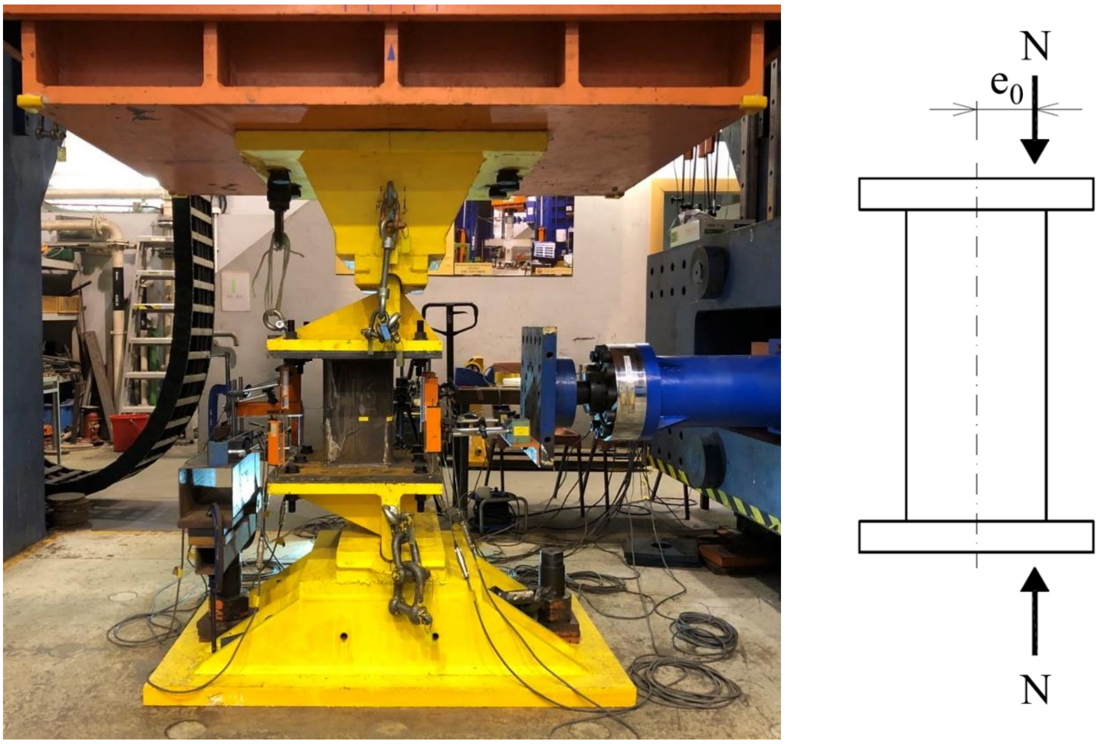

Fig. 4.12 Test set-up for stocky columns under eccentric compression

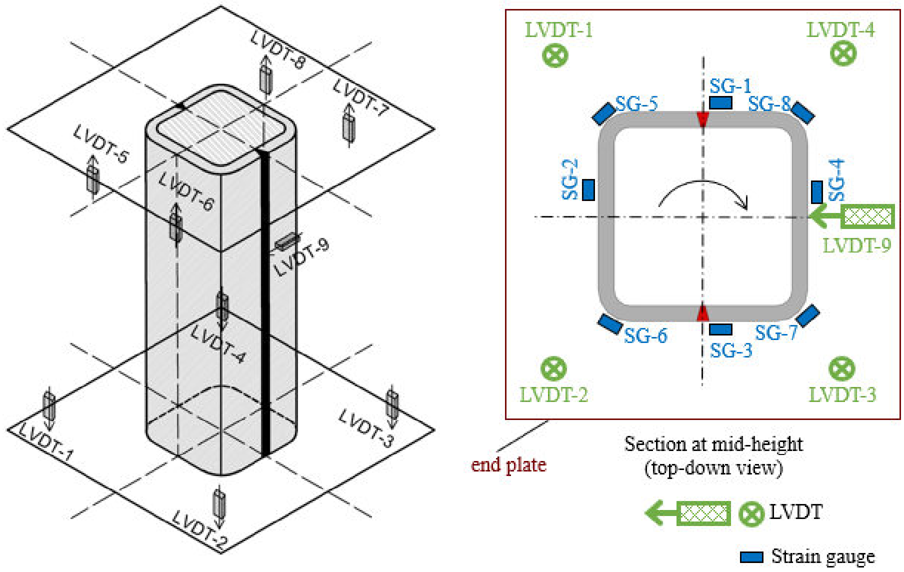

a) Series SA-E

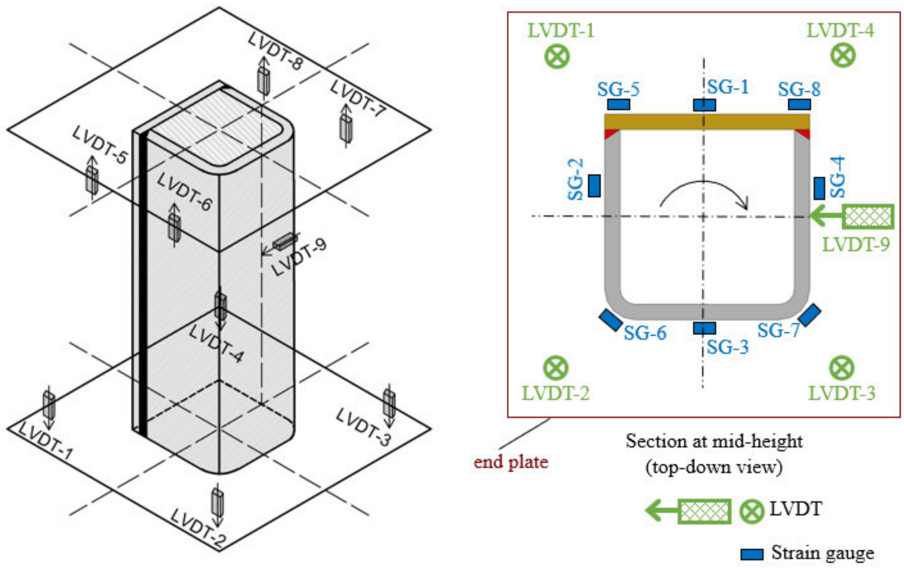

b) Series SB-E

Fig. 4.13 Instrumentation for stocky columns under eccentric compression

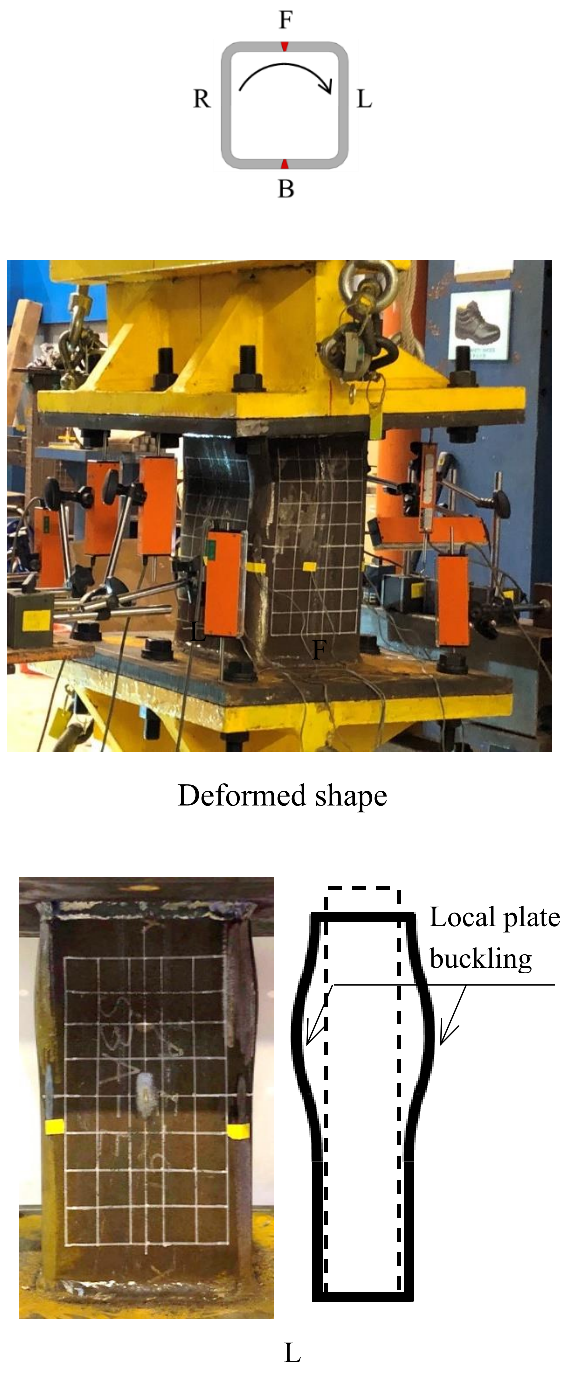

a) Test S3A-E

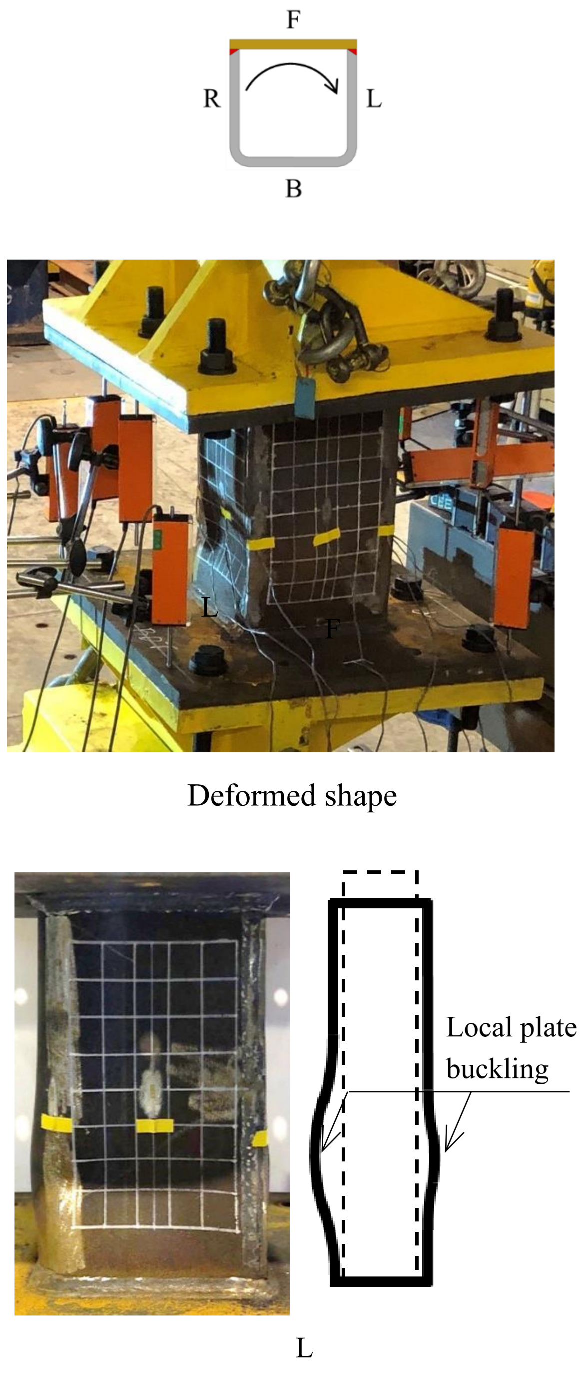

b) Test S3B-E

Fig. 4.14 Typical failure modes of stocky columns under eccentric compression: Tests S3A-E and S3B-E

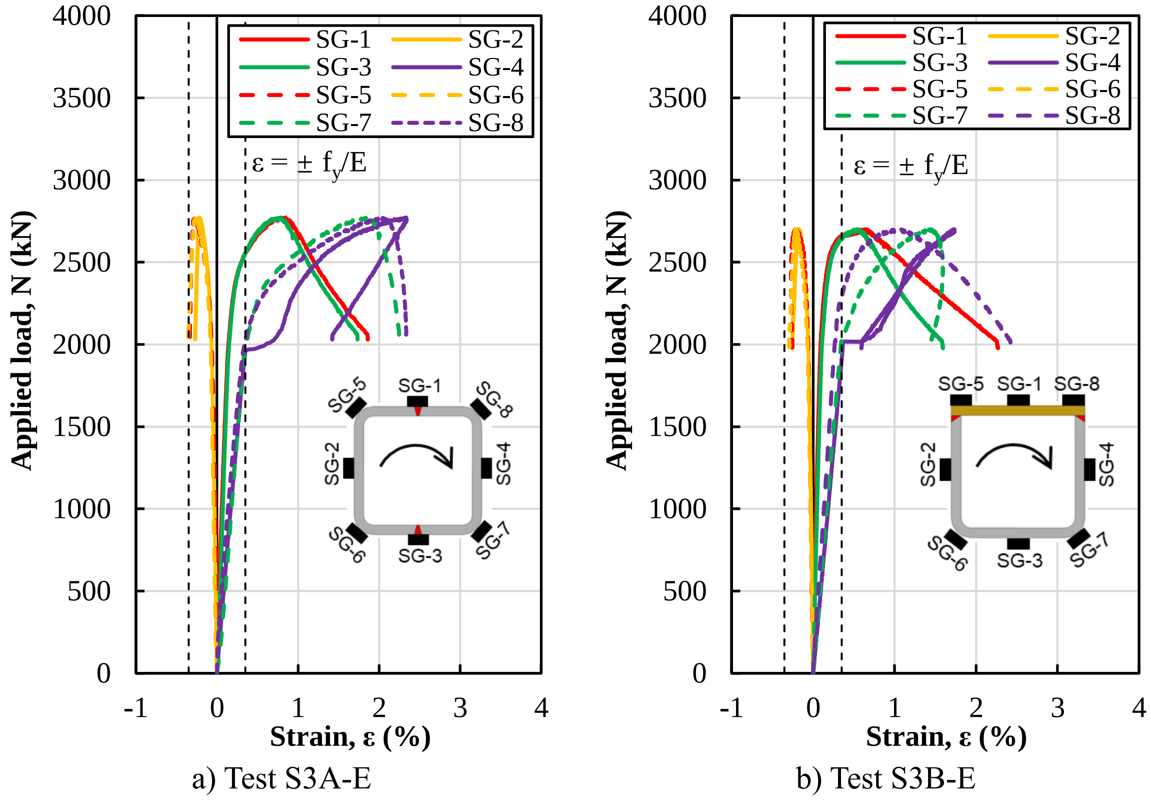

Fig. 4.15 Typical applied load-strain curves of stocky columns under eccentric compression: Tests S3A-E and S3B-E

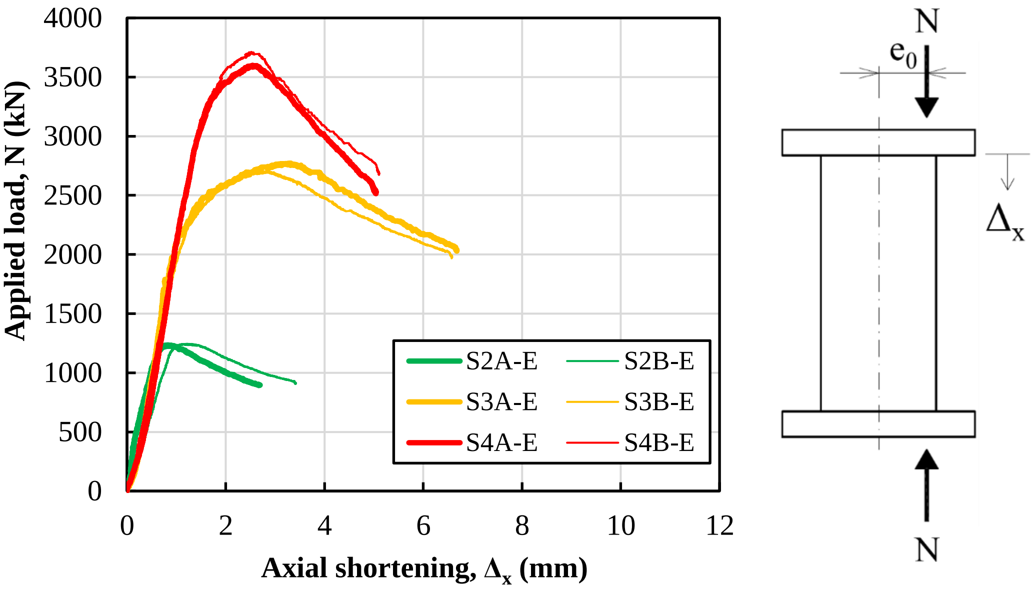

a) Applied load-axial shortening curves

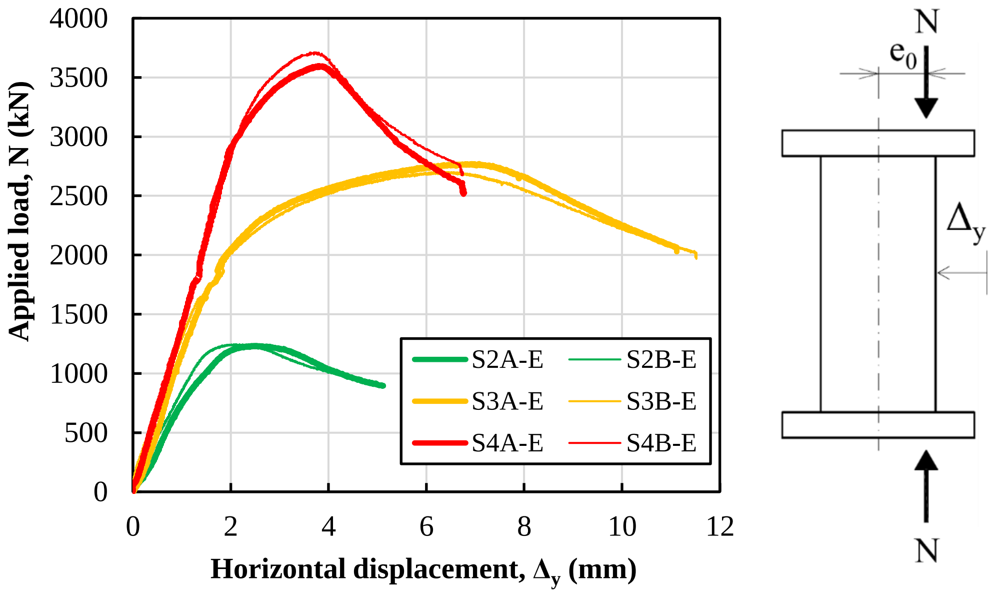

b) Applied load-horizontal displacement curves

Fig. 4.16 Applied load-displacement curves of stocky columns under eccentric compression

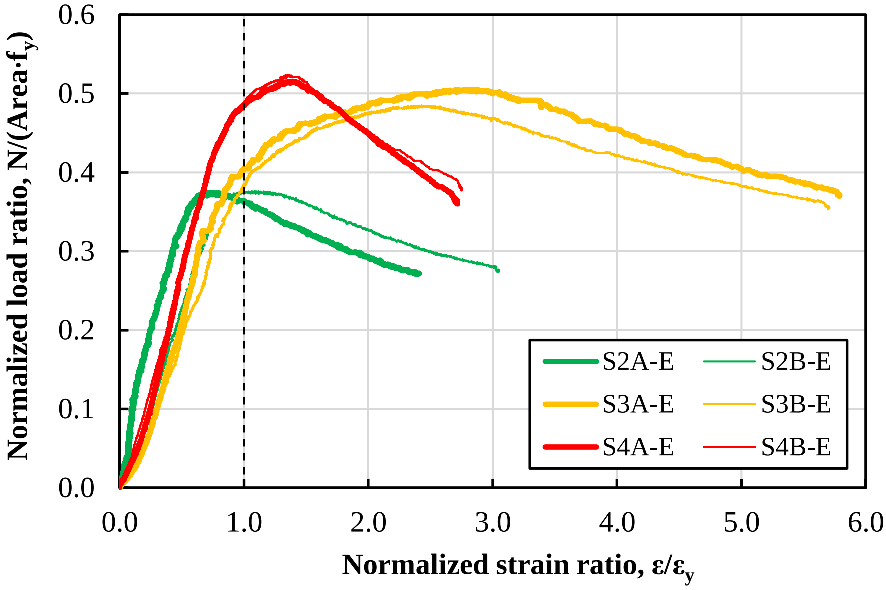

Fig. 4.17 Normalized load-strain curves of stocky columns under eccentric compression

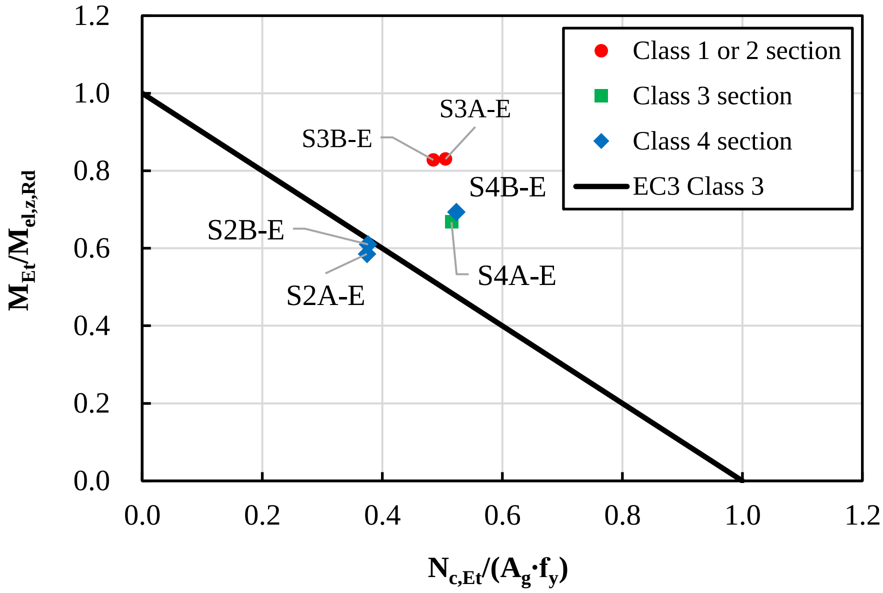

a) N-M interaction curve for Class 3 section

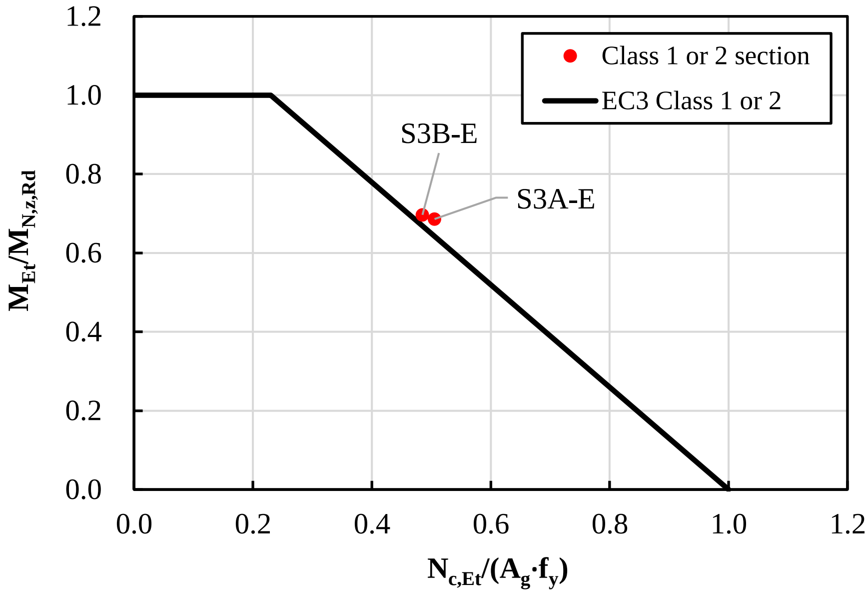

b) N-M interaction curve for Class 1 and 2 sections

Fig. 4.18 N-M interaction curves of EN 1993-1-1

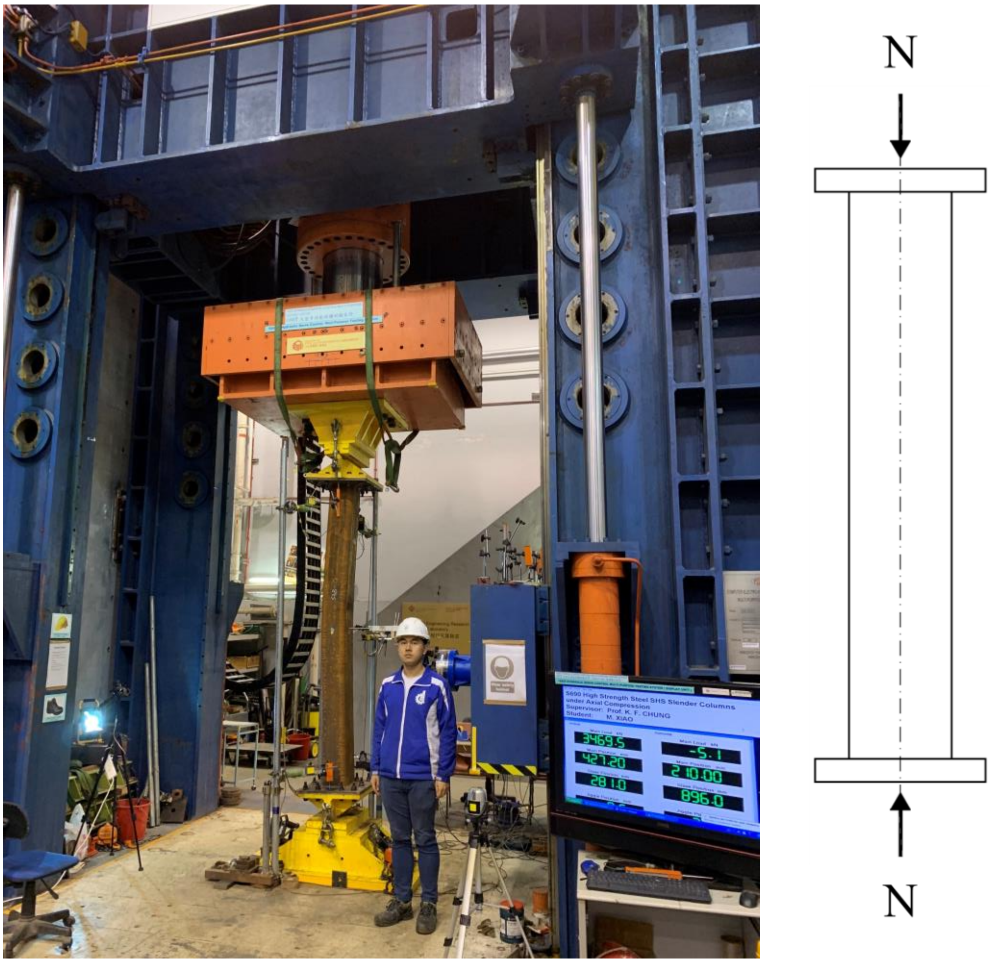

Fig. 4.19 Loading system of slender columns under concentric compression

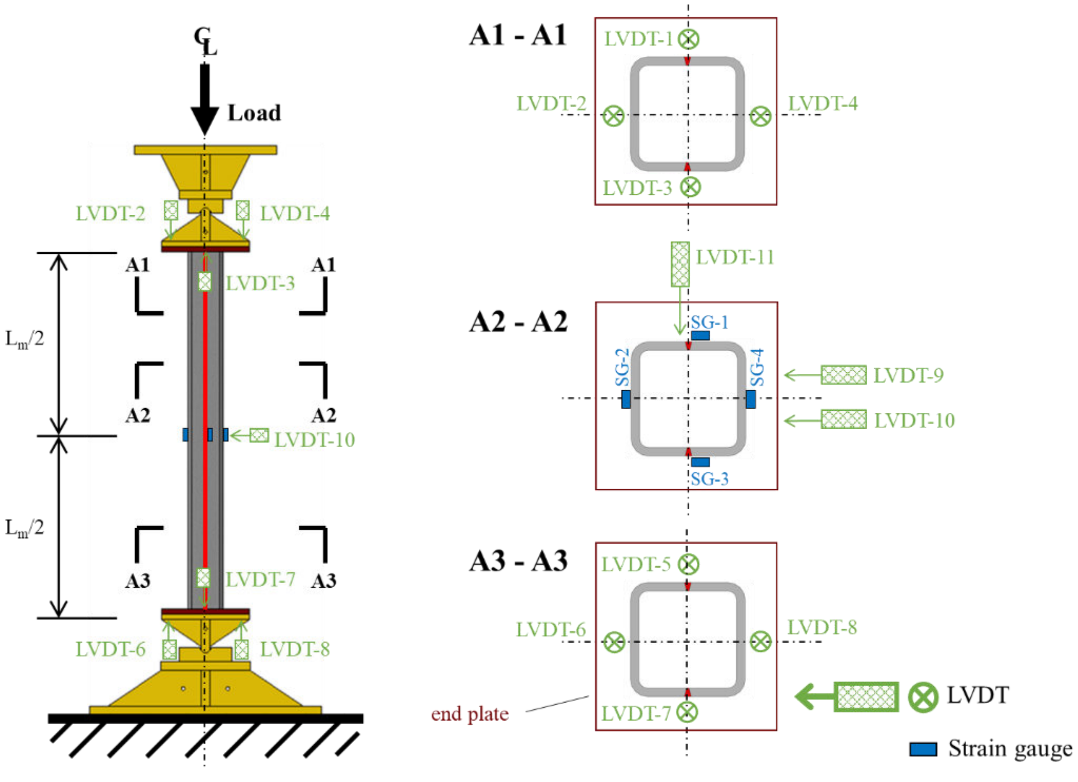

a) Series SA-P/Q

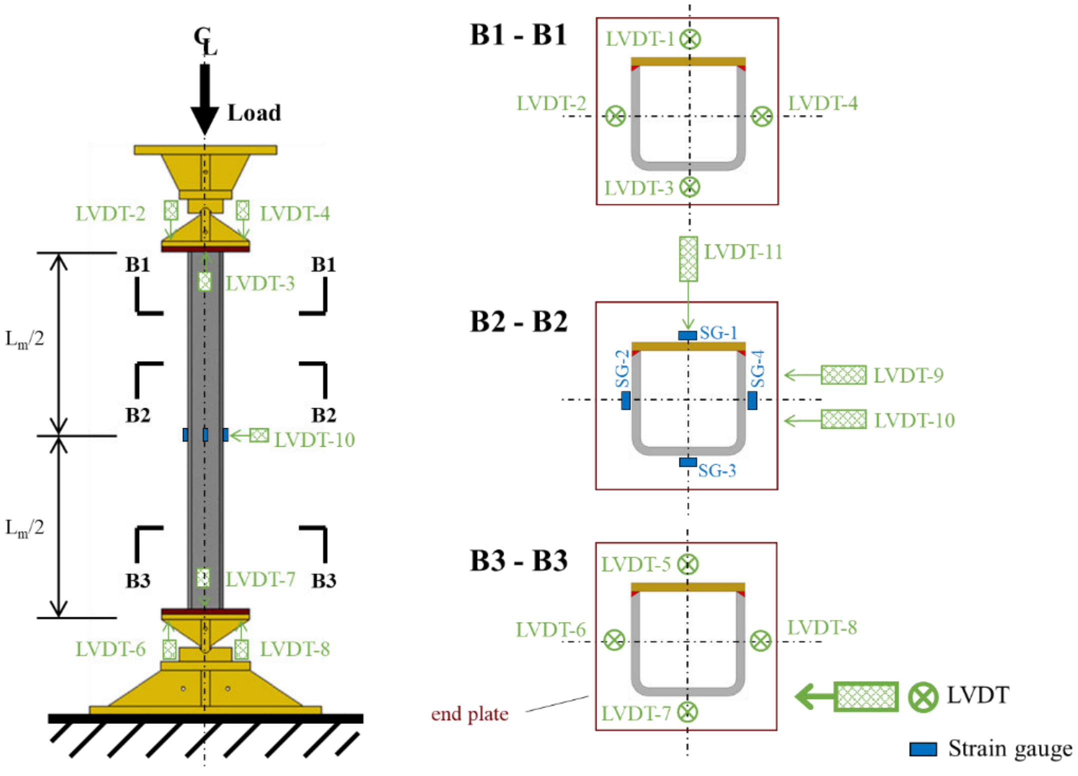

b) Series SB-P/Q

Fig. 4.20 Instrumentation for slender columns under concentric compression

Fig. 4.21 Failure modes of slender columns under concentric compression

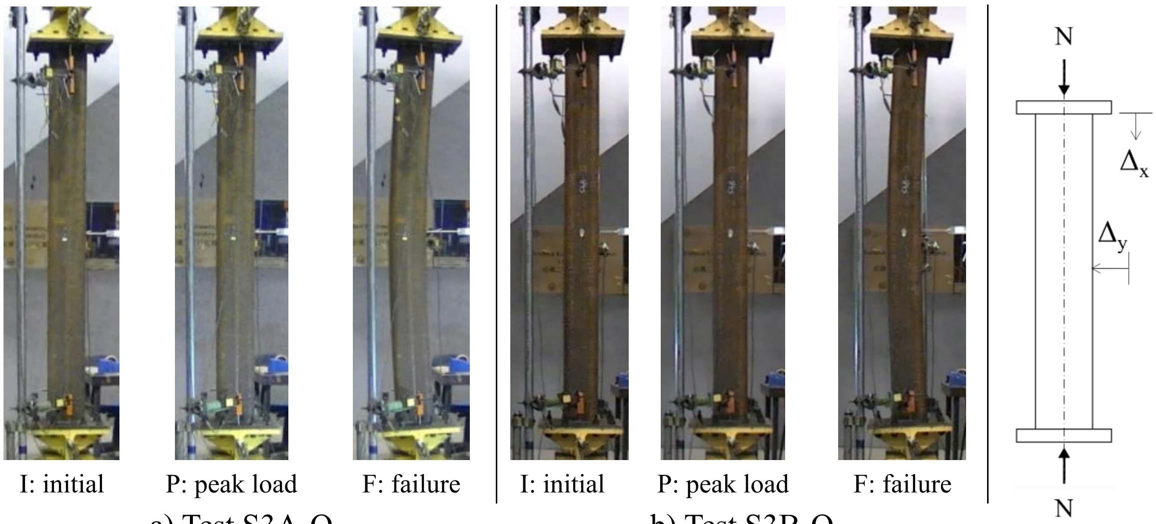

a) Test S3A-Q b) Test S3B-Q

Fig. 4.22 Typical failure modes of slender columns under concentric compression: Tests S3A-Q and S3B-Q

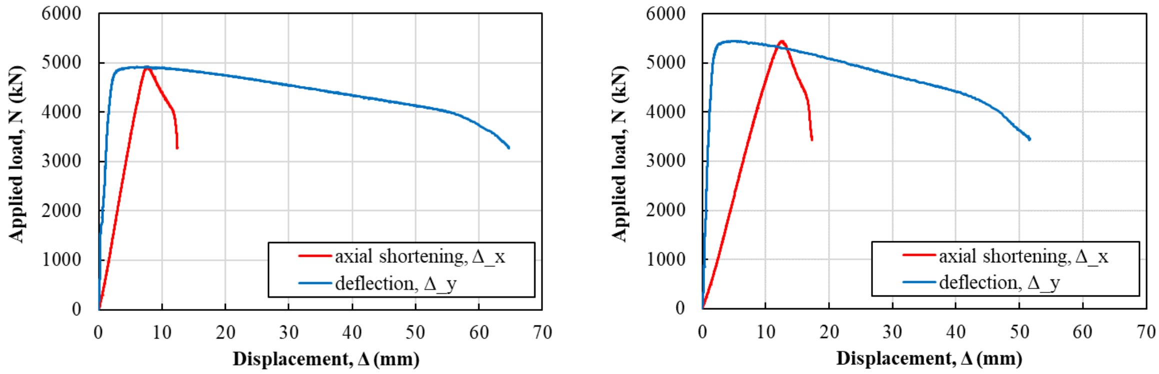

a) Test S3A-Q b) Test S3B-Q

Fig. 4.23 Typical applied load-displacement curves of slender columns under concentric compression: Tests S3A-Q and S3B-Q

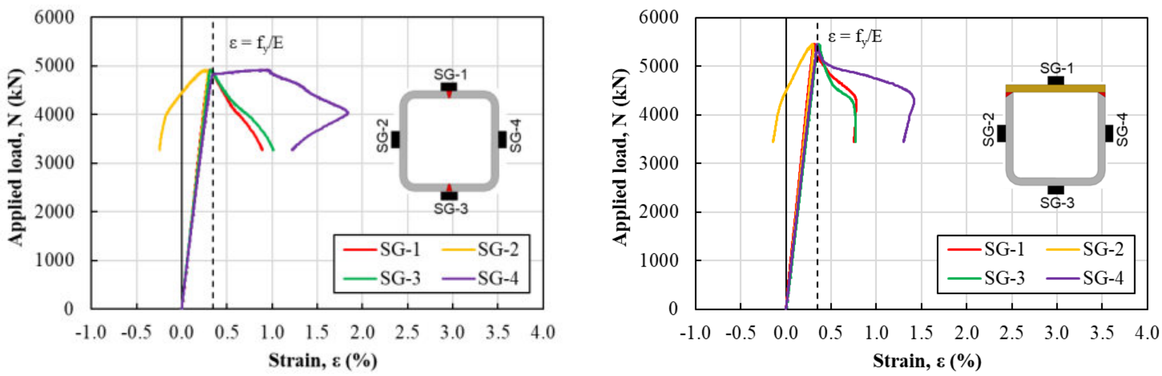

a) Test S3A-Q b) Test S3B-Q

Fig. 4.24 Typical applied load-strain curves of slender columns under concentric compression: Tests S3A-Q and S3B-Q

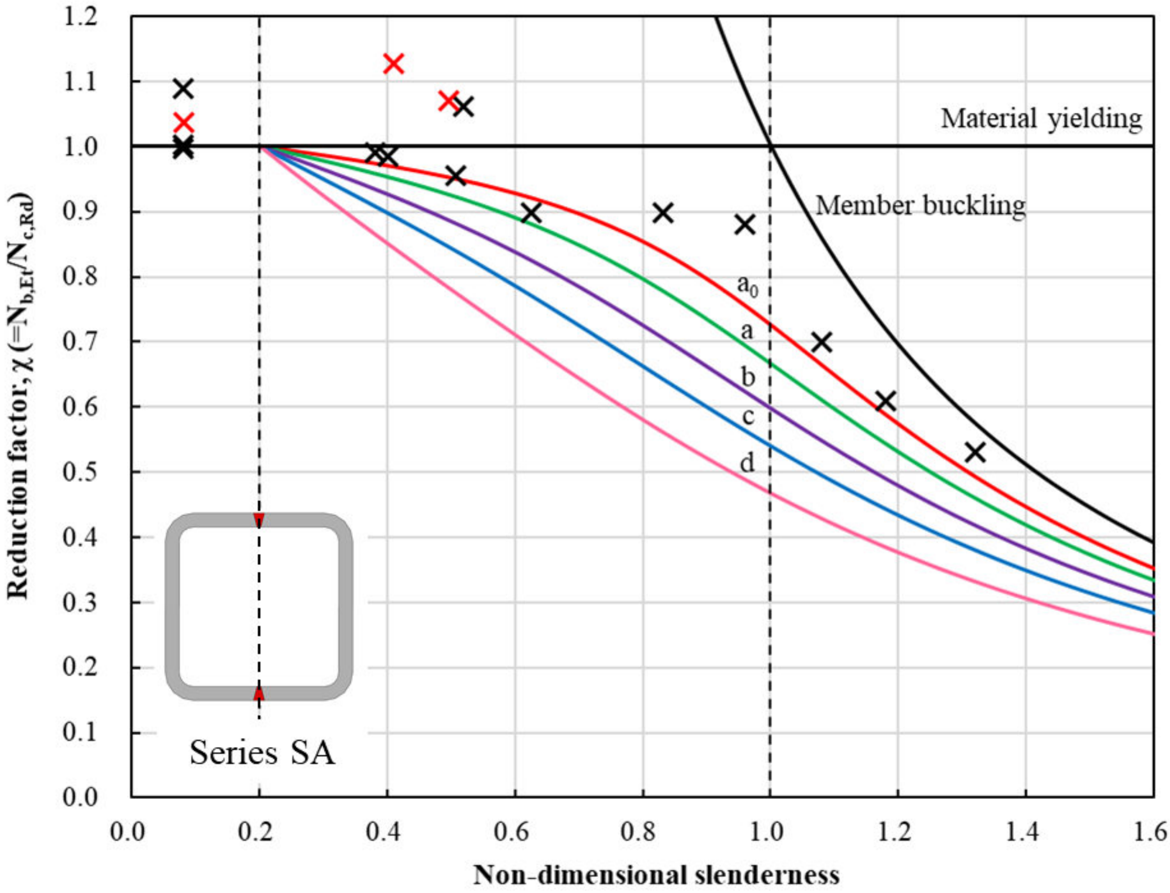

Note 1: A_g is used for calculating $N_{c,Rd}$ of Class 1, 2 and 3 sections; and A_{eff} is used for calculating $N_{c,Rd}$ of Class 4 sections.

Note 2: "**X**" denotes the Class 1, 2 or 3 section; "**X**" denotes the Class 4 section.

Fig. 4.25 Comparison between measured and predicted resistances of slender columns under concentric compression to EN 1993-1-1: Series SA

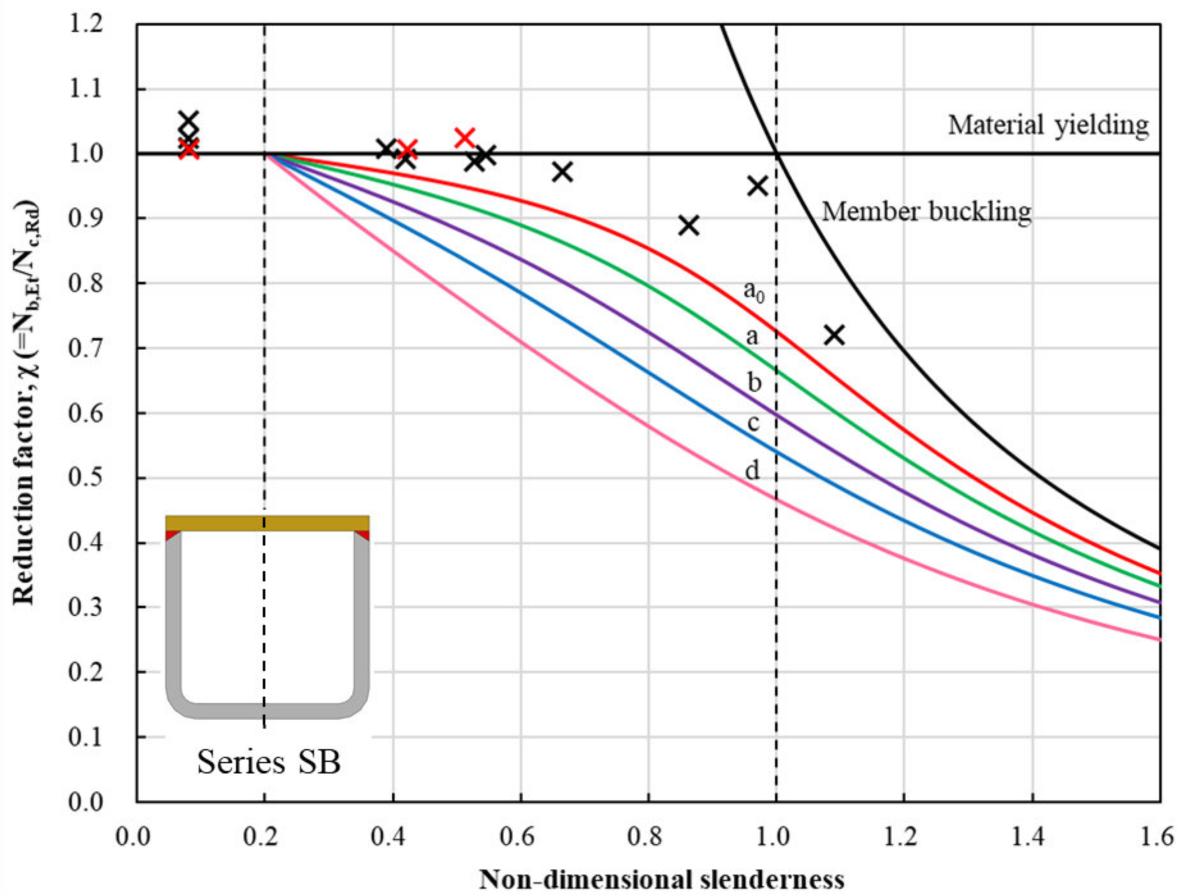

Note 1: A_g is used for calculating $N_{c,Rd}$ of Class 1, 2 and 3 sections; and A_{eff} is used for calculating $N_{c,Rd}$ of Class 4 sections.

Note 2: "**X**" denotes the Class 1, 2 or 3 section; "**X**" denotes the Class 4 section.

Fig. 4.26 Comparison between measured and predicted resistances of slender columns under concentric compression to EN 1993-1-1: Series SB

Table 4.1 Section classification of CFSHS (nominal dimensions)

Series	Designation	Nominal dimensions of section (mm)					c/t/ε	Section class
		B	H	t	R_{out}	c		
SA	(1) S1A	150	150	6	24	102	29.1	1
	(2) S2A	200	200	6	24	152	43.4	4
	(3) S3A	200	200	10	40	120	20.6	1
	(4) S4A	250	250	10	40	170	29.1	1
	(5) S5A	100	100	6	24	52	14.9	1
	(6) S6A	120	120	6	24	72	20.6	1
SB	(7) S1B	150	150	6	24	138	39.4	3
	(8) S2B	200	200	6	24	188	53.7	4
	(9) S3B	200	200	10	40	180	30.8	1
	(10) S4B	250	250	10	40	230	39.4	3
	(11) S5B	100	100	6	24	88	25.1	1
	(12) S6B	120	120	6	24	108	30.9	1

Note 1: for Series SA, $c = B - 2R_{out}$ or $c = H - 2R_{out}$, whichever is greater; for Series SB, $c = B - 2t$ or $c = H - t - R_{out}$, whichever is greater.

Note 2: $\varepsilon = \sqrt{235/f_y} = \sqrt{235/690} = 0.584$.

Table 4.2 Sectional properties of Class 4 sections (nominal dimensions)

Series	Section	A_g (mm^2)	A_{eff} (mm^2)	$W_{el,z}$ (mm^3)	$W_{eff,z}$ (mm^3)	A_{eff} / A_g	$W_{eff,z}$ / $W_{el,z}$
SA	S2A	4440	3697	270×10^3	242×10^3	0.83	0.90
SB	S2B	4548	3752	281×10^3	251×10^3	0.82	0.89

Table 4.3 Test programme of stocky columns under concentric compression

Series	Designation	c/t/ε	Section class	Measured dimensions of specimens (mm)					A_g (mm^2)	I_z (mm^4)	$\bar{\lambda}_z$
				B	H	t	R_{out}	L_m			
SA	(1) S1A-S	34.6	2	163.0	150.0	5.88	23.88	461	3355	1301×10^4	0.08
	(2) S2A-S	48.0	4	207.7	204.5	5.88	23.88	608	4497	2955×10^4	0.08
	(3) S3A-S	23.9	1	212.0	206.7	9.89	39.89	610	7297	4673×10^4	0.08
	(4) S4A-S	32.6	1	252.0	260.0	9.89	39.89	759	9143	8652×10^4	0.08
SB	(5) S1B-S	41.5	3	150.0	156.0	5.88	23.88	461	3355	1152×10^4	0.08
	(6) S2B-S	56.5	4	200.0	207.0	5.88	23.88	609	4542	2841×10^4	0.08
	(7) S3B-S	33.0	2	202.0	208.5	9.89	39.89	608	7432	4499×10^4	0.08
	(8) S4B-S	41.7	3	250.0	257.0	9.89	39.89	758	9341	8873×10^4	0.08

Note 1: for Series SA, $c = B - 2R_{out}$ or $H - 2R_{out}$, whichever is greater; for Series SB, $c = B - 2t$ or $c = H - t - R_{out}$, whichever is greater.

Note 2: for S1 and S2 sections, $\varepsilon = \sqrt{235/f_y} = \sqrt{235/733} = 0.566$; for S3 and S4 sections, $\varepsilon = \sqrt{235/f_y} = \sqrt{235/754} = 0.558$.

Table 4.4 Test results of stocky columns under concentric compression

Series	Designation	c/t/ε	Section class	A_{eff} (mm²)	$N_{c,Rd}$ (kN)	$N_{c,Et}$ (kN)	$\frac{N_{c,Et}}{A_g \cdot f_y}$	$\frac{N_{c,Et}}{N_{c,Rd}}$	Strength mobilization
SA	(1) S1A-S	34.6	2	NA	2459	2450	1.00	1.00	full-elastic
	(2) S2A-S	48.0	4	3606	2643	2745	0.83	1.04	--
	(3) S3A-S	23.9	1	NA	5502	5999	1.09	1.09	full-plastic
	(4) S4A-S	32.6	1	NA	6894	6914	1.00	1.00	full-elastic
SB	(5) S1B-S	41.5	3	NA	2459	2517	1.02	1.02	full-elastic
	(6) S2B-S	56.5	4	3644	2671	2719	0.82	1.02	--
	(7) S3B-S	33.0	2	NA	5604	5891	1.05	1.05	full-plastic
	(8) S4B-S	41.7	3	NA	7043	7108	1.01	1.01	full-elastic

Note 1: for Class 1, 2 and 3 sections, $N_{c,Rd} = A_g \cdot f_y$; for Class 4 sections, $N_{c,Rd} = A_{eff} \cdot f_y$.

Table 4.5 Test results of stocky columns under concentric compression (modified section classification)

Series	Designation	c'/t/ε	Section class (modified)	A_{eff} (mm²)	$N_{c,Rd}$ (kN)	$\frac{N_{c,Et}}{N_{c,Rd}}$	Strength mobilization
SA	(1) S1A-S	43.7	4	3188	2337	1.05	full-elastic
	(2) S2A-S	57.1	4	3606	2643	1.04	--
	(3) S3A-S	33.0	2	NA	5502	1.09	full-plastic
	(4) S4A-S	41.7	3	NA	6894	1.00	full-elastic
SB	(5) S1B-S	42.4	4	3211	2353	1.07	full-elastic
	(6) S2B-S	57.8	4	3644	2671	1.02	--
	(7) S3B-S	33.3	2	NA	5604	1.05	full-plastic
	(8) S4B-S	42.1	4	8950	7043	1.05	full-elastic

Note 1: for Series SA, c' = B - 3t or H - 3t, whichever is greater; for Series SB, c' = B - 2t or c = H - 2.5t, whichever is greater.

Table 4.6 Test programme of stocky columns under eccentric compression

Series	Designation	c/t/ε	Section class	Measured dimensions of specimens (mm)					A_g	I_z	$W_{pl,z}$	$W_{el,z}$
				B	H	t	R_{out}	L_m	(mm^2)	(mm^4)	(mm^3)	(mm^3)
SA	(1) S2A-E	46.4	4	210.0	202.3	5.88	23.88	328	4499	3007×10^4	336×10^3	283×10^3
	(2) S3A-E	22.4	1	214.0	203.5	9.89	39.89	329	7274	4715×10^4	533×10^3	441×10^3
	(3) S4A-E	31.4	1	265.0	253.0	9.89	39.89	529	9261	9523×10^4	856×10^3	719×10^3
SB	(4) S2B-E	53.1	4	198.0	206.7	5.88	23.88	329	4515	2772×10^4	325×10^3	280×10^3
	(5) S3B-E	29.0	1	198.5	210.0	9.89	39.89	329	7392	4342×10^4	520×10^3	438×10^3
	(6) S4B-E	38.1	3	250.0	260.3	9.89	39.89	529	9405	8966×10^4	843×10^3	717×10^3

Note 1: for Series SA, $c = H - 2R_{out}$; for Series SB, $c = H - t - R_{out}$.

Note 2: for S2 sections, $\varepsilon = \sqrt{235/f_y} = \sqrt{235/733} = 0.566$; for S3 and S4 sections, $\varepsilon = \sqrt{235/f_y} = \sqrt{235/754} = 0.558$.

Table 4.7 Test results of stocky columns under eccentric compression

Series	Designation	$c/t/\varepsilon$	Section class	A_g (mm^2)	A_{eff} (mm^2)	$W_{el,z}$ (mm^3)	$W_{eff,z}$ (mm^3)	$N_{c,Rd}$ (kN)	$N_{c,Et}$ (kN)	$\frac{N_{c,Et}}{N_{c,Rd}}$	e_0 (mm)	$M_{c,z,Rd}$ (kNm)	M_{Et} (kNm)	$\frac{M_{Et}}{M_{c,z,Rd}}$	$\frac{N_{c,Et}}{N_{c,Rd}}+\frac{M_{Et}}{M_{c,z,Rd}}$
SA	(1) S2A-E	46.4	4	4499	3531	283 x10^3	252 x10^3	3298	1235	0.48	99.5	185	123	0.66	1.14
	(2) S3A-E	22.4	1	7274	NA	441 x10^3	NA	5484	2772	0.51	99.5	402	276	0.69	1.19
	(3) S4A-E	31.4	1	9261	NA	719 x10^3	NA	6983	3599	0.52	100.5	646	362	0.56	1.08
SB	(4) S2B-E	53.1	4	4515	3563	280 x10^3	242 x10^3	3309	1246	0.48	100.5	178	125	0.71	1.18
	(5) S3B-E	29.0	1	7392	NA	438 x10^3	NA	5574	2704	0.49	101.0	392	273	0.70	1.18
	(6) S4B-E	38.1	3	9405	NA	717 x10^3	NA	7091	3713	0.52	101.0	541	375	0.69	1.22

Note 1: $M_{Et} = N_{c,Et} \cdot e_0$.

Note 2: for Class 1, 2 and 3 sections, $N_{c,Rd} = A_g \cdot f_y$; for Class 4 sections, $N_{c,Rd} = A_{eff} \cdot f_y$.

Note 3: for Class 1 and 2 sections, $M_{c,z,Rd} = W_{pl,z} \cdot f_y$; for Class 3 sections, $M_{c,z,Rd} = W_{el,z} \cdot f_y$; for Class 4 sections, $M_{c,z,Rd} = W_{eff,z} \cdot f_y$.

Table 4.8 Test results of stocky columns under eccentric compression (modified section classification)

Series	Designation	$c'/t/\varepsilon$	Section class (modified)	A_g (mm^2)	A_{eff} (mm^2)	$W_{el,z}$ (mm^3)	$W_{eff,z}$ (mm^3)	$N_{c,Rd}$ (kN)	$\frac{N_{c,Et}}{N_{c,Rd}}$	$M_{c,z,Rd}$ (kNm)	$\frac{M_{Et}}{M_{c,z,Rd}}$	$\frac{N_{c,Et}}{N_{c,Rd}}+\frac{M_{Et}}{M_{c,z,Rd}}$
SA	(1) S2A-E	55.5	4	4499	3531	283 x10^3	252 x10^3	3298	0.48	185	0.66	1.14
	(2) S3A-E	31.5	1	7274	NA	441 x10^3	NA	5484	0.51	402	0.69	1.19
	(3) S4A-E	40.4	3	9261	NA	719 x10^3	NA	6983	0.52	542	0.67	1.18
SB	(4) S2B-E	57.7	4	4515	3563	280 x10^3	242 x10^3	3309	0.48	178	0.71	1.18
	(5) S3B-E	33.6	2	7392	NA	438 x10^3	NA	5574	0.49	392	0.70	1.18
	(6) S4B-E	42.7	4	9405	8979	717 x10^3	692 x10^3	6770	0.55	521	0.72	1.27

Note 1: for Series SA, c' = B - 3t or H - 3t, whichever is greater; for Series SB, c' = B - 2t or c = H - 2.5t, whichever is greater.

Table 4.9 Test programme of slender columns under concentric compression

Series	Designation	c/t/ε	Section class	Measured dimensions of specimens (mm)					A_g	I_z	$\bar{\lambda}_z$
				B	H	t	R_{out}	L_m	(mm^2)	(mm^4)	
SA	(1) S1A-P	33.6	2	160.7	153.3	5.88	23.88	1280	3343	1266 x10^4	0.52
	(2) S2A-P	48.3	4	209.0	203.0	5.88	23.88	1580	4495	2982 x10^4	0.46
	(3) S3A-P	23.7	1	213.5	206.7	9.89	39.89	1278	7326	4754 x10^4	0.40
	(4) S4A-P	32.8	1	261.7	253.0	9.89	39.89	1579	9196	9240 x10^4	0.38
	(5) S5A-P	16.7	1	103.5	101.8	5.88	23.88	1979	2065	304 x10^4	1.18
	(6) S6A-P	23.3	1	125.4	119.3	5.88	23.88	1978	2528	561 x10^4	0.96
	(7) S1A-Q	33.4	2	159.5	152.8	5.88	23.88	2281	3322	1240 x10^4	0.83
	(8) S2A-Q	48.4	4	209.8	202.5	5.88	23.88	1978	4498	3001 x10^4	0.56
	(9) S3A-Q	23.6	1	220.5	196.6	9.89	39.89	2278	7266	4918 x10^4	0.63
	(10) S4A-Q	32.9	1	264.3	255.5	9.89	39.89	2279	9298	9546 x10^4	0.51
	(11) S5A-Q	16.9	1	104.1	100.7	5.88	23.88	2278	2058	305 x10^4	1.32
	(12) S6A-Q	23.3	1	125.3	118.9	5.88	23.88	2279	2522	558 x10^4	1.08
SB	(13) S1B-P	41.4	3	149.5	159.5	5.88	23.88	1279	3390	1164 x10^4	0.55
	(14) S2B-P	56.4	4	199.7	208.7	5.88	23.88	1580	4558	2848 x10^4	0.48
	(15) S3B-P	32.6	1	199.8	210.4	9.89	39.89	1280	7425	4415 x10^4	0.42
	(16) S4B-P	41.7	3	250.0	261.0	9.89	39.89	1580	9420	8987 x10^4	0.39
	(17) S5B-P	26.4	1	99.5	104.4	5.88	23.88	1979	2154	309 x10^4	1.19
	(18) S6B-P	32.5	1	120.1	125.2	5.88	23.88	1978	2640	566 x10^4	0.97
	(19) S1B-Q	41.6	3	150.3	158.8	5.88	23.88	2281	3390	1174 x10^4	0.86
	(20) S2B-Q	56.4	4	199.5	209.0	5.88	23.88	1978	4560	2845 x10^4	0.58
	(21) S3B-Q	32.7	1	200.4	210.2	9.89	39.89	2278	7433	4445 x10^4	0.67
	(22) S4B-Q	41.7	3	250.0	261.5	9.89	39.89	2279	9430	9002 x10^4	0.53
	(23) S5B-Q	26.9	1	101.2	104.4	5.88	23.88	2278	2173	322 x10^4	1.32
	(24) S6B-Q	32.6	1	120.3	125.0	5.88	23.88	2277	2640	568 x10^4	1.09

Note 1: for Series SA, $c = B - 2R_{out}$ or $H - 2R_{out}$, whichever is greater; for Series SB, $c = B - 2t$ or $c = H - t - R_{out}$, whichever is greater.

Note 2: for S1, S2, S5 and S6 sections, $\varepsilon = \sqrt{235/f_y} = \sqrt{235/733} = 0.566$; for S3 and S4 sections, $\varepsilon = \sqrt{235/f_y} = \sqrt{235/754} = 0.558$.

Table 4.10 Test results of slender columns under concentric compression

Series	Designation	c/t/ε	Section class	A_g (mm^2)	A_{eff} (mm^2)	$N_{c,Rd}$ (kN)	$\bar{\lambda}_z$	$N_{b,Rd}$ (kN)	$N_{b,Et}$ (kN)	$\frac{N_{b,Et}}{N_{b,Rd}}$	$\frac{N_{b,Et}}{N_{c,Rd}}$	Failure mode
SA	(1) S1A-P	33.6	2	3343	NA	2450	0.52	2039	2603	1.28	1.06	local
	(2) S2A-P	48.3	4	4495	3530	3295	0.41	2309	2981	1.29	1.15	overall
	(3) S3A-P	23.7	1	7326	NA	5524	0.40	4951	5448	1.10	0.99	overall
	(4) S4A-P	32.8	1	9196	NA	6933	0.38	6293	6867	1.09	0.99	overall
	(5) S5A-P	16.7	1	2065	NA	1513	1.18	674	919	1.36	0.61	overall
	(6) S6A-P	23.3	1	2528	NA	1853	0.96	1047	1632	1.56	0.88	overall
	(7) S1A-Q	33.4	2	3322	NA	2435	0.83	1565	2187	1.40	0.90	overall
	(8) S2A-Q	48.4	4	4498	3531	3392	0.49	2250	2913	1.29	1.09	overall
	(9) S3A-Q	23.6	1	7266	NA	5478	0.63	4220	4917	1.17	0.90	overall
	(10) S4A-Q	32.9	1	9298	NA	7010	0.51	5879	6698	1.14	0.96	overall
	(11) S5A-Q	16.9	1	2058	NA	1508	1.32	575	792	1.38	0.53	overall
	(12) S6A-Q	23.3	1	2522	NA	1849	1.08	916	1302	1.42	0.70	overall
SB	(13) S1B-P	41.4	3	3390	NA	2485	0.55	2031	2477	1.22	1.00	overall
	(14) S2B-P	56.4	4	4558	3572	3341	0.42	2320	2724	1.17	1.04	overall
	(15) S3B-P	32.6	1	7425	NA	5598	0.42	4963	5556	1.12	0.99	overall
	(16) S4B-P	41.7	3	9420	NA	7102	0.39	6409	7149	1.12	1.01	overall
	(17) S5B-P	26.4	1	2154	NA	1579	1.19	692	1227	1.77	0.78	overall
	(18) S6B-P	32.5	1	2640	NA	1935	0.97	1075	1839	1.71	0.95	overall
	(19) S1B-Q	41.6	3	3390	NA	2485	0.86	1547	2213	1.43	0.89	overall
	(20) S2B-Q	56.4	4	4560	3573	3438	0.51	2252	2852	1.27	1.06	overall
	(21) S3B-Q	32.7	1	7433	NA	5605	0.67	4181	5451	1.30	0.97	overall
	(22) S4B-Q	41.7	3	9430	NA	7110	0.53	5886	7027	1.19	0.99	overall
	(23) S5B-Q	26.9	1	2173	NA	1593	1.32	607	1257	2.07	0.79	overall
	(24) S6B-Q	32.6	1	2640	NA	1935	1.09	943	1402	1.49	0.72	overall
									Average:	***1.35***		

Note 1: for Class 1, 2 and 3 sections, $N_{c,Rd} = A_g \cdot f_y$; for Class 4 sections, $N_{c,Rd} = A_{eff} \cdot f_y$.
Note 2: $N_{b,Rd}$ is calculated with curve "c" (imperfection factor, α = 0.49) according to the buckling design rules given in EN 1993-1-1.

Table 4.11 Test results of slender columns under concentric compression (modified section classification)

Series	Designation	c'/t/ε	Section class (modified)	A_g (mm^2)	A_{eff} (mm^2)	$N_{c,Rd}$ (kN)	$\bar{\lambda}_z$	$N_{b,Rd}$ (kN)	$N_{b,Et}$ (kN)	$\frac{N_{b,Et}}{N_{b,Rd}}$	$\frac{N_{b,Et}}{N_{c,Rd}}$	Failure mode
SA	(1) S1A-P	42.6	4	3343	3184	2334	0.51	1959	2603	1.33	1.12	local
	(2) S2A-P	57.4	4	4495	3530	2587	0.41	2309	2981	1.29	1.15	overall
	(3) S3A-P	32.7	1	7326	NA	5524	0.40	4951	5448	1.10	0.99	overall
	(4) S4A-P	41.9	3	9196	NA	6933	0.38	6293	6867	1.09	0.99	overall
	(5) S5A-P	25.8	1	2065	NA	1513	1.18	674	919	1.36	0.61	overall
	(6) S6A-P	32.4	1	2528	NA	1853	0.96	1047	1632	1.56	0.88	overall
	(7) S1A-Q	42.4	4	3322	3176	2328	0.81	1523	2187	1.44	0.94	overall
	(8) S2A-Q	57.5	4	4498	3531	2662	0.50	2250	2913	1.29	1.09	overall
	(9) S3A-Q	32.7	1	7266	NA	5478	0.63	4220	4917	1.17	0.90	overall
	(10) S4A-Q	42.0	3	9298	NA	7010	0.51	5879	6698	1.14	0.96	overall
	(11) S5A-Q	26.0	1	2058	NA	1508	1.32	575	792	1.38	0.53	overall
	(12) S6A-Q	32.3	1	2522	NA	1849	1.08	916	1302	1.42	0.70	overall
SB	(13) S1B-P	43.5	4	3390	3224	2363	0.53	1950	2477	1.27	1.05	overall
	(14) S2B-P	58.3	4	4558	3572	2618	0.42	2320	2724	1.17	1.04	overall
	(15) S3B-P	33.6	2	7425	NA	5598	0.42	4963	5556	1.12	0.99	overall
	(16) S4B-P	42.8	4	9420	8985	6775	0.38	6146	7149	1.16	1.06	overall
	(17) S5B-P	26.9	1	2154	NA	1579	1.19	692	1227	1.77	0.78	overall
	(18) S6B-P	33.2	2	2640	NA	1935	0.97	1075	1839	1.71	0.95	overall
	(19) S1B-Q	43.3	4	3390	3225	2364	0.84	1503	2213	1.47	0.94	overall
	(20) S2B-Q	58.4	4	4560	3573	2694	0.51	2252	2852	1.27	1.06	overall
	(21) S3B-Q	33.6	2	7433	NA	5605	0.67	4181	5451	1.30	0.97	overall
	(22) S4B-Q	42.9	4	9430	8988	6777	0.51	5658	7027	1.24	1.04	overall
	(23) S5B-Q	26.9	1	2173	NA	1593	1.32	607	1257	2.07	0.79	overall
	(24) S6B-Q	33.1	2	2640	NA	1935	1.09	943	1402	1.49	0.72	overall
									Average:	***1.36***		

Note 1: for Series SA, c' = B - 3t or H - 3t, whichever is greater; for Series SB, c' = B - 2t or c = H - 2.5t, whichever is greater.

CHAPTER 5: COLD-BENDING EFFECTS OF S690 CFSHS

5.1 Introduction

This Chapter presented an experimental-numerical-analytical investigation into cold-bending effects of cold-formed square hollow sections (CFSHS). A total of 19 flat and curved coupons were extracted from four 10 mm thick CFSHS with $R_{in}/t = 3.0$, and they were then tested under uniaxial tension to obtain their stress-strain characteristics, and to determine any strength enhancement. Both 2D and 3D numerical models were established, to simulate transverse bending in forming round corners of these CFSHS, and they could predict the stress-strain characteristics and the strength enhancements at these corner regions of the cold-bent plates. An integration method was proposed to predict stress-strain characteristics of the corner regions under transverse bending. This method was further developed as a hand calculation method. Hence, the predictions on strength enhancements at the corner regions were achieved efficiently.

5.2 Experimental Investigation

5.2.1 Test programme

Initial stress-strain states in various parts of a CFSHS are induced by transverse bending and longitudinal welding, and different structural behaviour is exhibited in these parts, including flat portions, corner portions and welding seams. Two cold-formed sections without welding, i.e. Sections SA-nw and SB-nw, and two cold-formed welded sections, i.e. Sections SA and SB as shown in Fig. 5.1 are prepared. The cross-sectional dimensions of these four CFSHS are consistent with the other sections investigated in the present project, i.e. t = 10 mm and R_{in}/t = 3.0. As it is proposed to determine mechanical properties of various parts of the sections and to find out relationships between their stress-strain characteristics and the fabrication processes, a total of 19 flat and curved coupons are extracted from various parts of these CFSHS and then tested under monotonic tension forces. The locations where the coupons are extracted from are illustrated in Fig. 5.2. It should be noted that this test programme consists of four series with a total of 19 coupons, and their shapes, materials and quantities are summarized in Table 5.1. Series FP represents flat coupons extracted from flat portions away from the welding seams of the sections; Series FW represents flat coupons extracted from the welding seams of the sections; Series CS represents small curved coupons extracted from the corner portions of the sections; and Series CL represents large curved coupons extracted from the corner portions of the sections. The dimensions of these four series of coupons are shown in Fig. 5.3. It should be noted that, the gauge length, L_G, of Series FP, FW and CS coupons are taken 35 mm in accordance with EN ISO 6892-1 (CEN 2019g). It should be noted that despite the gauge length for Series CL coupons should be 84 mm, a reduced gauge length, L_{RG}, is taken for this series of coupons Due to limited lengths of the CFSHS. Fig. 5.4 shows Sections SA and SB after the coupons are extracted.

5.2.2 Test set-up and procedure

The set-up for flat coupon tests is identical to that introduced in Chapter 3. Besides, a new set-up is designed for curved coupon tests as illustrated in Fig. 5.5. Each of the ends of the curved coupon is connected to two steel plates with a grade 12.9 bolt. A third plate is connected to the other ends of these two plates and then directly gripped by the testing machine. Alignment is ensured before testing, and a tension force is applied vertically through the centre lines of all the bolts. The attachments used for Series CS and CL coupons are designed with bolts and bolt plates with proper dimensions, which have passed various resistance checks given in EN 1993-1-1 (CEN 2014) and EN 1993-1-8 (CEN 2010), including shear resistances of the bolts, bearing resistances of the plates, resistances of the net sections and detailing of the bolt holes, to ensure that material yielding along the gauge length is critical among all possible failure modes. As shown in the figure, a digital camera is mounted in front of the test set-up. High resolution photos are captured at an interval of 30 seconds during testing, and these photos are analysed with a simple image processing method to determine post-necking engineering strains within the gauge length of a coupon while pre-necking engineering strains are obtained from readings of strain gauges mounted on coupons. The loading procedure and the image process method are identical to those introduced in detail in Chapter 3.

The dimensions of all these coupons are measured before testing. However, it should be noted that large curvatures exist on both surfaces in the curved coupons with $R_{in}/t = 3.0$ and $R_{out}/t = 4.0$ as shown in Fig. 5.6 a), so the cross-sectional areas of the curved coupons should not be taken as a rectangle. A scanning-CAD method is employed to measure the areas accurately. As shown in Fig. 5.6 b), it is proposed to measure both dimensions of B and b physically with a calliper, and, then to measure the profile of the gripping end of the curved coupon with a scanner. The scanned area outlined in blue is calculated automatically with AutoCAD, and the scanned area outlined in red is readily obtained based on the proportional relationship between B and b.

5.2.3 Test results

All coupon tests have been conducted successfully. The deformed shapes of all 19 coupons at failure are shown in Fig. 5.7. Pre-necking strains are taken as the average readings of strain gauges, and post-necking strains are calculated with the image processing method on the elongations of the red grids. The measured areas and the key mechanical properties of all tests are summarized in Table 5.2, including the Young's modulus, E, the 0.2% proof strength, $f_{0.2}$, the tensile strength, f_u, the strain at tensile strength, ε_u and the strain at elongation limit, ε_L. For Series FP coupons, all the mechanical properties satisfy the requirements given in EN 1993-1-12 (CEN 2007) for parent metal of high strength steels, i.e. $f_{0.2} \geq 690$ N/mm^2, $f_u/f_{0.2} \geq 1.05$ and $\varepsilon_L \geq 10$ %.

a) Series FW vs Series FP

Compared with Series FP, the changes of E, $f_{0.2}$ and f_u of the other three Series are summarized in Table 5.3. By comparing Series FW with Series FP, a reduced Young's modulus, E_{FW}/E_{FP} = 0.78, is found, which indicates that the weld metal has a more softening elastic behaviour than the parent metal. As the weld metal has larger f_u and ε_u, thus no early failure will occur in the weld before the parent metal attains its tensile strength. The comparison is also illustrated in Fig. 5.8, showing engineering stress-strain curves of these four flat coupons. Very little variation is found between the curves of the two FP coupons extracted from Sections SA and SB. Although different post-buckling stress-strain characteristics are shown by the two weld metal coupons FW-A1 and FW-B1, both of them are regarded as qualified to match or overmatch the steel materials.

b) Series CS vs Series FP

Both Table 5.3 and Fig. 5.9 present a comparison between Series CS and Series FP. A reduction of 9 % is found in the E-value of Series CS curved coupons, which may be due to the loading history of bending-springback-tension (BST) processes at the corner regions, and a detailed discussion on this softening phenomenon is provided in Section 5.3.2. Besides, $f_{0.2}$ is increased by 6 % while f_u is increased by 10%. Such a significant enhancement in strength is due to the cold-working effects at the corner regions under transverse bending with a small R_{in}/t ratio. This effect also results in significant decreases in ε_u and ε_L as exhibited by the curved coupons. This is because there are large initial plastic strains at the corner regions, which modify the stress-strain characteristics of the curved coupons significantly.

c) Series CL vs Series CS

As summarized in Table 5.3, similar enhancements in strengths and reductions in deformation limits in those small curved coupons of Series CS are also found in those large curved coupons of Series CL. This indicates that the cold-working effects are consistent within the corner regions. However, the size effects of the large curved coupons should be further evaluated by comparing the engineering strains from the strain gauges attached around the coupons at the middle of the parallel length. Fig. 5.10 shows the arrangement of the strain gauges for Series CL coupons and their engineering stress-strain curves. Obviously, significant variations are observed among the seven strain gauges in the Series CL coupons. For each test, under the same stress level of $f_{0.2}$, these strains are significantly different in their values in the linear elastic range up to an elongation at 1.0%. The discrepancies found in these strains of both surfaces are probably attributed to the eccentricities of the applied loads through various attachments, which were inevitably induced during testing. Moreover, as the measured strengths of the large curved coupons in both tests are almost identical, and very consistent with those of the small curved coupons in Series CS as shown in Table 5.2, the variation of strains across the sections is considered to be insignificant, and thus can be ignored.

5.3 Numerical Analyses: 3D Transverse Bending Models

As demonstrated by the test results of the curved coupons, cold-working effects are induced after a steel plate is cold-bent. Due to the existing of these plastic strains, the load-extension behaviour of the corner portions is different from that of the flat portions under uniaxial tension. To further investigate the effects of plastic strains and strength enhancements under transverse bending, a 3D model is established with the commercial software package ABAQUS (2013), simulating the bending-springback-tension (BST) processes.

5.3.1 Constitutive model of the steel material

a) Von Mises yielding criterion

Von Mises yielding criterion is employed as default in ABAQUS to describe the stress-strain behaviour of most metallic materials, and it is also commonly used for steels. It is expressed as:

$$\sigma_{mises} = \frac{1}{\sqrt{2}}[(\sigma_{xx} - \sigma_{yy})^2 + (\sigma_{yy} - \sigma_{zz})^2 + (\sigma_{zz} - \sigma_{xx})^2 + 6(\tau_{xy}^2 + \tau_{yz}^2 + \tau_{zx}^2)] \quad \text{Eq. (5.1)}$$

where

σ_{mises} is the von Mises stress;

σ_{ii} is the normal stress, where i = x, y and z; and

τ_{ij} is the shear stress, where i = x, y and z, j = x, y, z, but i ≠ j.

The strain corresponding to von Mises stress, σ_{mises}, is defined as the equivalent plastic strain, PEEQ, and it is expressed as:

$$PEEQ = \frac{\sqrt{2}}{3}[(\varepsilon_{xx} - \varepsilon_{yy})^2 + (\varepsilon_{yy} - \varepsilon_{zz})^2 + (\varepsilon_{zz} - \varepsilon_{xx})^2 + 6(\gamma_{xy}^2 + \gamma_{yz}^2 + \gamma_{zx}^2)] \qquad \text{Eq. (5.2)}$$

where

ε_{ii} is the normal strain, where i = x, y and z; and

γ_{ij} is the shear strain, where i = x, y and z, j = x, y, z, but i ≠ j.

It should be noted that under transverse bending, the magnitudes of the shear stresses are found to be very small in all three directions in the cold-bent plate. To simplify this constitutive model for transverse bending, it is proposed to ignore those minor shear effects, and thus, remove the shear stress terms, τ_{ij} from Eq. (5.1). Therefore, the von Mises stress, σ_{mises}, is simplified as:

$$\sigma_{mises} = \frac{1}{\sqrt{2}}[(\sigma_{xx} - \sigma_{yy})^2 + (\sigma_{yy} - \sigma_{zz})^2 + (\sigma_{zz} - \sigma_{xx})^2] \qquad \text{Eq. (5.3)}$$

Similarly, after removing the shear strain terms, γ_{ij}, from Eq. (5.2), the equivalent plastic strain, PEEQ, is simplified as:

$$PEEQ = \frac{\sqrt{2}}{3}[(\varepsilon_{xx} - \varepsilon_{yy})^2 + (\varepsilon_{yy} - \varepsilon_{zz})^2 + (\varepsilon_{zz} - \varepsilon_{xx})^2] \qquad \text{Eq. (5.4)}$$

b) True stress-strain curve

When adopting the von Mises yielding criterion for numerical analyses, a true stress-true plastic strain curve should be incorporated into the model as the constitutive model of the parent metal, with isotropic hardening considered. In this project, this curve is readily obtained from a standard tensile test of a flat coupon. It should be noted that the engineering stress-strain curves of all the Series FP coupons extracted from four sections are identical as demonstrated in Section 5.2, so Coupon FP-B4 is selected as a typical one, and its results are thus presented as the true stress-true plastic strain curve after adopting the transformation method introduced in Chapter 3. Therefore, the true stress-true plastic strain curve (see Fig. 5.11) is directly incorporated into the finite element models to simulate the BST processes.

5.3.2 Simulation: curved coupons in Series CS

a) Establishment of models

Fig. 5.12 illustrates a 3D finite element model of the BST processes simulated with ABAQUS. Both the punch and the die are modelled as rigid bodies, and their dimensions are assigned according to the set-up for transverse bending as introduced in Chapter 3. A 10 mm thick S690 steel plate is modelled as a deformable body, which will be bent along its transverse direction numerically. The length and the width of the plate are both 200 mm, and only the portion at the middle of the parallel length of the curved coupon is extracted. The dimensions of the coupon are 48 mm in length and 4 mm in width. Compared with the curved coupon to be extracted, the dimensions of the plate are large enough to ensure that strains will distribute uniformly in the longitudinal direction along its the gauge length.

A solid element C3D8R is selected for the modelling of the plate, which is a three-dimensional linear solid element for general purposes of stress analyses. A mesh convergence study has been carried out as a pilot study, including various element sizes at 0.5, 1.0 and 2.0 mm. It is found that when the mesh size is equal to 1.0 mm, the numerical results converge well with limited computational costs, and this meshing strategy is, therefore, adopted for all the subsequent 3D models of transverse bending.

Simulation of the BST processes is divided into several steps as illustrated in Fig. 5.13: i) a bending force is imposed to the plate by the punch; ii) the force is removed after removal of punch, and springback occurs in the plate; iii) a curved coupon is extracted from the plate after springback; and iv) the coupon with initial strains is loaded with a tension displacement until failure. It should be noted that the final corner angle after springback, β', should be as close as possible to 90°. Normally the springback angle, $\Delta\beta$, for a 10 mm thick S690 steel plate is about 8°, as estimated with $\Delta\beta = f_u/100$ (SSAB 2017). This estimated value for $\Delta\beta$ is adopted in the trial-and-error iteration process to determine an accurate final corner angle.

It should be noted that a tested curved coupon extracted from a CFSHS has two parallel edges, as shown in Fig. 5.14 a). To have accurate numerical results, it is recommended to simulate a curved coupon with its two edges assigned to be parallel when it is extracted from the plate numerically. An iteration on the coupon dimensions has been carried out before establishing the models. Fig. 5.14 b) shows a simulated curved coupon extracted from the plate numerically after iterations, which has two parallel edges, and its cross-sectional area matches well with that of the tested coupon. Besides, as the gauge length, L_G, in the tested curved coupon is 35 mm, as shown in Fig. 5.15 a), the same L_G of 35 mm is taken in the simulated coupon, as shown in Fig. 5.15 b). Hence, the engineering strains of both coupons are very close to one another.

b) Numerical results

The engineering stress-strain curves of the tested curved coupon and the simulated curved coupon of Coupon CS-B2 are shown in Fig. 5.16. These engineering stress-strain curves are obtained from the applied load-extension curves, i.e. the applied loads are divided by their cross-sectional areas, and the measured extensions are divided by the assigned gauge lengths. For the tested curved coupon, its tensile strength f_u is 893 N/mm^2 with a corresponding strain ε_u at 2.07 %. For the simulated curved coupon, its tensile strength f_u is found to be 901 N/mm^2 with a corresponding strain ε_u only at 1.23 %. It is considered that the prediction on tensile strength is highly accurate with an error smaller than 1 %, though the tensile strain is underestimated, probably due to different softening behaviour between the tested coupon and the simulated coupon.

It should be noted that the predicted stress-strain curve follows closely to the measured one not only in the elastic range, but also in the large-deformed range up to necking. There are significant differences in these two stress-strain curves after their strains beyond 10 %.

In the test, softening is initiated when the engineering stress reaches 600 N/mm^2, but no significant softening occurs in the numerical model at the same stress level. It is considered that such a softening in strength may be attributed to the following two aspects:

- Loading history. As the tested curved coupon is extracted from a cold-bent plate after springback, and it is loaded with a tension force, the coupon actually undergoes a loading history of bending (transverse loading)-springback (transverse unloading)-tension (longitudinal loading). Although no load is applied onto the corner regions along the longitudinal direction during bending, longitudinal strains always exist due to the Poisson's effect. Such a loading history has induced large cyclic effects onto the tested coupon, and this may cause significant softening.

- Initial stress state. Another possible reason is the initial stress state of the CFSHS due to flame cutting. As demonstrated by the residual stress measurements in Chapter 3, the flame cutting is found to induce significant longitudinal tensile residual stresses onto the edges of the plates, with magnitudes as large as the yield strengths of the S690 steels. Therefore, the residual stresses due to flame cutting may have made some contributions to the softening as observed in the test.

The equivalent plastic strains, PEEQ, through the plate thickness along the centre line of the simulated cold-bent plate, are shown in Fig. 5.17. These values are obtained from the numerical models after successful analyses. The distribution of PEEQ between the inner surface and the outer surface is almost symmetrical about the neutral surface. However, the neutral surface does not coincide with the middle surface as shown in the figure. It should be noted that the inner elements shrink along the transverse direction, and stretch through thickness under compression. Hence, the outer elements stretch along the transverse direction, and shrink through thickness under tension. Therefore, the different deformed shapes of the elements result in a shift of the neutral surface towards the inner surface.

5.3.3 Simulation: flat coupons in Series FP

a) Establishment of models

It is considered that initial PEEQ due to transverse bending in the coupons plays a very important role in their strength enhancement in their tensile resistances. To investigate the effects of initial PEEQ, it is proposed to simulate a flat coupon in which the effects of transverse bending are incorporated through adoption of the PEEQ values obtained in the bending-springback (BS) process. The initial PEEQ values are shown in Fig. 5.17. The cross-sectional dimensions of the flat coupon are 3.88 x 9.52 mm, and its cross-sectional area is 36.93 mm^2. These dimensions match well with those of Coupon CS-B2 in Section 5.3.2. A control flat coupon is also simulated for a direct comparison, which is a flat coupon without any initial PEEQ. The initial states and the necking states of these two simulated flat coupons together with a simulated curved coupon are shown in Fig. 5.18.

b) Numerical results

A comparison is made among the engineering stress-strain curves of the tested coupons and the simulated coupons, as shown in Fig. 5.19. By comparing the curves between Models "Flat Coupon (Test)" and "Flat Coupon without iPEEQ (3D FEM)" in Fig. 5.19 a), it is found that they are similar with only a very minor difference after the on-set of necking. By comparing the stress-strain curves between Models "Flat Coupon with iPEEQ (3D FEM)" and "Curved Coupon (3D FEM)" Fig. 5.19 b), it is found that these two curves are very similar except for an early softening in the simulated curved coupon. Hence, it is demonstrated that a proper incorporation of the initial PEEQ values in the flat coupon is able to simulate the structural behaviour of the curved coupons modelled through the BST processes.

As demonstrated in the last paragraphs, the most significant difference between these two models of the flat and the curved coupons lies in their geometry. The curvatures in both the outer and the inner surfaces of the curved coupon result in a shift of the centroid. Therefore, a combined effect of tension and bending, i.e. an eccentric tension force, is applied to the curved coupon, thus resulting in a smaller applied force. However, it is shown that the geometry has an insignificant influence on the strength enhancement, and hence, this minor error may be ignored.

A direct comparison is also illustrated in Fig. 5.20, showing the changes of the sections at various states of the necked sections throughout testing.

Consequently, by incorporating initial PEEQ values into a flat coupon as its initial state of strains, this simplified flat coupon model is able to accurately and efficiently predict strength enhancements at the corner regions of a CFSHS under tension.

5.4 Numerical Analyses: 2D Transverse Bending Models

5.4.1 Establishment of models

A remarkable advantage of a 3D transverse bending model is that it can simulate the whole bending-springback-tension (BST) processes, and thus, directly incorporate the changes in geometry and the modified stress-strain behaviour of the curved coupon extracted from the corner regions. It is shown that a simulated flat coupon with initial PEEQ is able to achieve this purpose with a high accuracy. Hence, the problem may further be simplified into one that calculates the through-thickness distribution of initial PEEQ within a cold-bent plate. It is proposed to establish a 2D transverse bending model so that numerical results with sufficient accuracy are readily generated.

The 2D transverse bending model is established as illustrated in Fig. 5.21. Similar to the 3D model, both the punch and the die are modelled as rigid bodies while the steel plate is modelled as a deformable body. Interaction surfaces are set between the surfaces to enable friction between the punch and the plate as well as that between the die and the plate. Theoretically, transverse bending in this problem meets the description of a plane-strain problem, and the plate is modelled with the commonly used plane strain element CPE4R in ABAQUS. A bending force is imposed using a punch with a radius of R_p = 18 mm, and, thus, the plate is bent until its inner radius, R_{in}, reaches R_p. Then, the bending force is removed, and springback occurs in the plate. As discussed in Section 5.3, a compensation to the springback angle, $\Delta\beta$, should be included in the initial bending angle, β, so a trial-and-error iteration is performed to obtain the final corner angle, β', to be as close as possible to 90°.

In terms of the constitutive model of the steel, the von Mises yielding criterion is also adopted in the plane-strain problem. The true stress-true plastic strain used for establishing the 3D transverse bending model presented in Section 5.3 is also adopted in this 2D model.

5.4.2 Mesh convergence study

A mesh convergence study is carried out to establish a balance between numerical accuracy and computational efficiency. Table 5.4 summarizes the study programme with four mesh sizes adopted. It should be noted that although Mesh D@100 has 17 times more elements than Mesh A@4, the total computational time of the former one is only 16 minutes, which is usually acceptable.

A comparison on the contours of the transverse stresses is shown in Fig. 5.22, and it is evident that the stress patterns of Meshes C and D are very similar. The transverse stresses in Mesh B are also very similar to those two models with finer mesh sizes though the stresses along the centre line of the section is different. This is because a singularity problem occurs in the border lines between the compression zone (in blue) and the tension zone (in red), which is attributed to a sudden change in the transverse stresses close to the neutral surface. A more direct comparison is made by comparing the strains and stresses along the centre line of the cold-bent plate with different mesh sizes, as illustrated in Fig. 5.23. Another comparison is made onto the equivalent plastic strains. As shown in graph a), Meshes B, C and D exhibit almost identical patterns, and they are symmetrically distributed near their neutral surfaces, though accuracy of Mesh B for stresses along the centreline is not as good as the other two Models. The transverse stresses in graph b) are consistent with the contours as illustrated in Fig. 5.22. It should be noted that as more details are demonstrated by the curves shown in Fig. 5.23 b), it is found that both Meshes B and C have the similar singularity problem around their neutral surfaces due to the sudden changes of the transverse stresses. However, no such a problem is found in Mesh D as its transverse stresses vary very smoothly from the compression zone to the tension zone due to the refined mesh sizes adopted. In terms of longitudinal stresses, similar patterns are illustrated in graph c). The only difference is that Mesh B also transmits smoothly near its neutral surface, and this may be readily explained with a less acute change in the longitudinal stresses, when compared with that of the transverse stresses.

Based on the key findings of the convergence study on the models, it is proposed that for a 10 mm thick S690 steel plate with $R_{in}/t = 3.0$, different mesh sizes should be adopted depending on the specific interest of the investigation: i) if only the PEEQ values are needed to be solved, a mesh with 20 layers of elements may be adopted; ii) if the longitudinal stresses are also needed, a mesh with 50 layers of elements may be adopted; and iii) if all the field variables of the model are needed, it is highly recommended to further refine the mesh sizes of the 2D model, and a mesh of 100 layers of elements should be adopted. In general, the sudden change in the transverse stresses near the neutral surface demands a fine mesh through the plate thickness in order to avoid the singularity problem.

5.5 Analytical Solutions and Simplified Calculation Methods

5.5.1 Theoretical solutions

Moen et al. (2008) reported an analytical solution to describe both the residual strains and the residual stresses when a plate undergoes transverse bending. Transverse bending is regarded as a combination of two sequential mechanical processes, namely, i) plastic bending, and ii) elastic springback. An elastic-plastic material model is employed to reflect the stress-strain relationship under transverse bending. Transverse stresses are changed during springback because of release of applied moment to achieve moment equilibrium. It should be noted that the moment released after elastic springback, M_s, is equal to the moment due to plastic bending, M_b, and that is $M_s = M_b$. Hence, M_s and M_b are given by:

$$M_s = \int_{-t/2}^{+t/2} (\sigma_{x,s} \cdot y)\, dy \qquad \text{Eq. (5.5)}$$

$$M_b = \int_{-t/2}^{+t/2} (\sigma_{x,b} \cdot y)\, dy \qquad \text{Eq. (5.6)}$$

where

M_s is the moment released after elastic springback;

M_b is the moment due to plastic bending;

$\sigma_{x,s}$ is the transverse stress due to elastic bending; and

$\sigma_{x,b}$ is the transverse stress due to plastic bending.

Longitudinal stresses, $\sigma_{z,s}$, are calculated with the Poisson's ratio elastically:

$$\sigma_{z,s} = \nu_{el} \cdot \sigma_{x,s} \qquad \text{Eq. (5.7)}$$

Therefore, the transverse residual stresses, $\Delta\sigma_x$, and the longitudinal residual stresses, $\Delta\sigma_z$, are calculated:

$$\Delta\sigma_x = \sigma_{x,b} - \sigma_{x,s} \qquad \text{Eq. (5.8)}$$

$$\Delta\sigma_z = \sigma_{z,b} - \sigma_{z,s} \qquad \text{Eq. (5.9)}$$

Fig. 5.24 a) illustrates transverse stress distributions due to plastic bending and elastic springback as well as transverse residual stresses. However, since no force is applied to the longitudinal direction, the longitudinal stresses are generated due to the Poisson's effect only. Considering a typical value of the Poisson's ratio for steel, i.e. $\nu_{el} = 0.3$ for elastic deformations, and $\nu_{pl} = 0.5$ for plastic deformations, the longitudinal stress distributions are obtained as shown in Fig. 5.24 b).

5.5.2 Integration methods

Quach et al. (2006) reported an integration method to predict residual strains and residual stresses of the steel plates due to transverse bending, which is an analytical-numerical incorporated method developed based on the theoretical solution to sheeting bending. It can provide predictions with a high accuracy because of reduced number of assumptions. A critical one is to consider a shift of the neutral surface. Neglection of such a shift is acceptable for a thin plate with a large R_{in}/t, i.e. $t \leq 3$ mm and $R_{in}/t \geq 9.0$, since the thinner the plate is, the smaller the effect is. For the 10 mm thick plate with $R_{in}/t = 3.0$ in this project, the shift of the neutral surface is as large as 1.0 mm, so the effect should be carefully considered. Besides, the elastic strains and the strain hardening of the steel are also considered in the integration method. The theoretical backgrounds of this integration method are introduced as follows.

The theoretical solutions to sheet bending are reported in the literature. (Hill 1950, Hosford and Caddell 2011). For a plate under transverse bending (see Fig. 5.25), the radius of the neutral surface, R_n, is calculated as:

$$R_n = \sqrt{(R_c - \frac{t}{2})(R_c + \frac{t}{2})} \quad \text{Eq. (5.10)}$$

where

t is the plate thickness;

R_c is the corner radius at the middle surface, i.e. $R_c = (R_{in} + R_{out})/2$.

For an element in a thin plate under bending, y is the through-thickness distance of the element from the middle surface. So its engineering transverse strain is calculated as the elongation of the arch length, i.e. $(L_y - L_c)/L_c = (y \cdot \theta)/(R_c \cdot \theta) = y/R_c$. However, as the shift of the neutral surface is considered, the true transverse strain due to plastic bending, $\varepsilon_{x,b}$, is expressed as:

$$\varepsilon_{x,b} = ln(1 + \frac{s - y}{R_c - s}) \qquad \text{Eq. (5.11)}$$

where

s is the shift of the neutral surface, i.e. $s = R_n - R_c$.

To solve the transverse stresses and the longitudinal stresses through the plate thickness, it is necessary to employ a material model for the steel. Quach et al. (2006) proposed three types of material models for steels with different types of nonlinear and hardening behaviour, and they are: a) an elastic-linear hardening model, b) an elastic-nonlinear hardening model, and c) a nonlinear hardening model. The first model is considered to match best with the mechanical properties of the S690 high strength steels in this project.

This material model is as follows:

$$PEEQ = (\sigma_{yb} - \sigma_{y0})/H \qquad \text{Eq. (5.12)}$$

$$H = \frac{E_0 E_{st}}{E_0 - E_{st}} \qquad \text{Eq. (5.13)}$$

where

PEEQ is the equivalent plastic strain;

σ_{yb} is the yield stress for the steel under transverse bending, which is equal to the von Mises stress, σ_{mises};

σ_{y0} is the yield strength;

E_0 is the initial elastic modulus; and

E_{st} is the modulus at the strain hardening stage.

To develop the integration method, ω_b is defined as a ratio of the longitudinal stress to the transverse stress:

$$\omega_b = \frac{\sigma_{z,b}}{\sigma_{x,b}} \qquad \text{Eq. (5.14)}$$

where

$\sigma_{x,b}$ is the transverse stress due to plastic bending; and

$\sigma_{z,b}$ is the longitudinal stress due to plastic bending.

Combining Eq. (5.14) with the von Mises yielding criterion (see Eq. (5.3)), the stress components at the transverse and the longitudinal directions are expressed as:

$$\sigma_{x,b} = \pm \frac{\sigma_{yb}}{\sqrt{1 - \omega_b + \omega_b^2}} \qquad \text{Eq. (5.15)}$$

$$\sigma_{z,b} = \pm \frac{\omega_b \sigma_{yb}}{\sqrt{1 - \omega_b + \omega_b^2}} \qquad \text{Eq. (5.16)}$$

The transverse yield strain, $\varepsilon_{x,by,}$ is given by:

$$\varepsilon_{x,by} = \pm \frac{\sigma_{y0}(1 - {\nu_{el}}^2)}{E_0(1 - \nu_{el} + \nu_{el}^2)^{1/2}} \qquad \text{Eq. (5.17)}$$

The increment of the stress ratio $d\omega_b$ is then obtained as follows:

$$d\omega_b = \frac{2(1 - \omega_b + \omega_b^2)(\Omega_b - \omega_b)}{\sigma[(2 - \omega_b) + \Omega_b(2\omega_b - 1)]} d\sigma \qquad \text{Eq. (5.18)}$$

where the stress ratio, Ω_b, is given by:

$$\Omega_b = \frac{d\sigma_{z,b}}{d\sigma_{x,b}} = \frac{4\nu_{el}H(1 - \omega_b + \omega_b^2) - E_0(2 - \omega_b)(2\omega_b - 1)}{E_0(2\omega_b - 1)^2 + 4H(1 - \omega_b + \omega_b^2)} \qquad \text{Eq. (5.19)}$$

Finally, the integration formula is constituted. The transverse strain, $\varepsilon_{x,b}$, at any location of y is expressed as a function of ω_b and σ:

$$\varepsilon_{x,b} = \varepsilon_{x,by} \pm \left\{ \int_{\nu_{el}}^{\omega_b} \frac{[(1 - 2\omega_b)^2 - 2\nu_{el}(1 - 2\omega_b)(2 - \omega_b) + (2 - \omega_b)^2]\sigma}{2E_0(2\omega_b - 1)(1 - \omega_b + \omega_b^2)^{3/2}} d\omega_b + \int_{\sigma_{y0}}^{\sigma_{yb}} \frac{(1 - \omega_b^2)(1 - 2\nu_{el})}{E_0(2\omega_b - 1)(1 - \omega_b + \omega_b^2)^{1/2}} d\sigma \right\} \qquad \text{Eq. (5.20)}$$

Therefore, the equivalent plastic strain, PEEQ, the transverse strain, $\varepsilon_{x,b}$, the transverse stress, $\sigma_{x,b}$ and the longitudinal stress, $\sigma_{z,b}$ at an arbitrary location of y due to plastic bending are readily obtained, and the calculation process may be implemented with a spreadsheet or other programming languages. The through-thickness distributions of both the strains and the stresses are available, and they are directly compared with the numerical results. In the current project, by substituting the given parameters into Eqs. (5.10) to (5.20), the through-thickness distributions of both the strains and the stresses are available, and they are directly compared with the numerical results. It should be noted that the given parameters include t = 10 mm, R_{in} = 30 mm, R_{out} = 40 mm, σ_{y0} = 793 N/mm^2, E_0 = 217000 N/mm^2 and E_{st} = 397 N/mm^2.

A comparison on PEEQ is made between the results obtained from the 3D model and the integration method, as shown in Fig. 5.26 a). It is found that the initial PEEQ calculated with the integration method are underestimated, when compared with those results of the 3D model, though the error is small. Another comparison is made on the transverse strains between the results obtained from the two methods, as shown in Fig. 5.26 b). It is acceptable to have these insignificant errors, because the simplifications employed in the integration method, including the material model, the integration step size and reduced iterations, always reduce accuracy to some extent, but improve computational efficiency. In addition, Fig. 5.26 c) shows the longitudinal strains of the 3D model at the middle along the bending length, which are very small through-thickness strains, i.e. ε_z = 0.02%. This may be explained that the essence of transverse bending is a plane-strain problem, and longitudinal strains are very small, and thus, they may be ignored if simplification is needed.

5.5.3 Hand calculation method on strength enhancement

Fig. 5.27 demonstrates the calculation process of the hand calculation method. It considers a S690 steel plate with a specified R_{in}/t ratio. The corresponding through-thickness initial PEEQ values along the centre line of the cold-bent plate are readily calculated with the integration method (see Eq. (5.20)). First of all, a “virtual” flat coupon with its cross-sectional area of A is assumed to be extracted from the corner regions of the cold-bent plate (see graph a)). Then, the flat coupon is uniformly divided into several layers (see graph b) through the plate thickness, and each layer is assigned with the corresponding initial PEEQ values obtained above (see graphs c) and d)). Thus, the initial value of the PEEQ of each layer is plotted onto the corresponding locations along the horizontal axis of the true stress-true plastic strain curve as shown in graph e). When a tension force is applied to the coupon, all the layers deform uniformly, and, hence, their stress-strain data are readily found in graph f). Thus, the final PEEQ and σ_{mises} are determined (see graphs g) and h)). Since the coupon is under uni-axial tension, PEEQ and σ_{mises} are regarded as the strains and the stresses along the direction of tension, i.e. $\varepsilon_{z,plastic}$ and σ_z. The summation of the stresses multiplied with the areas of across the section gives the force of the section, F, and the elongation along the gauge length is calculated with PEEQ.

To plot a load-extension curve of the "virtual" flat coupon, the calculation of PEEQ and σ_{mises} is broken down into several steps in a calculation loop, so that a series of load-extension data are obtained. Fig. 5.28 shows a flowchart of the hand calculation process, which can be easily implemented with a computer programme. The loop begins with a small step size of ΔPEEQ. Normally, as a S690 curved coupon with $R_{in}/t = 3.0$ reaches its tensile strength when the total ΔPEEQ reaches about 2.0 %, the ΔPEEQ of each step is set 0.2 %, and the loop is completed after 10 steps. In step n, a ΔPEEQ of 0.2 % is superimposed into the PEEQ of the previous step, and both PEEQ (n) and F (n) are updated correspondingly, i.e. PEEQ (n) = PEEQ (n-1) + ΔPEEQ. Then repeat the abovementioned loop until n = 10. Finally, a series of data of both PEEQ (n) and F (n) are obtained, and it is presented as an engineering stress-strain curve by dividing the cross-sectional area and the gauge length of the "virtual" flat coupon.

Section 5.6.2 presents a comparison between the engineering stress-strain curves obtained from this hand calculation method and those obtained from the other methods, for a direct comparison.

5.6 Comparison among Various Methods

As demonstrated in the previous Sections, there are various methods to determine the stress-strain characteristics due to transverse bending and the strength enhancements at the corner regions of a cold-bent steel plate. The following methods are considered:

a) The experimental method, i.e. the curved coupon tests, can provide the most accurate results among all the methods, and all the mechanical properties are readily obtained after execution of the tests. However, this method is time-consuming, and requires careful preparation and execution.

b) The numerical method is also effective. A 3D transverse bending model is an alternative approach to predict strain distributions and strength enhancements at the corner regions. Accurate results are readily obtained with a validated model using certain computational resources. However, it is necessary to calibrate the model against test data. This process is rather demanding and requires extensive modelling techniques.

c) The third one is the integration method which is a simplified method developed based on the theory of sheet bending. Compared with the abovementioned experimental and numerical methods, there is no requirement on either laboratory resources or modelling techniques when adopting this method. As demonstrated in Section 5.5.2, only little accuracy is sacrificed, but the results are determined in an efficient way. To further develop this approach, a hand calculation method is proposed, which can predict the strength enhancements at the corner regions based on various parameters and data obtained from the integration method.

To evaluate the accuracy and the efficiency of these different methods, comparisons are made in the following Sections, among their predictions on both stress-strain characteristics and strength enhancements.

5.6.1 Through-thickness stress-strain characteristics

The mesh convergence study in Section 5.4.2 demonstrates that Mesh D@100 achieves a good balance between accuracy and efficiency. This 2D model is compared with the strains and the stresses obtained from the following methods: i) the theoretical solution, ii) the analytical solution, and iii) the 3D transverse bending model. Various stress and strain distributions through the plate thickness are illustrated in Fig. 5.29. The equivalent plastic strains, PEEQ, along the centre line of the cold-bent plate are shown in graph a). It is evident that the similar patterns are predicted with these four methods, but the variations in the magnitudes of PEEQ are found at the heights from the neutral surfaces. It is considered that highly accurate results are obtained with both the 3D and the 2D models, because the strain hardening of the steel and the large deformations of the elements are fully considered in the calculation of these two numerical methods. However, as the convergence of the 2D model has been well validated, the location of the neutral surface predicted with this model may be considered as the most accurate among all the methods, which is at 1.10 mm above the middle surface. Consistent patterns of the transverse stresses and the longitudinal stresses are also found in these four curves in graphs b) and c), respectively. In summary, compared with the other methods, the 2D model is shown to be able to provide highly accurate results of both the strains and the stresses with small computational resources. It is proposed to employ this 2D model to simulate the equivalent plastic strains and the residual stresses at the corner regions of the S690 CFSHS with R_{in}/t = 3.0. Hence, both the strains and the stresses predicted with this 2D transverse bending model are readily incorporated into the finite element models for the sequentially-coupled thermomechanical analyses the structural analyses in the subsequent Chapters.

5.6.2 Strength enhancements

As illustrated in Fig. 5.30, a comparison is made on the engineering stress-strain curves obtained with various methods, where Model "Flat Coupon with iPEEQ (Hand)" is the engineering stress-strain curve calculated with the hand calculation method. The results of this method agree very well with Models "Flat Coupon with iPEEQ (3D FEM)" and "Curved Coupon (3D FEM)", and only a very small difference is found in the softening behaviour of the curved coupon simulated with the 3D transverse bending model. As discussed in Section 5.3.2, the early softening in the stress-strain curve of Model "Curved Coupon (Test)" lies in loading histories and flame cutting on edges, but this softening behaviour does not affect strength enhancement at large deformations, and similar results are predicted with both the hand calculation method and the simulated flat coupon with initial PEEQ. Besides, the insignificant softening exhibited by Model "Curved Coupon (3D FEM)" has been discussed in Section 5.3.3, which is attributed to the loading eccentricity caused by the geometry change of the curved coupon. In summary, the hand calculation method is shown to be able to achieve a high accuracy as a simulated flat coupon with initial PEEQ does, and it is considered as an effective method to predict the strength enhancement at the corner regions of a cold-bent steel plate with a specified R_{in}/t.

5.7 Conclusions

An experimental-numerical-analytical investigation into the cold-bending effects of the S690 CFSHS is presented in this Chapter. Four 10 mm thick CFSHS with $R_{in}/t = 3.0$ are examined. Various methods are employed to obtain the stress-strain characteristics of the corner regions, and thus, to determine their strength enhancements at large deformations.

- The experimental method is shown to be able to provide the most accurate results among all the methods. However, this investigation is time-consuming, and requires careful preparation and execution of the tests.

- Both the 3D and the 2D numerical methods are developed, respectively. The accurate results are obtained with the validated 3D model using certain computational time. However, it is necessary to calibrate the model against the test data, which is a demanding process that requires extensive modelling techniques. Considering the essence of the plane-strain problem, the simplified 2D transverse bending model is established, which is able to provide accurate results using reduced computational resources. It is proposed to use this 2D model to predict the PEEQ values and the corresponding residual stresses at the corner regions for all the S690 CFSHS. Both the strains and the stresses obtained from this 2D model are readily incorporated into finite elements models for both sequentially-coupled thermomechanical analyses and structural analyses.

- The integration method, a simplified method developed based on the theory of sheet bending, has no specific requirement on either laboratory resources or modelling techniques. Only a small degree of accuracy is sacrificed, but the results are determined in a highly efficient way. This approach is further developed as a hand calculation method. Hence, the predictions on the strength enhancements at the corner regions are readily achieved.

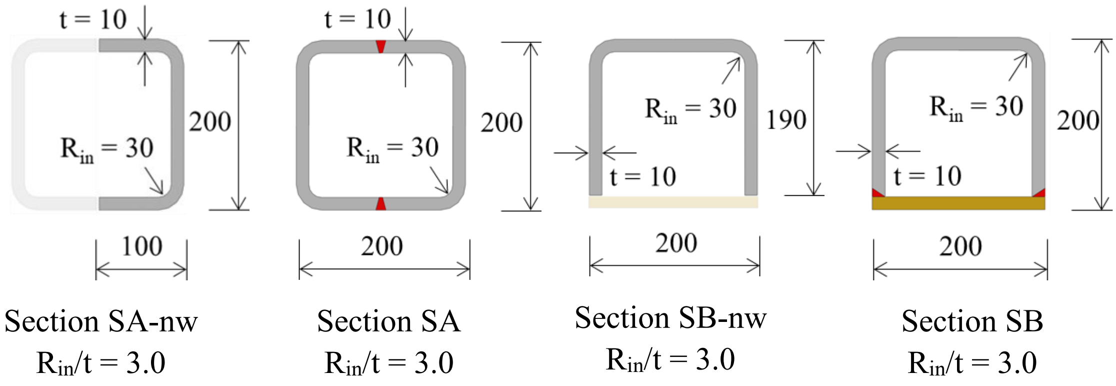

Fig. 5.1 Cold-formed square hollow sections (CFSHS)

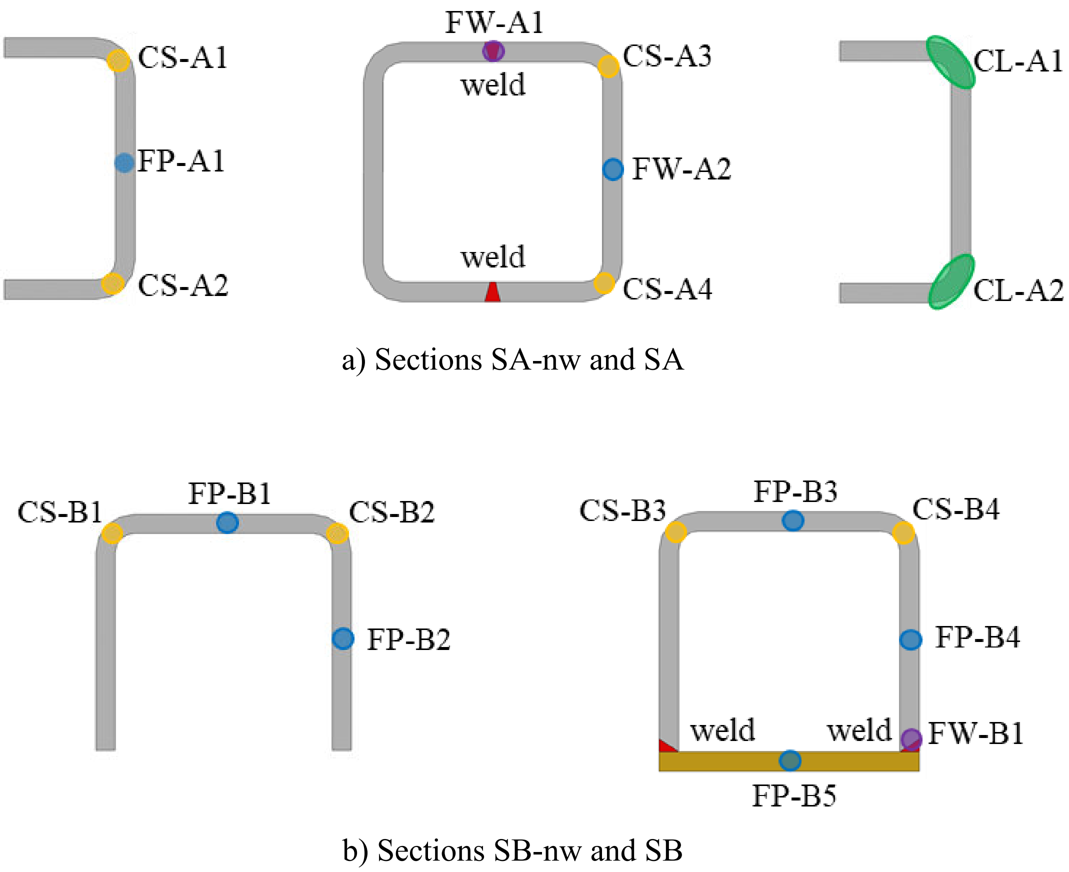

Fig. 5.2 Locations of coupons extracted from CFSHS

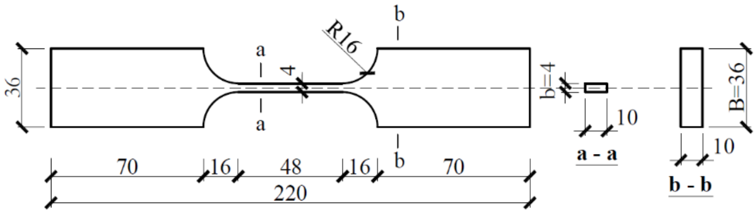

a) flat coupon for Series FP

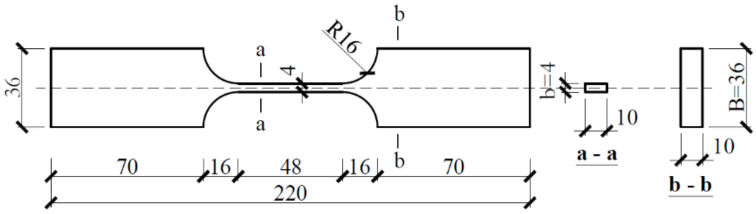

b) flat coupon for Series FW

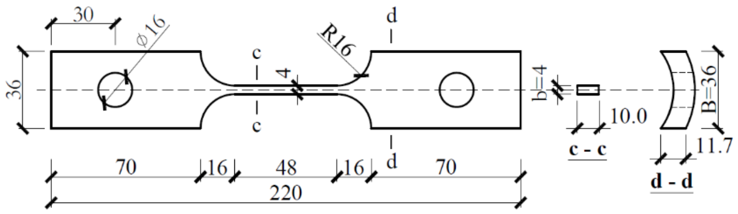

c) small curved coupon for Series CS

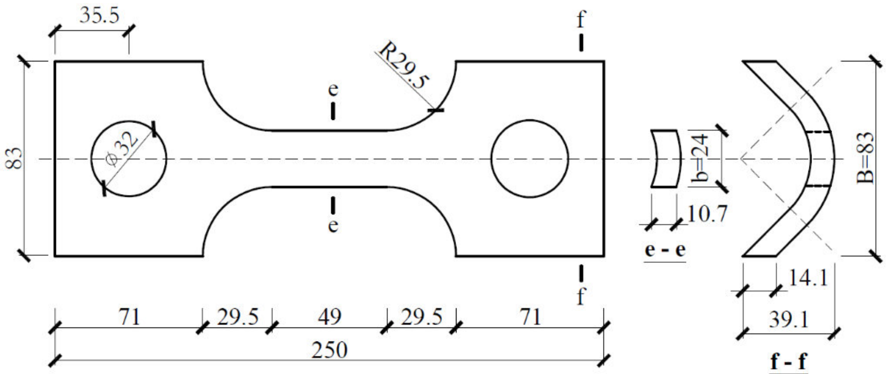

d) large curved coupon for Series CL

Fig. 5.3 Dimensions of coupons extracted from CFSHS

a) Section SA b) Section SB

Fig. 5.4 Sections SA and SB after coupons extracted

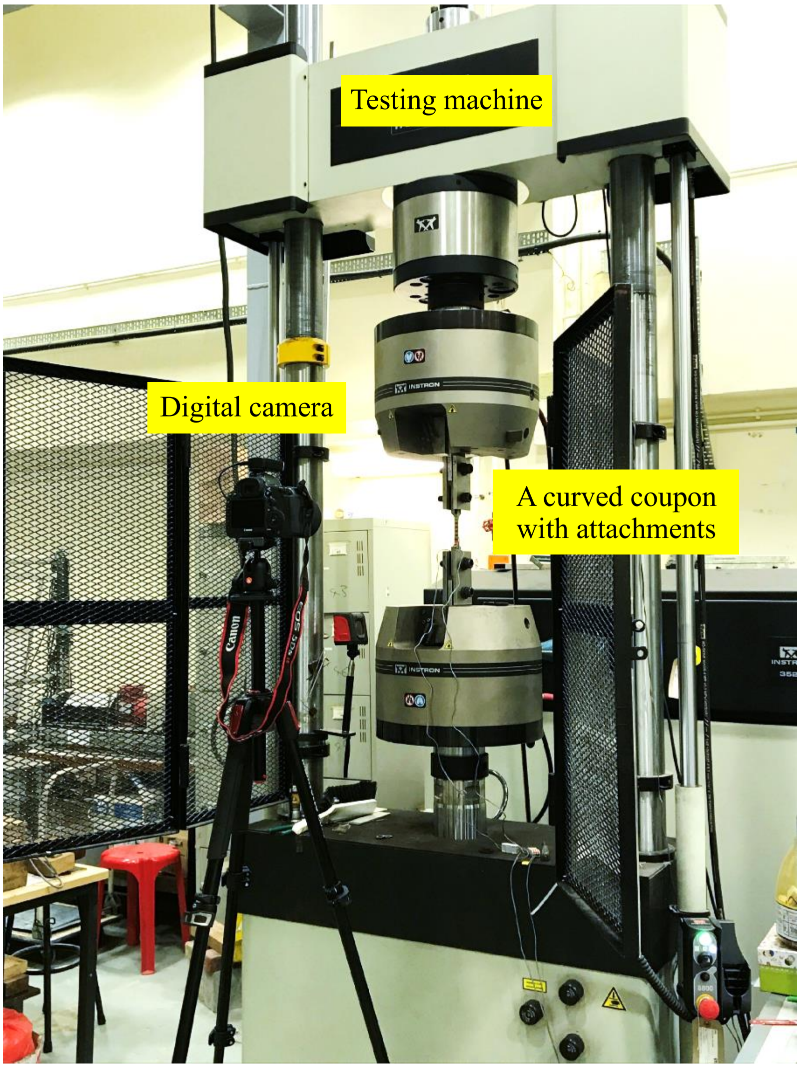

a) overall view

b) a curved coupon with attachments

Fig. 5.5 Test set-up for curved coupons

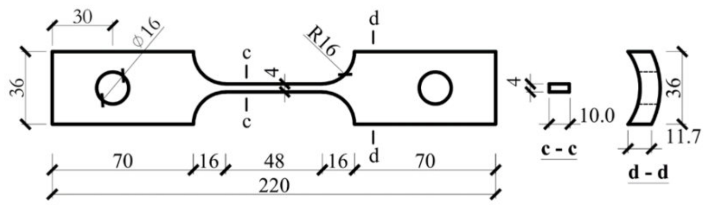

a) dimensions of coupon

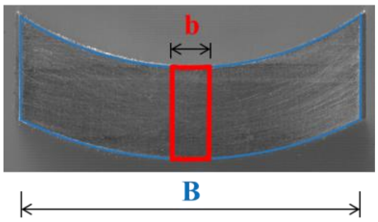

b) scanned gripping end of a coupon

Fig. 5.6 Measurements of dimensions along gauge length for Series CS coupon

A1 A2 B1 B2 B3 B4 B5

a) Series FP coupons

A1 B1

b) Series FW coupons

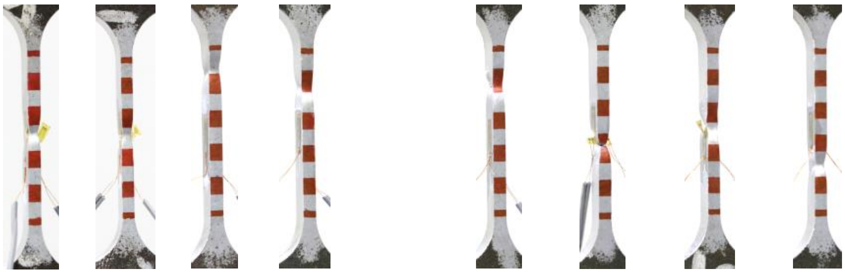

A1 A2 A3 A4 B1 B2 B3 B4

c) Series CS coupons

A1 A2

d) Series CL coupons

Fig. 5.7 All coupons after failure

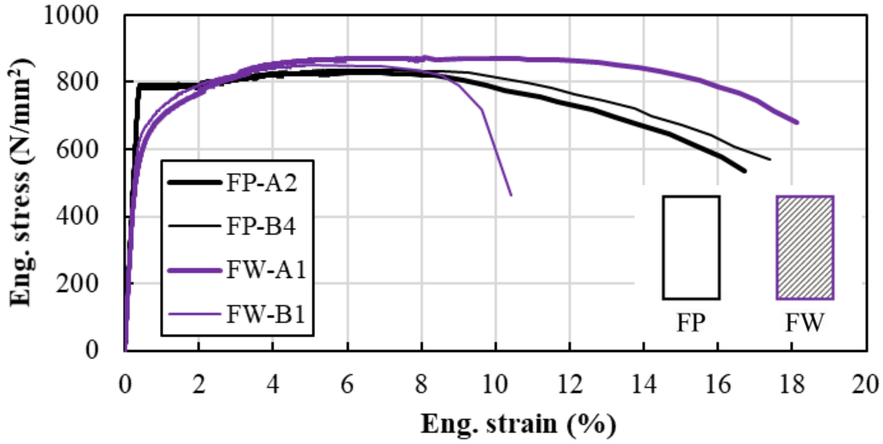

Fig. 5.8 Engineering stress-strain curves of Series FP and FW coupons

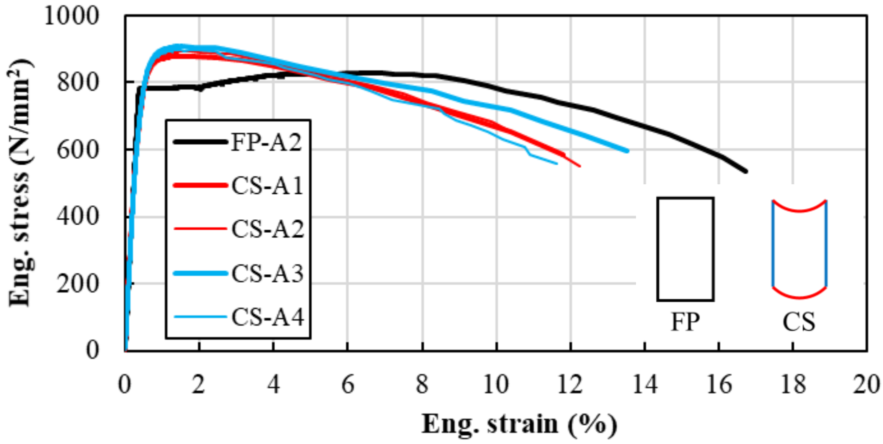

a) coupons from Sections SA-nw and SA

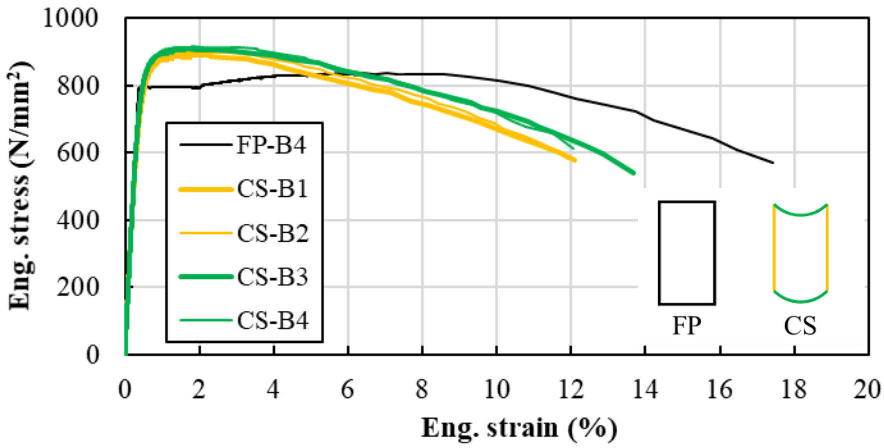

b) coupons from Sections SB-nw and SB

Fig. 5.9 Engineering stress-strain curves of Series FP and CS coupons

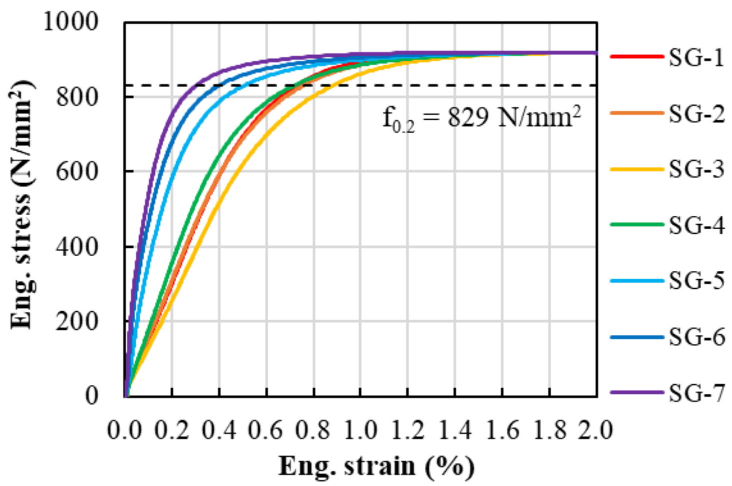

a) CL-A1

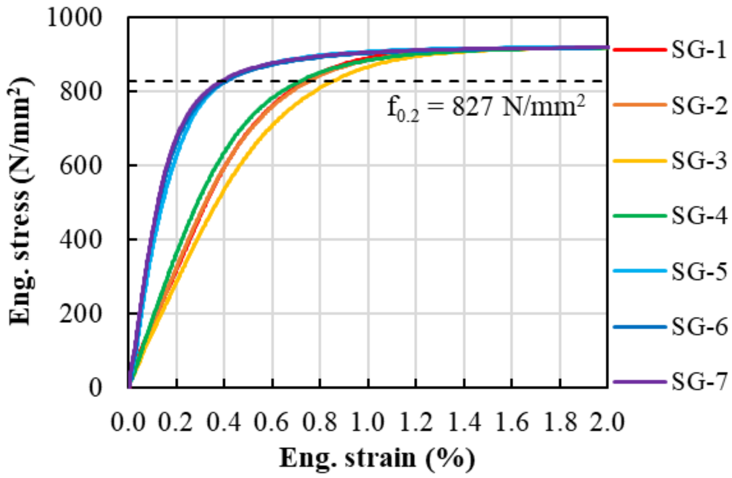

b) CL-A2

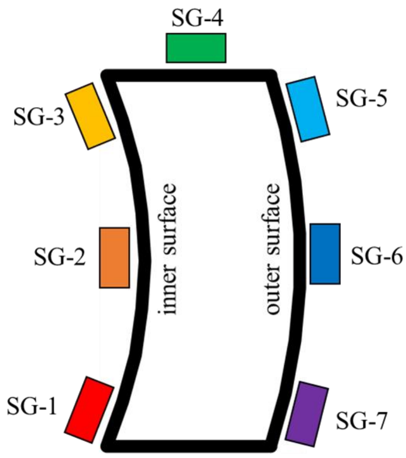

arrangement of strain gauges for Series CL

Fig. 5.10 Engineering stress-strain curves of Series CL coupons

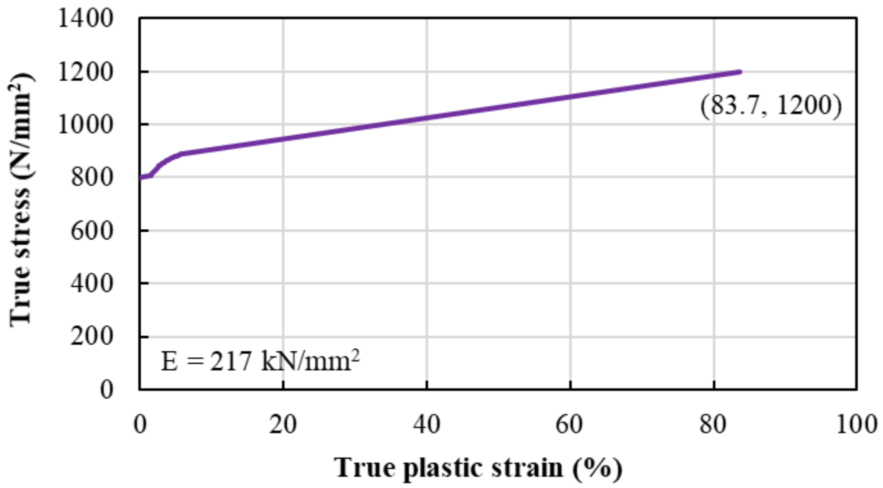

Fig. 5.11 True stress-true plastic strain curve for numerical analyses: Coupon FP-B4

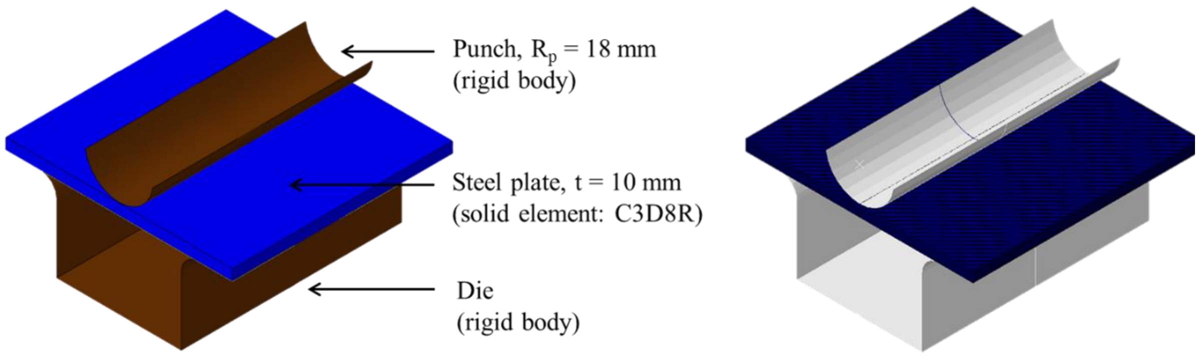

Interction surafaces of friction are provided between:

i) punch and plate, and

ii) die and plate.

Fig. 5.12 3D transverse bending model

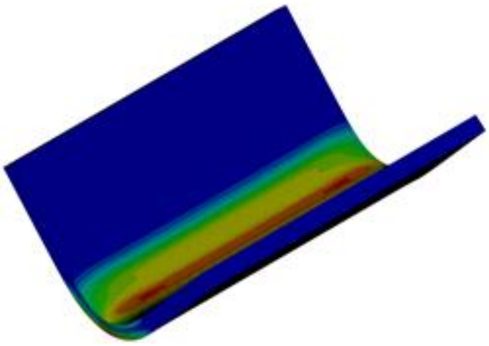

a) bending under a punch

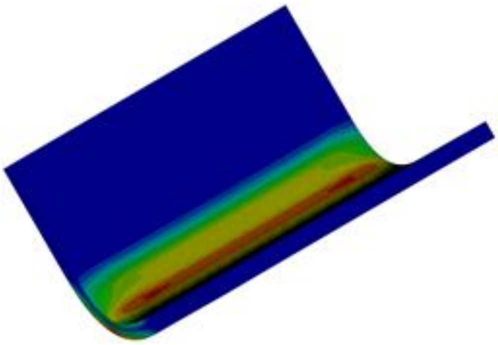

b) springback after removal of the punch

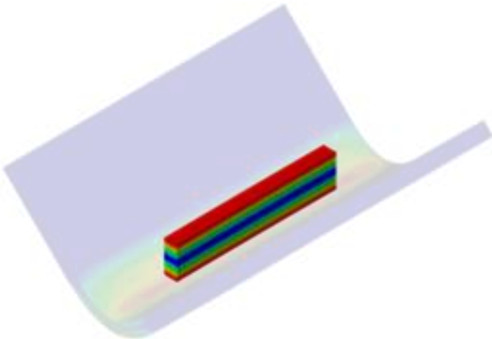

c) extraction of coupon

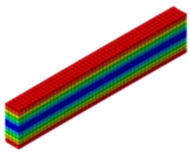

d) coupon with
initial strains

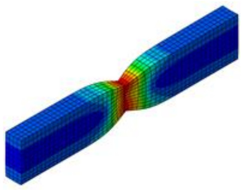

e) necking of coupon
under tension

Fig. 5.13 Simulation of bending-springback-tension (BST) processes

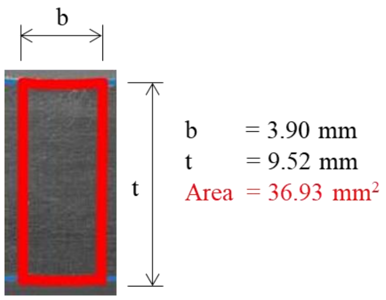

a) measured dimensions of a
curved coupon with AutoCAD

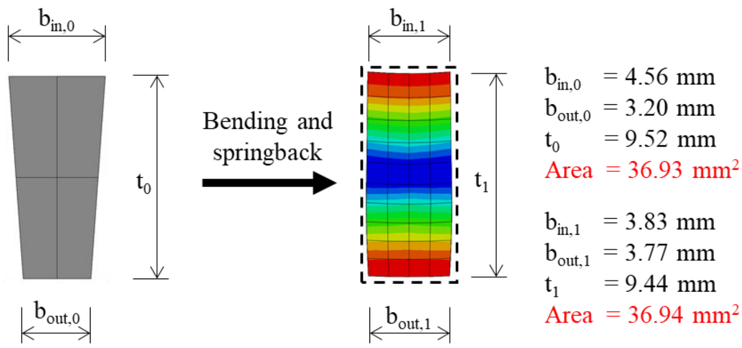

b) design dimensions of a
curved coupon in FEM after iterations

Fig. 5.14 Dimensions of curved coupons: Coupon CS-B2

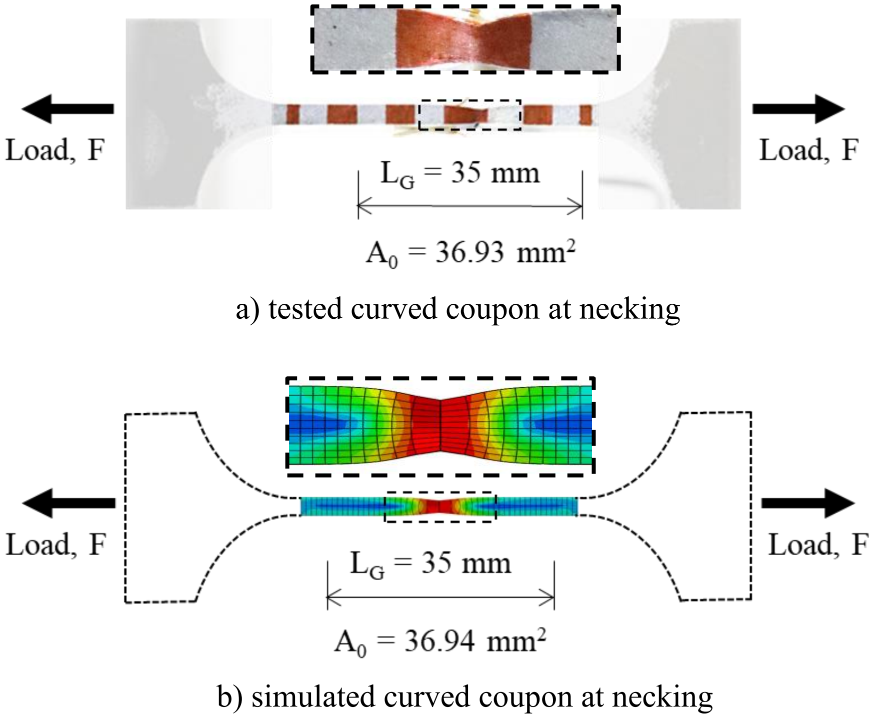

Fig. 5.15 Failure modes of curved coupons: Coupon CS-B2

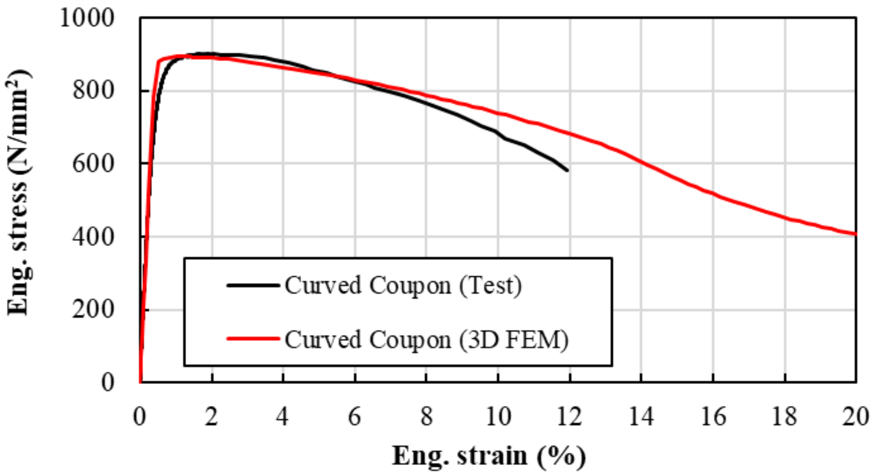

Fig. 5.16 Engineering stress-strain curves: Test vs 3D FEM (Coupon CS-B2)

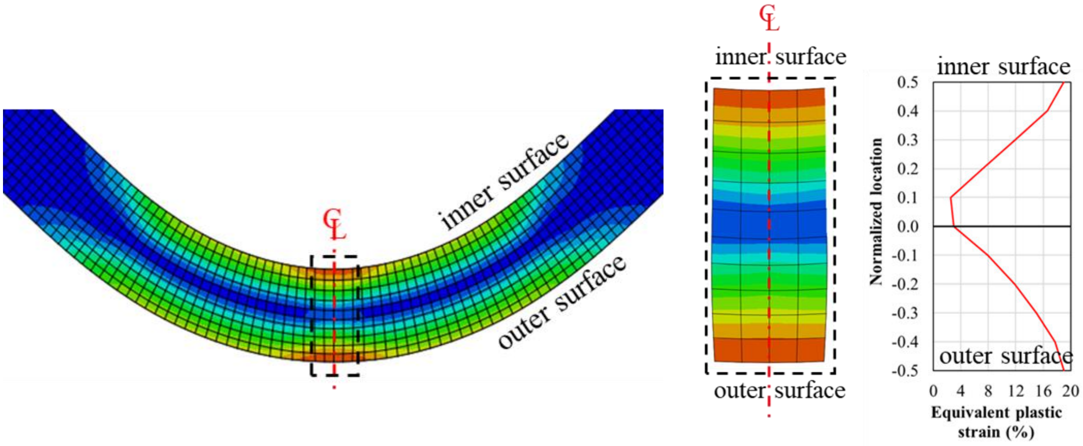

Fig. 5.17 Through-thickness equivalent plastic strains, PEEQ

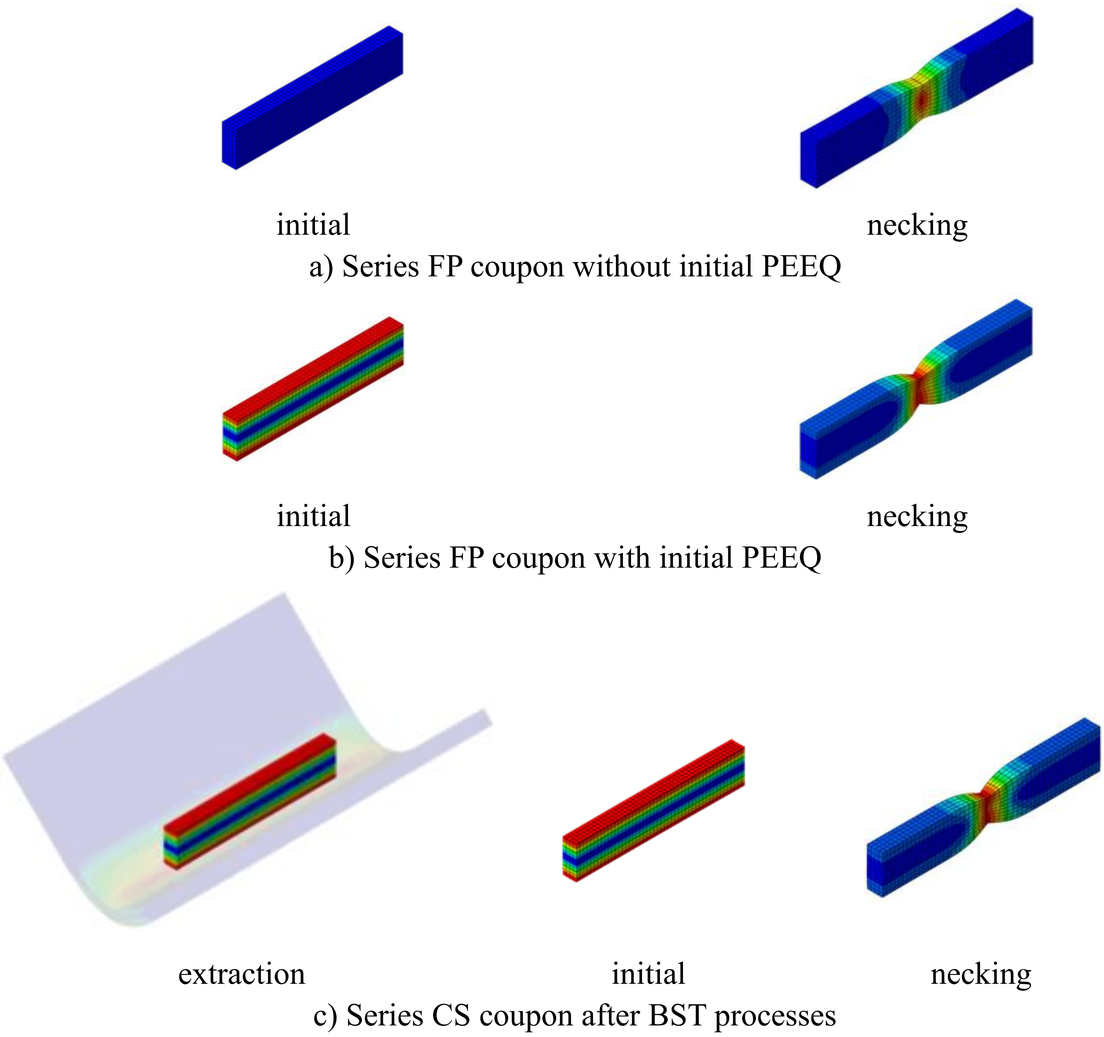

Fig. 5.18 Simulated coupons with different initial states of PEEQ

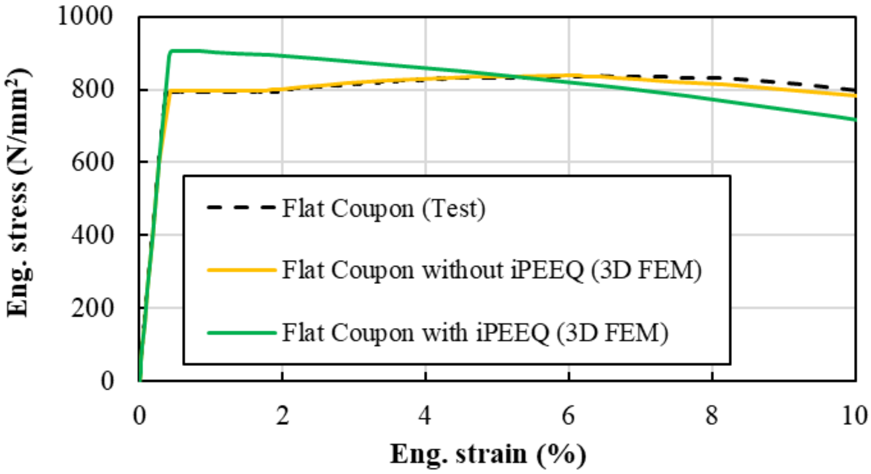

a) tested flat coupon and simulated flat coupons

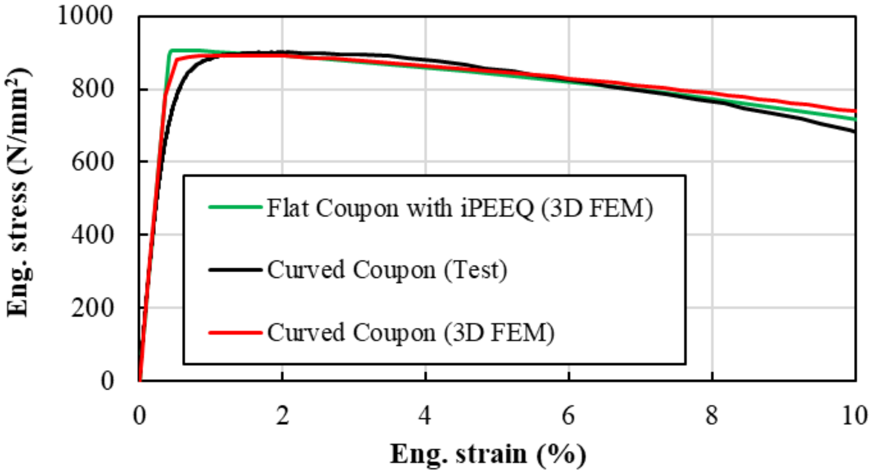

b) simulated flat coupon, tested curved coupon and simulated coupon

Fig. 5.19 Engineering stress-strain curves of flat and curved coupons: Tests vs 3D FEM (Coupon CS-B2)

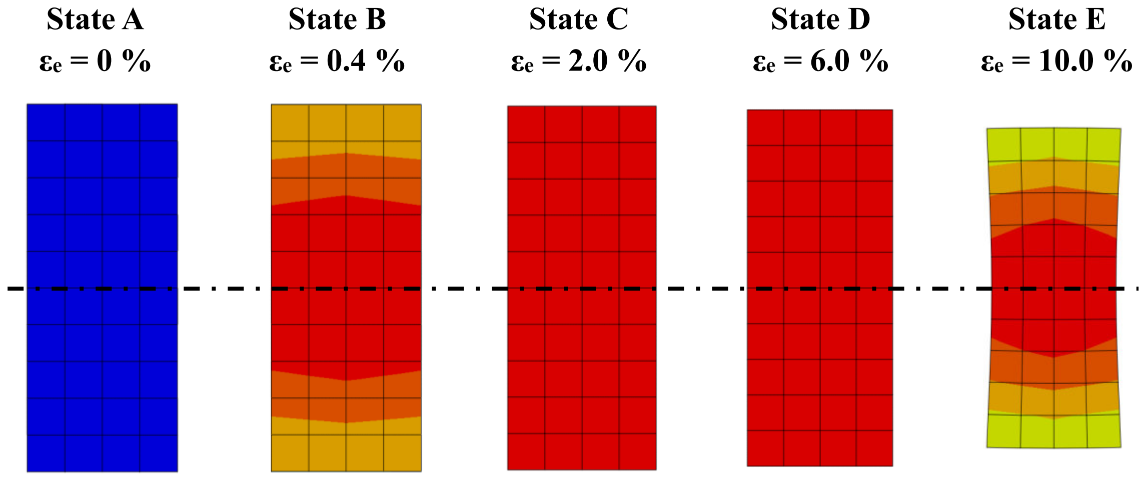

a) Series FP coupon without initial PEEQ

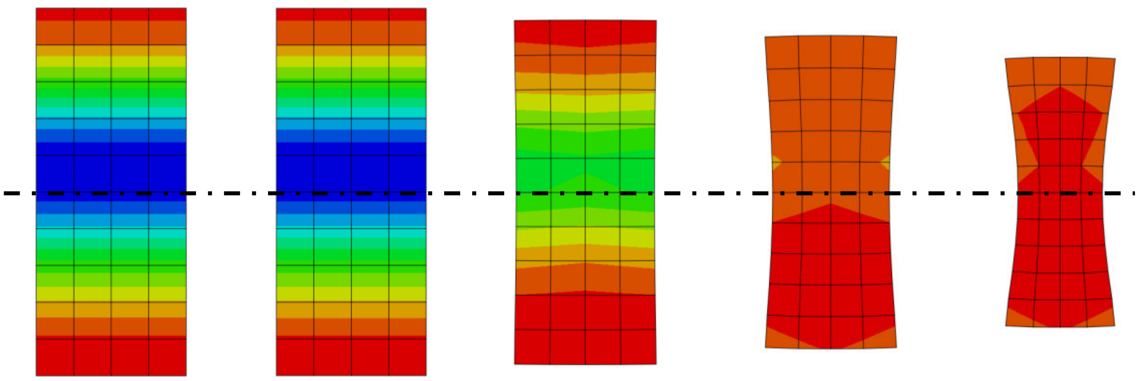

b) Series FP coupon with initial PEEQ

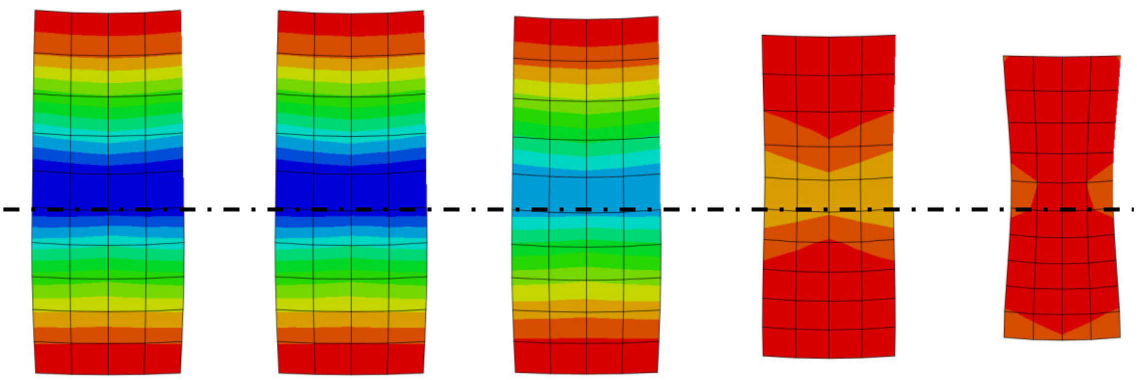

c) Series CS coupon after BST processes (Coupon CS-B2)

Fig. 5.20 Necked sections of simulated coupons with 3D FEM (Coupon CS-B2)

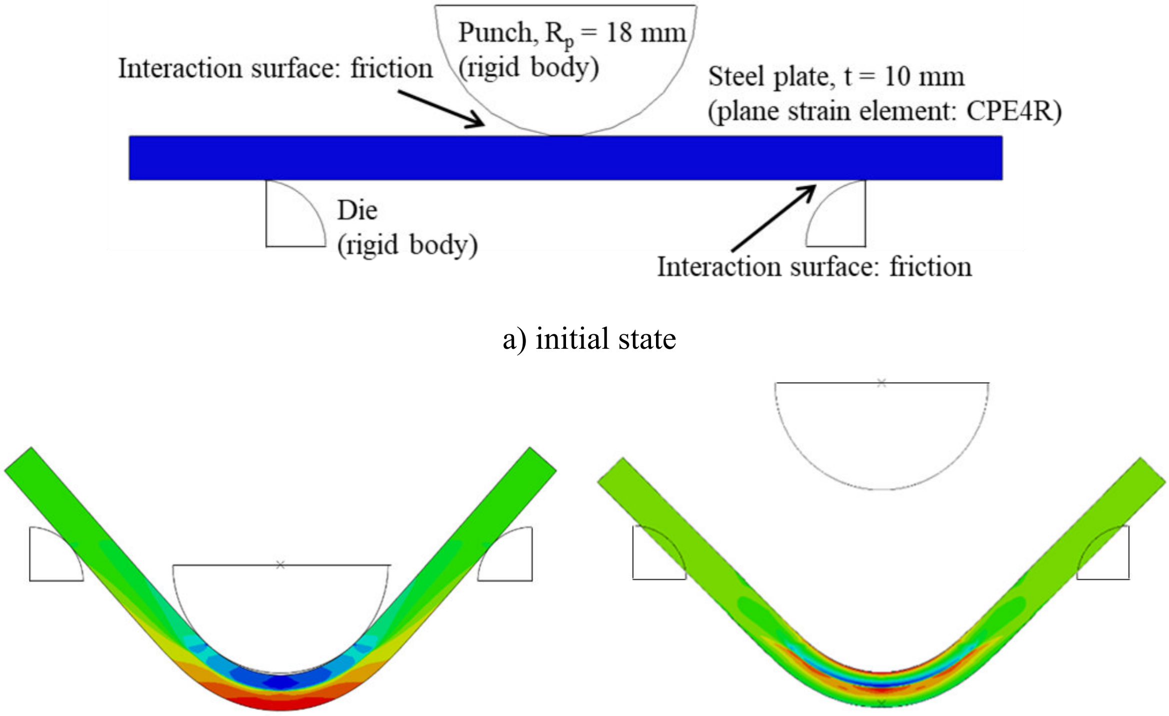

a) initial state

b) after bending

c) after springback

Fig. 5.21 Simulation processes of 2D transverse bending model (Mesh D@100)

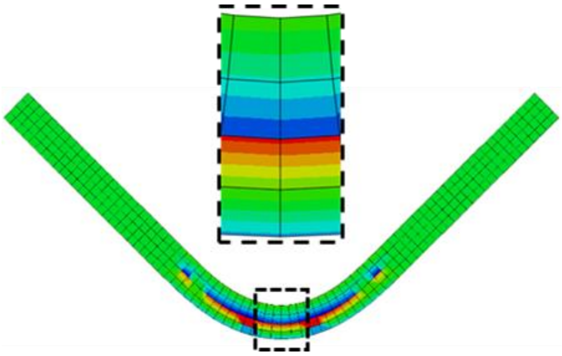

a) Mesh A@4

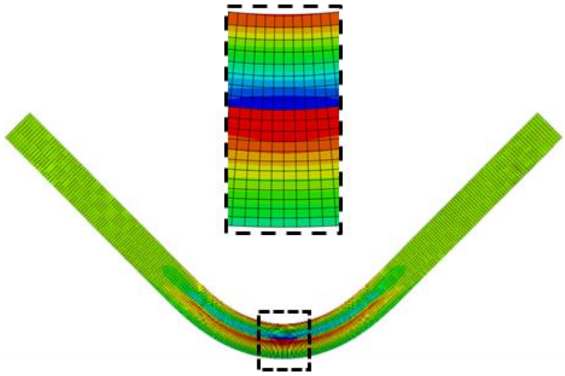

b) Mesh B@20

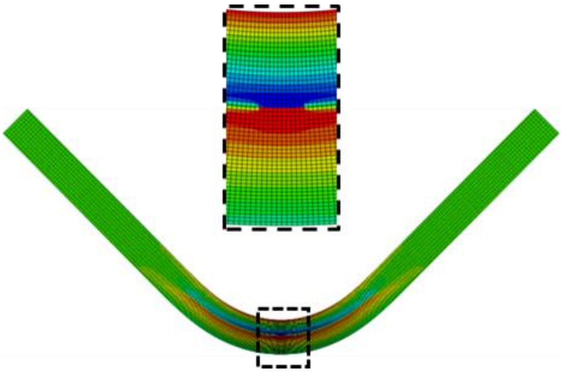

c) Mesh C@50

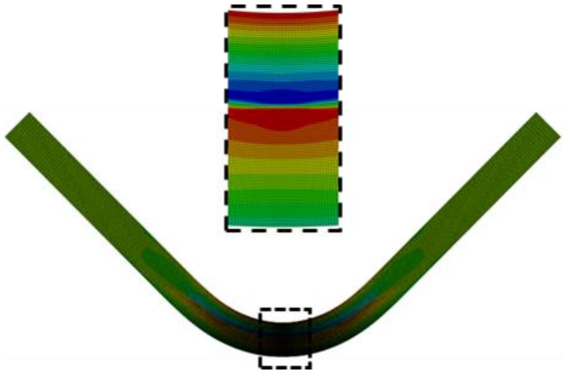

d) Mesh D@100

Fig. 5.22 Contours of transverse stresses of the cold-bent plate: 2D FEM with different meshes

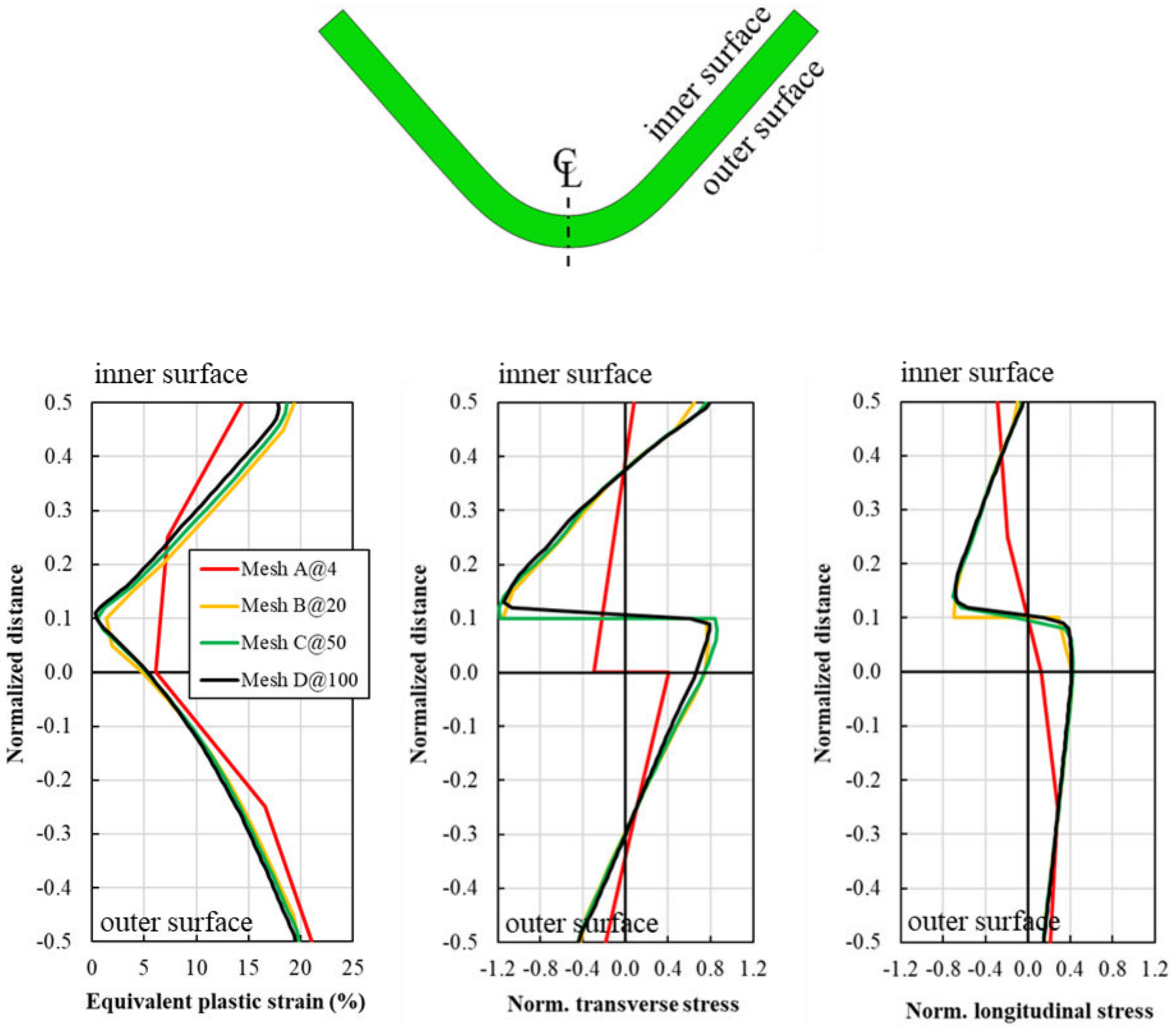

a) equivalent plastic strains b) transverse stresses c) longitudinal stresses

Fig. 5.23 Strains and stresses along the centre line of the cold-bent plate: 2D FEM with different meshes

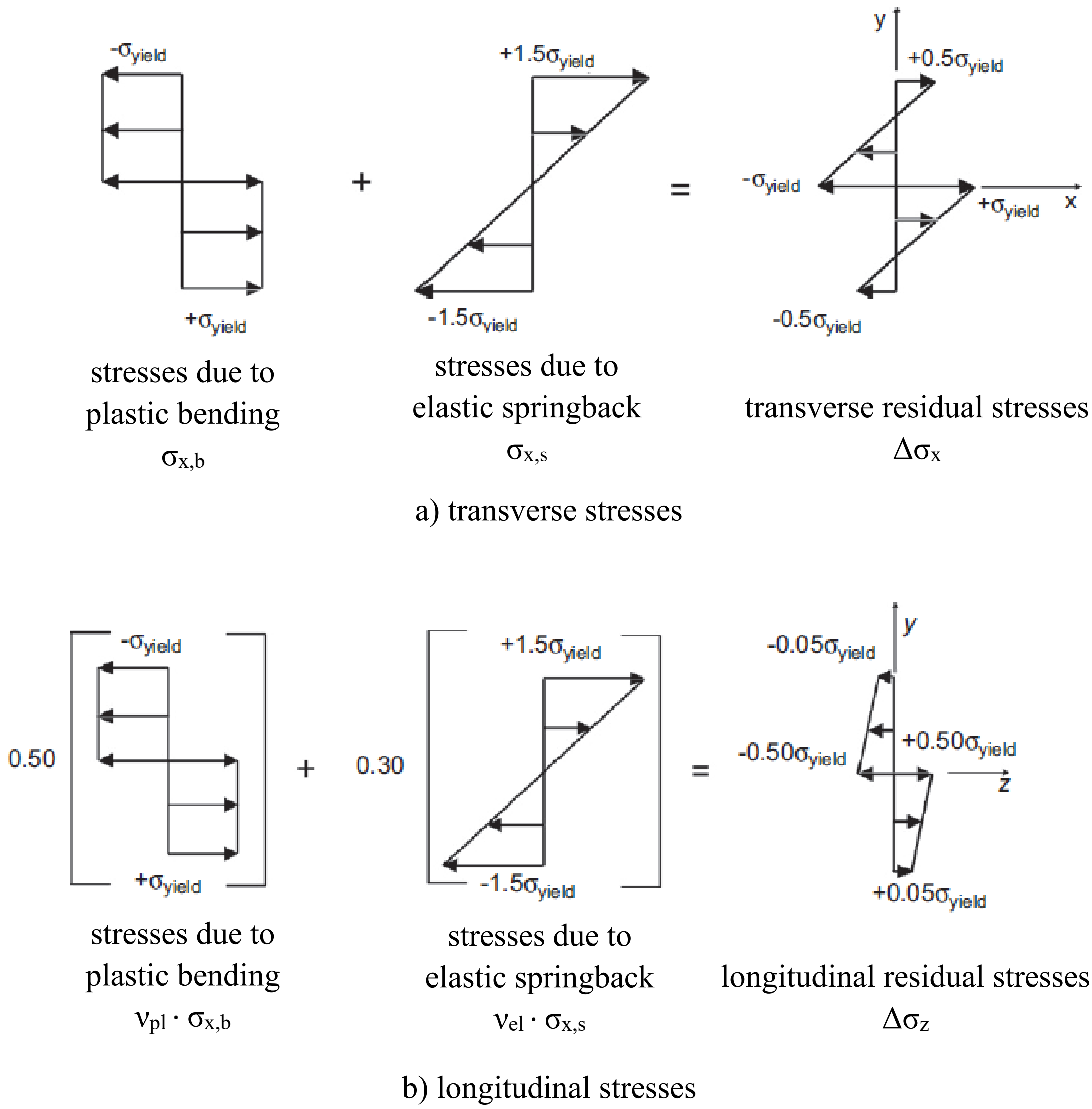

Fig. 5.24 Theoretical solutions to residual stresses due to transverse bending (Moen et al. 2008)

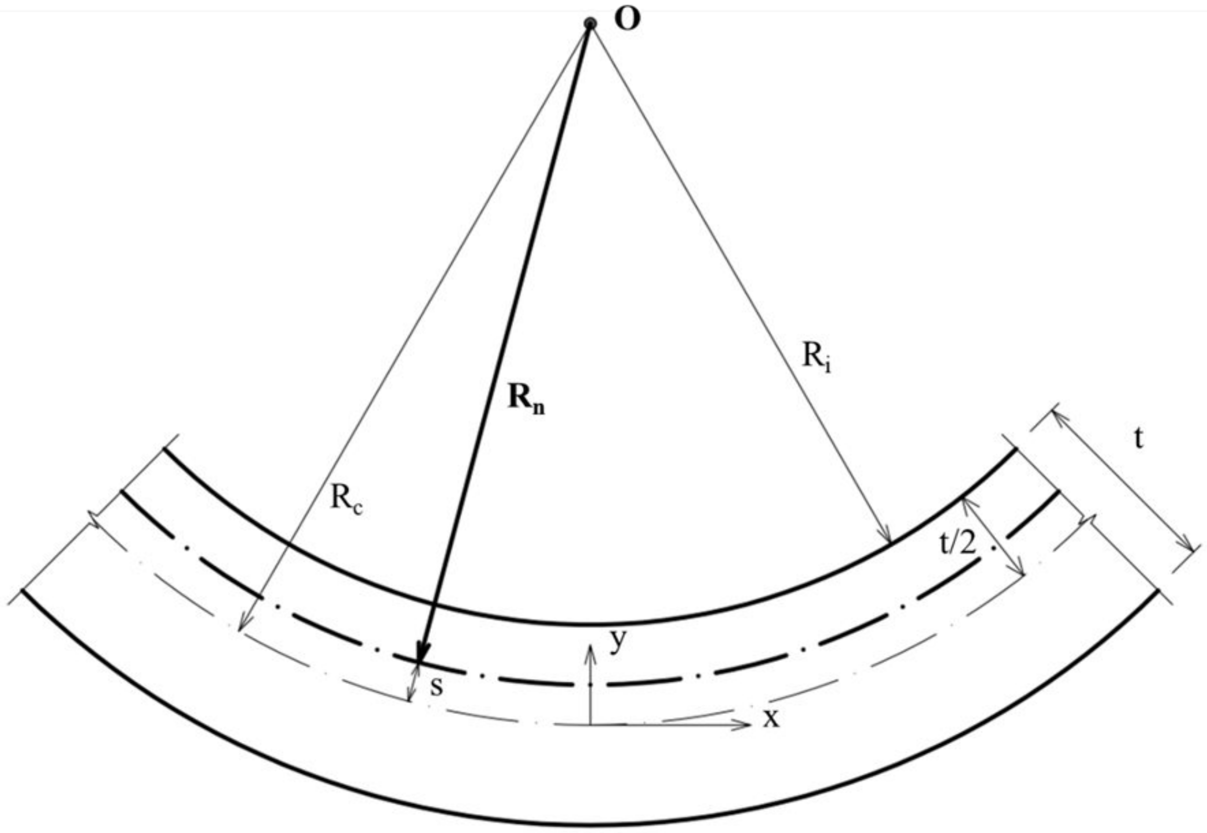

Fig. 5.25 Sketch of a plate under transverse bending

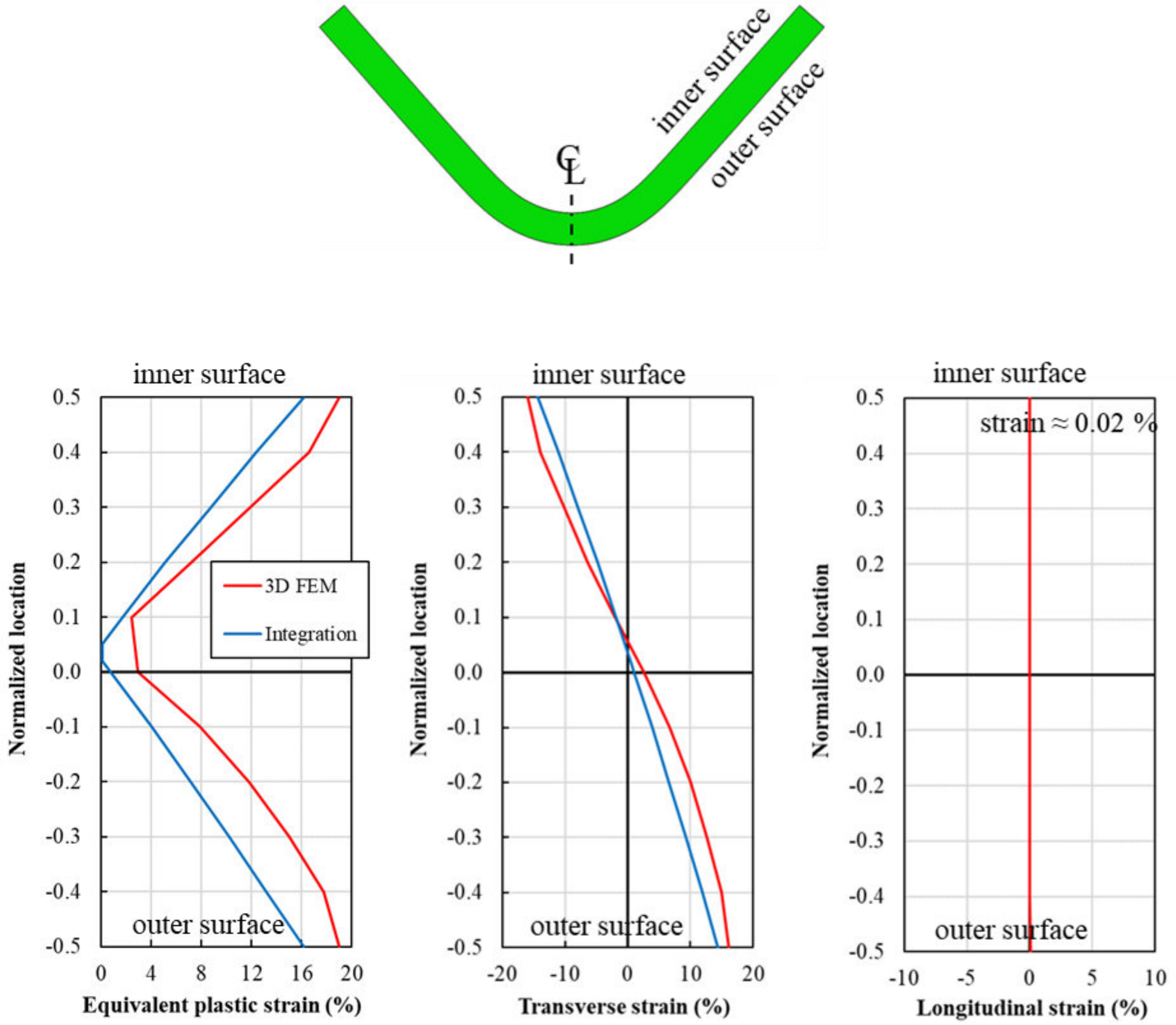

a) equivalent plastic strains b) transverse strains c) longitudinal strains (FEM only)

Fig. 5.26 Strains along the centre line of the cold-bent plate: 3D FEM vs integration method (Coupon CS-B2)

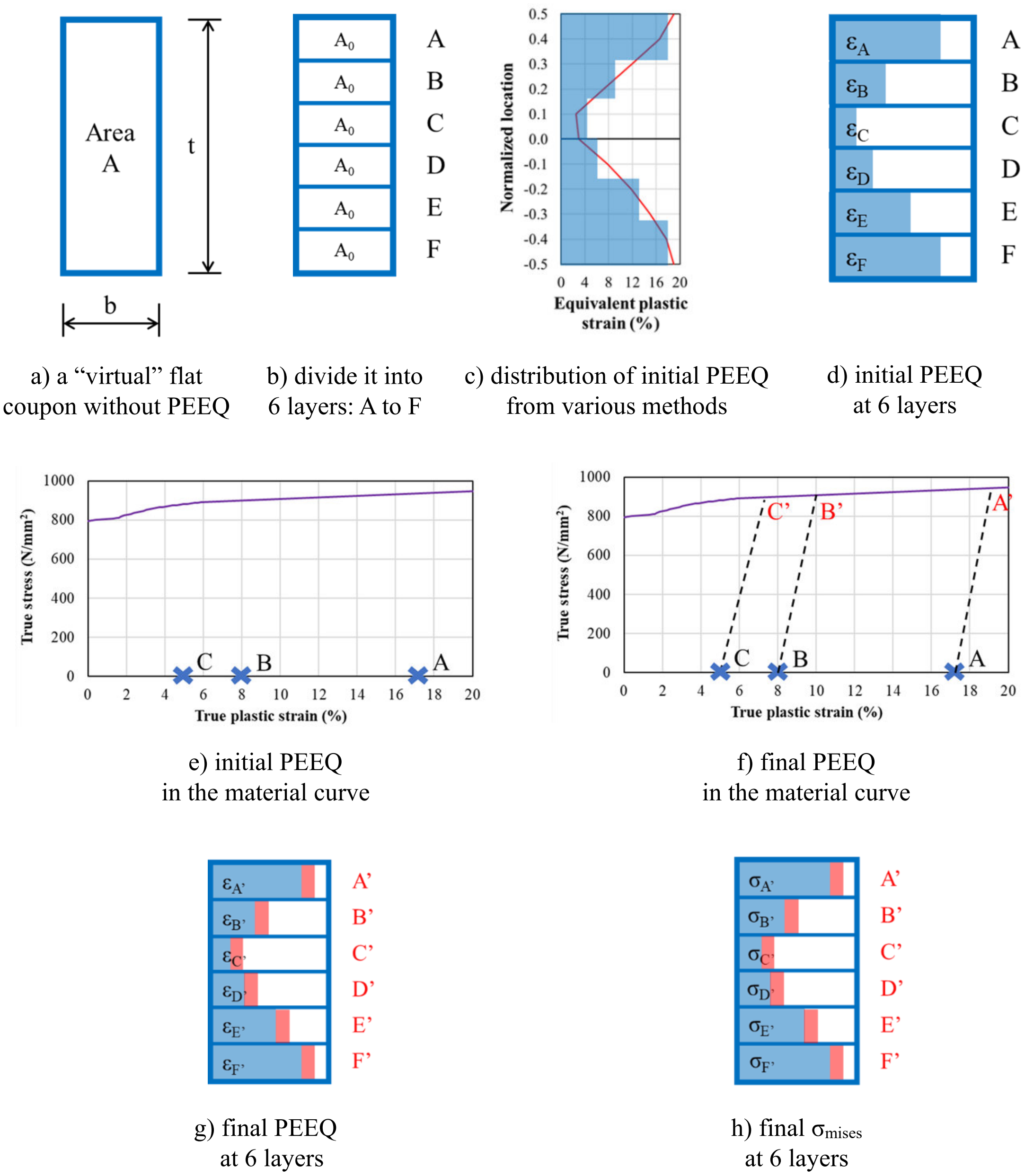

Fig. 5.27 Calculation process of the hand calculation method

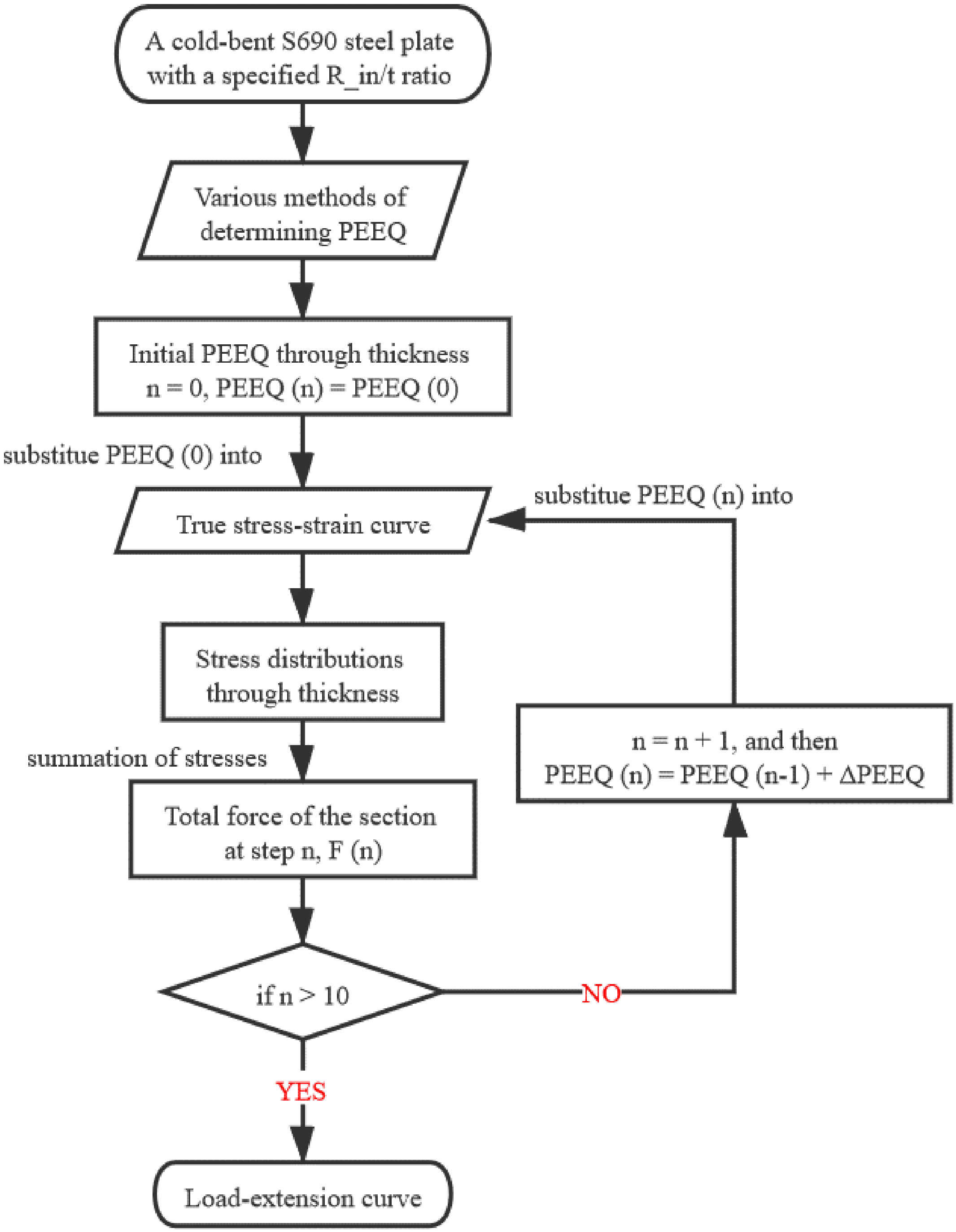

Fig. 5.28 Flowchart of the hand calculation method for predicting strength enhancement

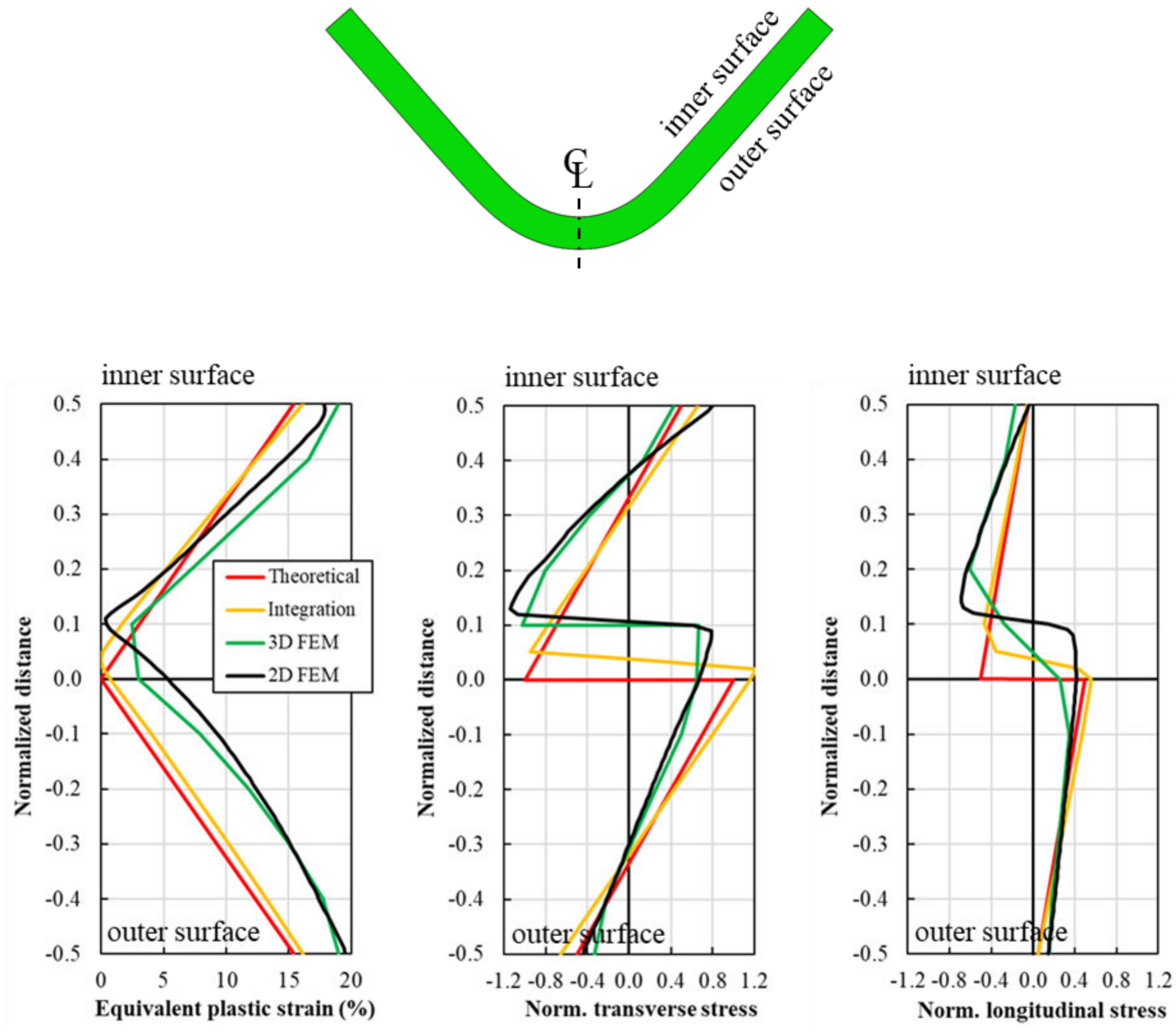

a) equivalent plastic strains b) transverse stresses c) longitudinal stresses

Fig. 5.29 Comparison of strains and stresses along the centre line of the cold-bent plate: Theory, integration method, 3D FEM and 2D FEM (Coupon CS-B2)

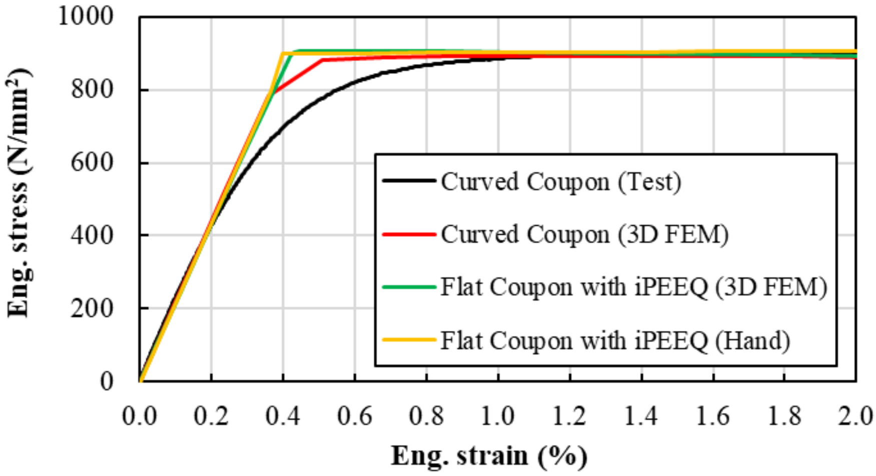

Fig. 5.30 Engineering stress-strain curves of flat and curved coupons: Test vs 3D FEM vs hand calculation (Coupon CS-B2)

Table 5.1 Test programme of all coupons extracted from S690 CFSHS

Series	Shape of coupon	Material along gauge length	Designation	t (mm)	b (mm)	A (mm^2)	$5.65 \cdot A^{0.5}$ (mm^2)
FP (no R_{in}/t)	Flat 4 x 10 mm	Flat portion of S690 steel	(1) FP-A1	9.70	3.94	38.22	34.93
			(2) FP-A2	9.72	3.95	38.39	35.01
			(3) FP-B1	9.68	3.94	38.14	34.89
			(4) FP-B2	9.64	3.94	37.98	34.82
			(5) FP-B3	9.77	3.95	38.59	35.10
			(6) FP-B4	9.76	3.94	38.45	35.04
			(7) FP-B5	9.79	3.94	38.57	35.09
			Average:	***9.72***	***3.94***	***38.34***	***34.98***
FW (no R_{in}/t)	Flat 4 x 10 mm	T Union GM 110 electrode	(1) FW-A1	9.34	3.94	36.80	34.27
			(2) FW-B1	9.29	3.97	36.88	34.31
			Average:	***9.23***	***3.96***	***36.84***	***34.29***
CS ($R_{in}/t = 3.0$)	Small curved 4 x 10 mm	Corner region of S690 steel	(1) CS-A1	9.55	3.91	38.01	34.83
			(2) CS-A2	9.56	3.90	37.27	34.49
			(3) CS-A3	9.54	3.90	37.01	34.37
			(4) CS-A4	9.55	3.90	37.59	34.64
			(5) CS-B1	9.52	3.91	37.64	34.66
			(6) CS-B2	9.52	3.90	36.93	34.33
			(7) CS-B3	9.53	3.91	36.92	34.33
			(8) CS-B4	9.56	3.91	36.71	34.23
			Average:	***9.54***	***3.91***	***37.26***	***34.49***
CL ($R_{in}/t = 3.0$)	Large curved 24 x 10 mm	Corner region of S690 steel	(1) CL-A1	9.53	23.96	219.44	83.70
			(2) CL-A2	9.56	23.95	219.99	83.80
			Average:	***9.55***	***23.96***	***219.72***	***83.75***

Table 5.2 Test results of all series of coupons

Series	Designation	A (mm)	E (kN/mm^2)	$f_{0.2}$ (N/mm^2)	f_u (N/mm^2)	$f_u/f_{0.2}$	ε_u (%)	ε_L (%)
FP (no R_{in}/t)	(1) FP-A1	38.2	222	784	830	1.06	5.34	17.34
	(2) FP-A2	38.4	218	783	827	1.06	5.49	16.72
	(3) FP-B1	38.1	221	796	839	1.05	5.54	17.64
	(4) FP-B2	38.0	218	791	837	1.06	6.62	15.43
	(5) FP-B3	38.6	217	790	833	1.05	6.28	16.59
	(6) FP-B4	38.5	217	795	837	1.05	6.26	16.45
	(7) FP-B5	38.6	218	787	829	1.05	5.54	16.43
	Average:	***38.3***	***219***	***789***	***833***	***1.06***	***5.87***	***16.67***
FW (no R_{in}/t)	(1) FW-A1	36.8	153	642	872	1.36	8.07	18.11
	(2) FW-B1	36.9	188	667	850	1.27	4.83	16.43
	Average:	***36.9***	***171***	***655***	***861***	***1.31***	***6.45***	***14.26***
CS (R_{in}/t = 3.0)	(1) CS-A1	38.0	196	832	879	1.06	1.55	11.81
	(2) CS-A2	37.3	196	827	895	1.08	1.79	12.26
	(3) CS-A3	37.0	198	844	908	1.08	1.53	13.53
	(4) CS-A4	37.6	195	838	898	1.07	1.52	11.62
	(5) CS-B1	37.6	196	831	891	1.07	1.78	12.11
	(6) CS-B2	36.9	193	830	901	1.09	2.07	11.93
	(7) CS-B3	36.9	210	852	909	1.07	1.61	13.68
	(8) CS-B4	36.7	206	850	916	1.08	1.81	12.06
	Average:	***37.3***	***199***	***838***	***900***	***1.07***	***1.71***	***12.38***
CL (R_{in}/t = 3.0)	(1) CL-A1	219.4	201	829	919	1.11	2.12	--
	(2) CL-A2	220.0	197	827	919	1.11	2.19	--
	Average:	***219.7***	***199***	***828***	***919***	***1.11***	***2.16***	***--***

Table 5.3 Key mechanical properties of all series of coupons

Series	E (kN/mm^2)	$f_{0.2}$ (N/mm^2)	f_u (N/mm^2)	ε_u (%)	ε_L (%)	E/E_{FP}	$f_{0.2}/f_{0.2,FP}$	$f_u/f_{u,FP}$	$\varepsilon_u/\varepsilon_{u,FP}$	$\varepsilon_L/\varepsilon_{L,FP}$
FP	219	789	833	5.87	16.67	1.00	1.00	1.00	1.00	1.00
FW	171	655	861	6.45	14.26	0.78	0.83	1.03	1.10	0.86
CS	199	838	900	1.71	12.38	0.91	1.06	1.08	0.29	0.74
CL	199	828	919	2.16	--	0.91	1.05	1.10	0.37	--

Table 5.4 Mesh convergence study of 2D transverse bending models

Model	Meshed layers through thickness	Global mesh size (mm)	Total number of elements	Computational time (min)	PEEQ on inner surface (%)	Normalized transverse stress on inner surface (/)
Mesh A@4	4	2.5	320	2	14.4	0.077
Mesh B@20	20	0.5	5560	2	19.4	0.643
Mesh C@50	50	0.2	20100	5	18.7	0.757
Mesh D@100	100	0.1	51000	16	17.8	0.795

CHAPTER 6: THERMOMECHANICAL ANALYSES FOR S690 CFSHS

6.1 Introduction

This Chapter presented a theoretical-numerical investigation into the temperatures and the residual stresses of four S690 cold-formed square hollow sections (CFSHS) due to welding.

The classic heat transfer mechanism was introduced as a basis of theory for this Chapter. Various thermal and mechanical properties for thermomechanical analyses were determined. A double-ellipsoidal heat source model was introduced to describe the energy distribution of a welding electrode. Based on this heat source model, an analytical solution to the temperature fields was then developed to predict fusion zones and to determine the lengths of the semi-axes adopted in the double-ellipsoidal model.

In order to predict the residual stresses of four CFSHS, the numerical models were established based on the theoretical studies and adopted to perform the sequentially-coupled thermomechanical analyses. In the numerical models, both the residual stresses due to transverse bending and the temperature fields due to longitudinal welding were incorporated. It was found that the residual stresses predicted with the numerical models matched well with the measurements of the sectioning method, and force equilibrium was well achieved in the results of these numerical models. Hence, this validated numerical method was considered to be qualified to predict the residual stresses in the S690 CFSHS.

To consider the fabrication effects into the structural analyses, the residual stresses and the plastic strains obtained from both the bending models and the thermomechanical analyses were simplified, and thus, were readily incorporated as the initial stress states of the numerical models for the structural analyses in Chapter 7.

6.2 Thermomechanical Properties in Heat Transfer

6.2.1 Basic formulae in heat transfer

The classic heat transfer theory is adopted in this project, and it is widely regarded as a complicated process of energy exchanging, involving conduction, convection and radiation.

Conduction is considered to be the most important part of heat transfer during welding as the energy in this form contributes the largest portion of heat energy input of the whole welding process. The net heat flux due to conduction is given by Fourier's Law, which is a simplified expression that describes a one-dimensional case of heat transfer:

$$q_{net,cd} = -\lambda \frac{dT}{dx} \qquad \text{Eq. (6.1)}$$

where

$q_{net,cd}$ is the net heat flux due to conduction (W/m^2);

dx is the material thickness (m);

dT is the temperature difference (K) from a hot area to a cold area across a thickness of dx; and

λ is the thermal conductivity (W/m/K).

However, as the real welding processes are more complicated than a one-dimensional heat transfer problem, a spatial- and time-dependent distribution of temperatures during welding should be considered. To specify the transient temperature fields in the vicinity of welding, the law of energy conservation is introduced as follows:

$$\frac{\partial T}{\partial t} = \frac{\lambda}{c\rho}\left(\frac{\partial^2 T}{\partial x^2} + \frac{\partial^2 T}{\partial y^2} + \frac{\partial^2 T}{\partial z^2}\right) + \frac{q_s}{c\rho} \qquad \text{Eq. (6.2)}$$

where

c is the specific heat (J/kg/K);

ρ is the mass density (kg/m^3), i.e. ρ = 7850 kg/m^3 for steels; and

q_s is the volumetric heat flux of the welding heat source (W/m^3).

It should be noted that the thermal properties mentioned above, i.e. the conductivity and the specific heat, are temperature-dependent. In order to incorporate these properties into heat transfer analyses, a detailed discussion on thermal properties of steels at elevated temperatures is presented in Section 6.2.2

In addition to conduction, convection and radiation are the other two forms of heat transfer. The net heat fluxes due to convection and radiation are given by Eqs. (6.3) and (6.4), respectively:

$$q_{net,cv} = \alpha \cdot (T_0 - T) \qquad \text{Eq. (6.3)}$$

where

$q_{net,cv}$ is the net heat flux due to convection (W/m^2);

α is the film coefficient ($W/m^2/K$);

T_0 is the ambient temperature (K); and

T is the material temperature (K).

$$q_{net,r} = \varphi \cdot \xi \cdot 5.67 \times 10^{-8}[(T_0 + 273)^4 - (\mathrm{T} + 273)^4] \qquad \text{Eq. (6.4)}$$

where

$q_{net,r}$ is the net flux due to radiation (W/m^2);

φ is the configuration factor, and it is taken to be 1.0 in this project for simplification; and

ξ is the emissivity coefficient.

It should be noted that the film coefficient, α, in Eq. (6.3) and the emissivity coefficient, ξ, in Eq. (6.4) are two thermal properties that vary insignificantly at elevated temperatures. Both of these two properties have large ranges of values for steels at ambient temperatures, but no specific values are given in EN 1993-1-2 (CEN 2009). To evaluate the sensitivity to both the film coefficient and the emissivity coefficient in heat transfer analyses and thermomechanical analyses, a pilot study was carried out by the author numerically. When α is taken to vary from 1 to 30 $W/mm^2/k$, the peak temperatures during welding change from 5977 to 5934 °C, i.e. with a decrease by only 0.7 %, and the corresponding maximum tensile residual stresses after cooling change from 585.5 to 584.1 N/mm^2, i.e. with a decrease by only 0.2 %. When ξ is taken to vary from 0.3 to 0.9, the peak temperatures during welding change from 7088 to 5099 °C, i.e. with a decrease by 28.1 %, and the corresponding maximum tensile residual stresses after cooling change only from 598.6 to 570.9 N/mm^2, i.e. with a decrease by only 4.6 %. In summary, the change of the film coefficients has only minor influences on the temperature histories and the residual stresses. However, the numerical results of the thermomechanical analyses are sensitive to the emissivity coefficients. In practical welding, it is demanding to precisely measure the emissivity coefficient of every steel plate as this coefficient is highly sensitive to the surface statue of the plate (Zhu et al. 2020).

According to the pilot study, it is recommended that the film coefficient, α, is therefore taken to be 25 $W/m^2/K$, which is a commonly adopted value for heat transfer analyses as in EN 1993-1-2. As the emissivity coefficient, ξ, is commonly taken to vary between 0.75 and 0.85 for cold-rolled steels in engineering practice, it is therefore to adopt to be 0.80 for all the heat transfer analyses in this project.

6.2.2 Thermomechanical properties at elevated temperatures

During welding, steel plates normally undergo quick changes in temperatures with large gradients. It is important to determine how the steel properties vary with temperatures during welding because these parameters allow the steels to behave differently in both heat transfer analyses and thermomechanical analyses. EN 1993-1-2 provides a set of reduction factors for temperature-dependent thermomechanical properties for S235 to S460 steels at elevated temperatures, and they are thermal conductivity, heat specific, thermal expansion coefficient, yield strength and Young's modulus. However, as there are limited studies on the temperature-dependent material properties of high strength steels, it is acceptable to employ these reduction factors in EN 1993-1-2 directly for the heat transfer analyses and the thermomechanical analyses for high strength S690 steels in this project accordingly to EN 1993-1-12.

The reduction factors for yield strength and Young's modulus are shown in Fig. 6.1. In this project, 6 and 10 mm thick S690 steel plates are used for manufacturing various members, and the curves shown in Fig. 6.2 represent typical true stress-strain characteristics of these plates at ambient temperatures as presented in Chapter 3. By adopting the reduction factors shown in Fig. 6.2, both the elastic and the plastic stress-strain characteristics of these two plates at elevated temperatures are obtained. Therefore, the constitutive models of these steel plates for the thermomechanical analyses are readily developed.

6.3 Heat Source Model

A heat source model is a tool that describes the distribution of the energy induced by an electrode during welding. In this project, a double-ellipsoidal heat source model is employed to describe the movement and the distribution of the heat source of arc welding. The model is a widely-adopted heat source model developed by Goldak et al. (1984). It should be noted that this model is demonstrated to has been working effectively together with various thermomechanical properties and welding parameters while the thermomechanical properties employed are introduced in Section 6.2. The welding parameters are introduced in the following paragraphs.

6.3.1 Weld parameters

Linear heat input energy is a controlling welding parameter that influences significantly the mechanical properties of the heat affected zones (HAZ) of a welded section. In order to control welding quality, this key parameter should be determined prior to welding by considering the plate thickness, the welding method, the chemical compositions and the mechanical properties of the steel. The linear heat input energy, q, is given by:

$$q = \frac{\eta \cdot U \cdot I}{v} \qquad \text{Eq. (6.5)}$$

where

q is the linear heat input energy (kJ/mm);

η is the efficiency of welding, normally taken to be 0.80 ~ 0.90 for GMAW;

U is the voltage (V);

I is the current (A); and

v is the speed of welding (mm/s).

In this project, a qualified welder is employed to carry out GMAW to all the specimens, so that the heat input is well controlled under 1.5 kJ/mm. Under such a low heat input, the mechanical properties of the HAZ have very little reductions in both strength and ductility. Typical welding parameters are presented in Section 6.5. For further information on the welding passes, the preheating temperatures and the interpass temperatures refer to Chapter 3.

6.3.2 Double-ellipsoidal heat source model

A heat source model is commonly employed in a heat transfer analysis to describe the distribution of energy during a welding process. Among many heat source models in the literature, one of the most efficient and commonly employed models is the double-ellipsoidal model (Goldak et al. 1984). With development of finite element methods, the double-ellipsoidal model has been extensively employed in heat transfer analyses in the past few decades that residual stresses of a welded section are readily predicted in thermomechanical analyses. The definition of the double-ellipsoidal heat source model is given by:

$$q_1\,(x, y, z, t) = \frac{6\sqrt{3}f_1 q}{abc_1\pi\sqrt{\pi}}\, exp(-\frac{3x^2}{a^2})\, exp(-\frac{3y^2}{b^2})\, exp(-\frac{3(z - vt)^2}{c_1^2}) \qquad \text{Eq. (6.6)}$$

$$q_2\,(x, y, z, t) = \frac{6\sqrt{3}f_2 q}{abc_2\pi\sqrt{\pi}}\, exp(-\frac{3x^2}{a^2})\, exp(-\frac{3y^2}{b^2})\, exp(-\frac{3(z - vt)^2}{c_2^2}) \qquad \text{Eq. (6.7)}$$

where

q_1 (x, y, z, t) is the power density in the front ellipsoid;

q_2 (x, y, z, t) is the power density in the rear ellipsoid;

q is the linear heat input energy (kJ/mm), as defined in Eq. (6.5);

f_1 is the portion of the heat deposited in the front ellipsoid;

f_2 is the portion of the heat deposited in the rear ellipsoid; and

a, b, c_1 and c_2 are the lengths of the semi-axes.

Fig. 6.3 illustrate a typical double-ellipsoidal heat source model, and the symbols defined above are also shown in the figure. The two normal distributions, i.e. one in the front ellipsoid and the other one in the rear ellipsoid, of the heat fluxes are presented along the z-axis. It should be noted that these two normal distributions have the same mean values, i.e. $\mu_1 = \mu_2 = 0$, but they have two different standard deviations, i.e. $\sigma_1 \neq \sigma_2$. However, the heat flux function must keep continuity at the point of $z = 0$, which means mathematically:

$$q_1\,(z = 0) = q_2\,(z = 0) \qquad \text{Eq. (6.8a)}$$

$$q_1'\,(z = 0) = q_2'\,(z = 0) = 0 \qquad \text{Eq. (6.8b)}$$

Due to:

$$f_1 + f_2 = 2 \qquad \text{Eq. (6.9)}$$

Therefore,

$$f_1 = \frac{2c_1}{c_1 + c_2} \qquad \text{Eq. (6.10)}$$

$$f_2 = \frac{2c_2}{c_1 + c_2} \qquad \text{Eq. (6.11)}$$

6.4 Analytical Solution to Temperatures due to Welding

A double-ellipsoidal heat source model is important for a thermomechanical analysis to predict temperatures with properly defined thermal properties and welding parameters. The temperature fields during welding are spatial- as well as time-dependent, i.e. T = T (x, y, z, t). As demonstrated in the previous Sections, the temperature fields in heat transfer are constituted with a number of variables as follows:

$$\mathrm{T}\,(\mathrm{x}, \mathrm{y}, \mathrm{z}, \mathrm{t}) = \mathrm{T}\,(\mathrm{x}, \mathrm{y}, \mathrm{z}, \mathrm{t}, \mathrm{T}_0, \lambda, \mathrm{c}, \mathrm{U}, \mathrm{I}, \eta, \mathrm{v}, \alpha, \xi, \mathrm{a}, \mathrm{b}, \mathrm{c}_1, \mathrm{c}_2) \qquad \text{Eq. (6.12)}$$

A total of 17 variables shown in Eq. (6.12) are categorized into five Groups from A to E as follows:

- Group A: the independent field variables, namely the spatial coordinates (x, y and z), the time of welding, t, and the ambient temperature, T_0. These 5 variables are independent variables.
- Group B: the temperature-dependent thermal properties, namely the thermal conductivity, λ, and the specific heat, c. These 2 variables are discussed in Section 6.2.2, and their values are readily determined in accordance with EN 1993-1-2.
- Group C: the welding parameters, namely the voltage, U, the current, I, the welding efficiency, η, and the welding speed, v. These 4 varibales are discussed in Section 6.3.1. The welding parameters of each welding pass should be meausred during welding for effective modelling.
- Group D: the coefficients for convection and radiation, namely the film coefficient, α, and the emissivity coefficient, ξ. These 2 variables are discussed in Section 6.2.1 while they are taken to be 25 $W/m^2/K$ and 0.80, respectively.
- Group E: the parameters of the double-ellipsoidal heat source model, namely the lengths of the semi-axes (a, b, c_1 and c_2).

It is found that except for the variables in Group E, all the other ones are readily employed in the thermomechanical analyses. To find a proper set of the lengths of the semi-axes of the double ellipsoidal heat source model, iterations should be carried out. Obviously, complicated calculations on temperature fields must be implemented with numerical methods. But the modelling process is quite demanding, and it probably takes much computational time to perform running heat transfer analyses numerically. Hence, it is proposed to develop an analytical solution to predict the temperature fields due to welding with a high level of accuracy.

Fachinotti et al. (2011) reported an analytical solution that is capable of predicting the temperature fields induced by a double-ellipsoidal model. The analytical solution is developed with an integration formula, which is given by:

$$T\,(x,y,z,t) = T_0 + \frac{3\sqrt{3}}{\pi\sqrt{\pi}}\frac{q}{\rho c} \times \int_0^t \frac{exp\,[-\dfrac{3x^2}{12\kappa(t\,-\,t')\,+\,a^2} - \dfrac{3y^2}{12\kappa(t\,-\,t')\,+\,b^2}]}{\sqrt{12\kappa(t\,-\,t')\,+\,a^2}\,\sqrt{12\kappa(t\,-\,t')\,+\,b^2}} \times [f_1 A_1(1+B_1) + f_2 A_2(1-B_r)]\,dt' \qquad \text{Eq. (6.13a)}$$

$$A_i \;=\; A\,(z,t,t',c_i) \;=\; \frac{exp\,[-\dfrac{3(z\,-\,vt')^2}{12\kappa(t\,-\,t')\,+\,c_i^2}]}{\sqrt{12\kappa(t\,-\,t')\,+\,c_i^2}} \qquad \text{Eq. (6.13b)}$$

$$B_i \;=\; B\,(z,t,t',c_i) \;=\; erf\,[\frac{c_i}{2}\,\frac{z\,-\,vt'}{\sqrt{\kappa(t\,-\,t')}\sqrt{12\kappa(t\,-\,t')\,+\,c_i^2}}] \qquad \text{Eq. (6.13c)}$$

It should be noted that the index, i, is taken to be 1 or 2, where “1” donates the front ellipsoid while “2” donates the rear ellipsoid.

where

ρ is the density (kg/m^3), which is taken to be 7850 kg/m^3 for steel;

c is the specific heat (J/kg/K), which is taken to be 600 J/kg/K for steel;

λ is the thermal conductivity (W/m/K), which is taken to be 25 W/m/K for steel; and

κ is the diffusion coefficient ($W \cdot m^2/J$), which is defined as $\kappa = \lambda/(\rho \cdot c) = 5.31\ W \cdot m^2/J$.

The integration formulae shown in Eq. (6.13) are implemented with the software MatLab in this project. After inputting the parameters of the formulae into the software, the analytical solution is able to provide details of the distributions of the temperatures at the time of t along x-, y- and z-axes, respectively. Therefore, the dimensions of the fusion zone are directly evaluated. After trial-and-error iterations, the best-fitted lengths of the semi-axes of the model are determined.

Heat transfer analyses can precisely predict temperature fields of the finite element models. However, the analytical solutions are more efficient in calculation as some assumptions may be introduced for simplification. One of the most important assumptions is that only the heat flux due to conduction is calculated in this analytical solution, i.e. the heat fluxes due to both convection and radiation are totally ignored. Besides, all the temperature-dependent thermal properties are taken to be constant. These two assumptions may reduce accuracy but significantly simplify the calculation process. Therefore, it is recommended to employ both the analytical solutions and the numerical methods simultaneously when predicting the temperature fields due to welding, so that a balance between accuracy and efficiency is readily achieved.

A heat transfer analysis of single-pass welding is developed numerically with ABAQUS (2013). The welding parameters incorporated in this analysis are consistent with the recorded values of the first welding pass of Section S3A, i.e. $U = 20.4$ V, $I = 150$ A, $v = 2.09$ mm/s, $\eta = 0.80$ and $q = 1.24$ kJ/mm. The analytical solution is also developed to predict the distributions of the temperatures with the same welding parameters incorporated. Fig. 6.4 illustrates a direct comparison on the dimensions of the fusion zones between the analytical solution and the numerical model, i.e. the half-widths along the x-axis of the fusion zones and the lengths along the z-axis of the fusion zones. It is defined that the fusion zones in this comparison are the areas where temperatures are larger than 1400 °C. As demonstrated by the numerical results in graph a), the half-width of the fusion zone is 3.0 mm along the x-axis, and its length is 8.5 mm along the z-axis while as demonstrated by the analytical results in graph b), the half-width of the fusion zone is 3.2 mm along the x-axis, and its length is 7.2 mm along the z-axis. The dimensions of the fusion zones obtained from these two methods are considered to in a good agreement. After several iterations, a set of welding parameters of the double-ellipsoidal heat source model are determined as summarized in Table 6.1, and these parameters are readily employed in the investigations of the heat transfer analyses in the subsequent Sections.

6.5 Sequentially-Coupled Thermomechanical Analyses

In order to predict residual stresses in S690 CFSHS, both transverse bending and longitudinal welding should be considered in the numerical simulation simultaneously. Fig. 6.5 shows a flowchart of numerical predictions for residual stresses in which three numerical models are developed consistently with ABAQUS, and they are: i) 2D transverse bending model, ii) 3D heat transfer model, and iii) 3D thermomechanical model.

As described in Chapter 5, both the initial plastic strains and the residual stresses of a S690 cold-bent plate with $R_{in}/t = 3.0$ have been successfully simulated with the 2D transverse bending models. Besides, the whole analysing processes of the models in items ii) and iii) are defined as a "sequentially-coupled thermomechanical analysis", which is a widely employed technique for simulating the temperatures and the residual stresses due to welding numerically. A validated heat transfer model is able to predict the temperature fields of a welded section due to welding. By incorporating both the initial stress-strain components due to transverse bending and the temperature fields due to longitudinal welding into a thermomechanical model, the resultant residual stresses of a CFSHS are readily predicted.

6.5.1 Investigation programme

A total of four welded CFSHS are investigated with the sequentially-coupled thermomechanical analyses, including i) two 6 mm thick Sections S1A and S1B, and ii) two 10 mm thick Sections S3A and S3B. Fig. 6.6 illustrates the dimensions of these four CFSHS, which are identical with all the other CFSHS covered in this project. The member lengths of Sections S1A and S1B are 560 mm, and the member lengths of Sections S3A and S3B are 760 mm. It should be noted that the member lengths of these sections are all larger than three times of the widths of these sections. This allows the residual stresses induced by both transverse bending and longitudinal welding to be distributed uniformly at both ends over a length about the width of the section. Hence, only the residual stresses at the mid-length are taken to be typical pattern, and thus, compared with those measured with the sectioning method.

Table 6.2 summarizes the investigation programme of the sequentially-coupled thermomechanical analyses. All the sections are fabricated with both transverse bending and longitudinal welding, and details of their fabrication processes are introduced in Chapter 3. It is presented in Table 6.2 that the welding parameters, the temperature histories and the residual stresses of Sections S3A and S3B are well measured and recorded, so the numerical models of these two sections are readily established. After a successful validation, the numerical models are able to simulate the temperature histories and the residual stresses of Sections S1A and S1B with a high level of accuracy.

Fig. 6.7 shows the sketches of four different types of multi-pass welding in the four CFSHS. The key welding parameters of each pass are summarized in Table 6.3, including the current, I, the voltage, U, the welding speed, v, the welding efficiency, η, and the linear heat input energy, q. As demonstrated in Section 6.3, these welding parameters are very important to the modelling accuracy of the heat transfer analyses and the thermomechanical analyses, because they define key parameters of the double-ellipsoidal heat source model, and thus, determine both the temperatures and the residual stresses of the CFSHS.

6.5.2 Establishment of models

Fig. 6.8 illustrates the modelling process of the multi-pass welding in Sections S1A and S1B. The sequences of four welding passes are shown in both graphs, with each welding pass allocated with the similar volume of the welding groove. Each graph shows that Passes 1 and 2 are welded sequentially at the top of the section, followed with Passes 3 and 4 welded sequentially at the bottom of the section. Similarly, Fig. 6.9 illustrates the modelling process of the multi-pass welding in Sections S3A and S3B. The only difference is that one more welding pass is imposed into each welding groove in Section S3A and S3B, because their plate thicknesses are increased from 6 to 10 mm.

Fig. 6.10 illustrates the boundary conditions of the thermomechanical models of Series SA and SB Sections. In general, the boundary conditions of these two Series of sections are similar. At one end of the specimen, the degrees of freedom for translation are fixed in all the three directions, i.e. $U_x = U_y = U_z = 0$ while at the other end, the degrees of freedom for translation are fixed in both directions in the plane of the section, i.e. $U_x = U_y = 0$. Hence, all the specimens can expand along their longitudinal direction freely during welding.

The material properties and the double-ellipsoidal heat source model are introduced in Sections 6.2 and 6.3, respectively, and, they are readily incorporated into the sequentially-coupled thermomechanical analyses.

6.5.3 Simplified residual stresses due to transverse bending

As demonstrated in Section 6.5.1, the residual stresses due to transverse bending should be incorporated into the thermomechanical analyses. The 2D transverse bending models developed in Chapter 5 are shown to be able to predict through-thickness residual stresses at the corner regions with a high level of accuracy using very little computational resources. In the present project, the CFSHS are fabricated with 6 and 10 mm thick plates, but only one R_{in}/t ratio is employed for all the cold-bent corners, i.e. $R_{in}/t = 3.0$. Therefore, two patterns of residual stresses due to transverse bending are readily obtained with the above-mentioned validated models, and they are: i) $t = 6$ mm and $R_{in} = 18$ mm, and ii) $t = 10$ mm and $R_{in} = 30$ mm, as shown in Fig. 6.11. It should be noted that these two patterns exhibited by 6 and 10 mm thick plates are very similar. This indicates that with the same R_{in}/t ratio, different plate thicknesses may not affect the distributions of the longitudinal residual stresses.

To incorporate the residual stresses predicted with the 2D transverse bending models into the 3D finite element models for thermomechanical analyses, the two patterns shown in Fig. 6.11 should be adopted in which the numbers of layers are significantly reduced. The through-thickness longitudinal stresses in the 6 mm plate are discretized into 3 layers. The values of the longitudinal stresses within one layer are taken to be the average stress within that layer. Similarly, the pattern in the 10 mm plate is discretized into 4 layers evenly. Therefore, the longitudinal residual stresses obtained from the 2D transverse bending models are readily incorporated into the 3D models for further investigation.

6.5.4 Simplification of models and mesh convergence study

a) Half models vs full models

Before carrying out a mesh convergence study, it is proposed to simplify full models into half models because high computational efficiency is achieved in the latter ones. Fig. 6.12 illustrates the establishment of both the full modes and the half models of the four CFSHS. Section S3A is taken as an example to demonstrate the modelling process: the full model represents the welding processes with six sequential analysing steps in which the six welds are activated one by one in each step, and these six welding passes are imposed onto the welding grooves of the section in sequence as shown in this figure. The half model is simplified by taking symmetry about the zx-plane of the full model, so that only the three welding passes at the top are performed numerically in this half model. It should be noted that the major difference between these two models lies in the welding sequences. Hence, both the top passes and the bottom passes of the section are assumed to be performed into the half model at the same time, which is different from the real welding sequences in the fabrication process. It is apparent that the half model can achieve high computational efficiency while ignoring welding sequences may result in errors in the residual strains across the section. Therefore, the effectiveness of this half model should be checked by comparing the residual strains between these two models.

Two full models and two half models are established, and they are referred as Models S3A-F, S3A-H, S3B-F and S3B-H. Fig. 6.13 shows a comparison of the longitudinal residual strains on both surfaces of Models S3A-F and S3A-H. As Section S3A is symmetrical about both the yz-plane and the zx-plane, the results of only half a section are shown in the graphs, namely the longitudinal residual strains from Points A to A'. It should be noted that the largest magnitude and gradient of the longitudinal residual strains are found at Points A and A', which are the locations of the weld centres. By comparing the results of the two models at these two Points and the other locations, very small differences are found in both the magnitude and the gradient of the residual strains. Hence, it is shown that welding sequences have very minor effects on the longitudinal residual strains.

Another comparison between the results of Models S3B-F and S3B-H is also carried out, as shown in Fig. 6.14. The residual strains around the whole perimeter of the sections are plotted in the graphs. The largest magnitude and gradient of the longitudinal residual stresses are found at Points D and D', which are the locations of the weld centres as well. Similarly, there are only small differences in both the magnitude and the gradient along the perimeter of the section, but there are some differences in the compressive residual strains between Points D to D' of these two models. In the half model, the compressive strains are found to be constant at -0.081 % from one weld to another, i.e. from Points D to D', due to symmetry of the section. But the compressive strains from Points D to D' are found to decrease from -0.074 % to -0.062 %. However, this variation in the residual strains along the flat plate is considered so small that it does not affect the overall residual strains of the section, and, thus, it effects could be ignored.

It is found that the results from the half models and those from the full models are very similar to one another, and only very small differences in the residual stresses are found within the flat plates in Section S3B. In summary, a half model is shown to be able to predict the residual strains with the same level of accuracy as a full model does, but the computational time is significantly decreased. It is recommended to employ half models to carry out the mesh convergence study, and also the investigations for the sequentially-coupled thermomechanical analyses.

b) Mesh convergence study

A mesh convergence study is carried out on Section S3A, to find out proper mesh sizes achieving a balance between accuracy and computational efficiency for the sequentially-coupled thermomechanical analyses of all four CFSHS. Fig. 6.15 shows three models with coarse to fine meshes. Different layers are provided across the plate thickness, i.e. three layers, four layers and six layers, respectively. The longitudinal residual stresses due to transverse bending shown in Fig. 6.11 b) are divided into the corresponding numbers of layers, and thus, incorporated into the corner regions of these three models with different mesh sizes. Fig. 6.16 shows the various through-thickness distributions of the longitudinal residual stresses at the corner regions of these three models.

Table 6.4 summarizes the programme and the results of the mesh convergence study. It is found that, with an increase in the numbers of the total elements, the computational time increases considerably. Fig. 6. 17 presents direct comparisons on the temperature fields and the longitudinal residual strains among the three models with different mesh sizes. Obviously, the mesh sizes have significant influences on the temperature fields in the heat transfer analyses, as shown in graph a). But the mesh sizes have some minor influences on the longitudinal residual strains, as shown in graph b). To precisely evaluate convergence of these three models with different mesh sizes, the maximum residual strains in each model are identified and compared. As presented in Table 6.4, the maximum tensile strain on the inner surface, $\varepsilon_{t,in,max}$, and the maximum compressive strain on the inner surface, $\varepsilon_{c,in,max}$, are selected as indicators to evaluate the convergence of the models with three mesh sizes. Fig. 6.18 shows the longitudinal residual strains on both surfaces. Since Section S3A is double-symmetrical, the results of only half a section is presented, from Points A to A'. For $\varepsilon_{t,in,max}$, there are very small variations among these three models, and the residual strains range between 0.379 % to 0.391 %. It is shown that the mesh sizes do not affect the tensile residual strains due to longitudinal welding. However, for $\varepsilon_{t,in,max}$, the variations among these three models are found to be quite large, and the residual strains range between -0.115 % to -0.164 %. These maximum compressive strains are all found at the corner regions with $R_{in}/t = 3.0$. It should be noted that the longitudinal strains change significantly through the plate thickness, and, in particular, the strains are found to be very small on both surfaces. Hence, a model with coarse mesh sizes may overestimate the strains on the inner surfaces.

It is found that the results from the models with three different mesh sizes are very similar to one another, and only very small differences in the residual strains are found at the corner regions because of the variation of the through-thickness residual strains due to transverse bending. In summary, considering a balance between accuracy and computational efficiency, Mesh B@5.0 is regarded to be the most qualified among the three models. And, this meshing strategy is employed for further investigations of the other three CFSHS in the sequentially-coupled thermomechanical analyses.

6.5.5 Numerical results

Table 6.5 summarizes the dimensions and the mesh sizes of four models. As convergence of Section S3A is fully checked in Section 6.5.4, it is proposed to adopt the equal meshing strategy for Section S3B, and to adopt the matched mesh sizes for Sections S1A and S1B by using three-layer, i.e. 2 mm per layer. Hence, the convergence of all these four sections are satisfied.

Fig. 6.19 shows the longitudinal stresses at the mid-length before and after welding in Sections S1A and S1B. The three-layer stresses due to transverse bending in Fig. 6.11 are incorporated into these models as their initial stress states. To accurately simulate the welding processes, the two-pass welding is realized with the “birth-and-death” technique, and each welding pass is activated sequentially with their welding parameters summarized in Table 6.3. After simulating the processes of welding and cooling with the thermomechanical analyses, the welds are filled into the grooves, and the residual stresses are successfully generated.

Similarly, Fig. 6.20 shows the longitudinal stresses at the mid-length before and after welding in Sections S3A and S3B. After following the simulation procedure described in the last paragraph, their residual stresses are successfully generated.

a) Temperature histories

With incorporation of the welding parameters, the double-ellipsoidal heat source model and the temperature-dependent thermomechanical properties of the steel, the heat transfer analyses are able to predict the temperature histories with a high level of accuracy. During welding, an infrared camera is employed to record the temperature histories for each welding pass at a location 15 mm away from the weld centres of Section S3A and S3B. Therefore, the temperature histories predicted with the numerical models are directly compared with those measured by the infrared camera as illustrated in Fig. 6.21. It should be noted that some sudden changes of temperatures during welding are captured by the infrared camera as shown in the both graphs. Some changes result from the flame heating between two welding passes, to maintain the interpass temperatures, as shown in graph b). The other sudden changes of temperatures shown in these graphs are due to the inevitable blocks by the welder, as the welder needs to move along the specimen while welding, and thus, acquisition of temperatures may be disturbed. Hence, some dash lines are plotted onto the graphs, to eliminate these sudden changes of temperatures and to demonstrate a direct comparison between the predicted and the measured temperature histories.

For Section S3A shown in graph a), the peak temperatures measured by the infrared camera are 349, 346 and 484 °C in sequence while the peak temperatures predicted with the numerical models are 306, 356 and 486 °C in sequence. For Section S3B shown in graph b), the peak temperatures measured by the infrared camera are 259, 304 and 361 °C in sequence while the peak temperatures predicted with the numerical models are 196, 304 and 437 °C in sequence.

In summary, it is considered that the temperatures predicted with these two numerical models are fairly close with those measured by the infrared camera.

b) Residual strains and residual stresses

The longitudinal residual stresses of Sections S3A and S3B measured with the sectioning method are presented in Chapter 3, and the measurements are readily compared with the numerical results predicted with the sequentially-coupled thermomechanical analyses.

It should be noted that the longitudinal residual stresses across a CFSHS should be self-equilibrant. To evaluate the residual stresses measured with the sectioning method and those predicted with the thermomechanical analyses, the total tension forces and the total compression forces across the sections are calculated, respectively. The residual stresses used for evaluating force equilibrium are taken to be the average values of both surfaces, i.e. the membrane residual stresses. As summarized in Table 6.6, the force equilibrium in each section is evaluated by presenting the total tension force of the section, F_T, the total compression force of the section, F_C, the resultant force of the section, F_R, and the ratio of $F_R / (F_C - F_T)$.

- For Section S3A measured with the sectioning method, i.e. Test "S3A-Sectioning", the resultant force, F_R, is found to be -92 kN while the ratio of $F_R / (F_C - F_T)$ is found to be 15.8 %.
- For Section S3A predicted with the thermomechanical analysis, i.e. Model "S3A-FEM", the resultant force, F_R, is found to be -34 kN while the ratio of $F_R / (F_C - F_T)$ is found to be 2.9 %.
- For Section S3B measured with the sectioning method, i.e. Test "S3B-Sectioning", F_R is found to be -96 kN while $F_R / (F_C - F_T)$ is found to be 25.0 %.
- For Section S3B predicted with the thermomechanical analysis, i.e. Model "S3B-FEM", F_R is found to be -15 kN while $F_R / (F_C - F_T)$ is found to be 1.5 %.

According to the ratios of $F_R / (F_C - F_T)$ summarized in Table 6.6, it is evident that the numerical results achieve a higher level of force equilibrium across the sections, when compared with those measured with the sectioning method.

The major differences between the predicted and the measured results lie in the tensile residual stresses in the vicinity of the welds. It is considered that the total compression forces are significantly underestimated by the sectioning method. Theoretically, the ratios of F_R / (F_C – F_T) in both FEM should be zero, but the resultant forces of both sections are shown to be in compression. A pilot study carried out by the author shows that, a sequentially-coupled thermomechanical without any residual stress due to transverse bending achieves force equilibrium very well, i.e. F_R / (F_C – F_T) is equal to about zero. However, incorporation of the non-uniform through-thickness residual stresses due to transverse bending modifies the state of the force equilibrium of the membrane residual stresses. Moreover, the four cold-bent corners in Model S3A-FEM show this effect, when compared with only two cold-bent corners in Model S3B-FEM. That is why a larger ratio of F_R / (F_C – F_T) is found in Model S3A-FEM than that in Model S3B-FEM.

To make a direct comparison on the residual strains, both the predicted and the measured results are plotted in the same graph, as shown in Figs. 6.22 and 6.23, illustrating the longitudinal residual strains at the mid-length of the sections. Fig. 6.22 shows a comparison between the predicted and the measured results of the longitudinal residual strains in Section S3A, from Points A to A'. One major difference between the results is the tensile residual strain. The tensile residual strain predicted numerically on the outer surface is 0.381 %, which is located at the weld centre of the section, i.e. Point A, while the residual strain measured with the sectioning method at Point A is only 0.139 %. Similar difference is also found on results along the inner surface, with 0.388 % and 0.157 % as the predicted and the measured results. It is apparent that the tensile residual strains are underestimated by the sectioning method.

Another major difference is the large tensile strains at the corner regions measured with the sectioning method, and this is considered as the error of the measuring method. Before cutting a strip from a CFSHS, the outer surface of the strip is under tension at the longitudinal direction, but under compression at the transverse direction. This longitudinal tensile strain is then released after the strip is cut from the section. However, the measured longitudinal strain on the outer surface after cutting is actually larger than its real magnitude. Hence, this is because the cutting also releases transverse compressive strains, as large as $0.5\varepsilon_y$, superimposition into the longitudinal tensile strains on the outer surface due to the Poisson's effect, thus resulting in an overestimated longitudinal strain measured from the outer surface. It should be noted this error cannot be avoided in the sectioning method when large transverse residual strains exist within the measured regions (Huang et al. 2013).

Another comparison on the results of Section S3B is illustrated in Fig. 6.23. It is found that the predicted and measured tensile strains on the outer surfaces at their weld centres, i.e. Point D, are 0.344 % and 0.034 %, respectively. And the predicted and the measured tensile strains on the inner surfaces at their weld centres are 0.378 % and 0.254 %, respectively. Similarly, due to the very large R_R/F_C of Test S3B-Sectioning shown in Table 6.6, it is considered that the tensile residual strains are underestimated by the sectioning method as well. Besides, the overestimated tensile stresses are also considered to be attributed to the error inevitably caused by the sectioning method.

Fig. 6.24 presents the longitudinal residual strains of Sections S1A and S3A. Small differences are found between these two sections, and they are considered to be caused by the differences in the plate thicknesses, the corner radii, the weld sizes and the numbers of layers through the plate thickness. Similar differences are also found between the two curves of Sections S1B and S3B in Fig. 6.25, which are also believed to be attributed to the reasons above.

6.6 Simplified Patterns of Longitudinal Residual Stresses

6.6.1 Simplification of longitudinal residual stresses

The contours of longitudinal residual stresses in Sections S3A and S3B are illustrated in Figs. 6.26 and 6.27, respectively. As shown in the figures, the resultant longitudinal residual stresses predicted with the numerical models consist of two parts, i.e. Part i): the residual stresses at the corner regions due to transverse bending, and Part ii): the residual stresses across the section due to longitudinal welding. The distributions of these two parts of residual stresses are very different. Part i) has a large variation through the plate thickness as shown in Fig. 6.11, but it is basically constant at the same through-thickness location within the corner regions. Part ii) basically distributes uniformly across the plate thickness, but it varies considerably within the section, and the largest tensile residual stresses are found to be in the vicinity of the welds with their magnitudes larger than the yield strengths of the steels.

Due to the different patterns of these two parts of residual stresses in a CFSHS, it is suggested to incorporate these two patterns independently into the models for structural analyses. Chapter 7 demonstrates how to incorporate the initial plastic strains and the residual stresses due to transverse bending into structural analyses. In this Section, the simplified residual stress patterns due to welding are proposed.

Considering the uniform through-thickness distribution of the longitudinal residual stresses in Section S3A, it is proposed to take the average residual stresses among four layers of elements, and these averaged longitudinal residual stresses around the middle surface of the section are shown in Fig. 6.28 a), which are referred as “Full RS”. This pattern is simplified into an approximated one with several polylines according to force equilibrium, and then, it is plotted onto the same graph, which is referred as “Approximated RS”. Moreover, this approximated pattern may be further simplified into “Simplified RS” as shown in Fig. 6.28 b). This simplified pattern consists of two tension zones and one compression zone. Each tension zone takes up a width of 4t in the vicinity of the welds, with its tensile residual stress equal to the yield strength, f_y; and the compression zone takes up the remaining part of the section, with its residual stress equal to $\beta \cdot f_y$. β is readily calculated according to force equilibrium of the whole section, and it is equal to -0.073 in Section S3A.

Similarly, “Full RS”, “Approximated RS” and “Simplified RS” in Section S3B are also proposed, as shown in Fig. 6.29. The simplified pattern has two tension zones and three compression zones. Each tension zone takes up a width of 3.5t in the vicinity of the welds, with its tensile residual stress equal to the yield strength, f_y; each compression zone at the side takes up a width of H - 7.5t, with its compressive stress equal to $\beta_1 \cdot f_y$; and the compression zone at the bottom takes up a width of B - 2t, with its compressive stress equal to $\beta_2 \cdot f_y$. Both β_1 and β_2 are readily calculated according to force equilibrium of the whole section, and they are equal to -0.097 and -0.253, respectively, in Section S3B.

6.6.2 Numerical studies into columns with two different patterns of residual stresses

In order to evaluate the differences between the two residual stress patterns, i.e. Patterns "Full RS" and "Simplified RS", a numerical investigation into columns of various member lengths with Sections S3A and S3B under compression is carried out, as shown in Table 6.7. For each section, six models with three non-dimensional slenderness ratios, $\bar{\lambda}$, are designed to cover the slenderness ratios of the columns tested in Chapter 4. Besides, for each section and each slenderness ratio, both Patterns "Full RS" and "Simplified RS" are incorporated into the analyses, respectively, so the numerical predictions on the member resistances, N_{FEM}, are compared directly. Establishment of these numerical models for columns under compression is demonstrated in detail in Chapter 7, including their material properties, boundary conditions, meshing strategies, geometric imperfections and initial stress-strain characteristics.

For all these 12 models, as shown in Table 6.7, the values of N_{FEM} predicted with two RS patterns are found to be very close, with their errors all smaller than 1 %. Moreover, to have a direct comparison between the load-deformation behaviour of columns with these two different RS patterns, the applied load-axial shortening curves of each member are plotted onto the same graph, as shown in Figs. 6.30 and 6.31. Moreover, for each model, the deformed shapes at three representative stages, i.e. "initial", "peak load" and "critical failure", are illustrated. It is found that the deformed shapes predicted with two different RS patterns are identical at all these stages.

It is fully demonstrated through the numerical results of these columns under compression that there is no significant difference by using Patterns "Full RS" and "Simplified RS" for numerical analyses. Both the two patterns can be adopted to predict the member resistances of various columns to the same level of accuracy. Therefore, it is proposed to adopt the simplified patterns of longitudinal residual stresses in the further numerical investigation in this project, including calibration of the structural models, and parametric studies in Chapter 7. According to force equilibrium, the simplified residual stress patterns for four sections in Series SA and four sections in Series SB are proposed, as summarized in Tables 6.8 and 6.9. Effectiveness of these simplified residual stress patterns is demonstrated in subsequent numerical investigations.

6.7 Conclusions

This Chapter presents a theoretical-numerical investigation into the temperatures and the residual stresses of four S690 CFSHS due to welding. In order to predict the temperature fields and the residual stresses, both the analytical solution and the numerical analyses are developed. The key findings of this investigation are:

- The analytical solution and the numerical method are developed based on the welding parameters, the temperature-dependent thermomechanical properties and the double-ellipsoidal heat source model. The analytical solution is shown to be effective to predict the dimensions of the fusion zones due to welding, which is useful for determining the lengths of the semi-axes adopted in the double-ellipsoidal heat source model.

- The numerical predictions on the residual stresses of the S690 CFSHS through sequentially-coupled thermomechanical analyses are shown to match well with the measurements of the sectioning method, and force equilibrium is well achieved in these residual stresses.

- The simplified patterns of the residual stresses of the S690 CFSHS are developed based on the numerical results of the sequentially-coupled thermomechanical analyses, and these patterns are thus readily adopted as the initial stress states of the numerical models for the structural analyses in Chapter 7.

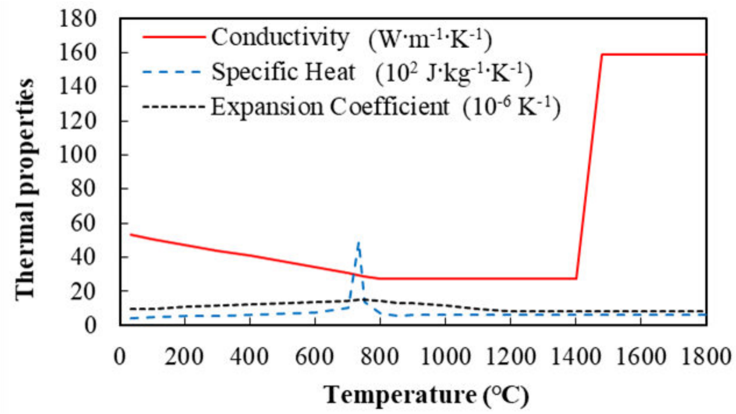

a) thermal properties

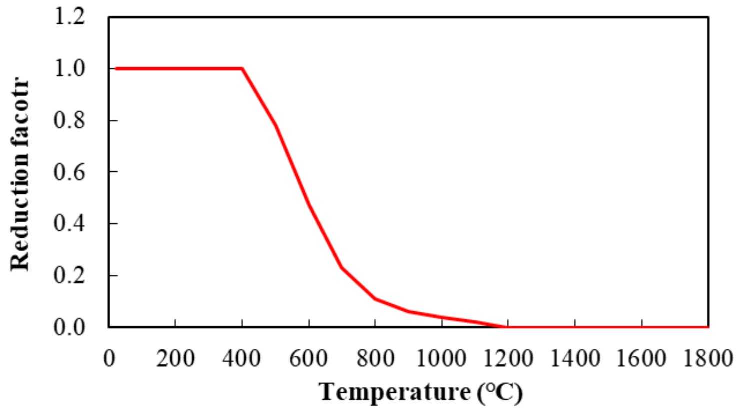

b) yield strength

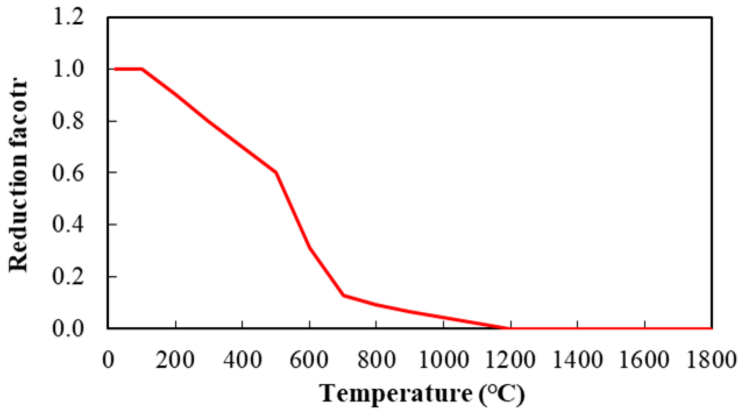

c) Young's modulus

Fig. 6.1 Reduction factors for thermal and mechanical properties of S690 steels at elevated temperatures (CEN 2009b)

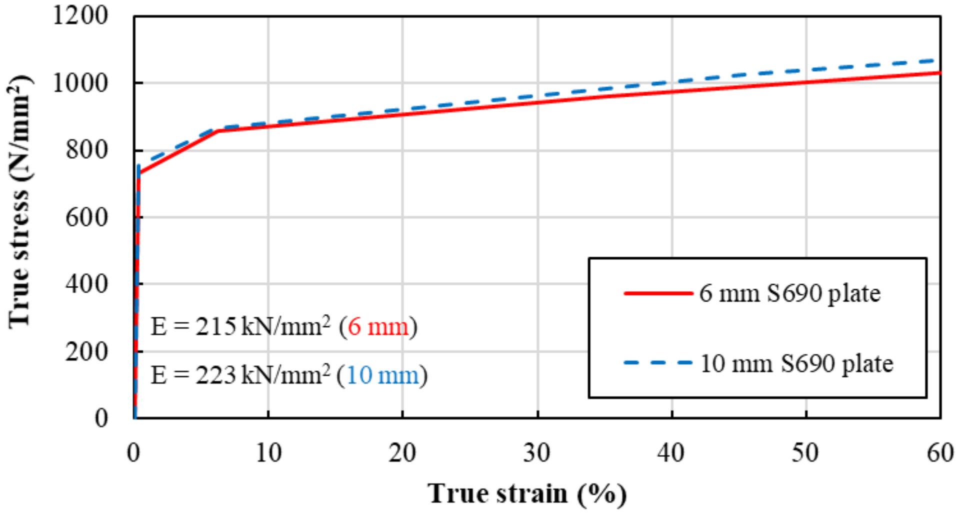

Fig. 6.2 True stress-strain curves at ambient temperatures

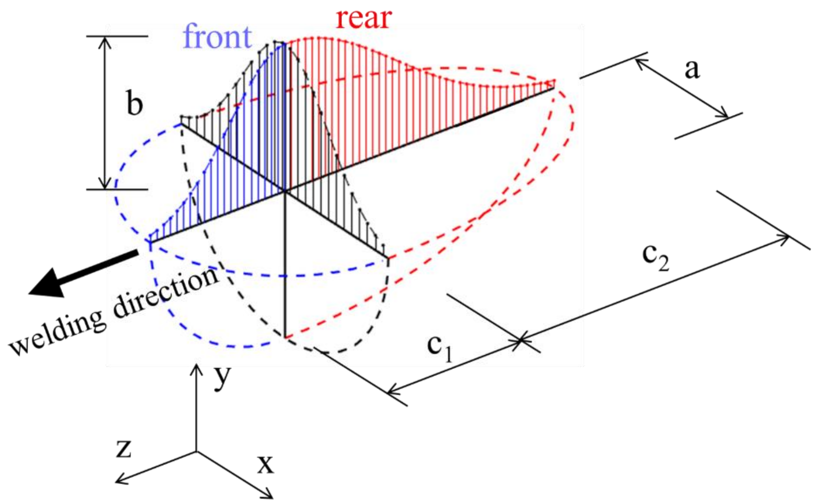

Fig. 6.3 Double-ellipsoidal heat source model (Goldak et al. 1984)

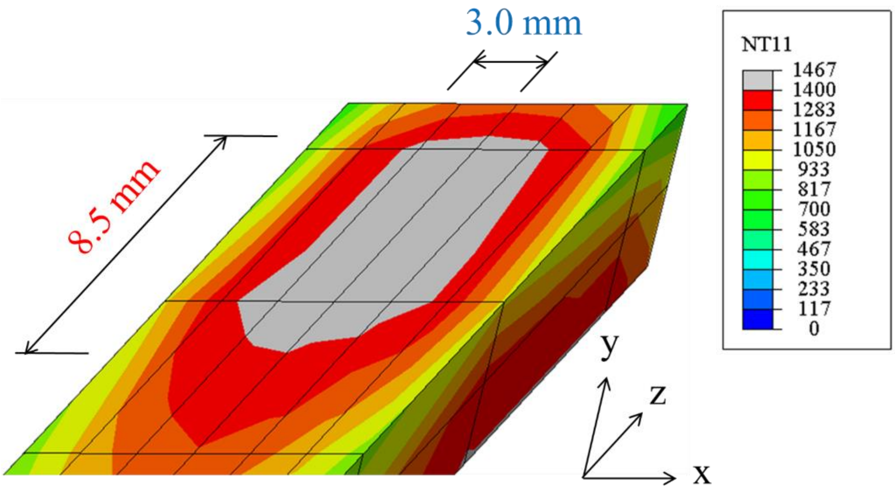

max temperature = 1467 ℃
a) numerical method

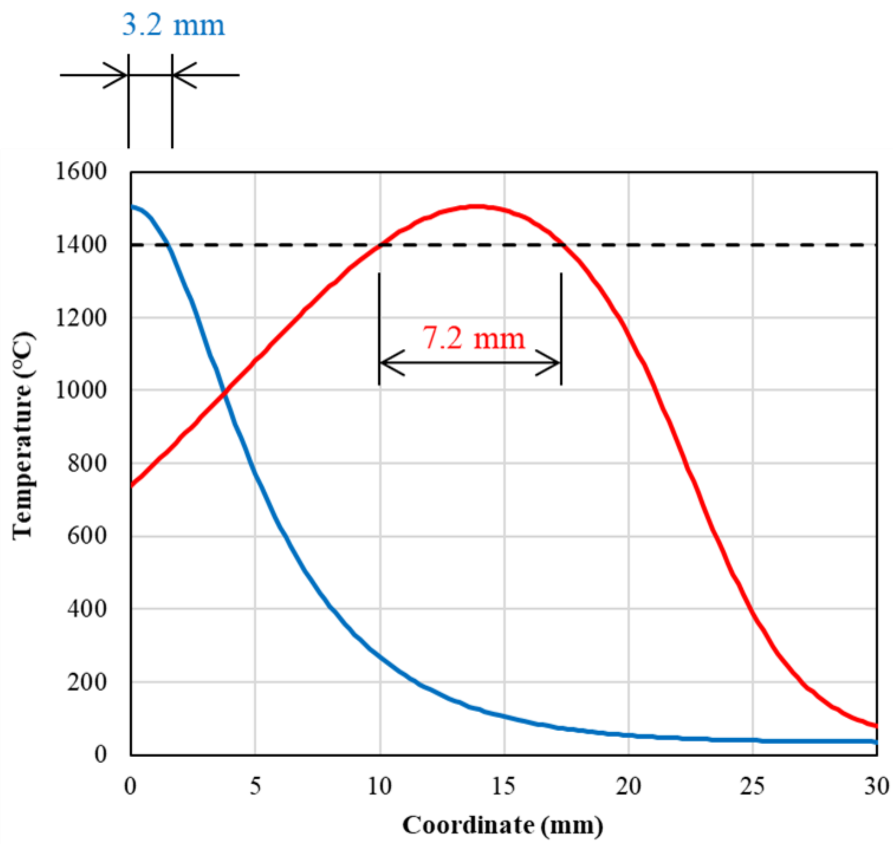

max temperature = 1504 ℃
b) analytical solution

Fig. 6.4 Predicted dimensions of fusion zones

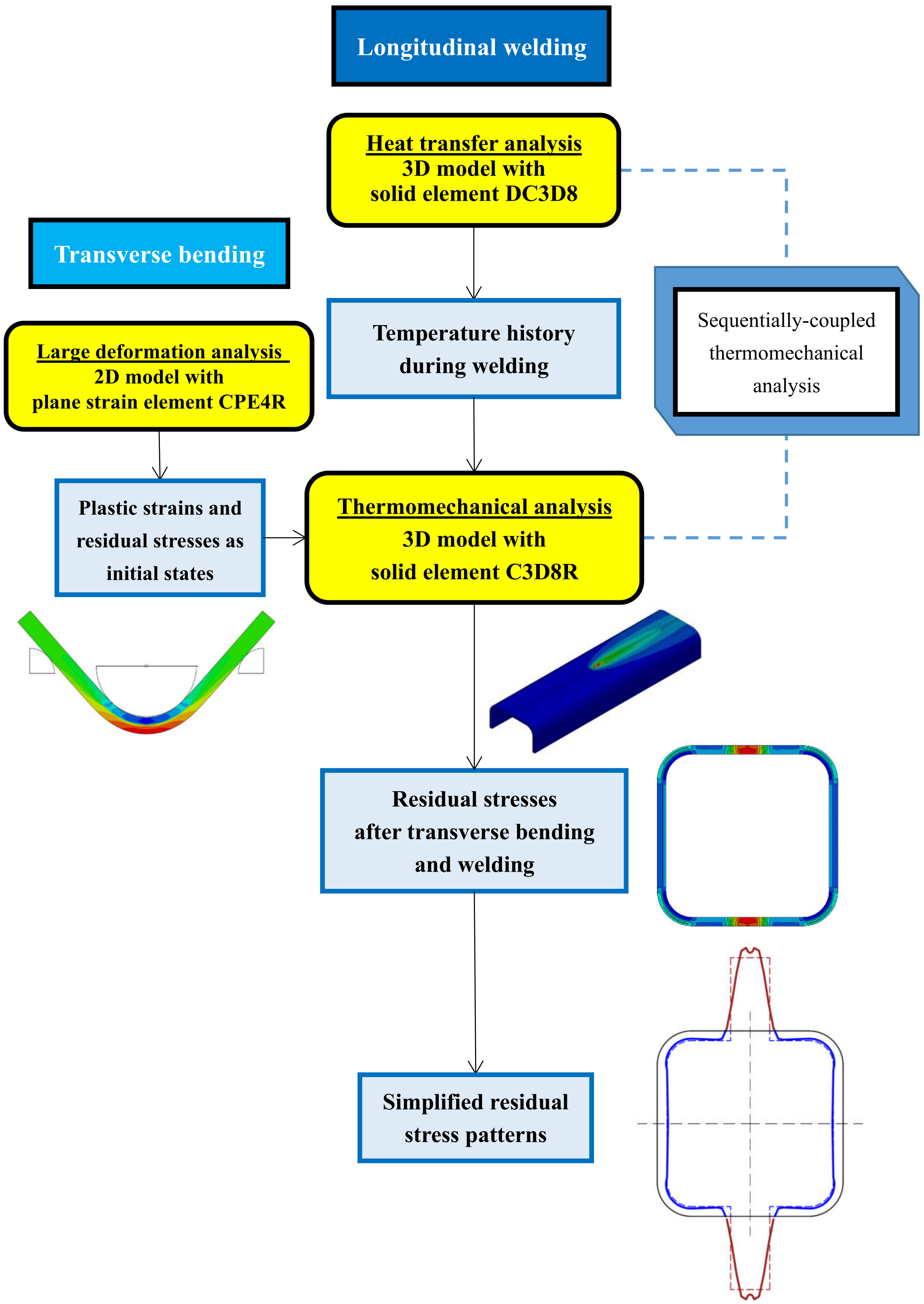

Fig. 6.5 Flowchart of numerical predictions for residual stresses

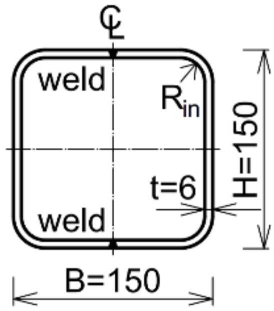

a) Section S1A
6 x 150 x 560

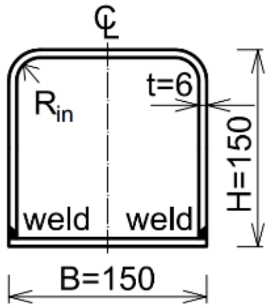

b) Section S1B
6 x 150 x 560

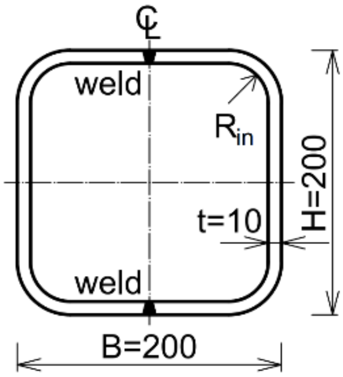

c) Section S3A
10 x 200 x 760

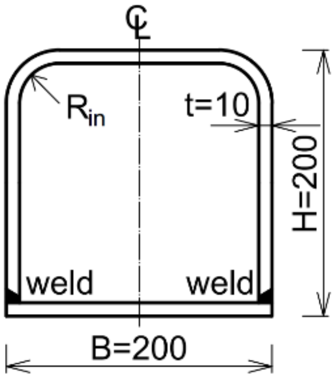

d) Section S3B
10 x 200 x 760

Fig. 6.6 CFSHS for sequentially-coupled thermomechanical analyses

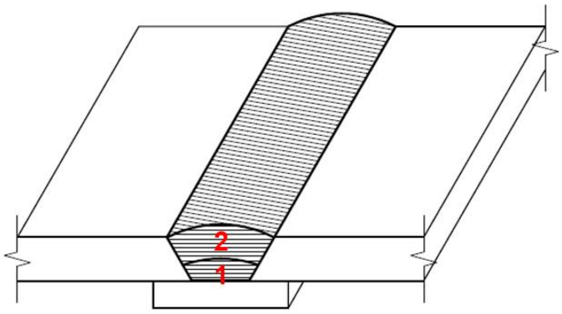

a) Section S1A

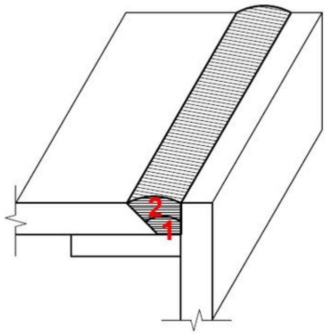

b) Section S1B

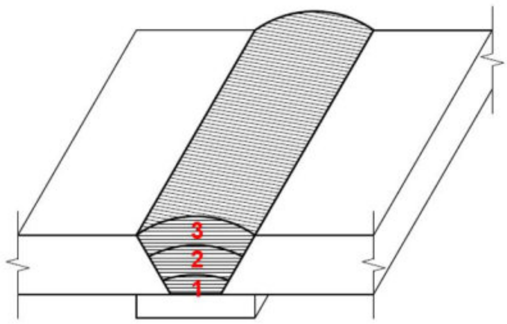

c) Section S3A

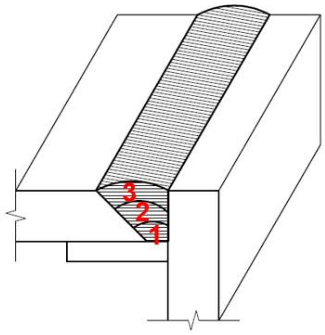

d) Section S3B

Fig. 6.7 Sketches of multi-pass welding in four CFSHS (top welds only)

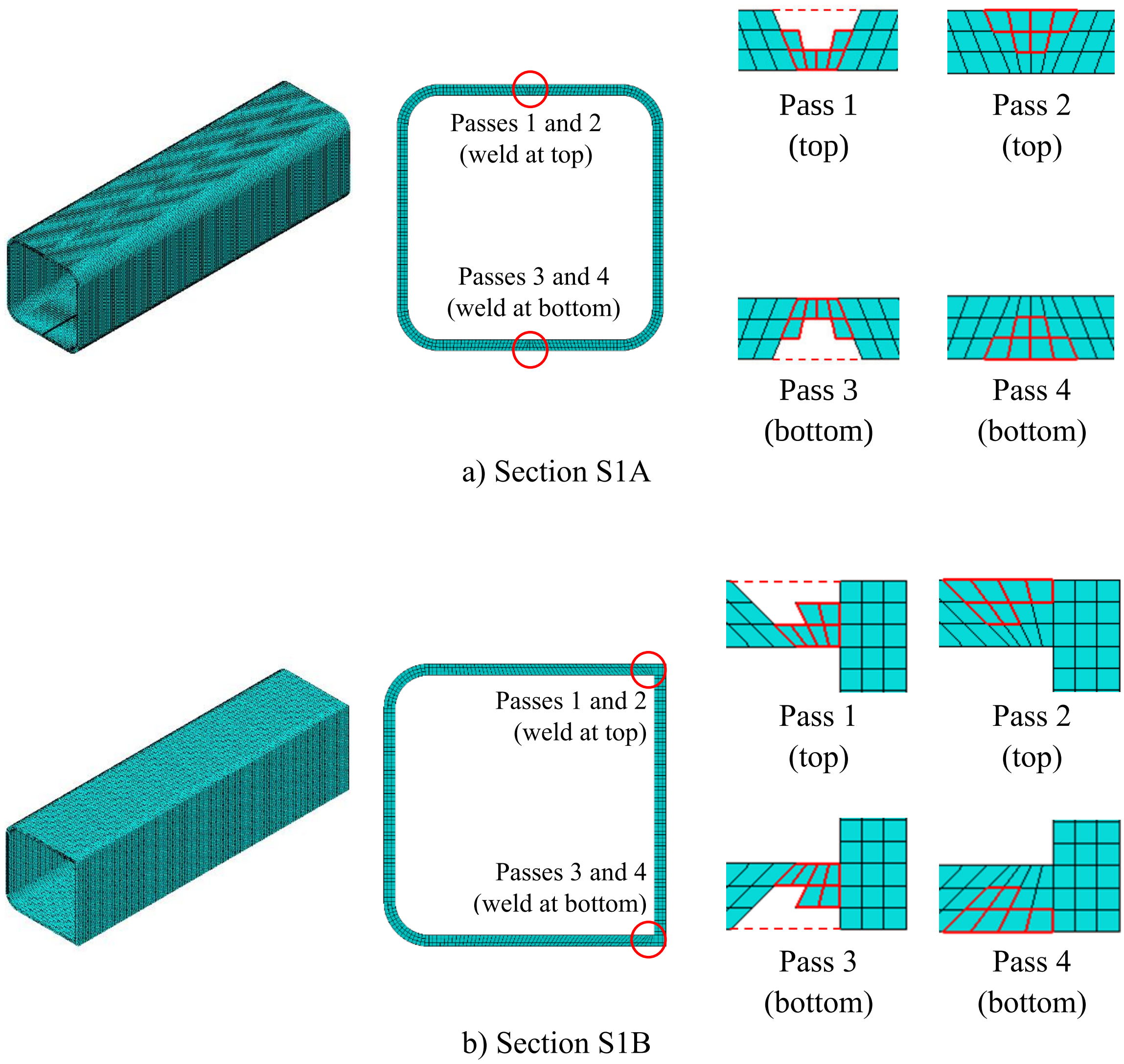

Fig. 6.8 Modelling of multi-pass welding in Sections S1A and S1B

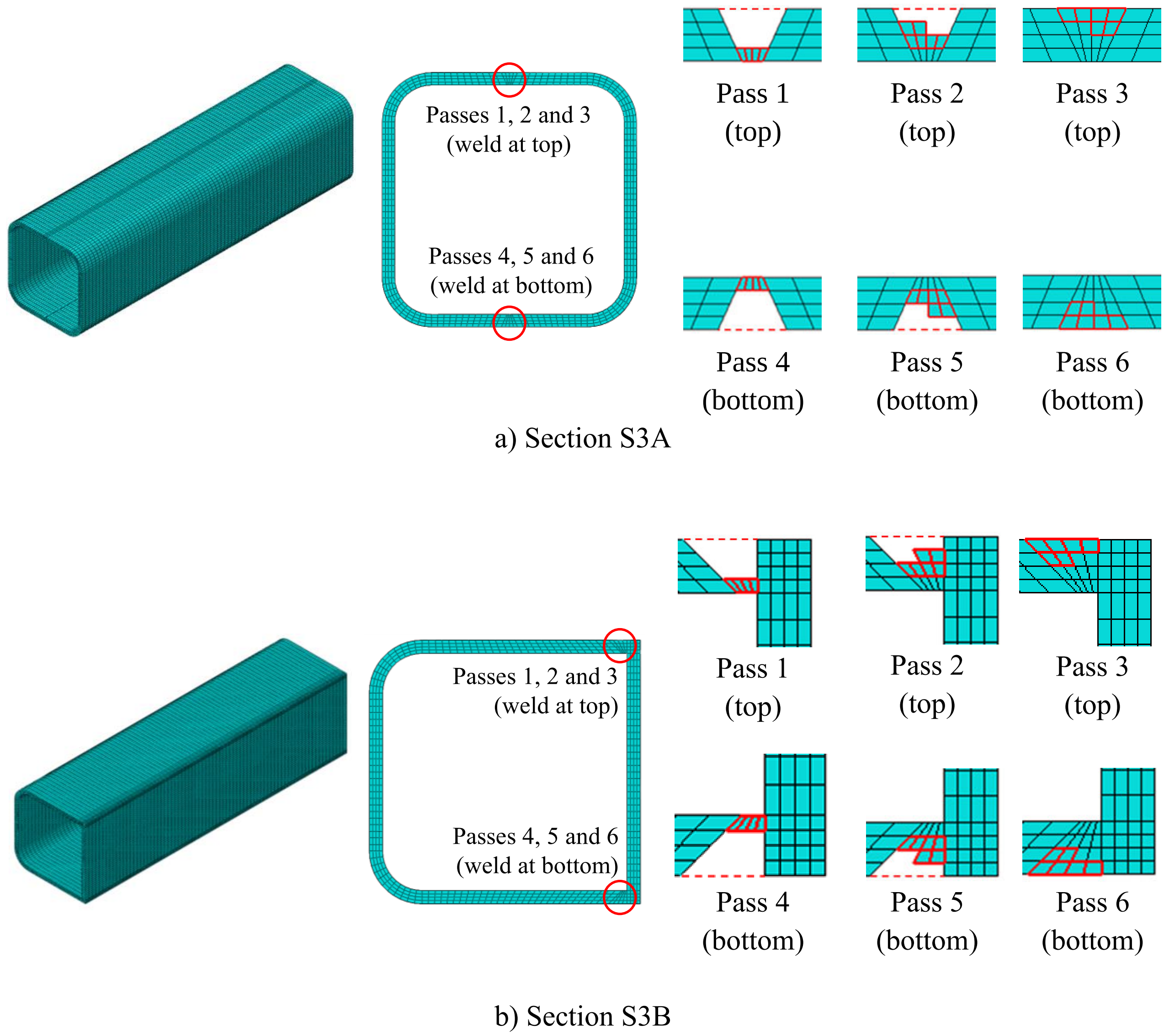

Fig. 6.9 Modelling of multi-pass welding in Sections S3A and S3B

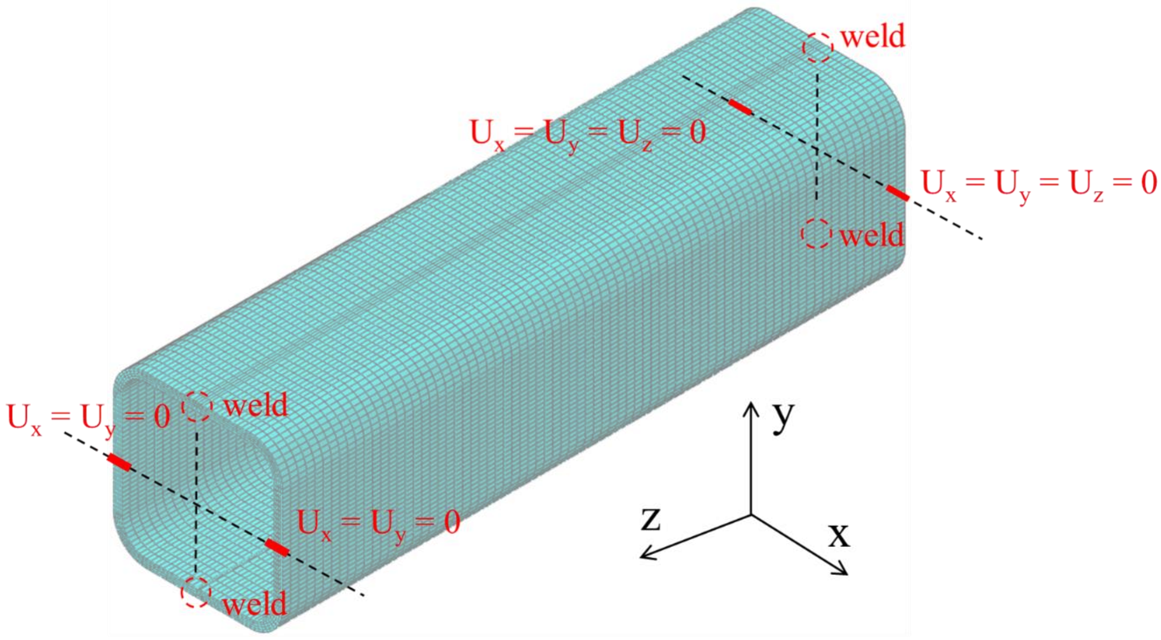

a) Series SA: Sections S1A and S3A

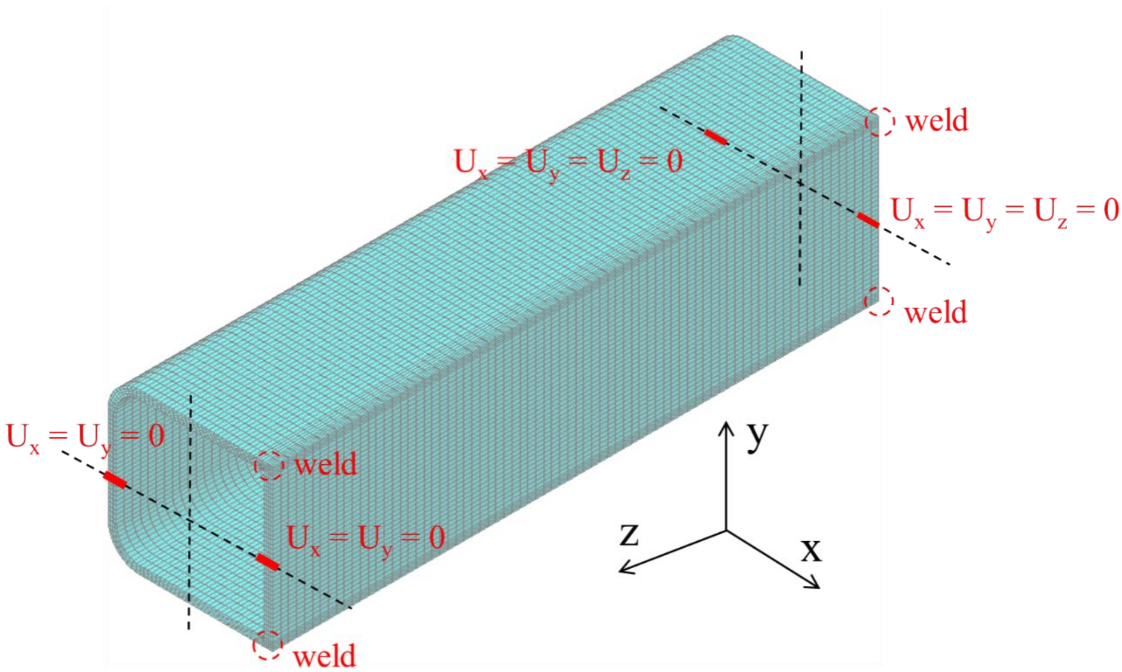

b) Series SB: Sections S1B and S3B

Fig. 6.10 Boundary conditions for thermomechanical analyses

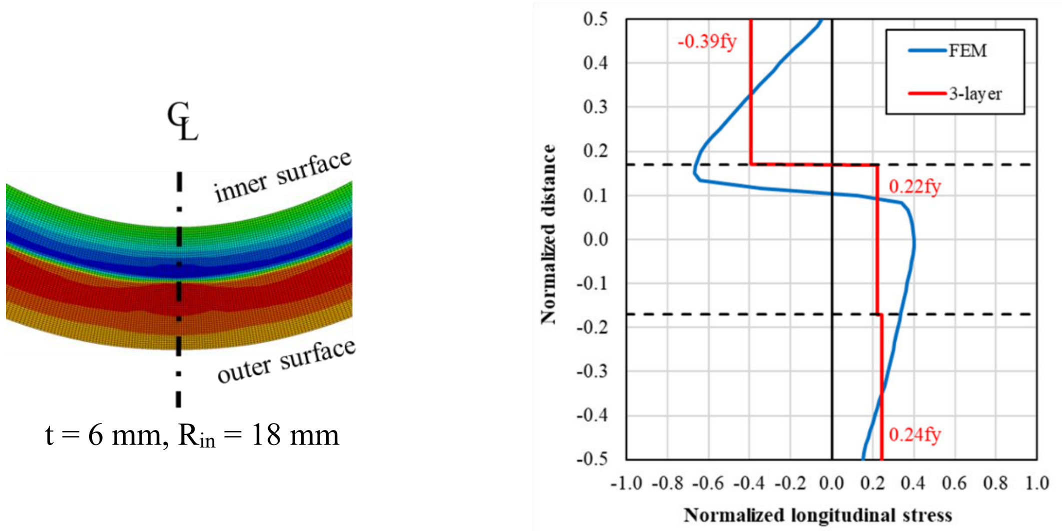

a) at the corner regions of 6 mm plates: Sections S1A and S1B

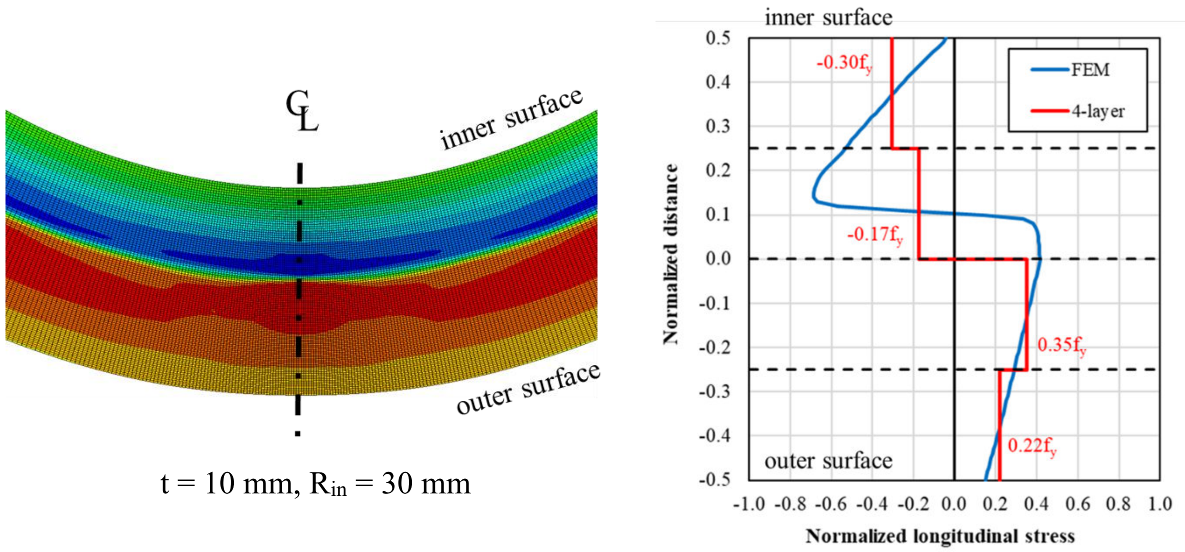

b) at the corner regions of 10 mm plates: Sections S3A and S3B

Fig. 6.11 Longitudinal residual stresses due to transverse bending

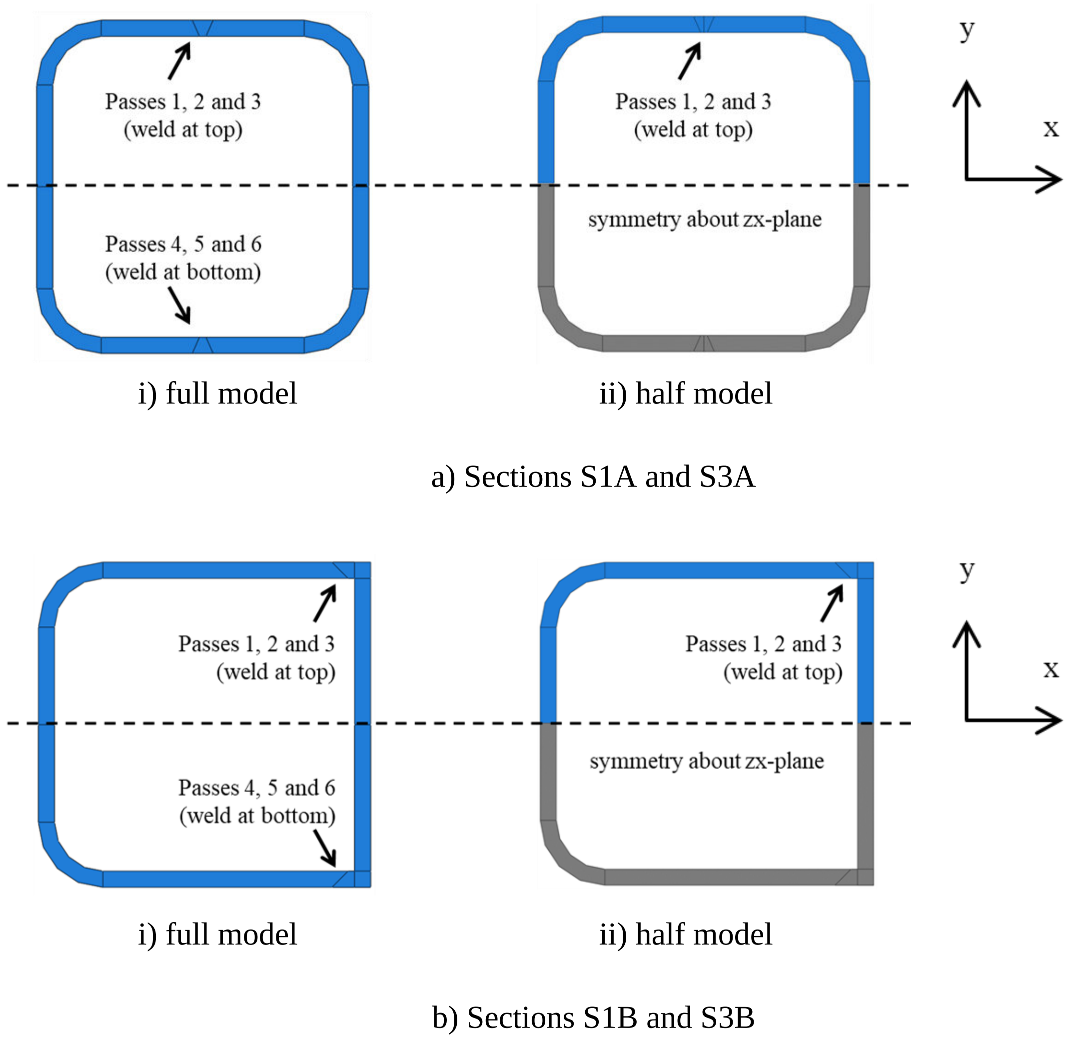

Fig. 6.12 Establishment of full models and half models

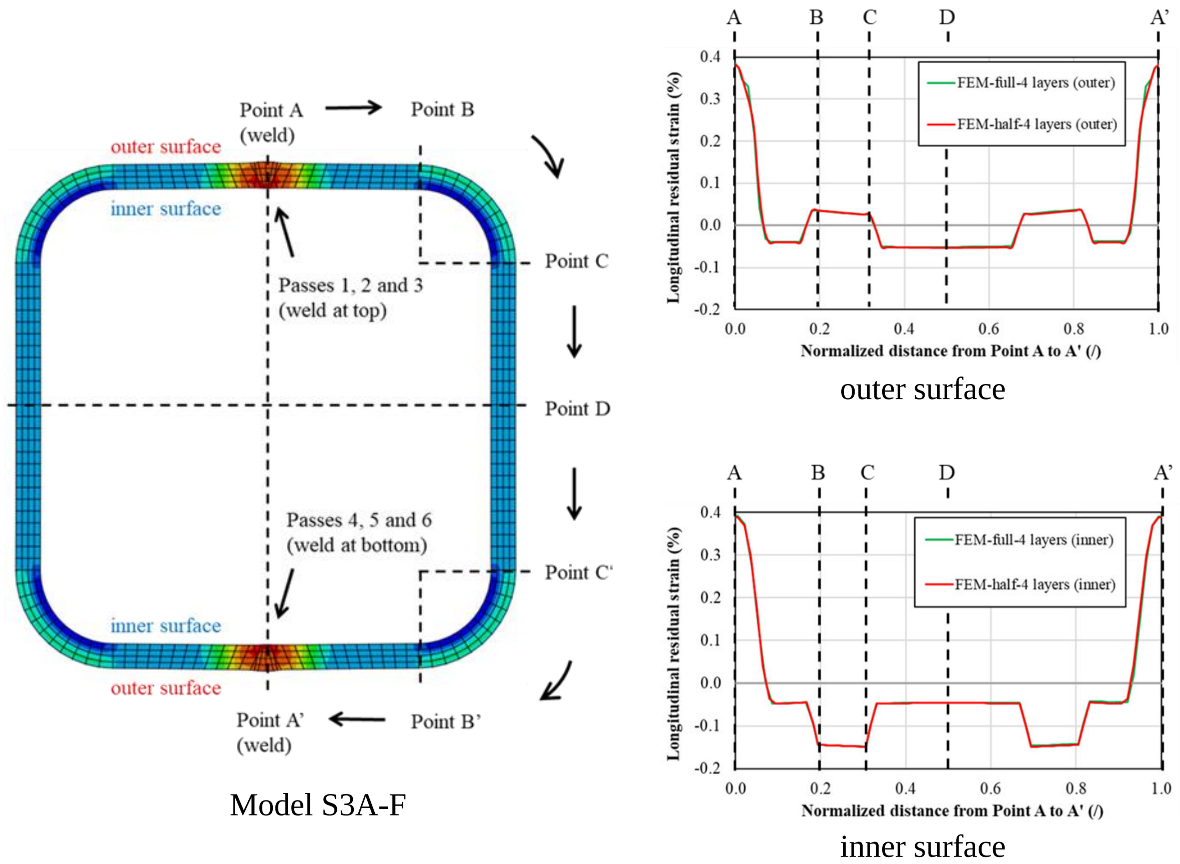

Fig. 6.13 Longitudinal residual strains in Section S3A: full model vs half model

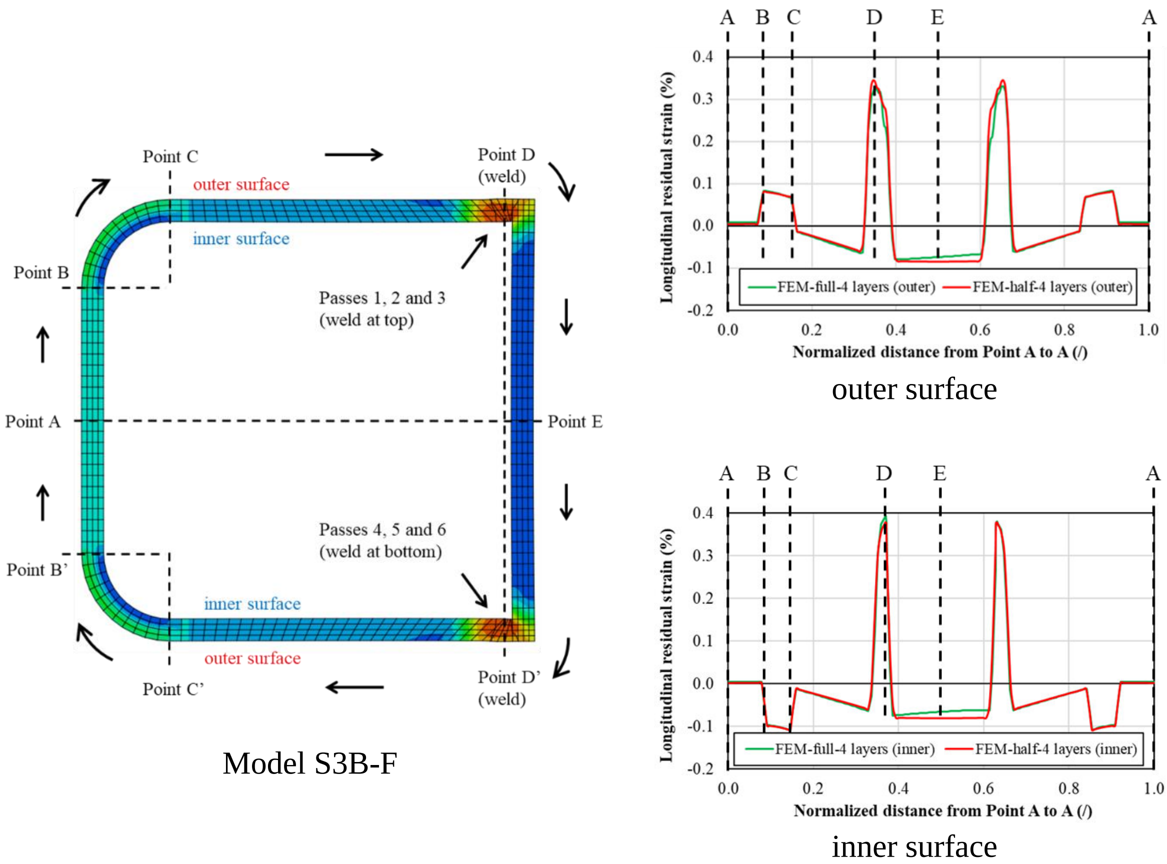

Fig. 6.14 Longitudinal residual strains in Section S3B: full model vs half model

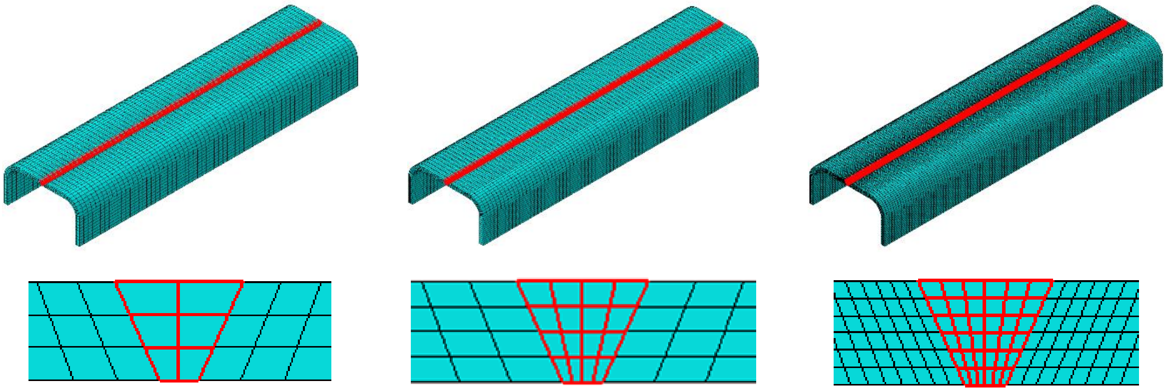

a) Mesh A@6.7 b) Mesh B@5.0 c) Mesh C@3.3

Fig. 6.15 Mesh sizes of mesh convergence study: Section S3A

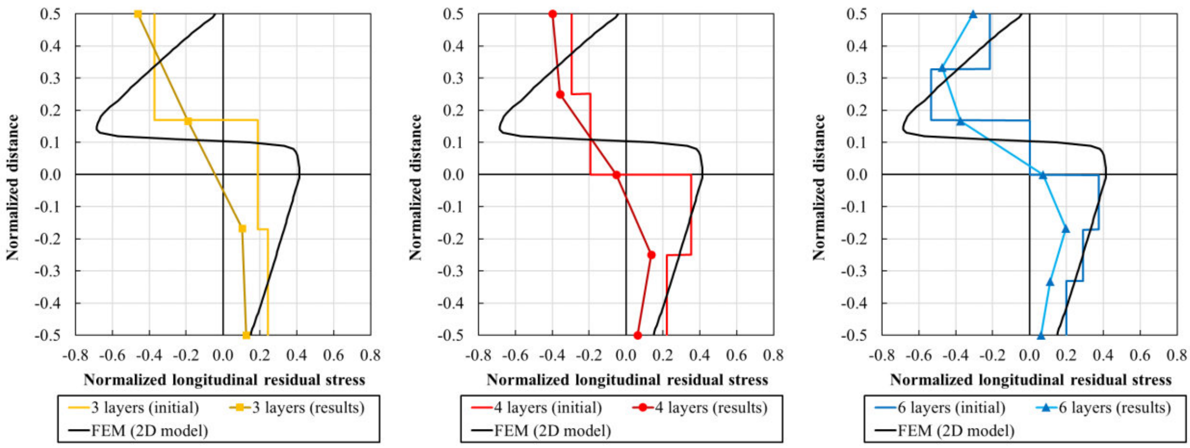

a) Mesh A@6.7 b) Mesh B@5.0 c) Mesh C@3.3

Fig. 6.16 Longitudinal residual stresses due to transverse bending: initial states vs results

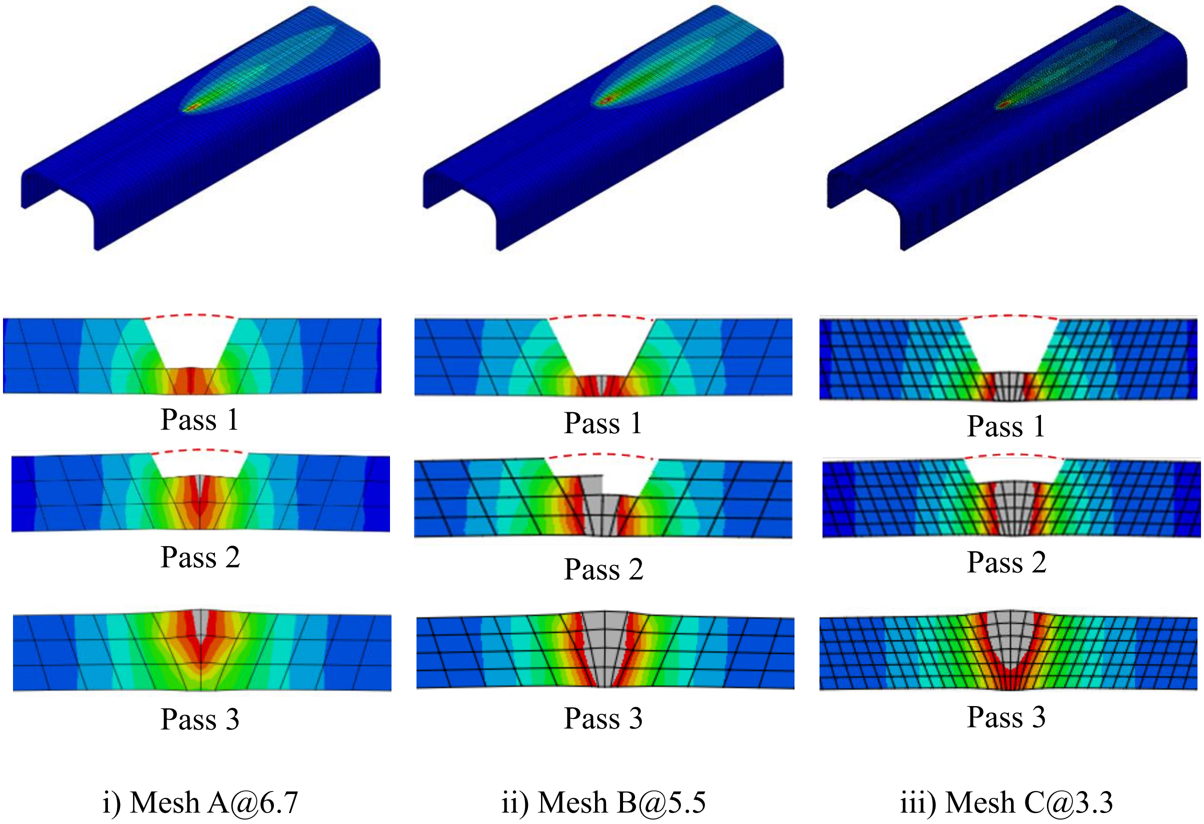

a) temperature fields in heat transfer analyses
(the range of the temperatures: 0 ~ 1400 ℃)

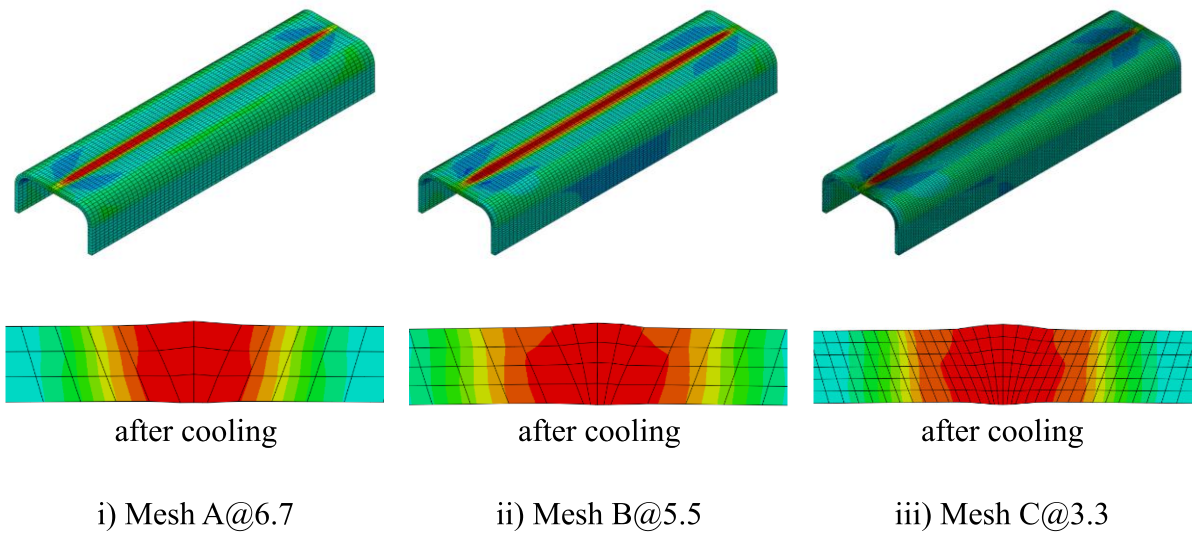

b) longitudinal residual strains in thermomechanical analyses
(the range of the longitudinal residual strains: -0.2 ~ 0.4 %)

Fig. 6.17 Distributions of temperatures and residual strains in the vicinity of welding

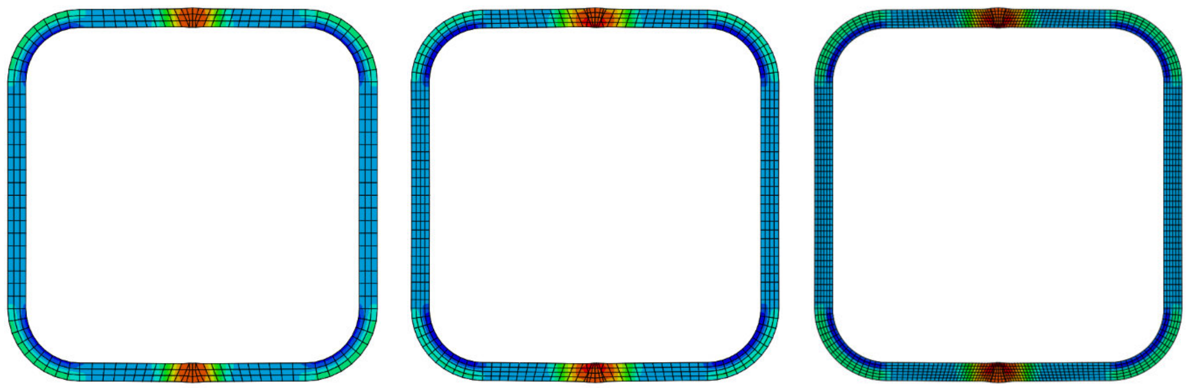

i) Mesh A@6.7 ii) Mesh B@5.5 iii) Mesh C@3.3

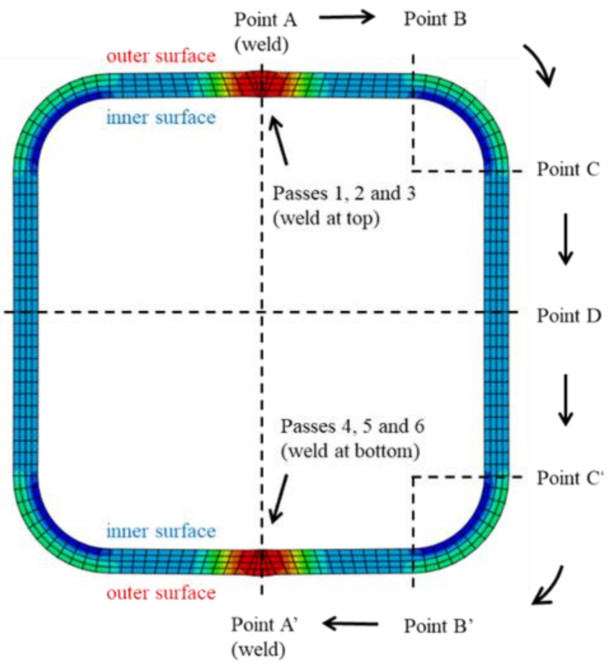

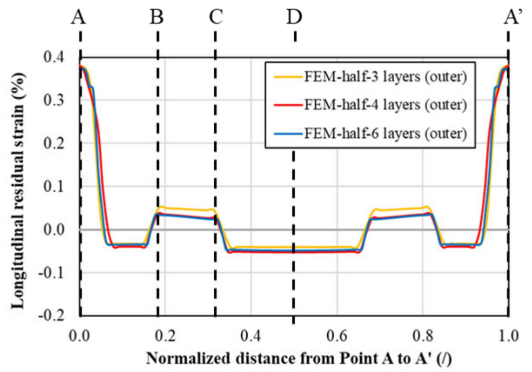

outer surface

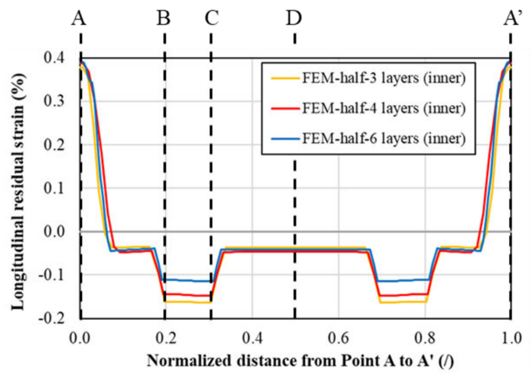

inner surface

Fig. 6.18 Longitudinal residual strains of mesh convergence study: Section S3A

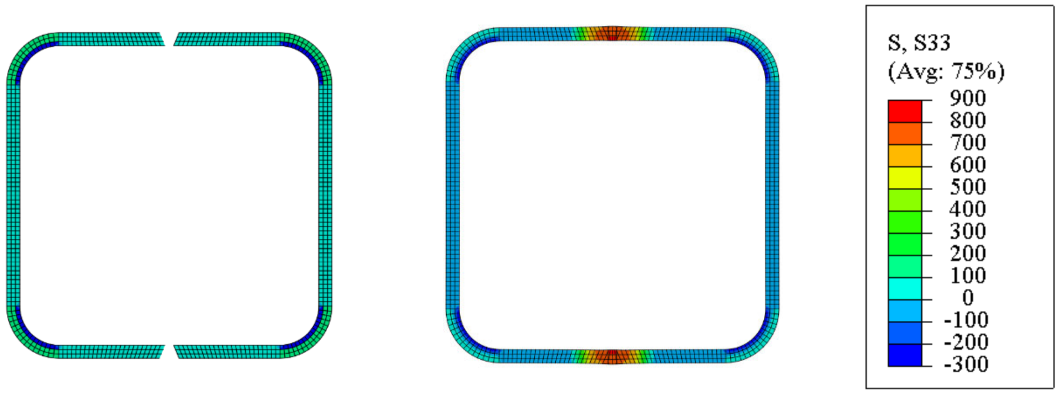

before welding after welding

a) Section S1A

6 x 150 x 560

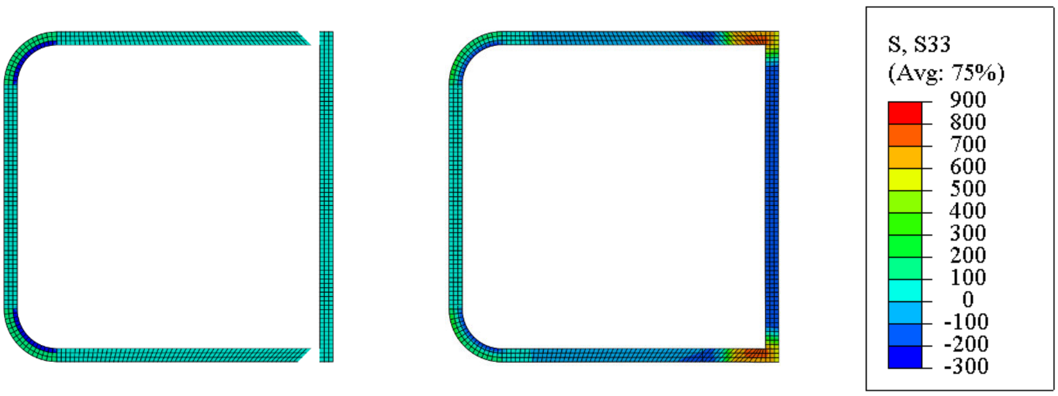

before welding after welding

b) Section S1B

6 x 150 x 560

Fig. 6.19 Longitudinal stresses at the mid-length before and after welding: Sections S1A and S1B

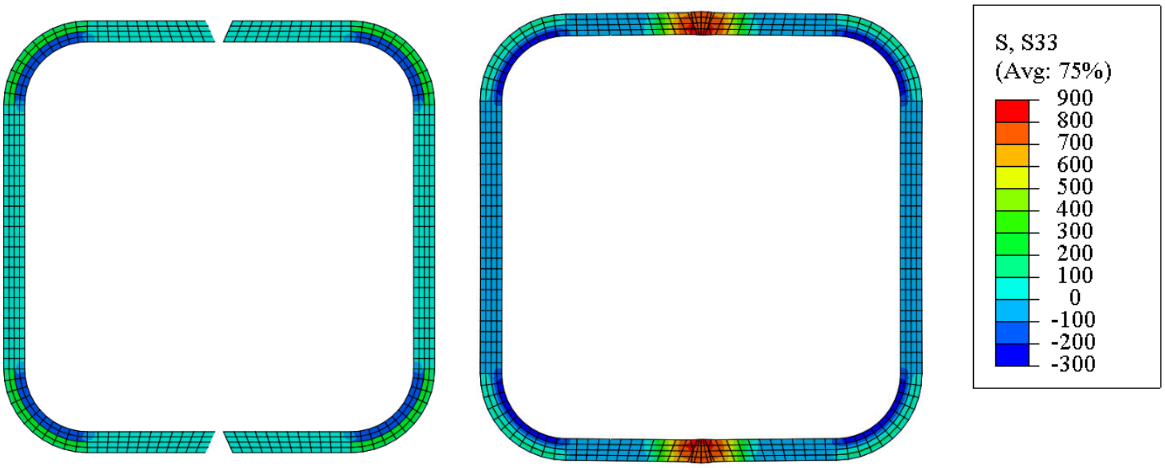

before welding after welding

a) Section S3A

10 x 200 x 760

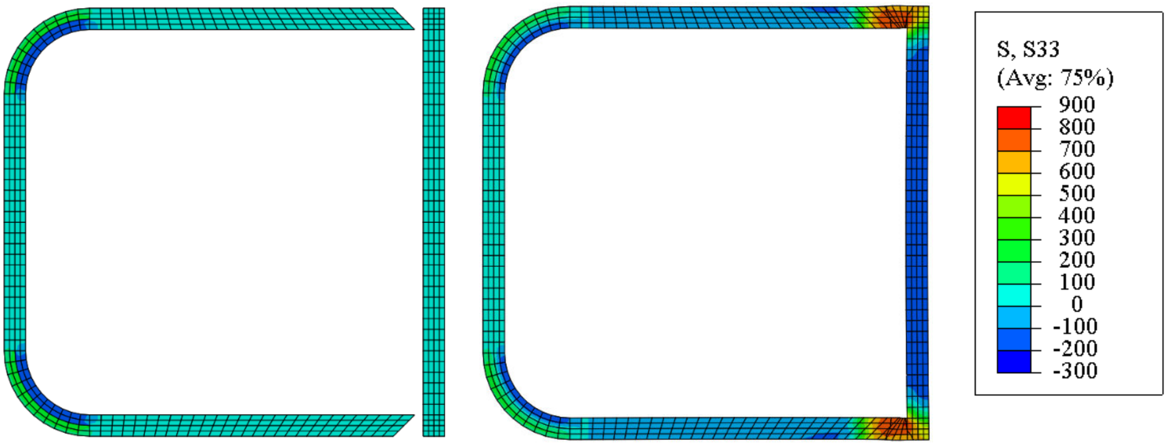

before welding after welding

b) Section S3B

10 x 200 x 760

Fig. 6.20 Longitudinal stresses at the mid-length before and after welding: Sections S3A and S3B

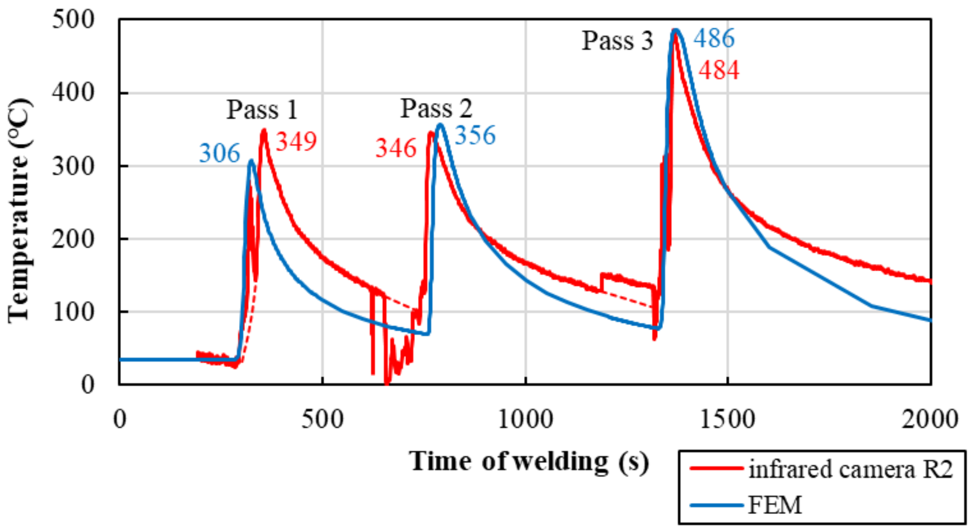

a) Section S3A

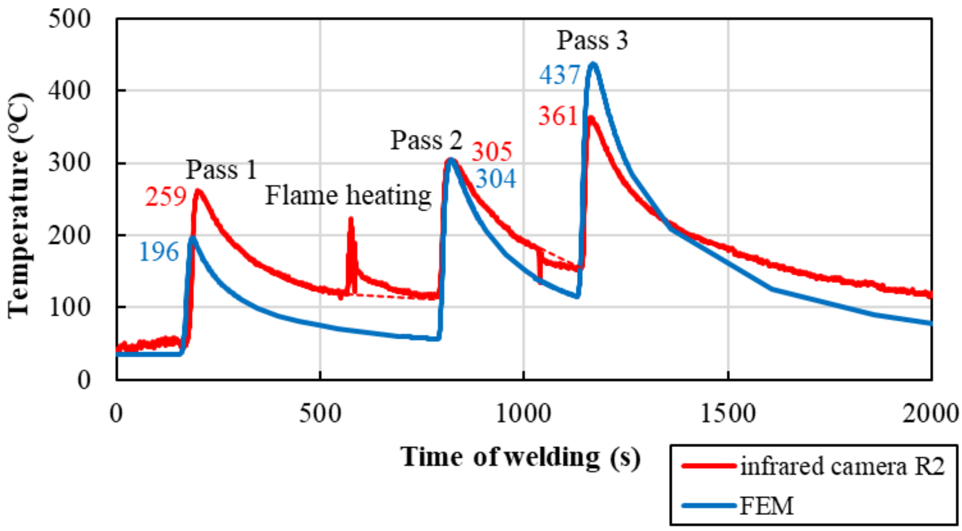

b) Section S3B

Fig. 6.21 Temperature histories at specific locations in Sections S3A and S3B

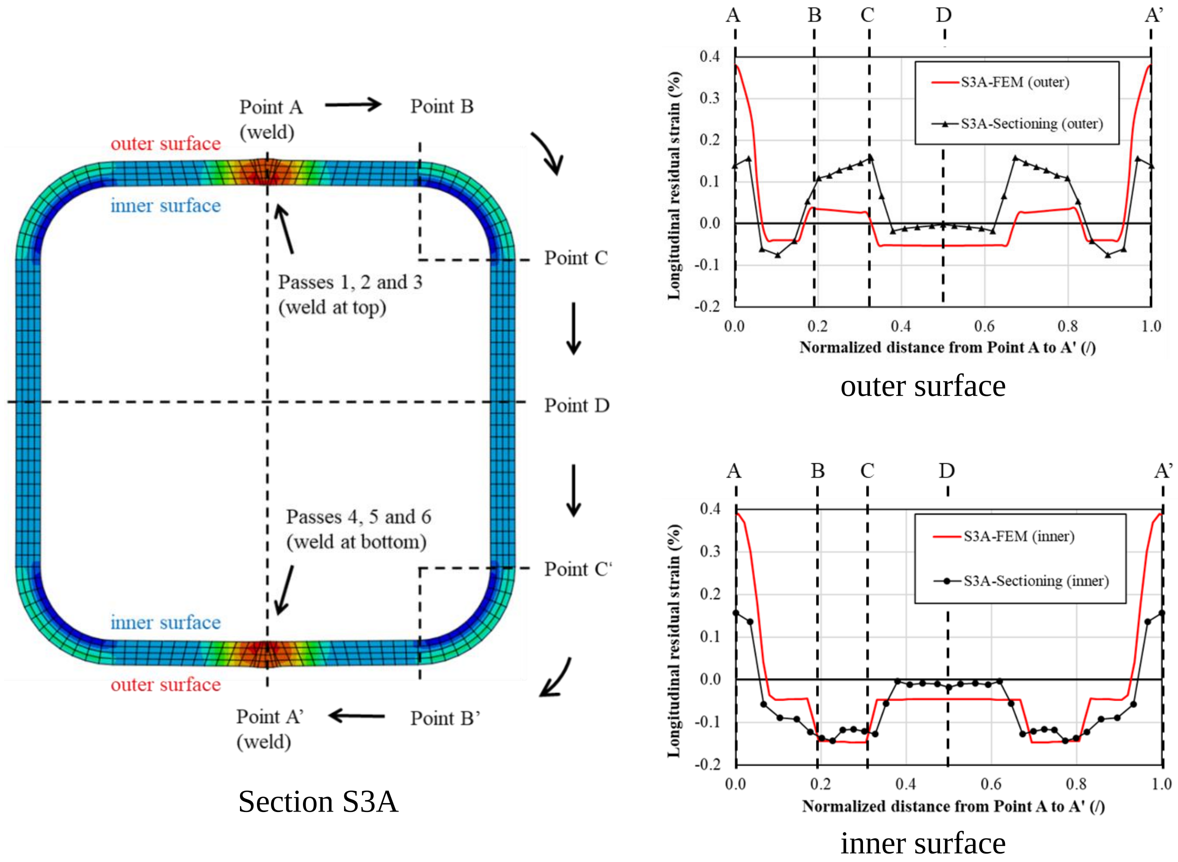

Fig. 6.22 Longitudinal residual strains in Section S3A: FEM vs sectioning method

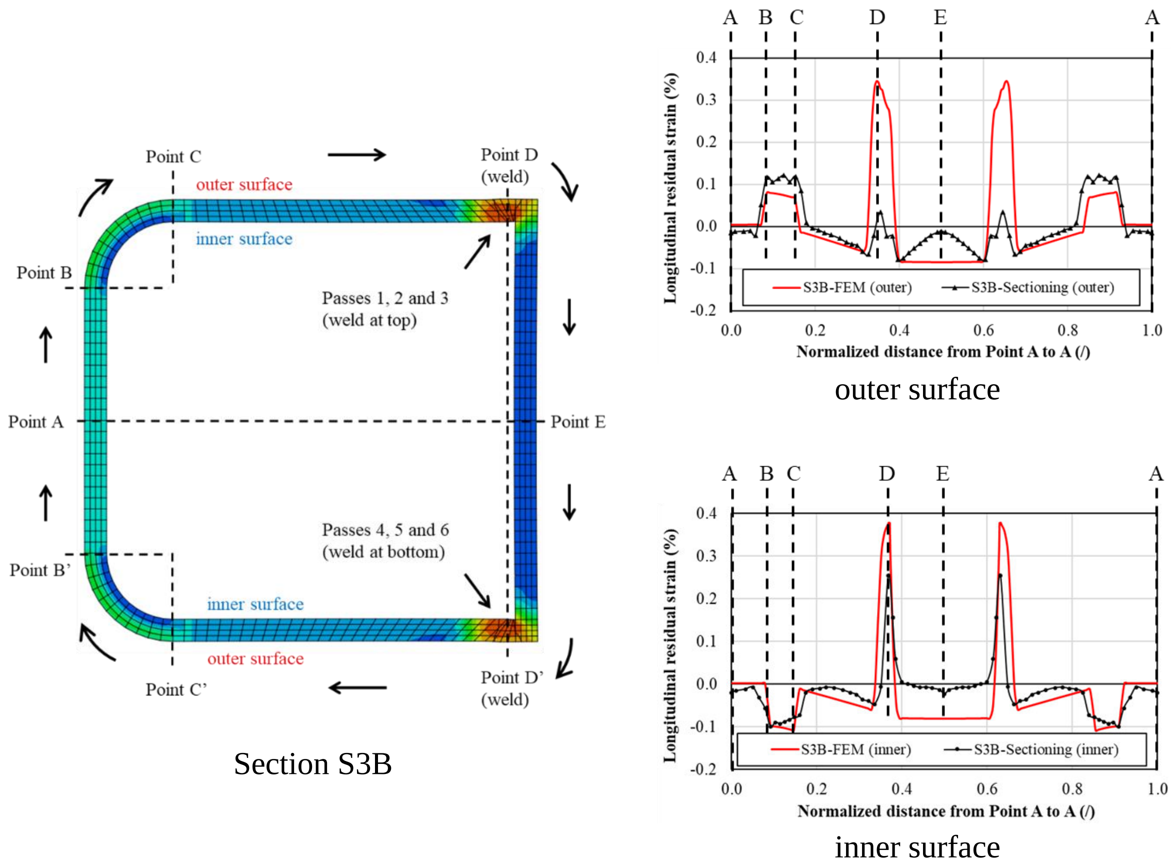

Fig. 6.23 Longitudinal residual strains in Section S3B: FEM vs sectioning method

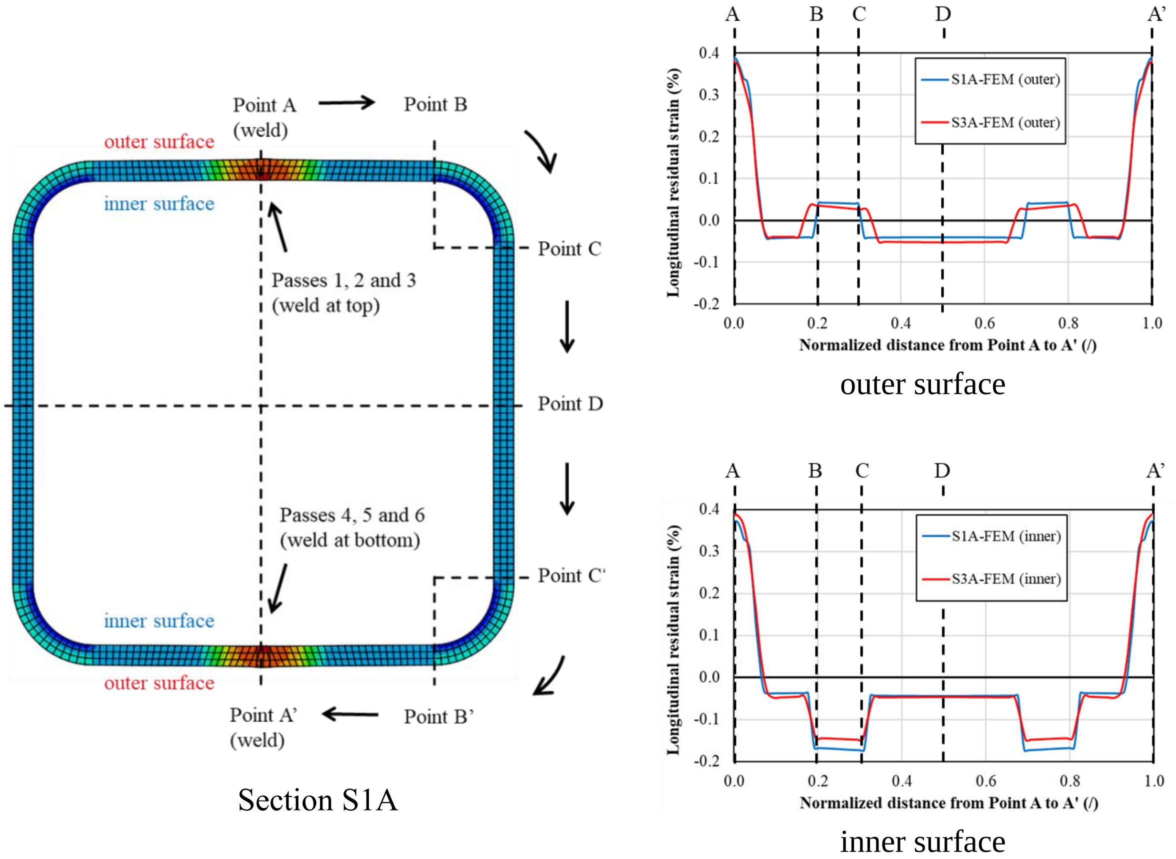

Fig. 6.24 Longitudinal residual strains in Sections S1A and S3A

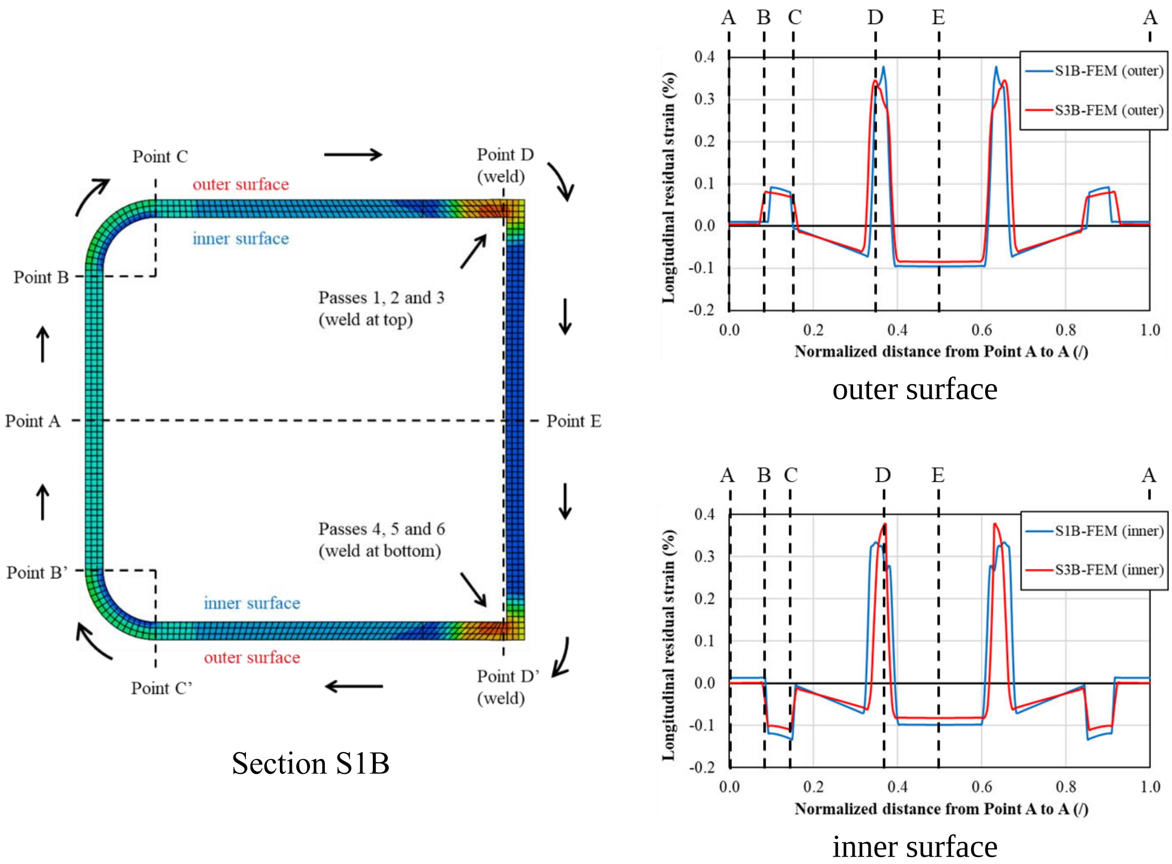

Fig. 6.25 Longitudinal residual strains in Sections S1B and S3B

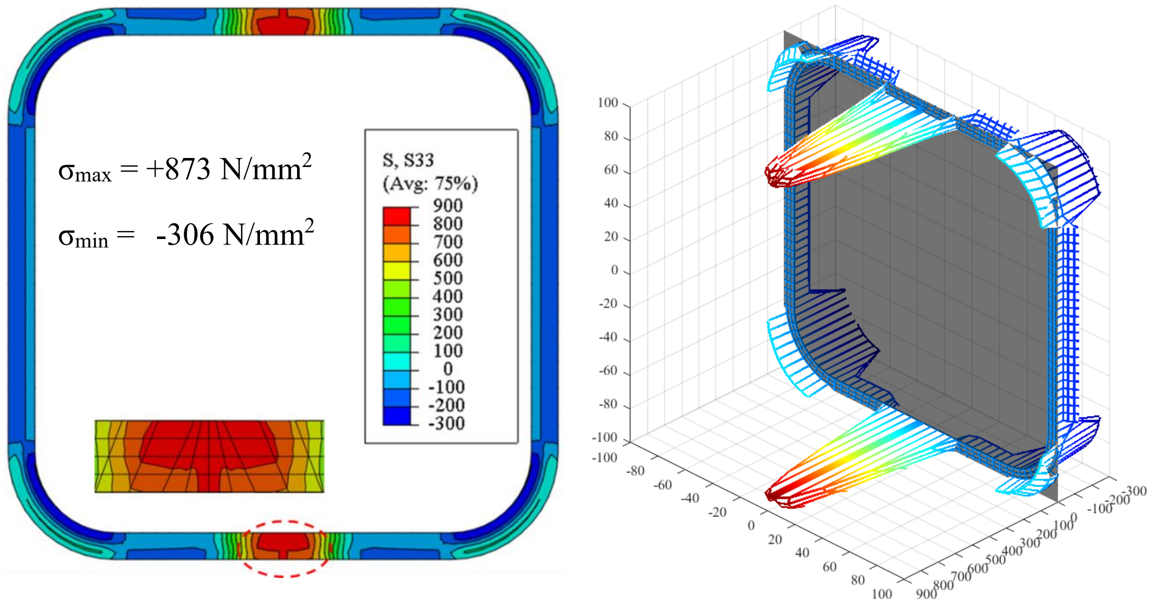

Fig. 6.26 Contours of longitudinal residual stresses in Section S3A

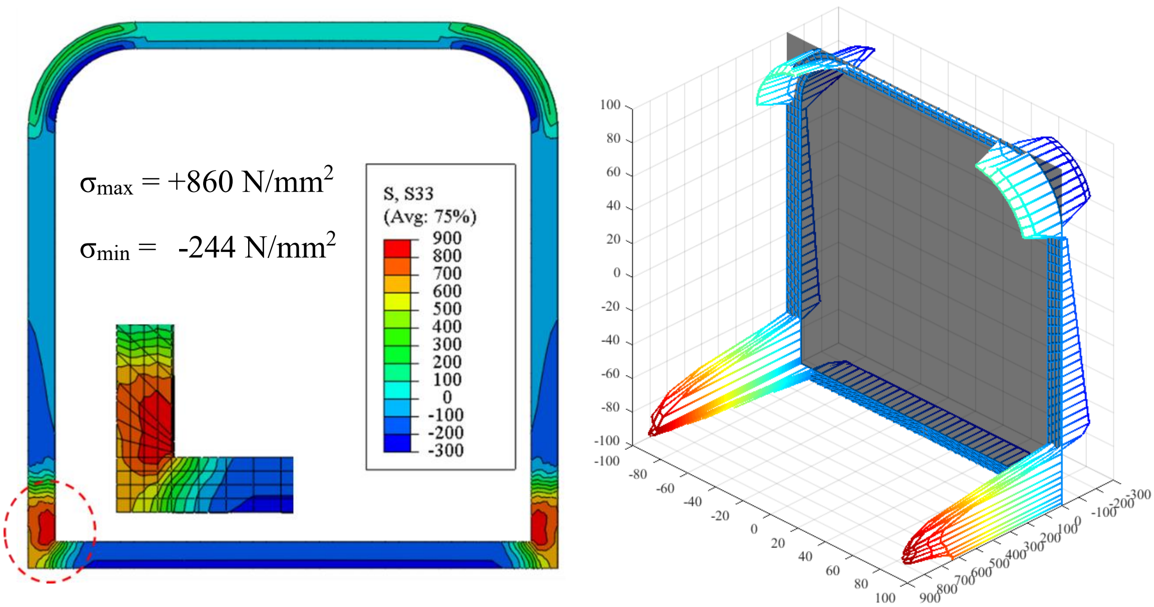

Fig. 6.27 Contours of longitudinal residual stresses in Section S3B

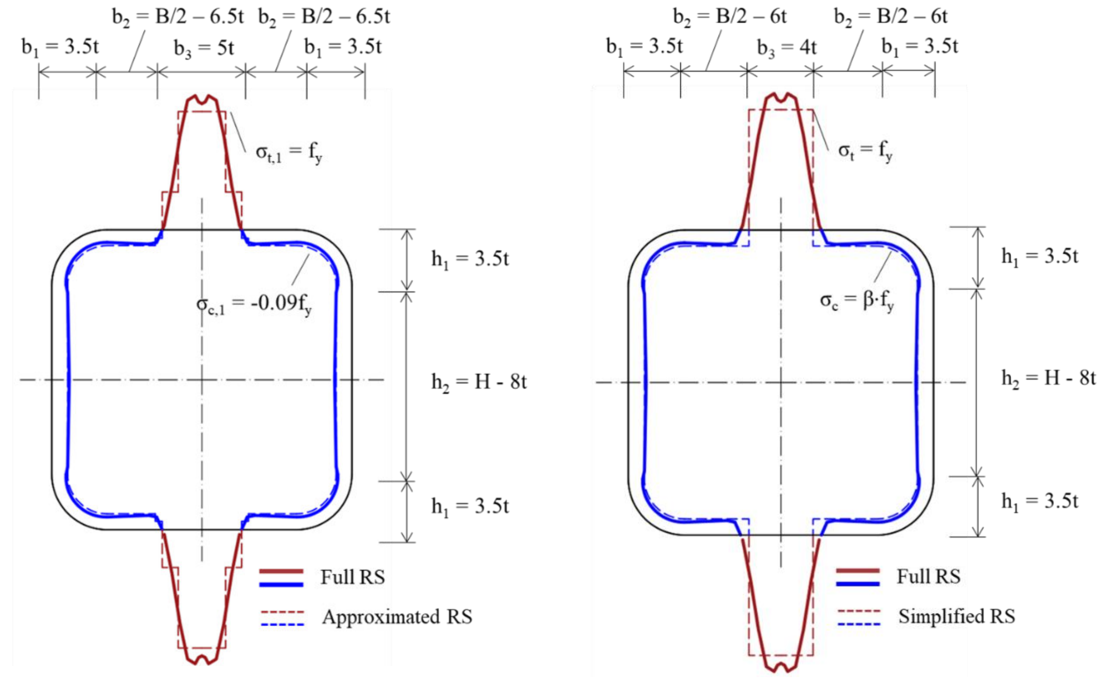

a) Full RS vs Approximated RS　　　　b) Full RS vs Simplified RS

Fig. 6.28　Longitudinal residual stress patterns in Section S3A

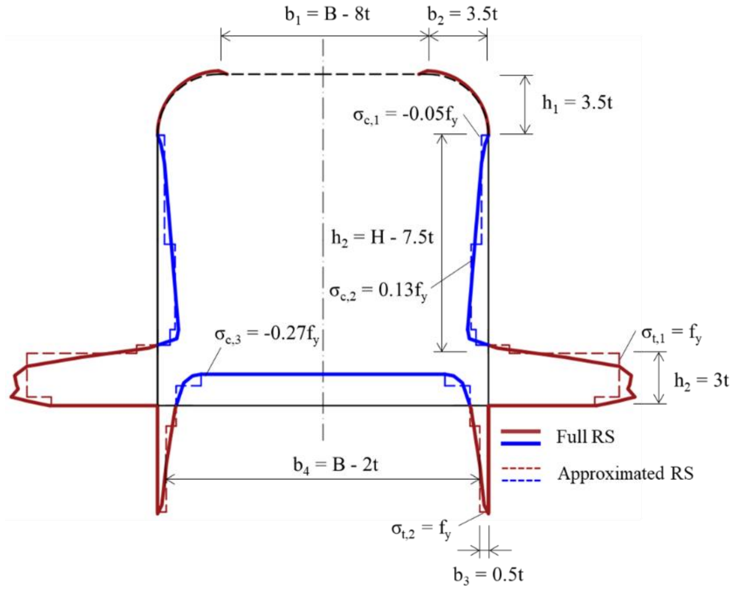

a) Full RS vs Approximated RS

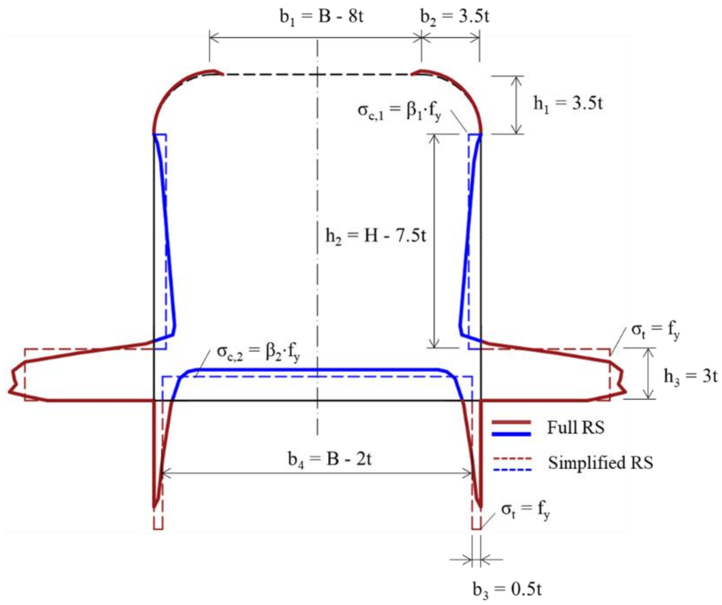

b) Full RS vs Simplified RS

Fig. 6.29 Longitudinal residual stress patterns in Section S3B

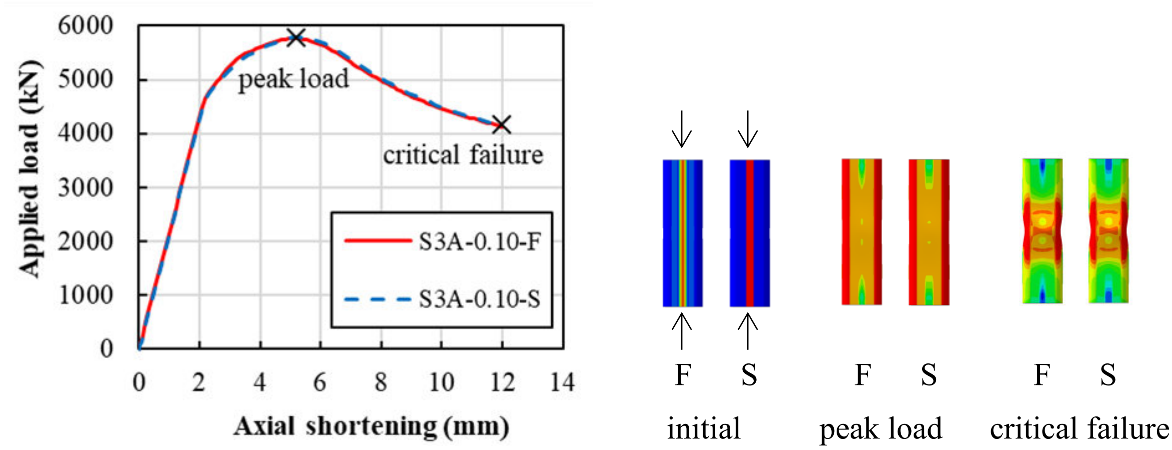

a) S3A-0.10

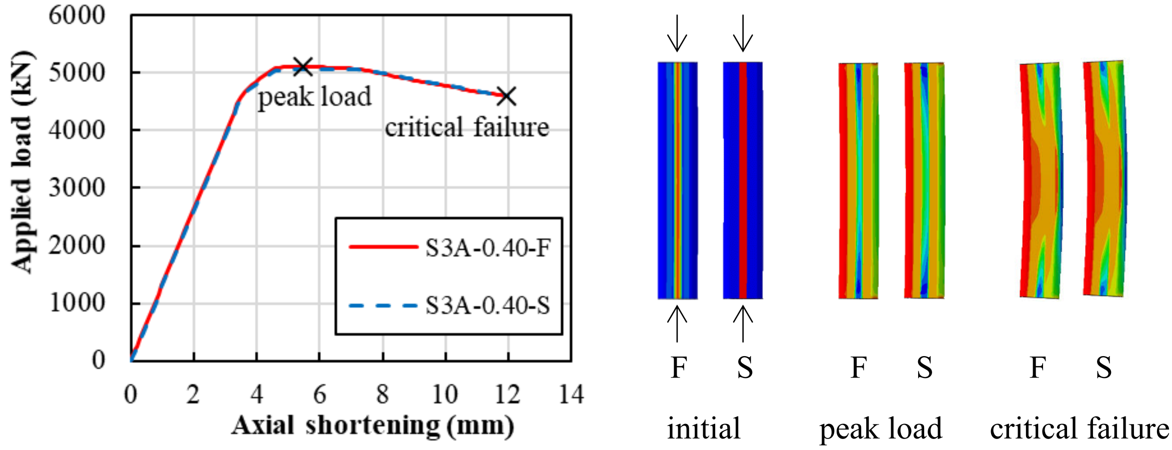

b) S3A-0.40

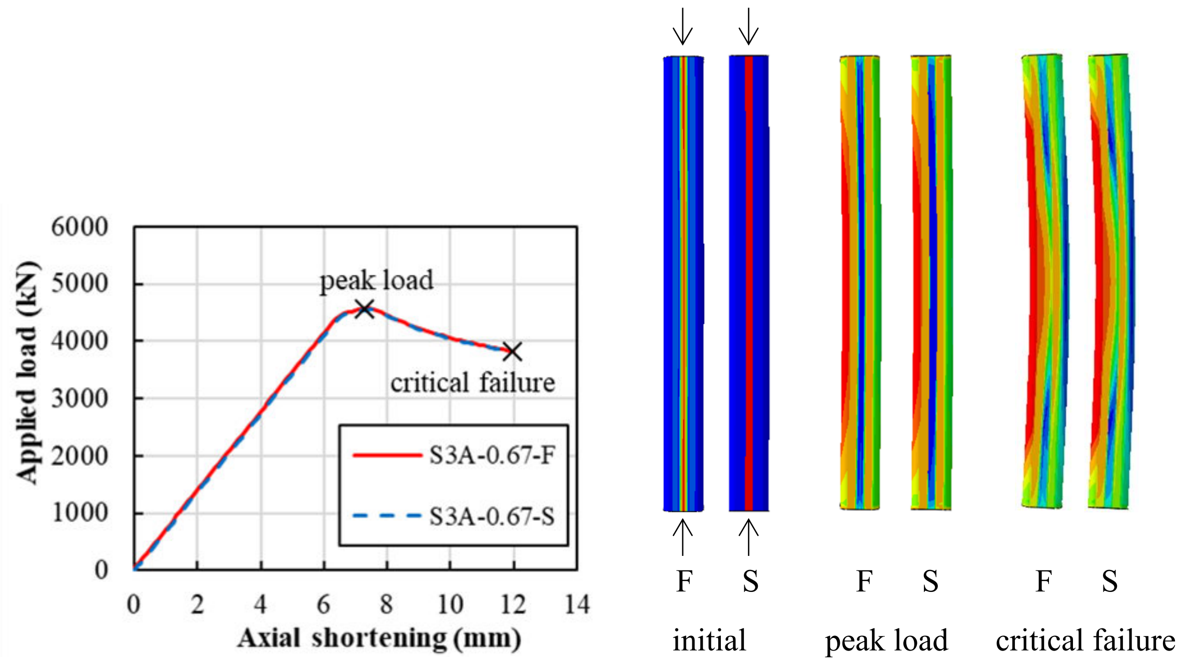

c) S3A-0.67

Fig. 6.30 Load-shortening curves of columns with Section S3A

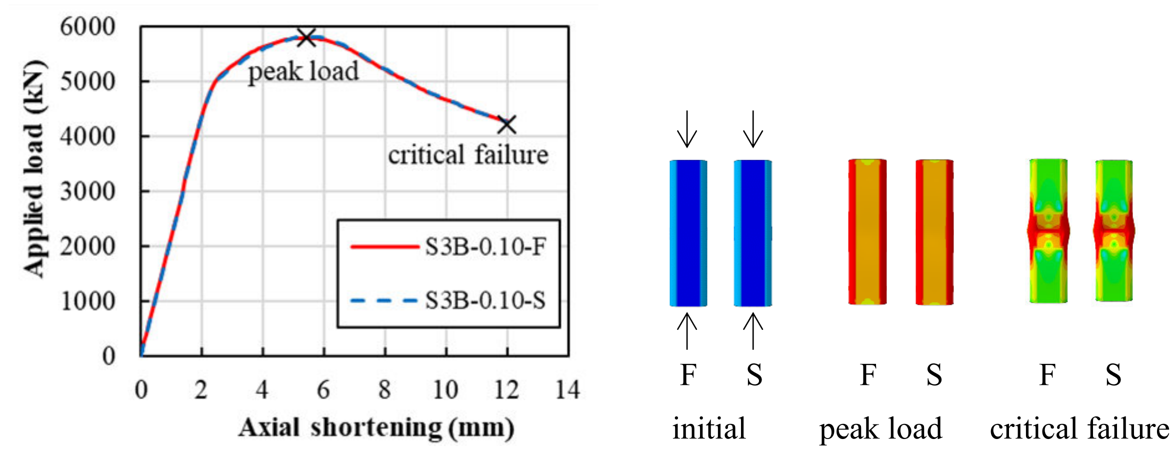

a) S3B-0.10

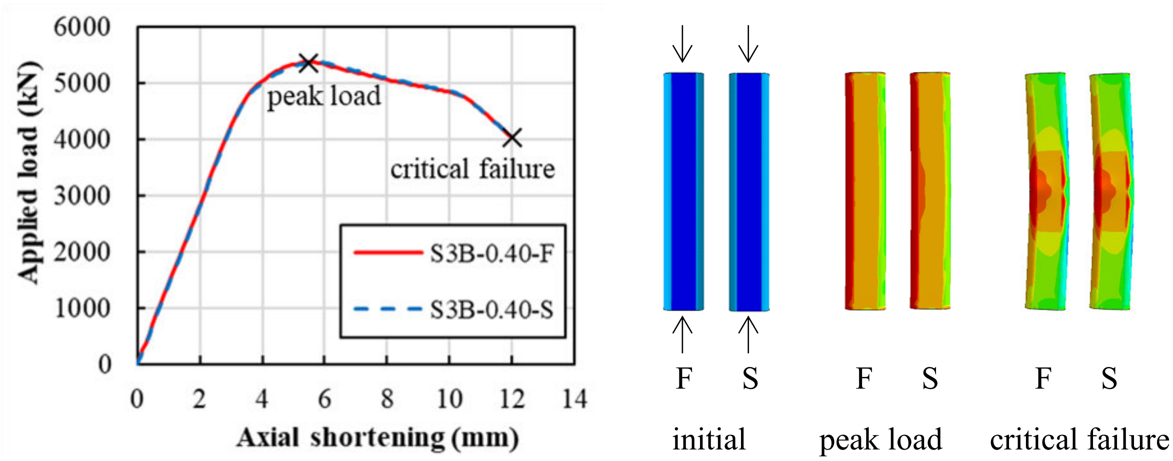

b) S3B-0.40

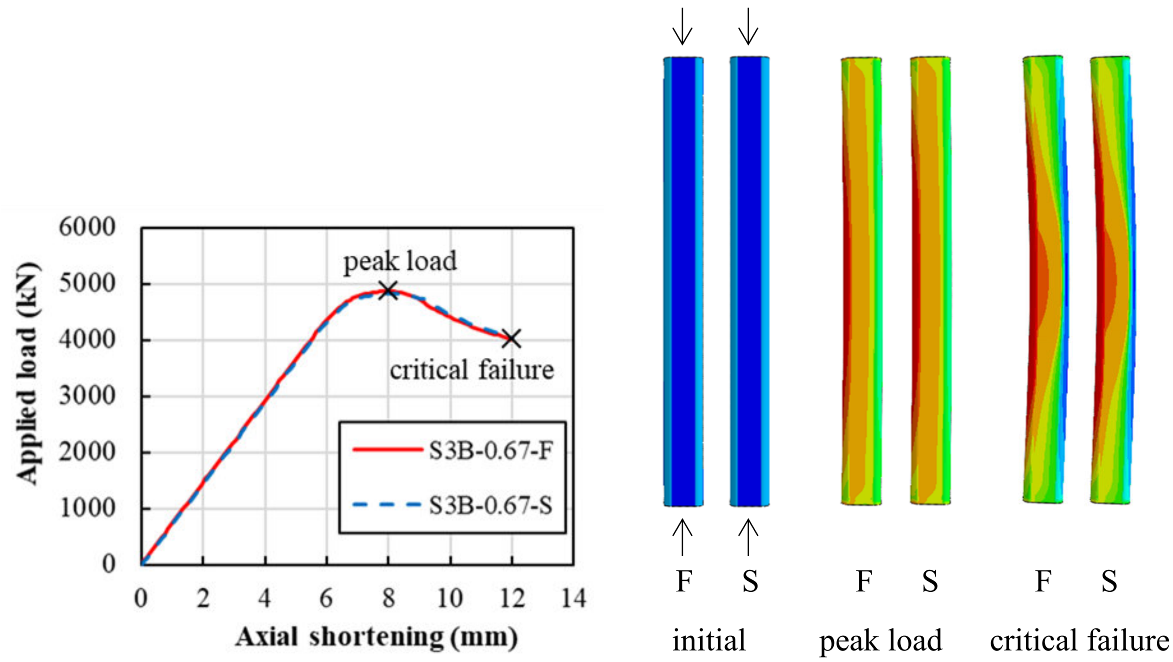

c) S3B-0.67

Fig. 6.31 Load-shortening curves of columns with Section S3A

Table 6.1 Parameters adopted in the double-ellipsoidal heat source model

Length of semi-axis (mm)				η
a	b	c_1	c_2	
5.0	10.0	7.5	22.5	0.80

Table 6.2 Investigation programme and scope of work

Section	Fabrication process		Experimental measurement			Numerical modelling		
	transverse bending	longitudinal welding	welding parameters	temperature histories	residual stresses	transverse bending	heat transfer analysis	thermomechanical analysis
(1) Section S1A	Y	Y	Y	--	--	Y	Y	Y
(2) Section S1B	Y	Y	Y	--	--	Y	Y	Y
(3) Section S3A	Y	Y	Y	Y	Y	Y	Y	Y
(4) Section S3B	Y	Y	Y	Y	Y	Y	Y	Y

Table 6.3 Measured welding parameters of all welding passes

Section	Weld pass	Current, I (A)	Voltage, U (V)	Welding speed, v (mm/s)	Welding efficiency, η	Line hear input energy, q (kJ/mm)
(1) S1A	1 (back welding)	135 ~ 145	19.6	2.60	0.80	0.81 ~ 0.87
	2	180 ~ 190	21.4	4.41	0.80	0.70 ~ 0.74
(2) S1B	1 (back welding)	130 ~ 140	19.7	2.81	0.80	0.73 ~ 0.79
	2	185 ~ 195	21.1	3.81	0.80	0.82 ~ 0.86
(3) S3A	1 (back welding)	145 ~ 155	20.4	2.09	0.80	1.13 ~ 1.21
	2	200 ~ 210	23.0	4.11	0.80	0.90 ~ 0.94
	3	185 ~ 195	23.1	2.86	0.80	1.20 ~ 1.26
(4) S3B	1 (back welding)	160 ~ 170	20.2	2.81	0.80	0.92 ~ 0.98
	2	200 ~ 210	22.6	3.80	0.80	0.95 ~ 1.00
	3	190 ~ 200	22.8	3.35	0.80	1.03 ~ 1.09

Table 6.4 Programme and results of mesh convergence study

Model	Global mesh size (mm)	Local mesh size at weld groove (mm)	Number of elements			Total number of elements	Computational time (hours)	$\varepsilon_{t,in,max}$ (%)	$\varepsilon_{c,in,max}$ (%)
			through thickness	at corner	along length				
(1) Mesh A@6.7	6.7	3.5	3	9	66	11,880	12	0.379	-0.164
(2) Mesh B@5.0	5.0	2.1	4	11	76	23,104	31	0.389	-0.148
(3) Mesh C@3.3	3.3	1.4	6	16	115	88,920	145	0.391	-0.115

Table 6.5 Investigation programme of numerical models for sequentially-coupled thermomechanical analyses

Model	Dimensions (mm)					Number of welding passes	Number of layers through thickness	Total number of elements
	t	R_{in}	B	H	L			
(1) Section S1A	6	18	150	150	560	2	3	55,860
(2) Section S1B	6	18	150	150	560	2	3	46,368
(3) Section S3A	10	30	200	200	760	3	4	23,104
(4) Section S3B	10	30	200	200	760	3	4	23,408

Table 6.6 Force equilibrium in Sections S3A and S3B

Section	Residual stress	Total tension force, F_T (kN)	Total compression force, F_C (kN)	Resultant force, $F_R = F_T + F_C$ (kN)	$F_R / (F_C - F_T)$ (%)
Section S3A	S3A (Sectioning)	246	-338	-92	15.8
	S3A (FEM)	567	-601	-34	2.9
Section S3B	S3B (Sectioning)	144	-240	-96	25.0
	S3B (FEM)	486	-501	-15	1.5

Table 6.7 Numerical results of columns with two residual stresses patterns

Section	Specimen	$\bar{\lambda}$	Residual stress pattern	N_{FEM} (kN)	$N_{c,Rd}$ (kN)	N_{FEM} / $N_{c,Rd}$
Section S3A	(a) S3A-0.10	0.10	Full RS	5761	5458	1.06
			Simplified RS	5781	5458	1.06
	(b) S3A-0.40	0.40	Full RS	5107	5458	0.94
			Simplified RS	5067	5458	0.93
	(c) S3A-0.67	0.67	Full RS	4576	5458	0.84
			Simplified RS	4554	5458	0.83
Section S3B	(a) S3B-0.10	0.10	Full RS	5789	5594	1.03
			Simplified RS	5813	5594	1.04
	(b) S3B-0.40	0.40	Full RS	5377	5594	0.96
			Simplified RS	5393	5594	0.96
	(c) S3B-0.67	0.67	Full RS	4856	5594	0.87
			Simplified RS	4821	5594	0.86

Table 6.8 Simplified longitudinal residual stresses for Series SA sections

Section	f_y (N/mm^2)	β
Section S1A	733	-0.056
Section S2A	733	-0.089
Section S3A	754	-0.073
Section S4A	754	-0.056

Table 6.9 Simplified longitudinal residual stresses for Series SB sections

Section	f_y (N/mm^2)	β_1	β_2
Section S1B	733	-0.074	-0.192
Section S2B	733	-0.053	-0.137
Section S3B	754	-0.097	-0.253
Section S4B	754	-0.074	-0.192

CHAPTER 7: NUMERICAL INVESTIGATION INTO S690 CFSHS COLUMNS

7.1 Introduction

This Chapter presented a numerical investigation into the structural performance of S690 cold-formed square hollow section (CFSHS) columns under compression.

A total of 30 numerical models were established and successfully validated against the test data. It was shown that both the failure modes and the resistances obtained from the numerical predictions were consistent with all the test results presented in Chapter 4.

In order to evaluate the member resistances of the columns with different combinations of fabrication processes, material models, initial states and non-dimensional slenderness, a series of parametric studies were developed based on the validated numerical models. A total of 52 parametric studies were carried out, demonstrating the influences of various effects.

Design recommendations were then proposed according to the direct comparison among the test data, the parametric studies and the design rules, to improve the design of S690 CFSHS columns under axial buckling given in EN 1993-1-1 (CEN 2014). It was summarized that the design curve with a smaller imperfection factor should be adopted, so that the structural advantages of the S690 CFSHS were readily exploited in an effective design of columns under axial buckling

7.2 Validation of Models

An experimental investigation into S690 CFSHS columns under compression is presented in detail in Chapter 4. All the tests have been conducted successfully. Numerical models should be carefully calibrated against the test data, and the validated models are considered to be capable of predicting accurate member resistances of columns, and thus, to build a database for improving the current design rules.

7.2.1 Combability of solid elements

In this Chapter, all the numerical models are established with ABAQUS (2013) using a commonly used solid element C3D8R. Table 7.1 summarizes the solid elements used in Chapters 5 to 7 for various purposes of numerical analyses, including two types of solid elements (see Fig. 7.1): i) element C3D8R for stress-strain analyses, and ii) element DC3D8 for heat transfer analyses. It should be noted that the degrees of freedom as well as the nodal numbers of these two types of solid elements are identical, so that combability among different analyses is satisfied. Although the plane strain elements CPE4R are used for 2D transverse bending models as demonstrated in Chapter 5, it is feasible to incorporate all the strain and stress components from the 2D models into the 3D models for structural analyses.

7.2.2 Material properties

True stress-strain characteristics of S690 steel plates are employed in structural analyses for model validation. Fig. 7.2 shows the true stress-strain curves of steel materials, where both the curves of the 6 mm and the 10 mm thick S690 steel plates are converted from the test data with the image processing method as demonstrated in Chapter 3. It should be noted that a true stress-strain curve of S355 steel plate a typical Young's modulus of 205 kN/mm^2 and a typical yield strength of 400 N/mm^2 is also adopted in the modelling.

7.2.3 Stocky columns under concentric compression

a) Investigation programme

Chapter 4 demonstrates the test programme and the results of a total of 8 S690 CFSHS stocky columns under concentric compression. The same designations are adopted in this Chapter for model validation, and the corresponding investigation programme is summarized in Table 7.2. All the models for validation are established according to the measured dimensions shown in the table.

b) Establishment of models

Fig. 7.3 shows the boundary conditions of the finite element models of the stocky columns under concentric compression. Each end of the S690 stocky column is attached with an end plate made of S355 steel. Both the end plates have large rigidity, and "tie" interactions are assigned between the end plates and the column.

In terms of boundary conditions, all six degrees of freedom are fixed at the bottom end, i.e. $U_x = U_y = U_z = 0$ and $R_x = R_y = R_z = 0$ while five degrees of freedom are fixed at the top end except the translation degree along the x-axis, i.e. $U_y = U_z = 0$ and $R_x = R_y = R_z = 0$. An axial displacement is applied along the x-axis through the centre of the top end plate so the load-displacement behaviour of the column under concentric compression is readily determined.

c) Mesh convergence study

To achieve a good balance between accuracy of numerical predictions and computational costs, it is necessary to conduct a mesh convergence study before validating the models for structural analyses. Test S3A-S is employed to demonstrate the convergence of the numerical results. Fig. 7.4 shows three models established with solid elements in the same aspect ratio but in different sizes. It should be noted that their global mesh sizes are controlled by the numbers of elements through the plate thickness, i.e. three, four and six layers through thickness, respectively.

Table 7.3 summarizes the investigation programme and the results of the mesh convergence study. In order to evaluate the convergence of models, the section resistances, $N_{c,FEM}$, predicted by these three numerical models are compared with the measured section resistance, $N_{c,Et}$, of Test S3A-S. It is found that the results converge well when Mesh B@4-layer is adopted. Although Mesh A predicts satisfactory results when compared with $N_{c,Et}$, it is acceptable to adopt Mesh B for accurate analyses, as the computational time increases by only 25 minutes.

According to the results of the mesh convergence study, it recommended to adopt the four-layer meshing strategy for all 10 mm thick sections for subsequent numerical studies in this Chapter. Besides, it is proposed to adopt the three-layer meshing strategy for those 6 mm thick sections. Since this 2.0 mm-per-layer meshing in 6 mm thick sections is finer than that 2.5 mm-per-layer meshing in 10 mm thick sections, the numerical results calculated by the former meshing strategy can converge as well for sure.

d) Initial states: plastic strains and residual stresses

Initial plastic strains and residual stresses are inevitably induced by transverse bending and longitudinal welding during fabrication of CFSHS. In order to properly consider the influences on structural performance caused by these effects due to fabrication processes, these strain and stress components are simplified and incorporated into numerical models as initial states.

- Plastic strains and residual stresses due to transverse bending

  Fig. 7.5 shows the initial equivalent plastic strains and the longitudinal residual stresses at the corner regions of a 10 mm thick S690 plate with R_{in}/t of 3.0, which is a key finding of the numerical studies demonstrated in Chapter 5. It should be noted that the distributions of strains and stresses in a 6 mm thick plate are very similar to those of a 10 thick plate. To consider the cold-bending effects in a three-layer or a four-layer model for structural analysis, it is proposed to take average values of the strains and the stresses within each layer. Fig. 7.6 illustrates the three-layer through-thickness distributions of both the strains and the stresses, which are readily incorporated into the corner regions for the structural analyses of S690 CFSHS with 6 mm thick steel plates. Similarly, the 4-layer distributions shown in Fig. 7.7 are readily incorporated into the structural analyses of S690 CFSHS with 10 mm thick steel plates.

- Residual stresses due to longitudinal welding

  Fig. 7.8 illustrates the longitudinal residual stresses for Series SA and SB sections obtained from the thermomechanical analyses presented in Chapter 6. In order to incorporate these residual stresses into structural analyses efficiently, it is proposed to convert the complex distributions into simplified block-shaped patterns according to force equilibrium of the whole sections, as shown in Fig. 7.9. The effectiveness of these “Simplified RS” patterns has been demonstrated in Chapter 6, and the “Simplified RS” patterns can be used to predict identical structural behaviour of those columns under compression with the “Full RS” patterns.

- Combined initial plastic strains and residual stresses

  The initial equivalent plastic strains shown in Figs. 7.6 and 7.7 are readily input into the structural analyses as the initial states of strains of the curved corners. Figs. 7.10 a) and 7.11 a) illustrate the initial equivalent plastic strains of Series SA and SB sections, where the stresses due to transverse bending and longitudinal welding are considered simultaneously. Therefore, the values of the longitudinal residual stresses due to longitudinal welding shown in Fig. 7.9 should be considered together with the longitudinal residual stresses due to transverse bending, as shown in Figs. 7.6 and 7.7. Therefore, the resultant initial states of longitudinal residual stresses in Sections S3A and S3B are determined, as illustrated in Figs. 7.10 b) and 7.11 b), respectively.

e) Initial state: geometric imperfection

Initial geometric imperfections, v_0, are measured prior to testing. It is found that all the measurements are very small, i.e. smaller than 0.5 mm, along the member length of the all the columns, and thus, these may be ignored.

Normally, geometric imperfections should be considered in modelling. In order to quantify how v_0 affects the section resistances numerically, and how to select a proper value for model validation, it is proposed to carry out a sensitivity study on Tests S1A-S and S3A-S. The models are established accordingly, complying with the boundary conditions, the mesh sizes, the plastic strains and the residual stresses as described in this Section. v_0 is normalized with plate thickness, t, and five v_0/t values, i.e. 0.010, 0.025, 0.050, 0.075 and 0.100, are investigated in this sensitivity study.

Fig. 7.12 shows the results of the sensitivity study. The measured section resistance of the test, $N_{c,Et}$, is compared with the predicted section resistances of the models, $N_{c,FEM}$, to evaluate the effects of v_0/t. For Test S1A-S, the ratio of $N_{c,Et}/N_{c,FEM}$ varies from 0.961 to 1.050 when v_0/t increases from 0.010 to 0.100; and for Test S3A-S, the ratio of of $N_{c,Et}/N_{c,FEM}$ varies from 0.997 to 1.057 when v_0/t increases from 0.010 to 0.100. Obviously, the section made of a thinner plate, i.e. Test S1A-S in 6 mm thick, is more sensitive to the change of v_0/t than that made of a thicker one, i.e. Test S3A-S in 10 mm thick. It is found that when v_0/t is smaller than 0.050, the numerical results are overestimated with $N_{c,Et}/N_{c,FEM}$ smaller than 1.0. On the contrary, when v_0/t is taken to be larger than 0.050, conservative results are predicted. Hence, it is proposed to adopt $v_0/t = 0.050$ to validate all the columns under concentric compression, so that a balance between safety margin and accuracy of numerical prediction will be achieved.

f) Results

Table 7.4 compares the test data and the numerical results of 8 stocky columns under concentric compression. The measured section resistances, $N_{c,Et}$, of all these tests are shown to be larger than the predicted section resistances, $N_{c,FEM}$. Fig. 7.13 shows a comparison between the failure modes of Test S3A-S obtained from the test and predicted by the FEM, respectively. It is found that these two failure modes are very similar. Moreover, the failure modes of all the tests predicted by FEM are shown in Fig. 7.14, and they are highly consistent with the failure modes of the tests. A detailed comparison is found in Fig. 7.15, showing the load-axial shortening curves between all the tests and all the numerical models. It is found that, with consideration of the non-linearity of materials, the effects due to fabrication processes and the geometric imperfections, all the numerical models are well validated. It is considered that these validated numerical models are able to predict accurate load-deformation characteristics of stocky columns under concentric compression.

7.2.4 Stocky columns under eccentric compression

a) Investigation programme

Chapter 4 demonstrates the test programme and the results of a total of 6 S690 CFSHS stocky columns under eccentric compression. The same designations are adopted in this Chapter for model validation, and the corresponding investigation programme is summarized in Table 7.5. All the models for validation are established according to the measured dimensions shown in the table.

b) Establishment of models

Fig. 7.16 shows the boundary conditions of the finite element models of the stocky columns under eccentric compression. Each end of the S690 stocky column is attached with an end plate made of S355 steel. Both the end plates have large rigidity, and “tie” interactions are assigned between the end plates and the column.

In terms of boundary conditions, five degrees of freedom are fixed at the bottom end, i.e. $U_x = U_y = U_z = 0$ and $R_x = R_y = 0$ while four degrees of freedom are fixed at the top end, i.e. $U_y = U_z = 0$ and $R_x = R_y = 0$. Such a pair of boundary conditions at both ends allow for free rotation of the column about the z-axis. An axial displacement is applied along the x-axis with a loading eccentricity, e_0, from the centre of the top end plate, so the load-displacement behaviour of the column under eccentric compression is readily determined.

The mesh sizes for model validation are determined based on the results of mesh convergence study demonstrated in Section 7.2.3 c), and the same meshing strategy is adopted for all the stocky columns under eccentric compression. Fig. 7.17 shows the typical mesh sizes of the numerical model for validating Test S3A-E.

c) Initial states: plastic strains and residual stresses

The simplified patterns of the residual stresses and the plastic strains are proposed in Section 7.2.3. These patterns are incorporated into the numerical models as the initial states to validate the stocky columns under eccentric compression.

d) Initial state: geometric imperfection

Initial geometric imperfections, v_0, are measured prior to testing. It is found that all the measurements are very small, i.e. smaller than 0.5 mm, along the member length of the all the columns, and thus, these may be ignored.

As demonstrated by the sensitivity study in Section 7.2.3, it is proposed to adopt $v_0/t = 0.050$ to validate all the columns under eccentric compression, so that a balance between safety margin and accuracy of numerical prediction will be achieved.

e) Results

Table 7.5 compares the test data and the numerical results of 6 stocky columns under eccentric compression. The measured section resistances, $N_{c,Et}$, of most of tests are larger than the predicted section resistances, $N_{c,FEM}$, except for two tests with Class 4 sections, i.e. Tests S2A-E and S2B-E. Fig. 7.18 shows a comparison between the failure modes of Test S3A-E obtained from the test and predicted by the FEM, respectively. It is found that these two failure modes are very similar. Moreover, the failure modes of all the tests predicted by FEM are shown in Fig. 7.19, and they are highly consistent with the failure modes of the tests. A detailed comparison is found in Fig. 7.20, showing the load-axial shortening curves between all the tests and all the numerical models. It is found that, with consideration of the non-linearity of materials, the effects due to fabrication processes and the geometric imperfections, all the numerical models are well validated. Hence, these validated numerical models are able to predict accurate load-deformation characteristics of stocky columns under eccentric compression.

7.2.5 Slender columns under concentric compression

a) Investigation programme

Chapter 4 demonstrates the test programme and the results of a total of 24 S690 CFSHS slender columns under concentric compression. The same designations are adopted in this Chapter for model validation, and the corresponding investigation programme is summarized in Table 7.6. All the models for validation are established according to the measured dimensions shown in the table.

b) Establishment of models

Fig. 7.21 shows the boundary conditions of the finite element models of the slender columns under concentric compression. Each end of the S690 slender column is attached with an end plate made of S355 steel. Both the end plates have large rigidity, and "tie" interactions are assigned between the end plates and the column.

In terms of boundary conditions, five degrees of freedom are fixed at the bottom end, i.e. $U_x = U_y = U_z = 0$ and $R_x = R_y = 0$ while four degrees of freedom are fixed at the top end, i.e. $U_y = U_z = 0$ and $R_x = R_y = 0$. Such a pair of boundary conditions at both ends allow for free rotation of the column about the z-axis. An axial displacement is applied along the x-axis through the centre of the top end plate, so the load-displacement behaviour of the column under concentric compression is readily determined.

The mesh sizes for model validation are determined based on the results of mesh convergence study demonstrated in Section 7.2.3 c), and the same meshing strategy is adopted for all the slender columns under concentric compression. Fig. 7.22 shows the typical mesh sizes of the numerical model for validating Test S3A-P.

c) Initial states: plastic strains and residual stresses

The simplified patterns of the residual stresses and the plastic strains are proposed in Section 7.2.3. These patterns are incorporated into the numerical models as the initial states, to validate the slender columns under concentric compression.

d) Initial states: geometric imperfection and loading eccentricity

It should be noted that a slender column is not always "perfectly" straight along its member length direction, and the concentric loading may not exactly go through the centroid of the section. Fig. 7.23 shows the initial geometric imperfection existing in a slender column under concentric compression, including: i) initial out-of-straightness, ν_0, and ii) initial loading eccentricity, e_0. Both ν_0 and e_0 are measured prior to testing and summarized in Table 7.6. Those initial states may significantly affect member resistances of slender columns, and thus, they should be carefully considered into model validation.

A sensitivity study is carried out to quantify how ν_0 and e_0 influence the member resistances of slender columns under compression. The models are established accordingly, complying with the boundary conditions, the mesh sizes, the plastic strains and the residual stresses as described in this Section. A total of 12 sensitivity studies are carried out to compared with the measured member resistance, $N_{b,Et}$, of Test S3A-Q, with ν_0 of 0.5, 1.0, 1.5 and 2.0 mm and e_0 of 1.0, 2.0 and 3.0 mm.

Fig. 7.24 shows the results of 12 sensitivity studies. It is found that the predicted member resistances, $N_{b,FEM}$, have the consistent linear relationships between $N_{b,Et}/N_{b,FEM}$ and v_0 with three different values of e_0, and the variations among different combinations of v_0 and e_0 are found to be insignificant. As shown in Table 7.6, the measured v_0 and e_0 of Test S3A-Q are both equal to 2.0 mm, and its $N_{b,Et}/N_{b,FEM}$ is found to be 1.028 as shown in Fig. 7.24. This indicates that, by incorporating the measured v_0 and e_0 into structural analyses, the numerical predations could match well with the test results. Therefore, it is proposed to input the measured values of v_0 and e_0 summarized in Table 7.6 into the structural analyses as their initial states, to validate the slender columns under concentric compression.

e) Results

Table 7.6 compares the test data and the numerical results of 16 slender columns under concentric compression. The measured section resistances, $N_{b,Et}$, of most of the tests are larger than the predicted section resistances, $N_{b,FEM}$. Fig. 7.25 shows a comparison between the failure modes of Test S3A-Q obtained from the test and predicted by the FEM, respectively. It is found that these two failure modes are very similar. A detailed comparison is found in Figs. 7.26 to 7.29, showing the load-displacement curves between all the tests and all the numerical models. It is found that, with consideration of the non-linearity of materials, the effects due to fabrication processes, the initial loading eccentricities and the geometric imperfections, all the numerical models are well validated. Hence, these validated numerical models are able to predict accurate load-displacement behaviour of slender columns under concentric compression.

7.3 Parametric Studies of Slender Columns under Concentric Compression

7.3.1 Investigation programme

Tables 7.7 and 7.8 summarize the investigation programmes of the parametric studies for slender columns under concentric compression with Sections S3A and S3B, respectively. The parameters under investigation include: (A) type of section, (B) material model, (C1) initial state: GI (geometric imperfection), (C2) initial state: PEEQ (equivalent plastic strain), (C3) initial state: RS (residual stress), and (D) non-dimensional slenderness. In summary, this series of parametric studies consider various effects that may significantly influence member resistances under axial buckling, including two types of sections, two material models, five combinations of initial states and four non-dimensional slenderness ratios. A total of 52 combinations of parameters are investigated, and their results are considered to be able to well demonstrate the structural performance of S690 CFSHS slender columns under concentric compression in various cases.

Establishment of the models in parametric studies are consistent with that described in Section 7.2.5 b), except that both end plates are excluded from the analyses for simplification. The mesh sizes for model validation are determined based on the results of mesh convergence study given in Section 7.2.3 c), and the same meshing strategy is adopted for all the parametric studies.

7.3.2 Material models

Fig. 7.30 illustrates two different material models employed in this series of parametric studies. Typical mechanical properties are used in both material models that their Young's moduli, E, are both taken to be 205 kN/mm^2, and their yield strengths, f_y, are both taken to be 690 N/mm^2. The difference between these two models lies in the hardening behaviour after yielding:

i) The linear hardening model shown in graph a) exhibits a strain hardening behaviour with a slope of 1.05 from yielding to necking, with its tensile strength, f_u, equal to 725 N/mm^2, and the curve no longer goes up, but remains flat up to a true strain over 120 %.

ii) The non-linear hardening model shown in graph b) has a short yielding plateau after its first yield, followed with a non-linear strain hardening behaviour until its tensile strength is reached, and this material curve continues to rise with a gentle slope up to its true strain over 100%.

7.3.3 Initial states

Three initial states shown in Tables 7.7 and 7.8 are taken into account simultaneously. When GI is taken to be the smaller values, i.e. $L_{eff}/1500$ and $L_{eff}/1000$, the effects of PEEQ and RS are considered. The patterns of PEEQ and RS are directly input into the numerical models as demonstrated in detail in Section 7.2.3 d). However, when GI is taken to be $L_{eff}/500$, this large geometric imperfection is considered to represent all these three initial states at the same time. Hence, the effects of PEEQ and RS are both excluded from the analyses. Therefore, a total of five combinations of initial states are adopted for this series of parametric studies.

7.3.4 Results

Tables 7.9 and 7.11 summarize the results of 32 parametric studies on Section S3A, and Table 7.13 summarizes the results 20 parametric studies on Section S3B. Among these parametric studies, the material models used in Tables 7.9 and 7.13 are “S690, linear hardening” while the material models used in Table 7.11 are “S690, non-linear hardening”. The member resistance, $N_{b,FEM}$, of each numerical model is determined and then normalized with the design section resistance, $N_{c,Rd}$. The reduction ratios of $N_{b,FEM}/N_{c,Rd}$ are employed to directly evaluate various combinations of effects. Detailed comparisons are made in Tables 7.10, 7.12 and 7.14, to evaluate the changes of reduction ratios when different combinations of initial states are adopted.

a) Section S3A, linear hardening

A comparison among a total of 20 parametric studies on Section S3A are presented in Table 7.10, including five combinations of initial states and four non-dimensional slenderness, $\bar{\lambda}$. As shown in the table, “Case a” only considers GI of $L_{eff}/1500$ but excludes PEEQ and RS from the initial states, and they have the largest reduction ratios among all the five combinations of initial states. If only RS is added into modelling, i.e. “Case b”, the predicted member resistances all decrease, but such a decrease caused by RS becomes less significant when the $\bar{\lambda}$ increases from 0.6 to 1.8. Moreover, if PEEQ and RS are both added into the model with GI of $L_{eff}/1500$, i.e. “Case c”, the member resistances increase slightly, and this enhancement due to cold-forming effects also diminishes as the $\bar{\lambda}$ increases from 0.6 to 1.8. Therefore, it is reasonable to incorporate both PEEQ and RS for slender columns under compression, in particular, when the $\bar{\lambda} \leq 1.0$.

Considering both PEEQ and RS but increasing GI from $L_{eff}/1500$ to $L_{eff}/1000$, i.e. “Case d”, up to 3.4 % smaller reduction ratios are found when compared with those of “Case c”, which is considered to be insignificant. However, if only GI of $L_{eff}/500$ is incorporated into the analyses as the initial state, i.e. “Comb e”, its reduction ratios are the largest among “Case c”, “Case d.” and “Case e”, but it decreases significantly as the $\bar{\lambda}$ increases from 0.6 to 1.8, and it finally becomes the smallest one when the $\bar{\lambda} \geq 1.4$.

b) Section S3A, non-linear hardening

Another comparison on 12 parametric studies on Section S3A are summarized in Table 7.12. The only difference between the models in Tables 7.10 and 7.12 lies in the hardening behaviour of two material models. By comparing the results of "Case c", "Case d" and "Case e" in Table 7.12, it is found that the key findings are similar to what are discussed in the last paragraph based on the data summarized in Table 7.10.

After comparing the results between Tables 7.10 and 7.12, it is found that the reduction ratios of "Case c" and "Case d" summarized in Table 7.12 are all larger than those summarized in Table 7.10, but the enhancement caused by the non-linear hardening model, namely "S690, non-linear hardening", is limited by member slenderness. When the $\bar{\lambda}$ reaches to 1.8, the effect of non-linear hardening becomes very small, and thus, it may be ignored. This is because the failure of a very slender column is governed by Euler's elastic failure instead of material failure, and the strain hardening will have little contribution to the failure of the member. However, the results of "Case e" summarized in the two tables are the same. This is because PEEQ is excluded from these analyses.

c) Section S3B, linear hardening

Table. 7.14 summarizes a total of 20 parametric studies on Section S3B, and the results are compared with one another as shown in Table 7.14. The key findings shown in this table are basically similar to those found in Table 7.10. "Case a" has the largest member resistance, and "Case c" has the second largest one. By comparing "Case b" with "Case c", it is found that the enhancement caused by PEEQ becomes less significant as the $\bar{\lambda}$ increases. Obviously, "Case d" exhibits smaller than "Case c" due to the larger GI assigned into the structural analyses. The behaviour of "Case e" with Section S3B is a bit different from that with Section S3A, as it keeps the smallest one among "Case c", "Case d" and "Case c" when the $\bar{\lambda} \geq 1.0$.

7.3.5 Summary

In summary, Series SA and SB sections have very similar structural performance which is influenced by the parameters under investigation. RS plays an essential role in accessing these member resistances. As demonstrated by the parametric studies, the member resistances are significantly decreased when $\bar{\lambda}$ is small, i.e. $\bar{\lambda}$ = 0.6. However, its effect is obviously reduced as $\bar{\lambda}$ increases from 0.6 to 1.8. For PEEQ, it readily enhances the member resistances when $\bar{\lambda}$ is small, i.e. $\bar{\lambda}$ = 0.6, but such an enhancement tends to be minor or even trivial as a column becomes very slender, i.e. $\bar{\lambda} \geq 1.4$. This is because the failure of a very slender column is governed by Euler's elastic failure instead of material failure, and the initial plastic strains present at the corner regions may have little contribution to the member resistances. In terms of material model, the non-linear hardening model predicts an increased member resistance when $\bar{\lambda}$ is small, i.e. $\bar{\lambda}$ = 0.6, compared with that predicted by the linear hardening model. But this enhancement significantly diminishes as $\bar{\lambda}$ increases from 0.6 to 1.8.

To achieve accurate numerical predictions, it is proposed to take all three initial states into account at the same time, i.e. "Case c" and "Case d". It is shown that these two combinations of initial states are able to predict accurate member resistances of S690 CFSHS. An alternative method with simplification is to incorporate a large GI only, i.e. "Case e" GI = $L_{eff}/500$, to represent all the initial states of the column. This combination of initial states is also considered to predict the structural performance with sufficient accuracy, but the member resistances predicted with this simplified initial state are found to be conservative when $\bar{\lambda}$ is large, i.e. $\bar{\lambda}$ $\geq$ 1.4.

7.4 Design Recommendations for Slender Columns under Concentric Compression

Chapter 4 compares the member resistances obtained from the column tests and predicted by the design rules given in EN 1993-1-1. It is found that the current design rules are conservative as the design curve with a large imperfection factor, namely the design curve “c”, is adopted for the CFSHS under axial buckling. In order to achieve design of S690 CFSHS members with improved structural efficiency, it is recommended to adopt the curves with a smaller imperfection factor. An expanded database of member resistances is successfully built, as demonstrated by the parametric studies in Section 7.3, and a direct comparison is made among the test data, the parametric studies and the design rules. As compared in Section 7.3, the accurate predictions are successfully achieved by selecting two combinations of parameters:

i) “Case c”: S690 linear hardening, GI = $L_{eff}/1500$, PEEQ and RS; and

ii) “Case d”: S690 linear hardening, GI = $L_{eff}/1000$, PEEQ and RS.

Fig. 7.31 shows a comparison among the test data, the parametric studies and the design rules for all Series SA sections with their section classes ranging from 1 to 3. Obviously, all the numerical results are above the design curve “b”, and most of them even above the design curve “a”. Moreover, it is shown that the test data attain considerably larger member resistances than the numerical predictions, which proves that there is sufficient safety margin when directly adopting the design curve “b” for the columns with Series SA sections under axial buckling.

Fig. 7.32 shows another comparison among the test data, the parametric studies and the design rules for all Series SB sections with their section classes ranging from 1 to 3. Similarly, all the numerical results and test data are above the design curve “b”, and most of them even above the design curve “a”. Moreover, the test data of Series SB sections exhibit larger resistances than those of Series SA sections, as all the test data shown in Fig. 7.32 are above the design curve “a_0”. Hence, it is reasonable to adopt the design curve “b” for the columns with Series SB sections under axial buckling.

In summary, a small imperfection factor should be adopted for the design of member resistances of columns with S690 CFSHS. It is proposed to adopt the design curve “b”, which is able to predict considerably larger member resistances than the design curve “c” recommended by EN 1993-1-1 for CFSHS. Therefore, the improved design rules allow for an efficient design of S690 CFSHS members under axial buckling.

7.5 Conclusions

This Chapter presents a numerical investigation into the structural performance of S690 CFSHS columns under compression. A total of 30 numerical models are established and carefully validated against the test data presented in Chapter 4. A total of 52 parametric studies are developed based on the validated numerical models, generating a database of members resistances considering various combinations of parameters. The design methods are improved by comparing the test data, the parametric studies and the design curves. The key findings of this investigation are listed as follows:

- All the numerical models are successfully validated, with consideration of the effects of transverse bending and longitudinal welding. With incorporation of the initial plastic stains and the residual stresses, which are predicted in Chapters 5 and 6, into the structural analyses as initial states, the accurate numerical predictions are generated.

- The influences on structural performance of member resistances caused by various effects are evaluated, including types of sections, material models, geometric imperfections, initial equivalent plastic strains, residual stresses and non-dimensional slenderness. Material models, initial equivalent plastic strains and residual stresses affect member resistances when their non-dimensional slenderness ratios are small, but these effects are significantly eliminated as the member becomes slender.

- Two combinations of initial states are selected to predict the structural behaviour of the members under concentric compression. By comparing the test data, the parametric studies and the design curves, it is found that the current design rules given in EN 1993-1-1 are conservative by simply adopting the design curve "c" for all CFSHS members under axial buckling. It is recommended to adopt a design curve with a smaller imperfection factor to improve the design. It is shown that the design curve "b" matches well with all the test data and all the parametric studies. Therefore, it is proposed to adopt the design curve "b" for S690 CFSHS columns under axial buckling.

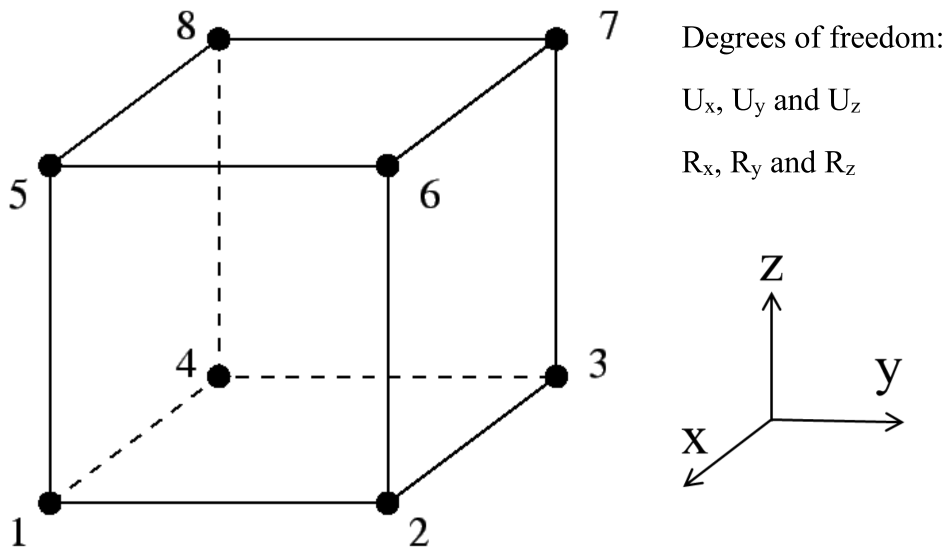

Fig. 7.1 Typical 8-nodal linear solid element in ABAQUS (C3D8R and DC3D8)

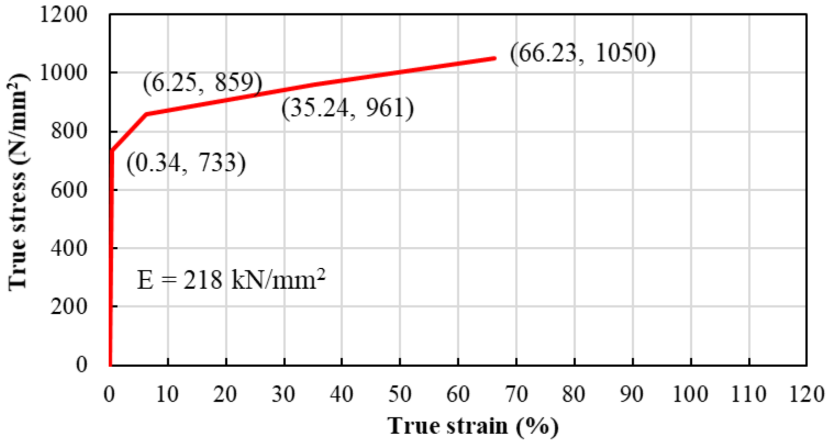

a) 6 mm thick S690 plate

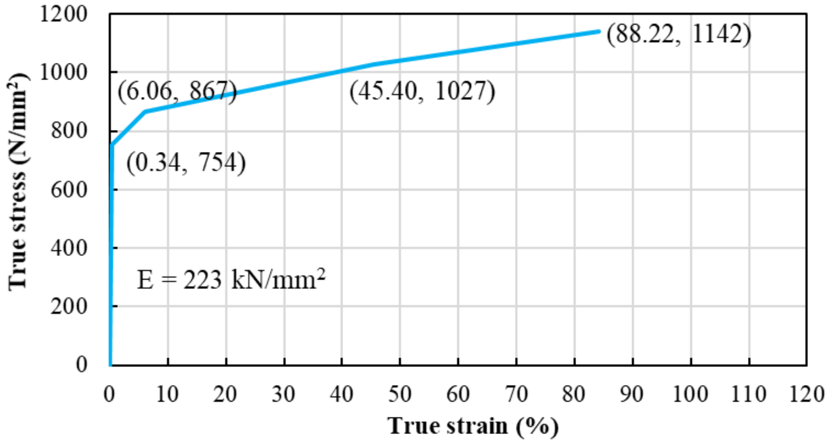

b) 10 mm thick S690 plate

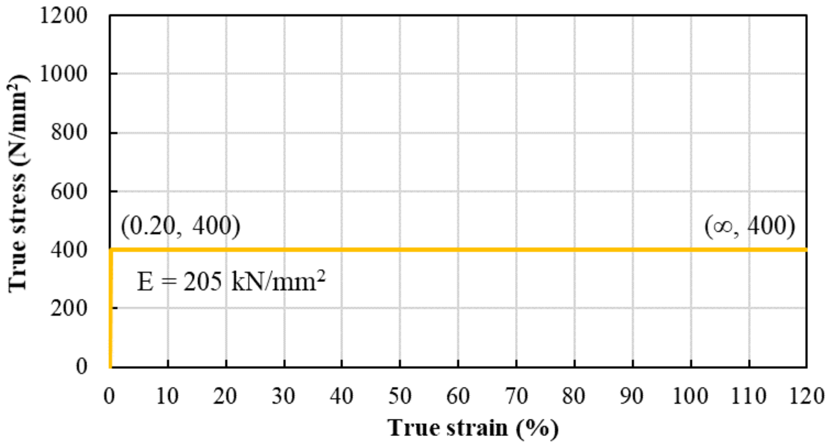

c) 20 mm thick S355 plate

Fig. 7.2 Material models for model validation

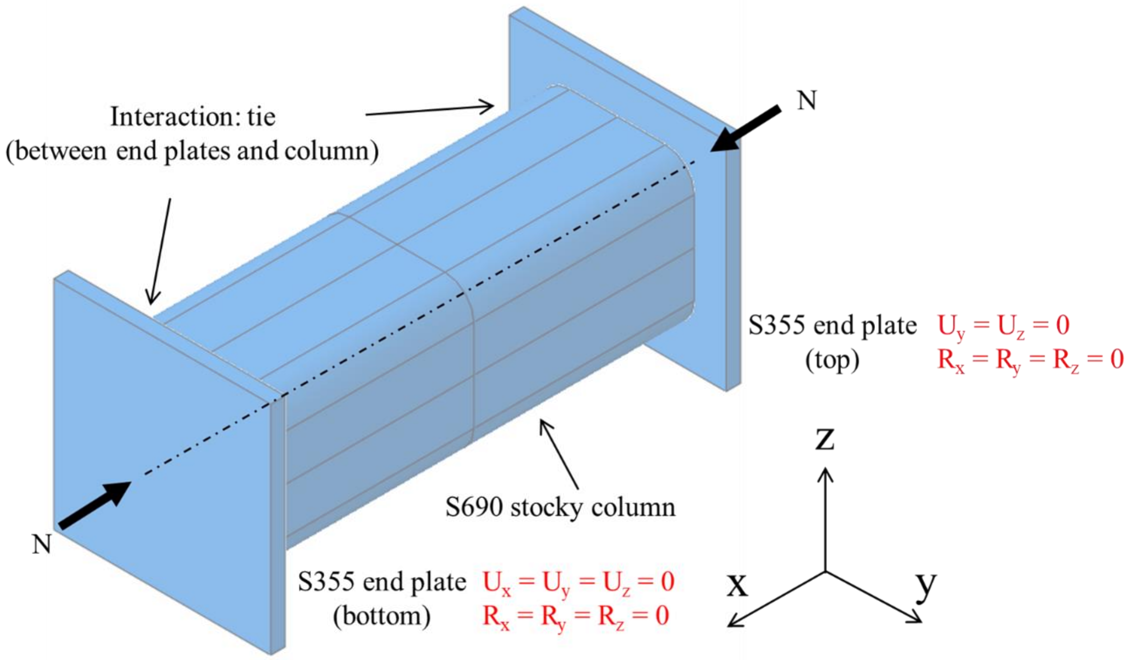

Fig. 7.3 Boundary conditions for stocky columns under concentric compression

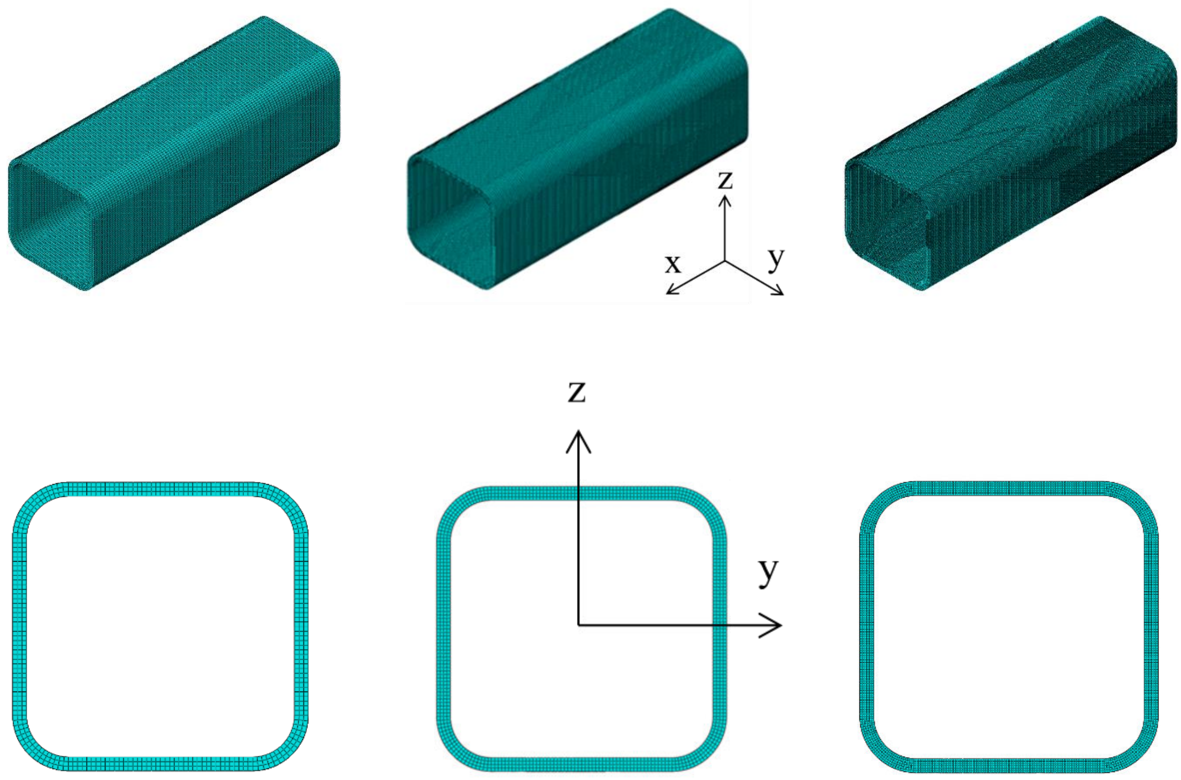

a) Mesh A@3-layer b) Mesh B@4-layer c) Mesh C@6-layer

Fig. 7.4 Mesh sizes for mesh convergence study: Test S3A-S

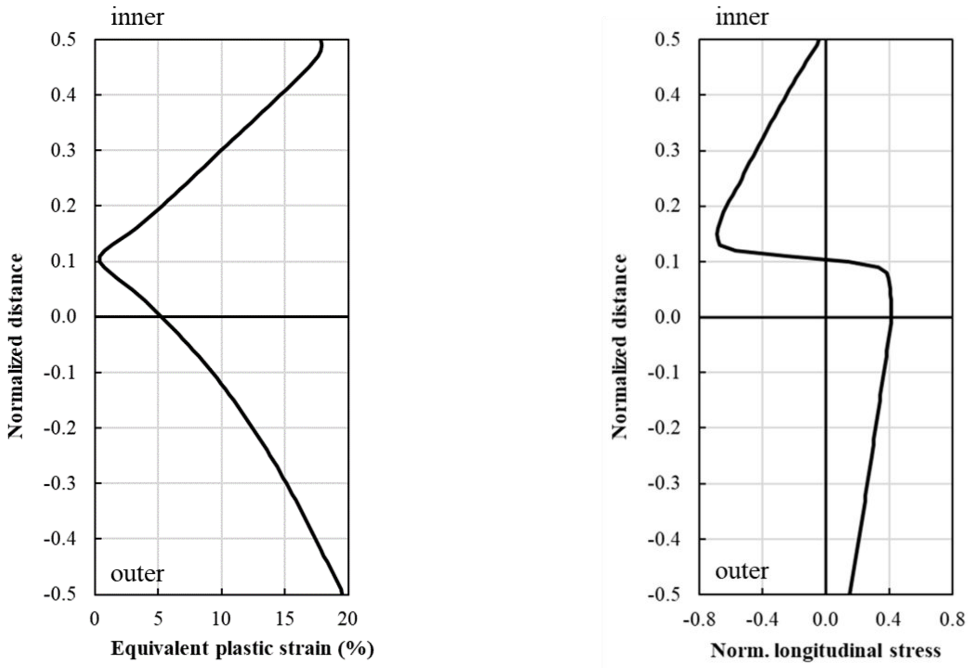

a) Equivalent plastic strains b) Longitudinal residual stresses

Fig. 7.5 Typical equivalent plastic strains and longitudinal residual stresses at the corner regions

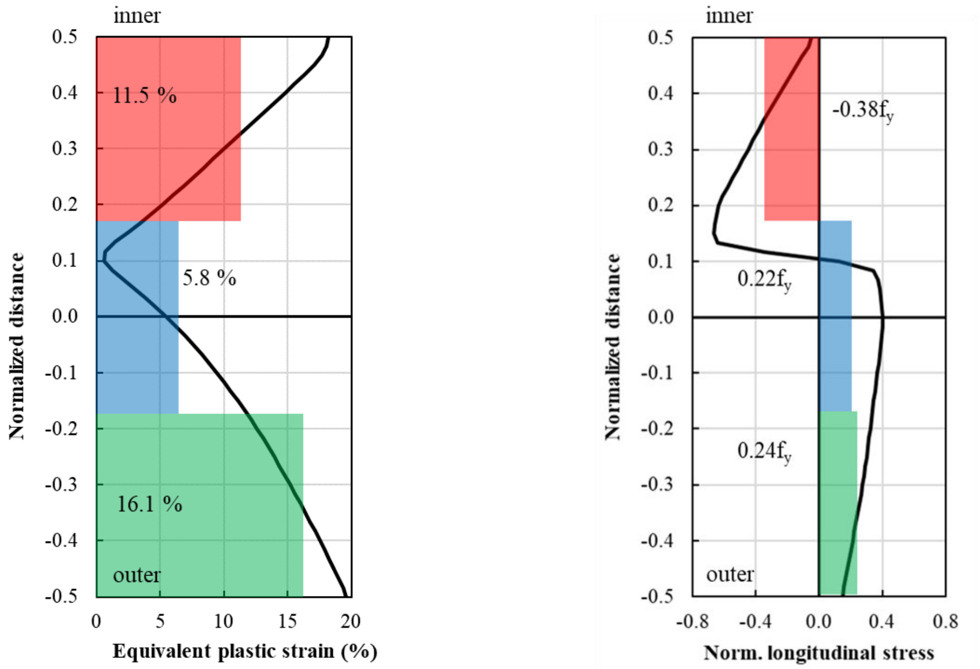

a) Equivalent plastic strains b) Longitudinal residual stresses

Fig. 7.6 Distributions of initial strains and stresses at the corner regions of 6 mm thick plate

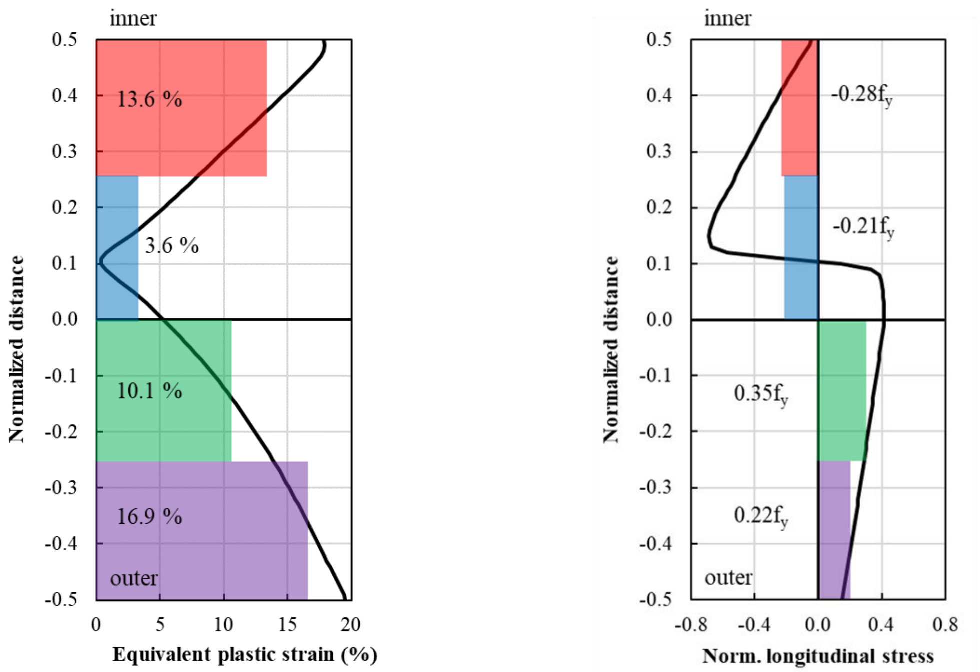

a) Equivalent plastic strains b) Longitudinal residual stresses

Fig. 7.7 Distributions of initial strains and stresses at the corner regions of 10 mm thick plate

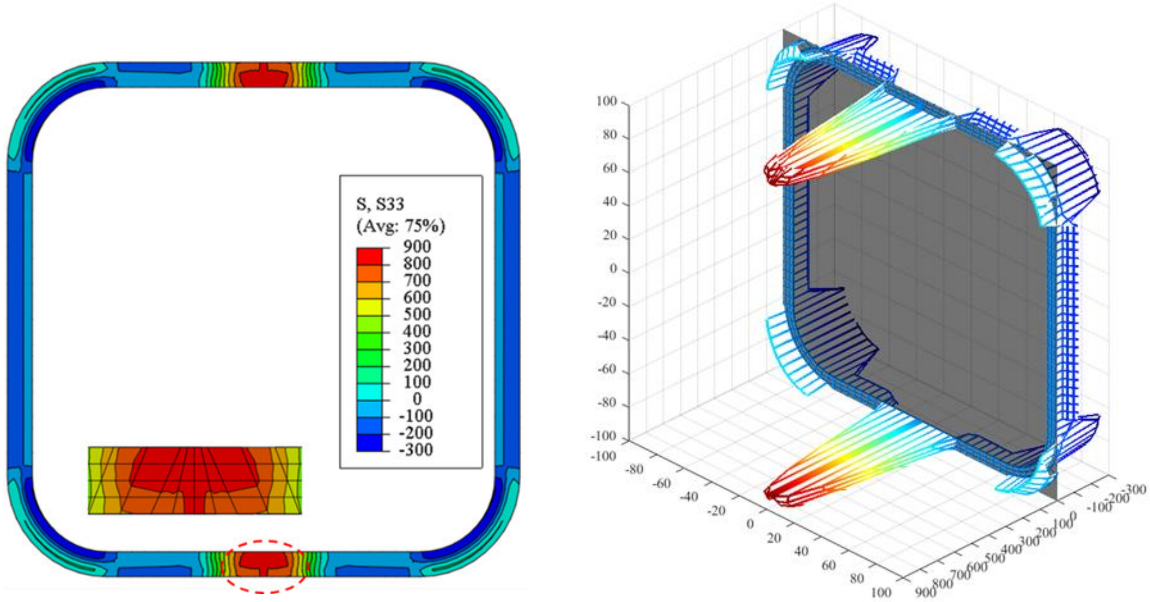

a) Series SA section

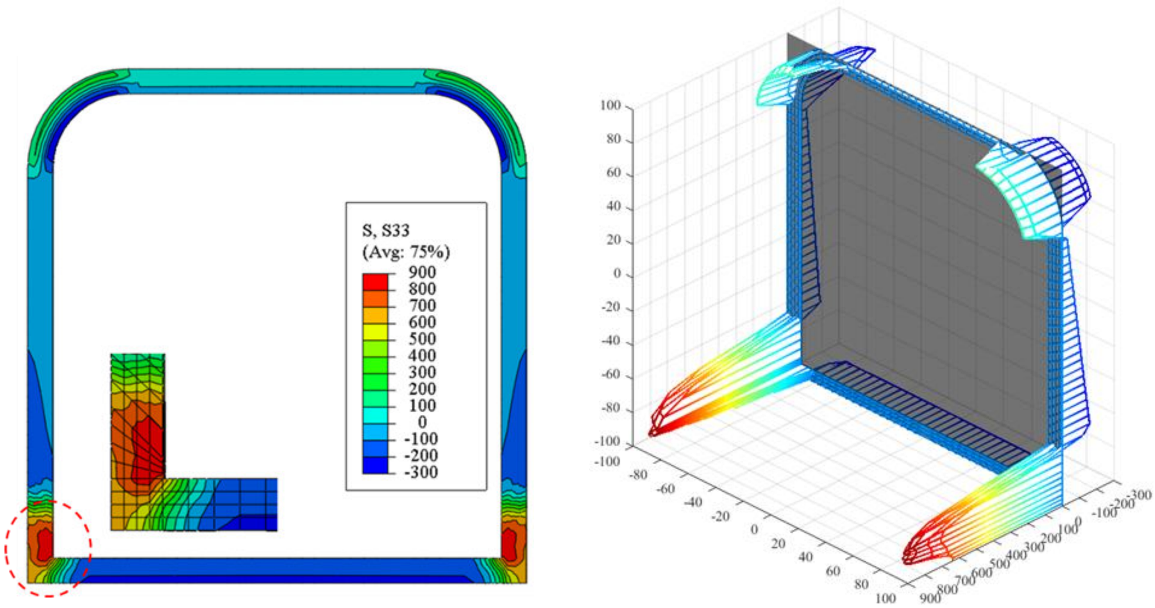

b) Series SB section

Fig. 7.8 Typical longitudinal residual stresses obtained from thermomechanical analyses

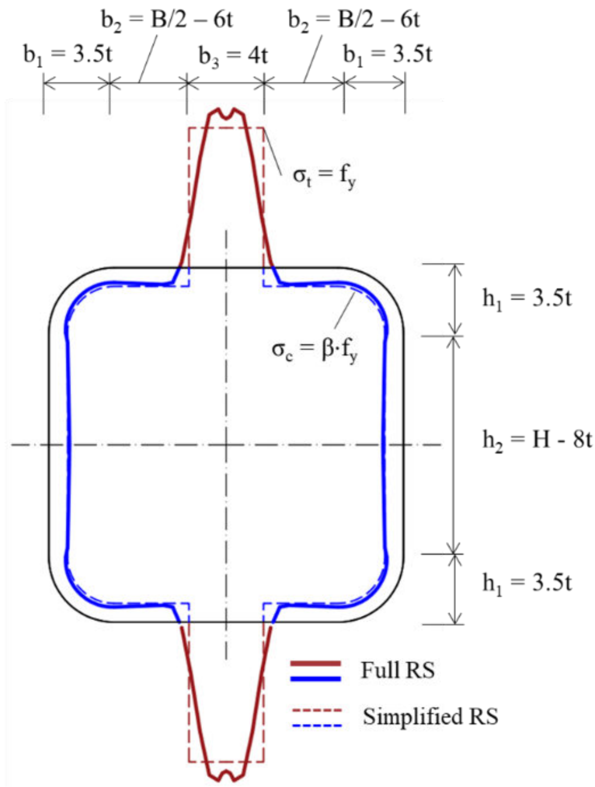

a) Series SA section

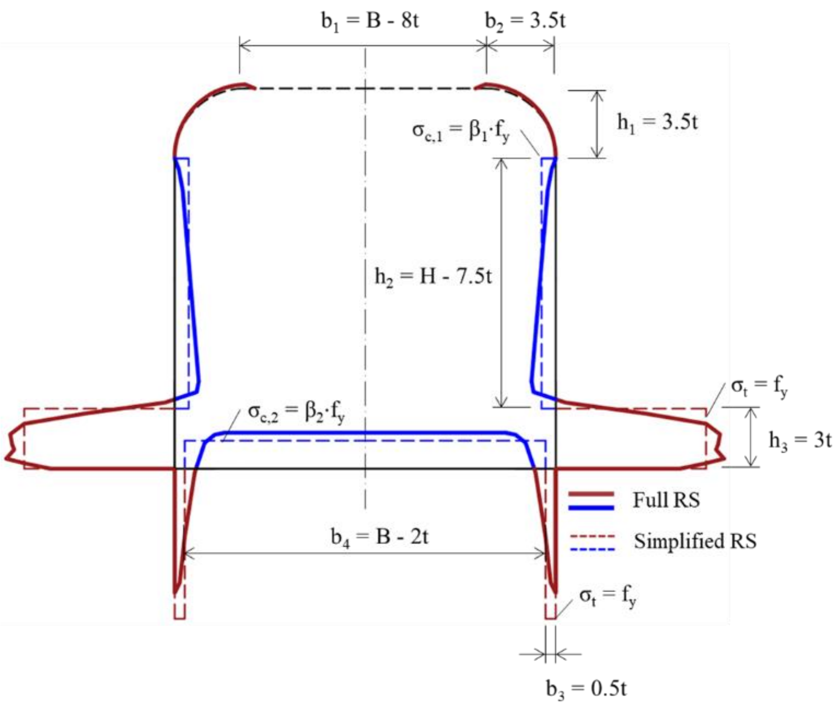

b) Series SB section

Fig. 7.9 Simplified longitudinal residual stresses due to welding

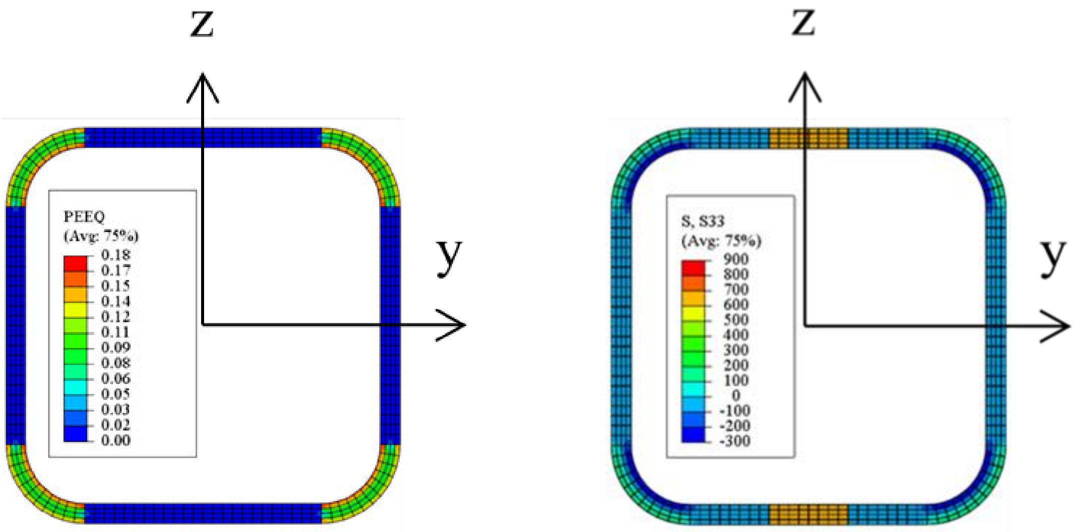

a) equivalent plastic strains b) longitudinal residual stresses

Fig. 7.10 Initial states of sections: Section S3A

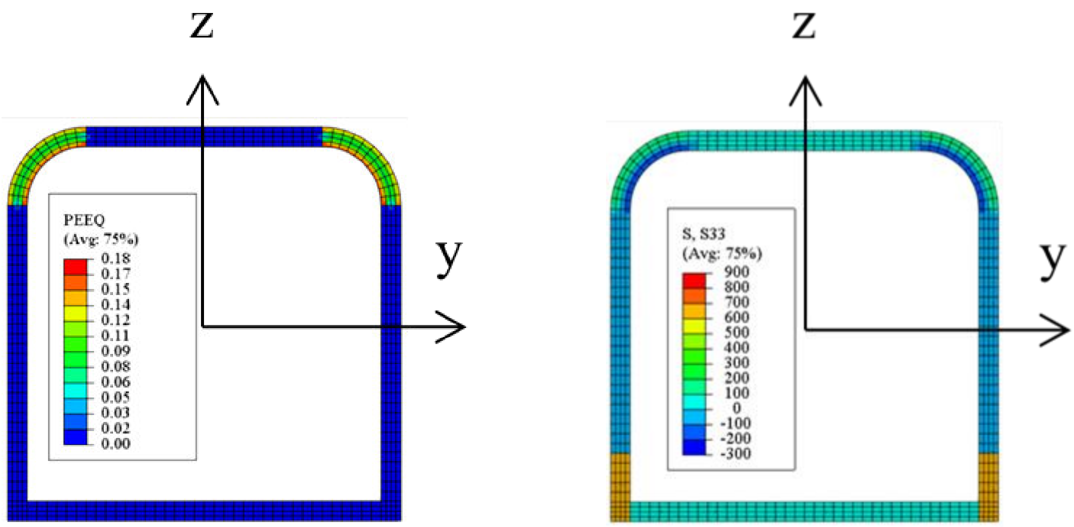

a) equivalent plastic strains b) longitudinal residual stresses

Fig. 7.11 Initial states of sections: Section S3B

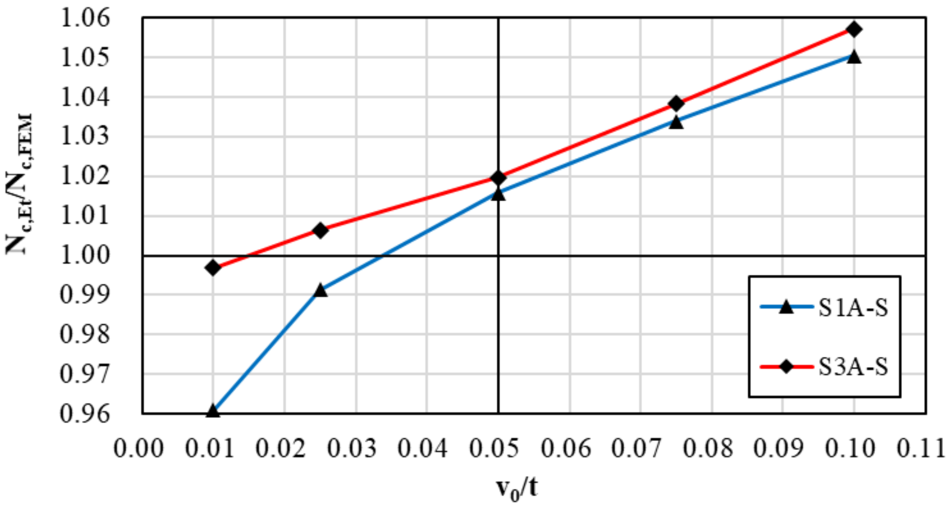

Fig. 7.12 Sensitivity study on geometric imperfection: Tests S1A-S and S3A-S

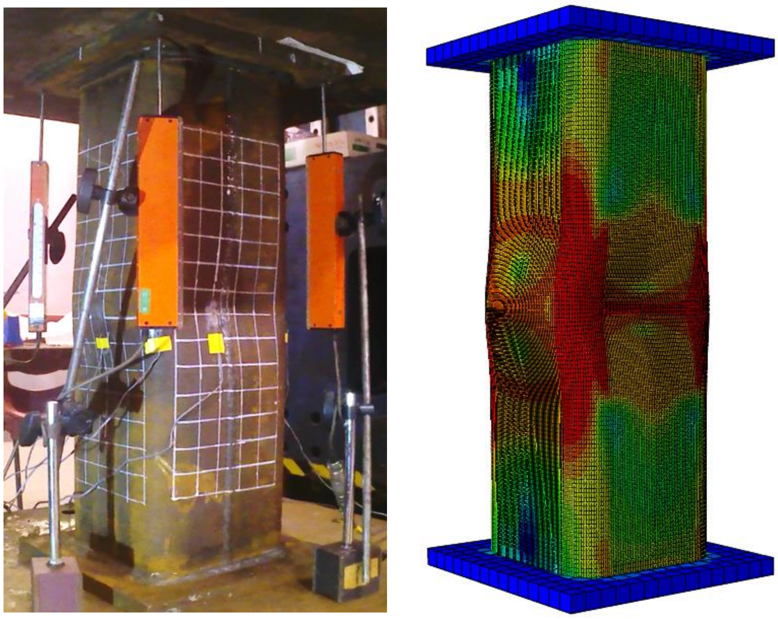

Fig. 7.13 Comparison between failure modes:
stocky columns under concentric compression—Test S3A-S

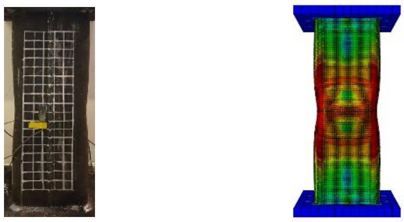

a) Test S1A-S

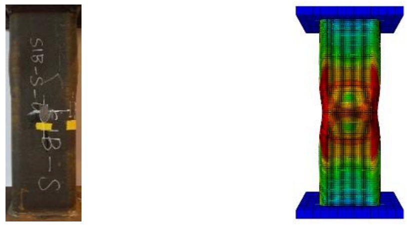

b) Test S1B-S

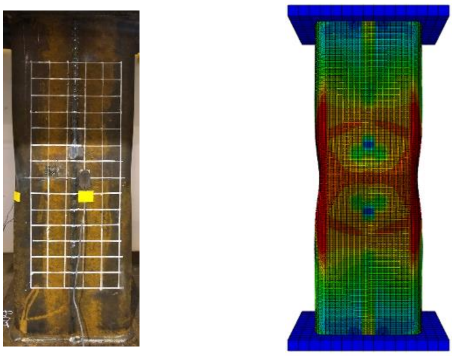

c) Test S2A-S

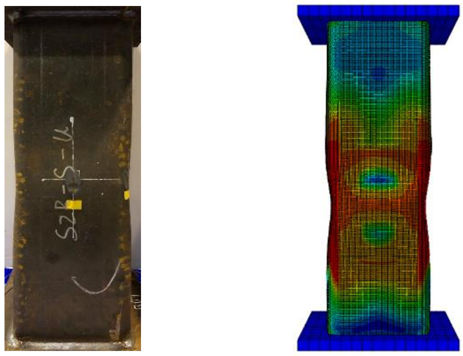

d) Test S2B-S

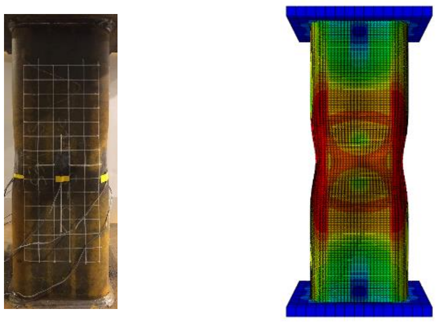

e) Test S3A-S

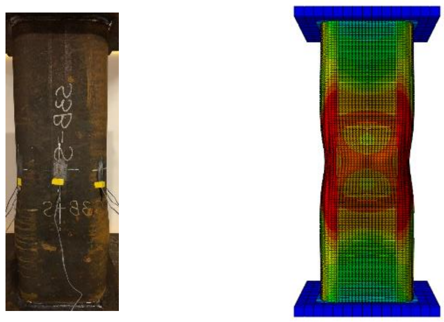

f) Test S3B-S

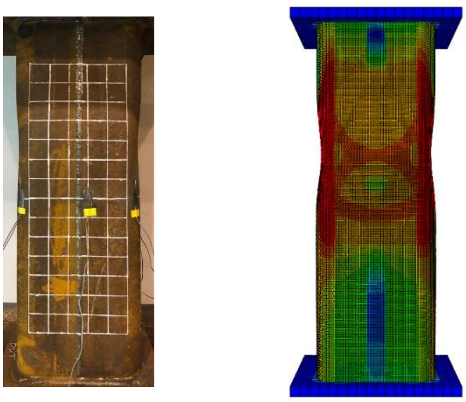

g) Test S4A-S

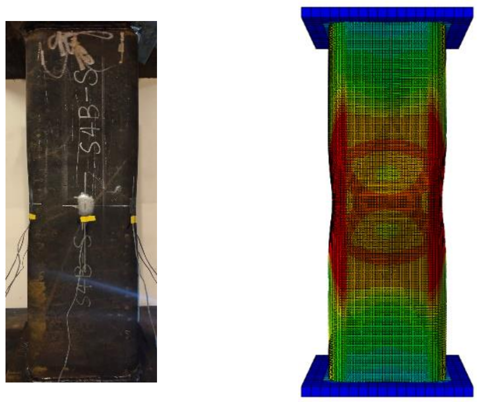

h) Test S4B-S

Fig. 7.14 Comparison between failure modes: stocky columns under concentric compression—Series S

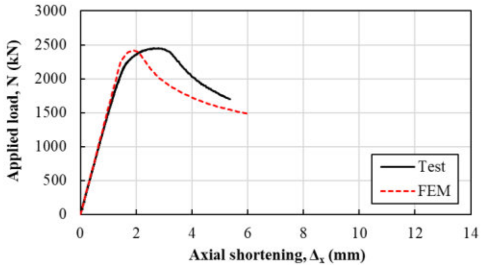

a) Test S1A-S

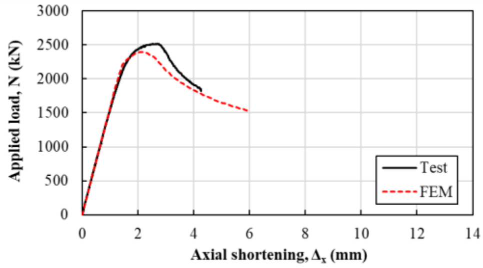

b) Test S1B-S

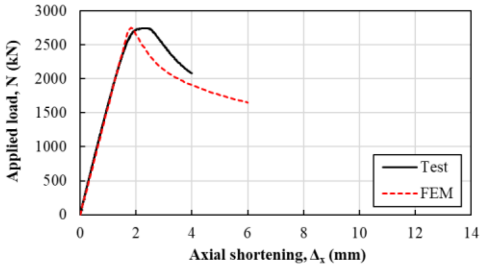

c) Test S2A-S

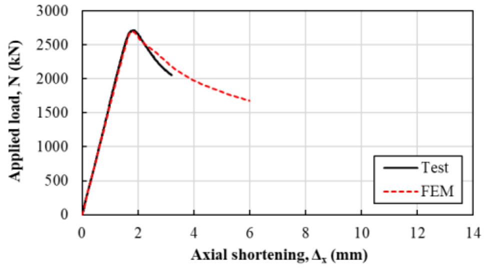

d) Test S2B-S

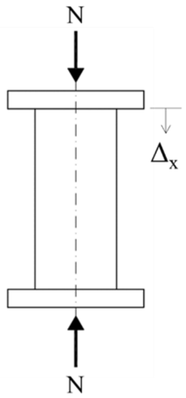

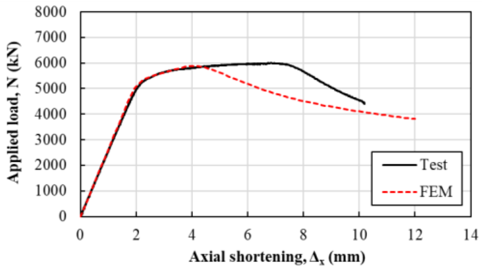

e) Test S3A-S

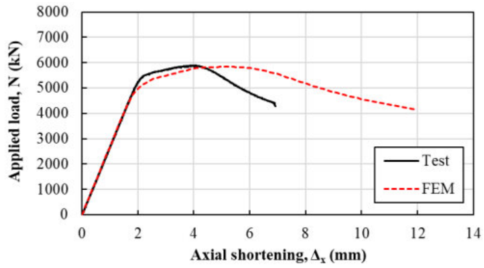

f) Test S3B-S

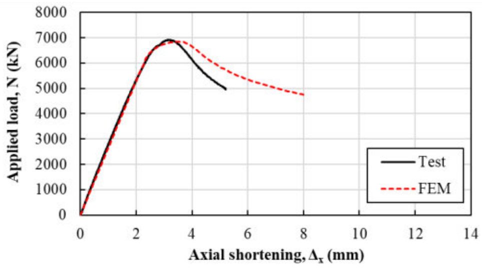

g) Test S4A-S

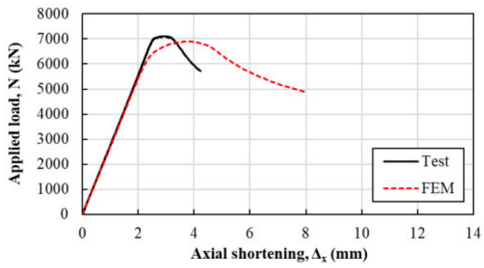

h) Test S4B-S

Fig. 7.15 Comparison between load-displacement curves: stocky columns under concentric compression—Series S

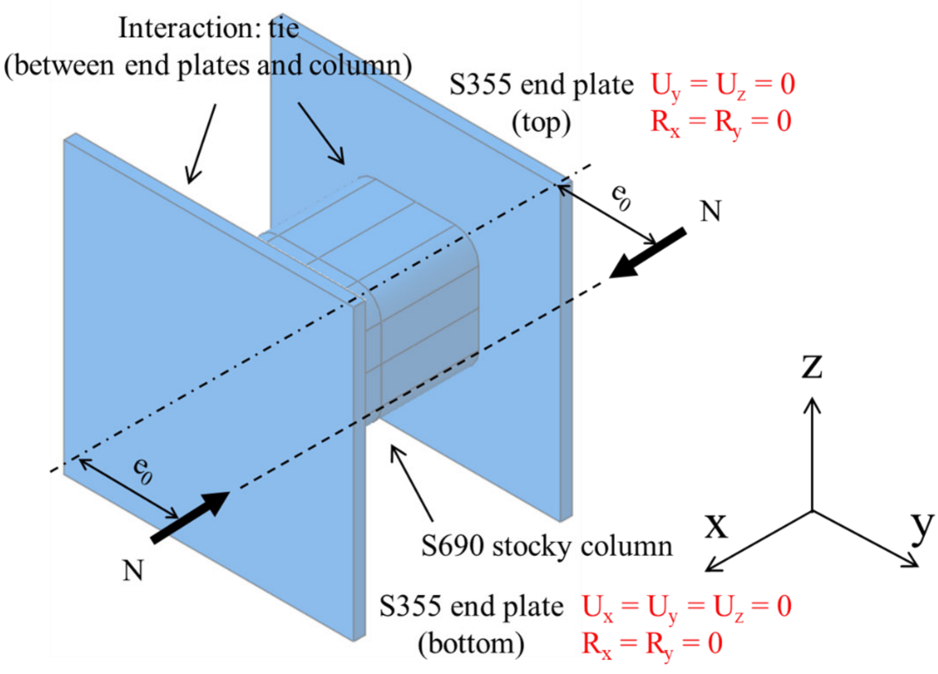

Fig. 7.16 Boundary conditions for stocky columns under eccentric compression

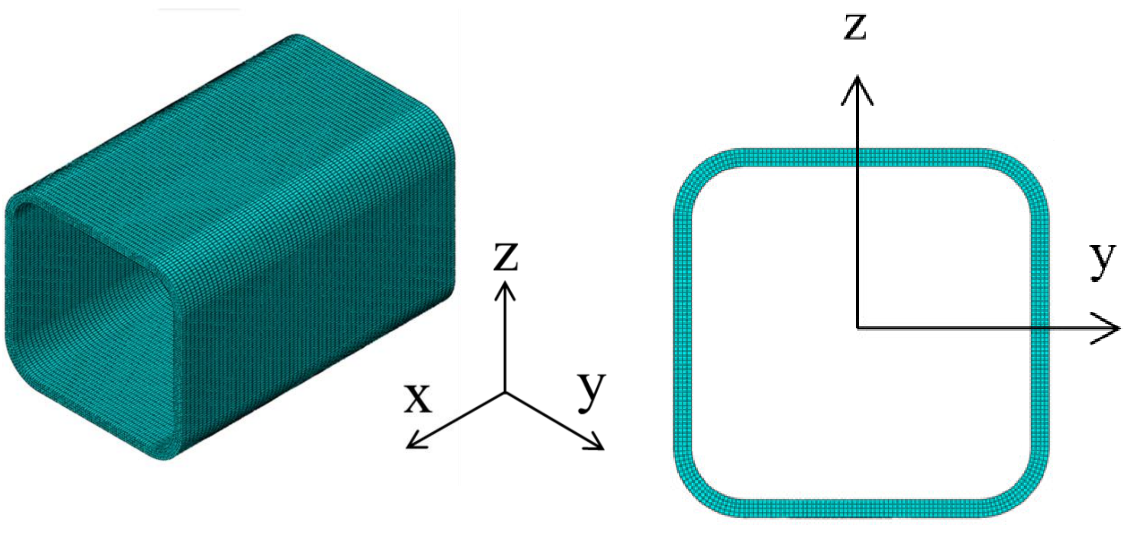

Fig. 7.17 Mesh sizes of stocky column under eccentric compression: Test S3A-E

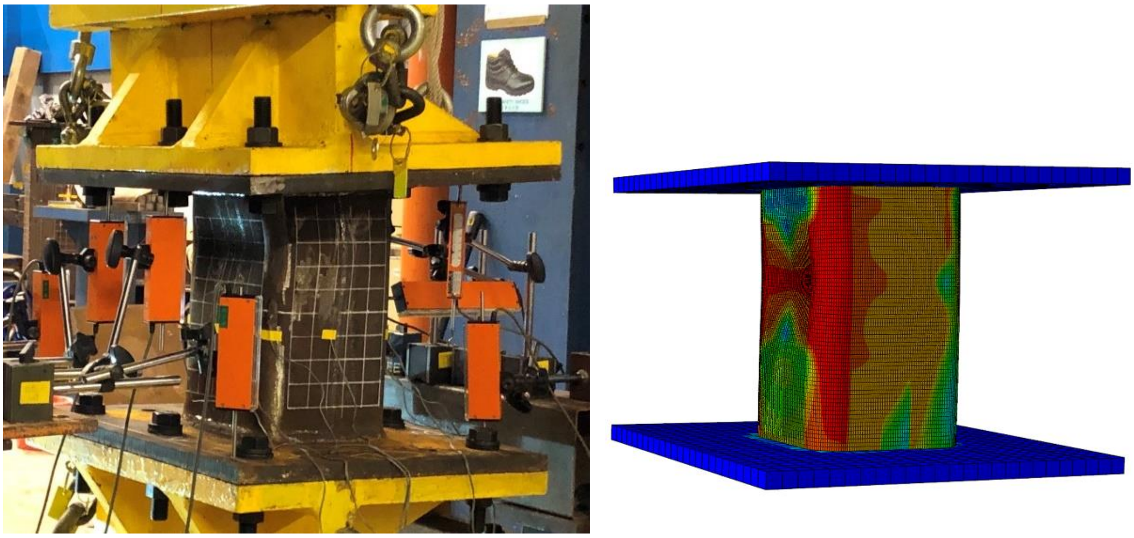

Fig. 7.18 Comparison between failure modes:
stocky columns under eccentric compression—Test S3A-E

a) Test S2A-E

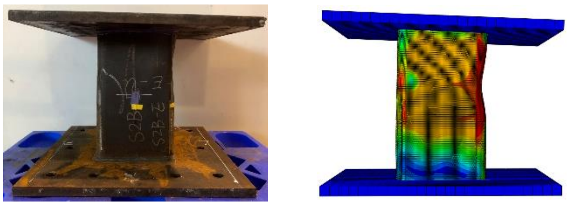

b) Test S2B-E

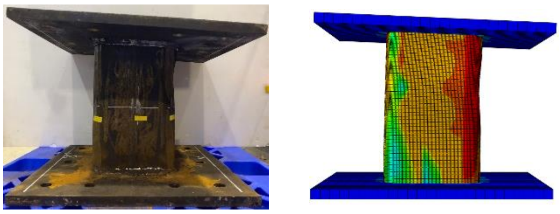

c) Test S3A-E

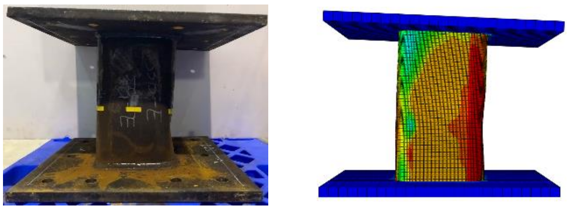

d) Test S3B-E

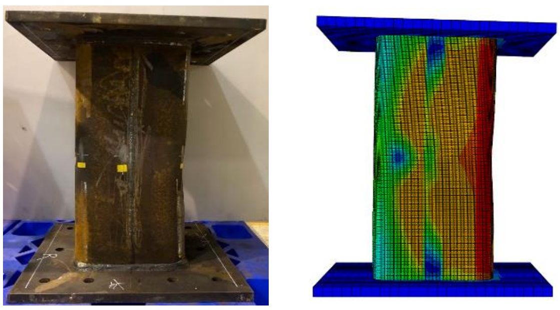

e) Test S4A-E

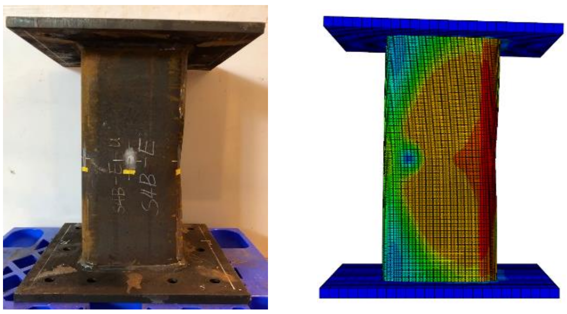

f) Test S4B-E

Fig. 7.19 Comparison between failure modes:
stocky columns under eccentric compression—Series E

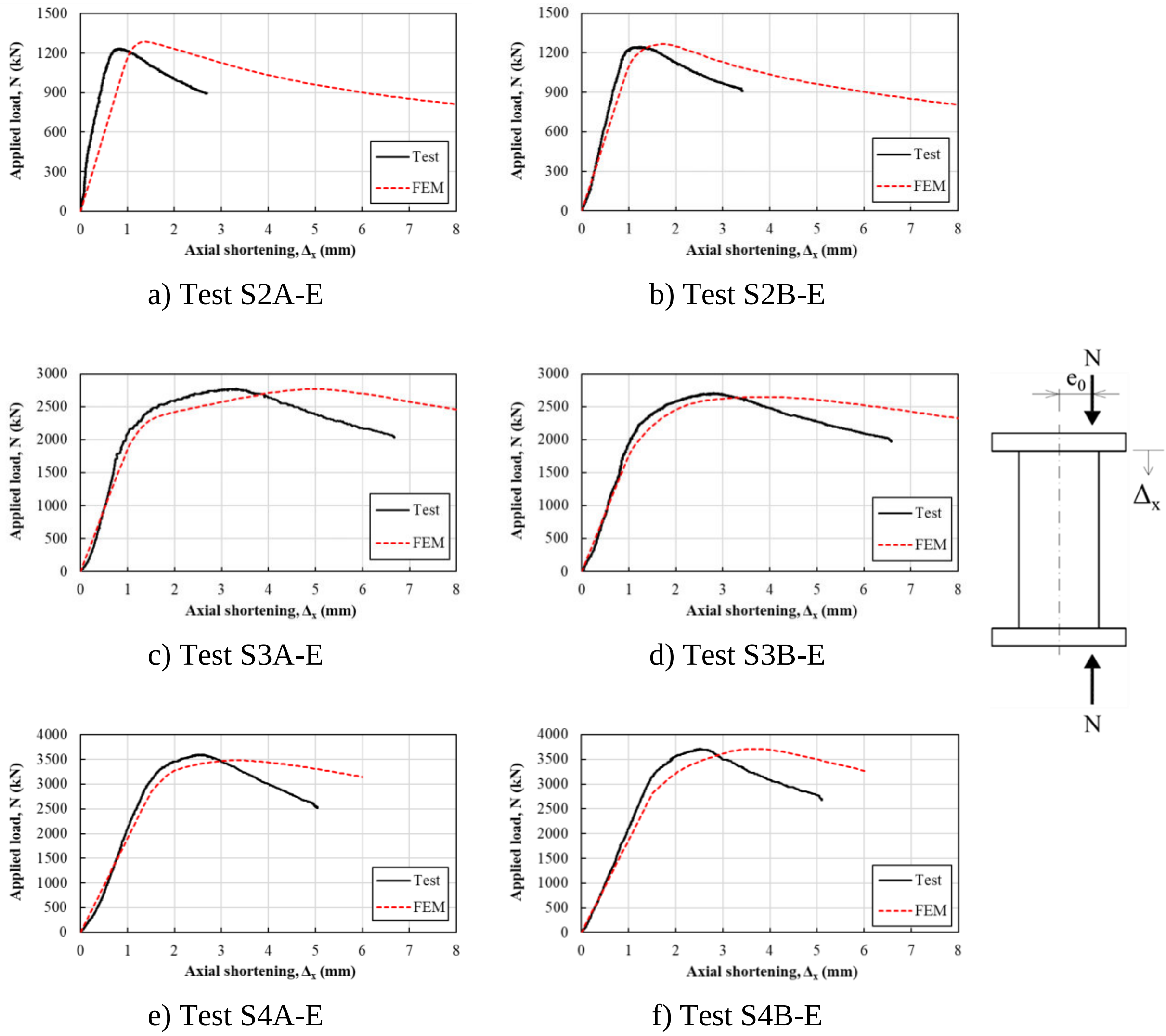

a) Test S2A-E
b) Test S2B-E
c) Test S3A-E
d) Test S3B-E
e) Test S4A-E
f) Test S4B-E

Fig. 7.20 Comparison between load-displacement curves: stocky columns under eccentric compression—Series E

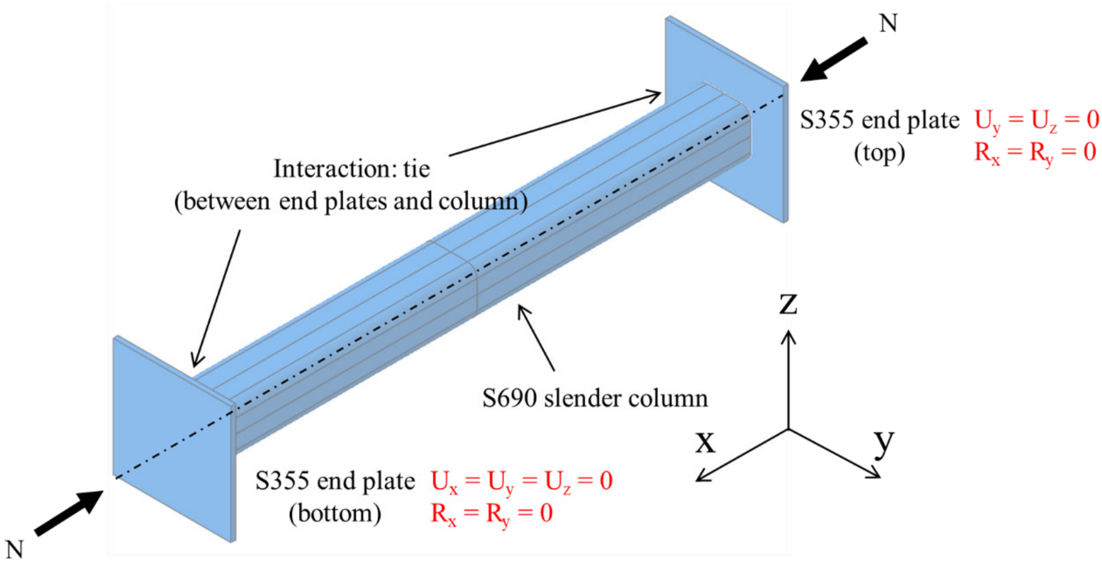

Fig. 7.21 Boundary conditions for slender columns under concentric compression

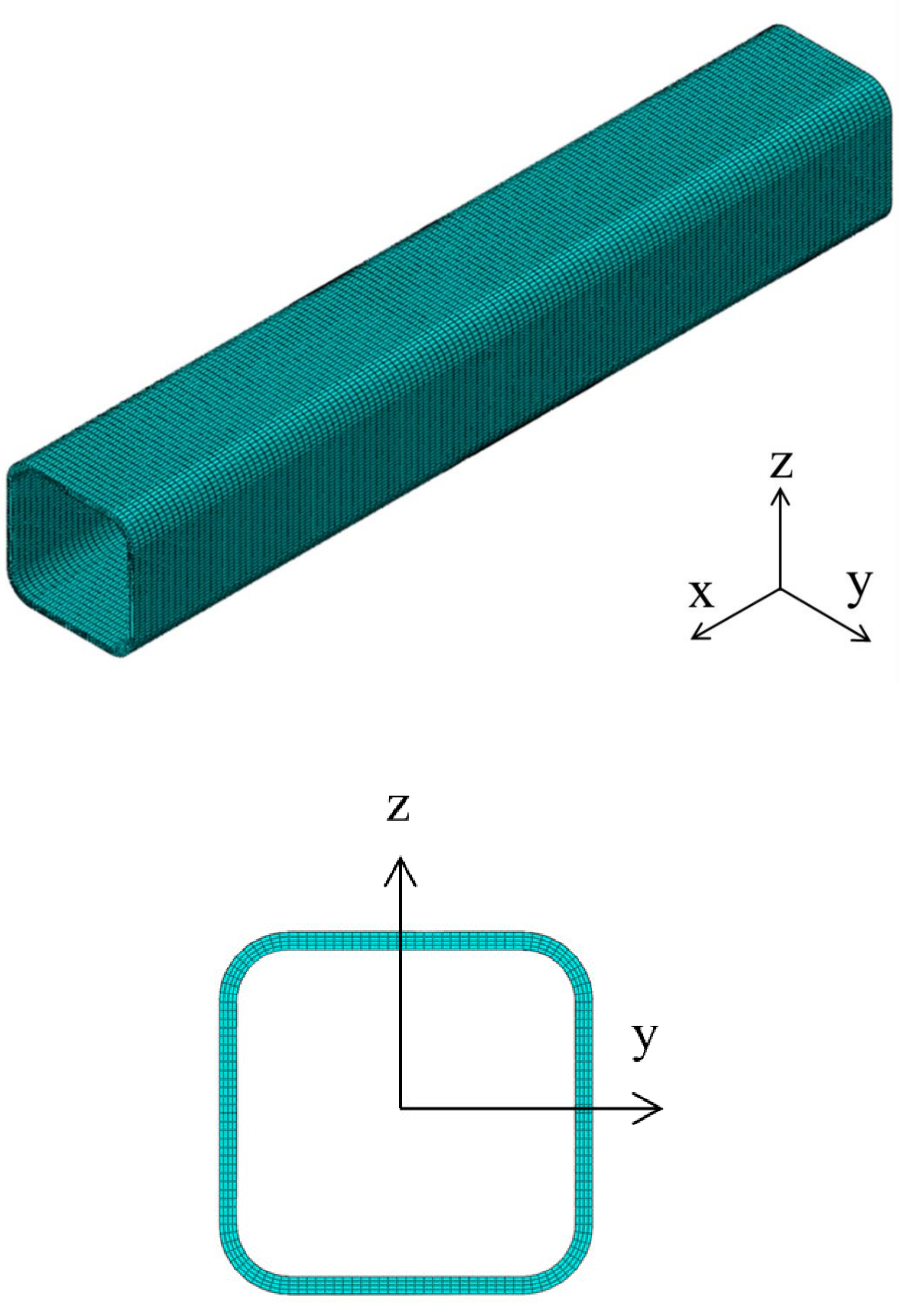

Fig. 7.22 Mesh sizes of slender column under concentric compression: Test S3A-P

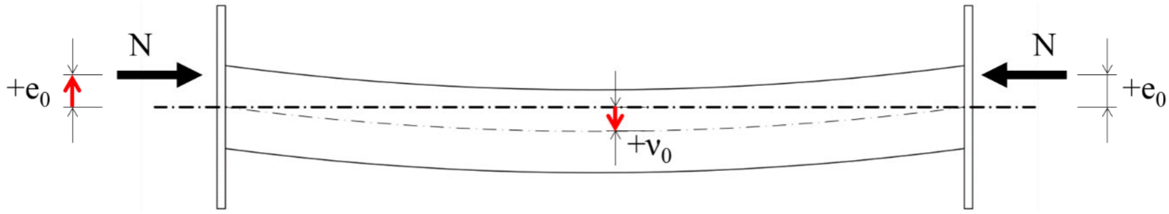

Fig. 7.23 Initial out-of-straightness and initial loading eccentricity

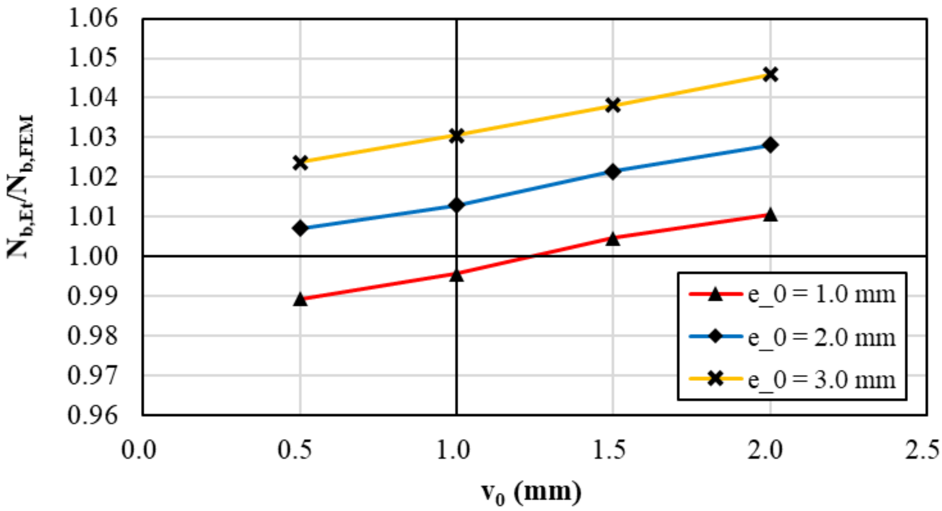

Fig. 7.24 Sensitivity study on out-of-straightness and loading eccentricity: Test S3A-Q

Fig. 7.25 Comparison between failure modes:
slender columns under concentric compression—Test S3A-Q

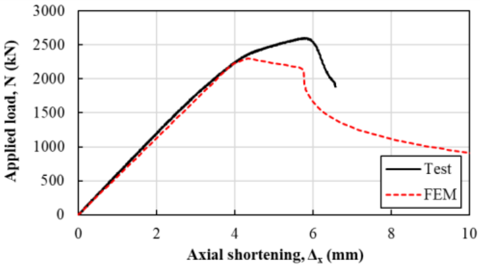

a) Test S1A-P

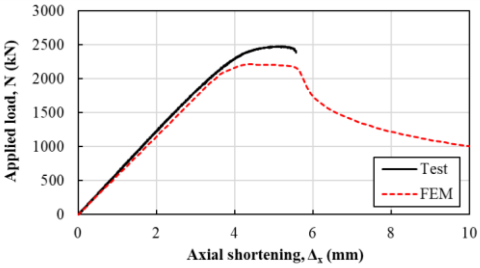

b) Test S1B-P

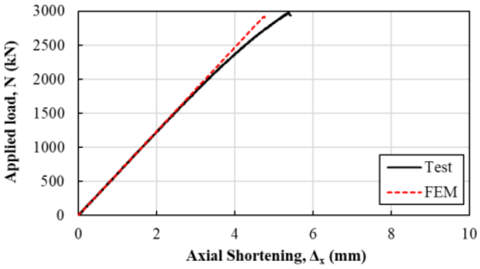

c) Test S2A-P

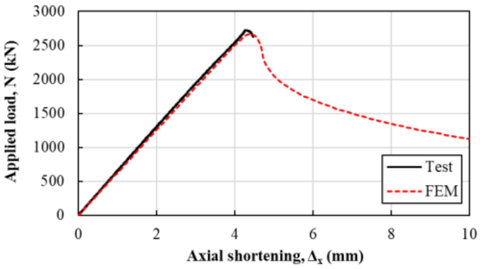

d) Test S2B-P

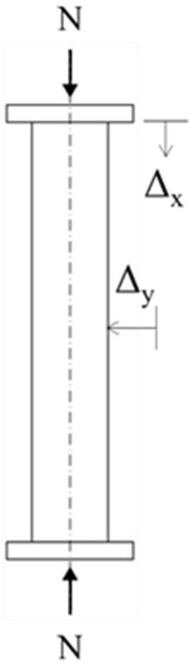

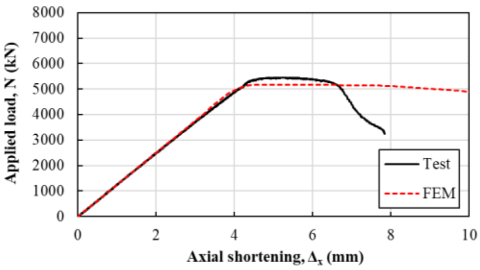

e) Test S3A-P

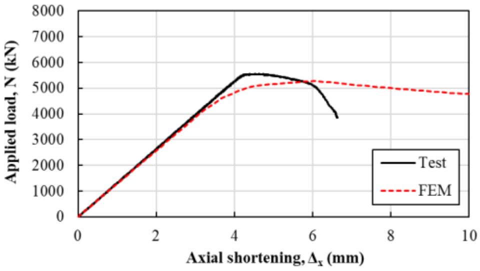

f) Test S3B-P

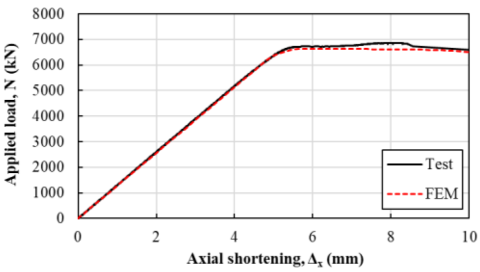

g) Test S4A-P

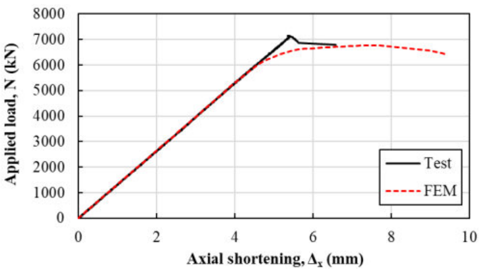

h) Test S4B-P

Fig. 7.26 Comparison between load-shortening curves: slender columns under concentric compression—Series P

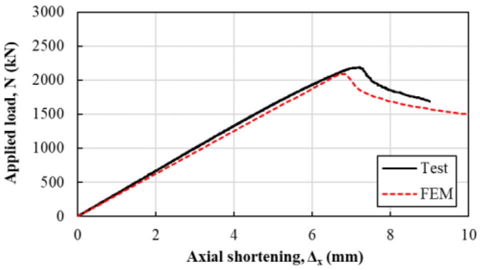

a) Test S1A-Q

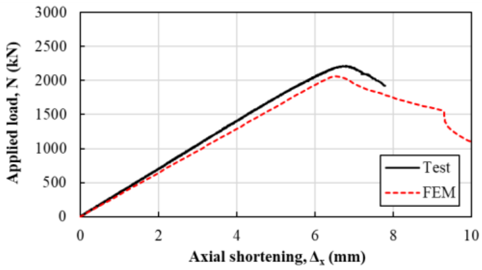

b) Test S1B-Q

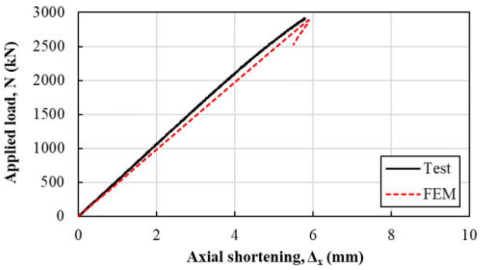

c) Test S2A-Q

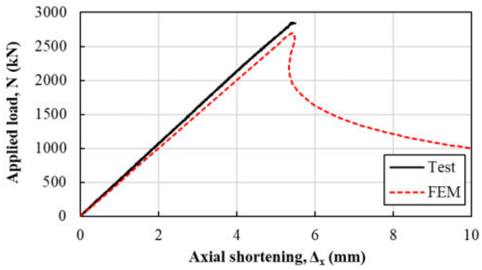

d) Test S2B-Q

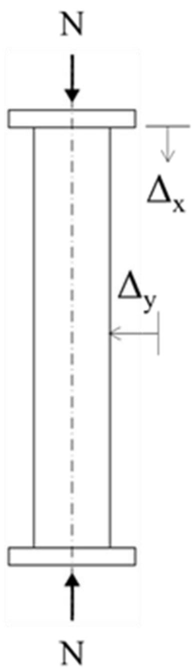

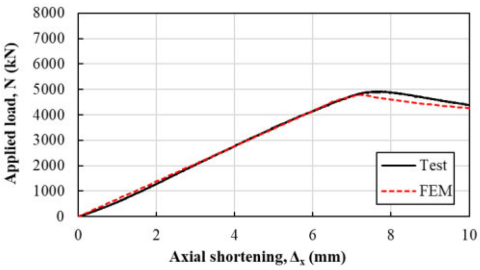

e) Test S3A-Q

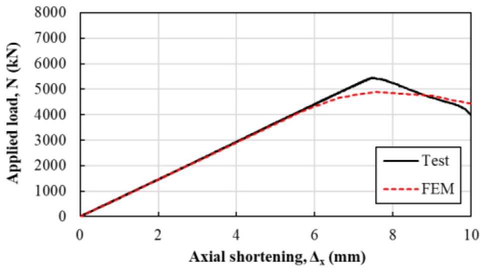

f) Test S3B-Q

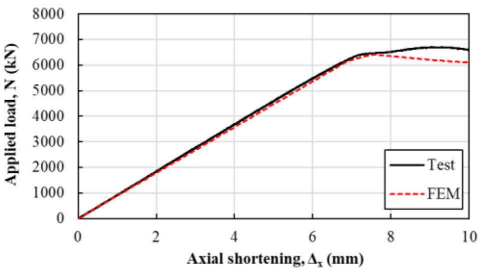

g) Test S4A-Q

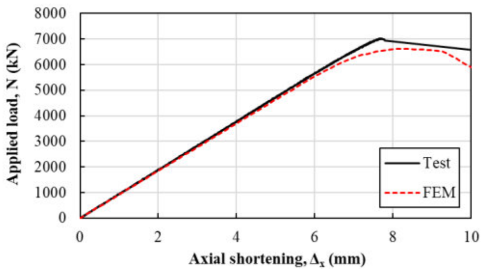

h) Test S4B-Q

Fig. 7.27 Comparison between load-shortening curves: slender columns under concentric compression—Series Q

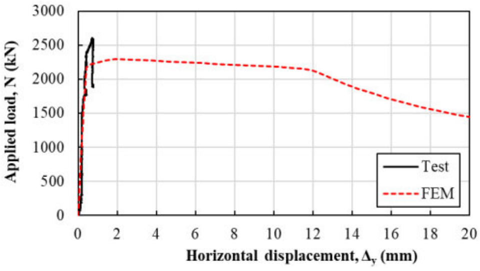

a) Test S1A-P

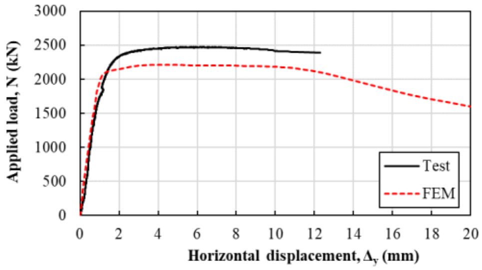

b) Test S1B-P

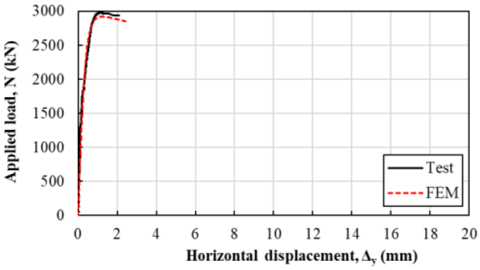

c) Test S2A-P

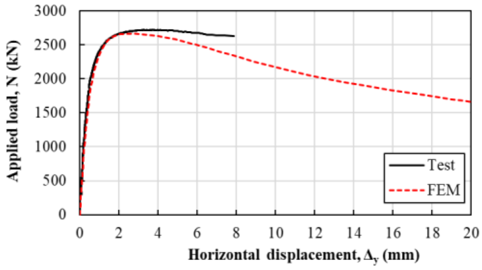

d) Test S2B-P

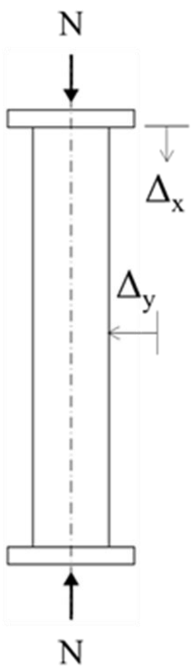

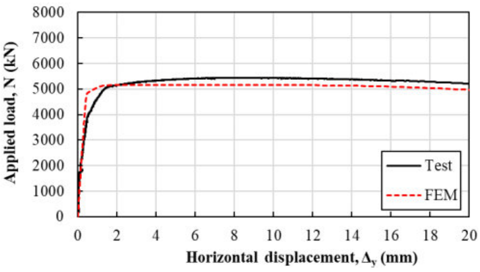

e) Test S3A-P

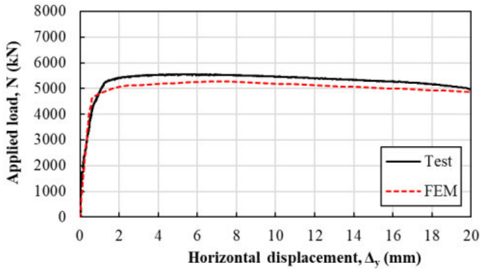

f) Test S3B-P

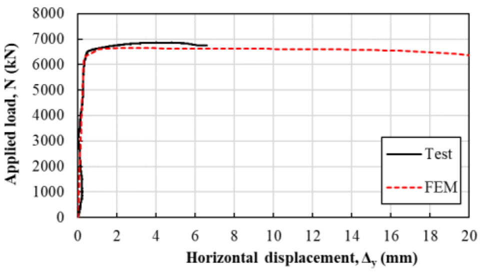

g) Test S4A-P

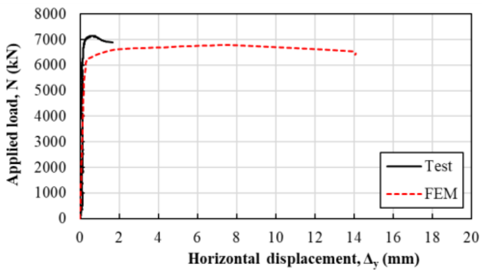

h) Test S4B-P

Fig. 7.28 Comparison between load-deflection curves: slender columns under concentric compression—Series P

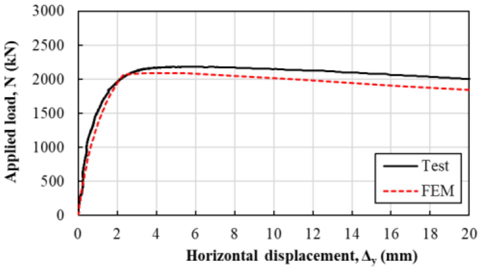

a) Test S1A-Q

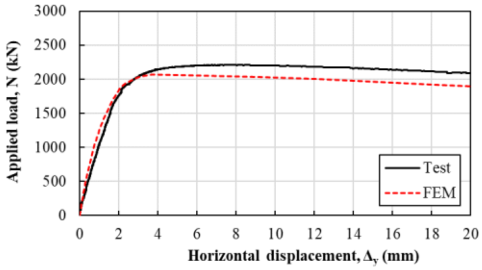

b) Test S1B-Q

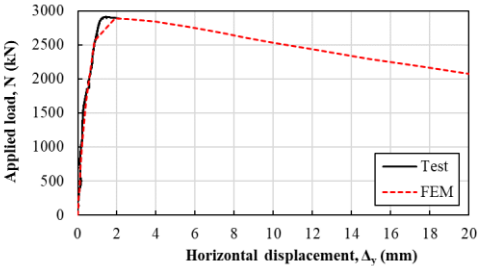

c) Test S2A-Q

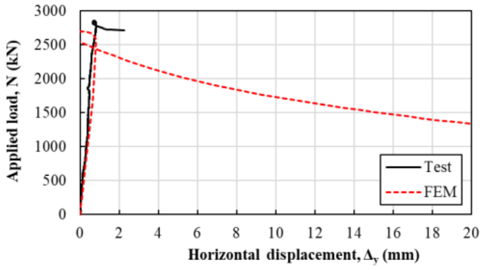

d) Test S2B-Q

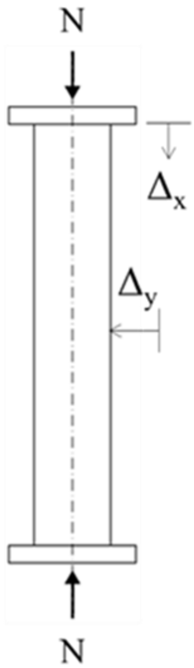

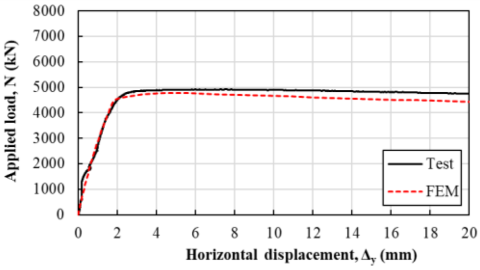

e) Test S3A-Q

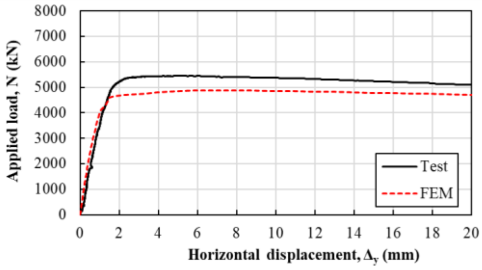

f) Test S3B-Q

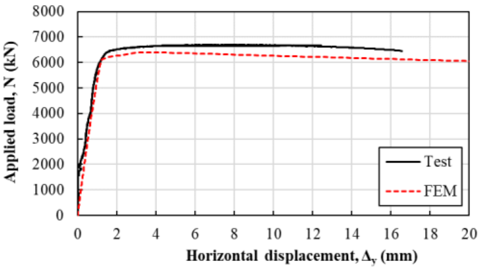

g) Test S4A-Q

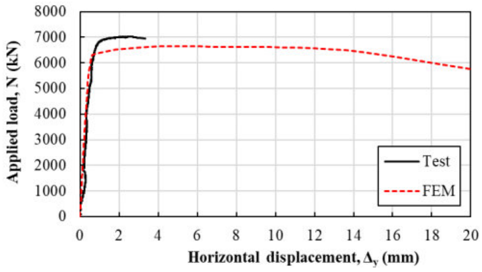

h) Test S4B-Q

Fig. 7.29 Comparison between load-deflection curves: slender columns under concentric compression—Series Q

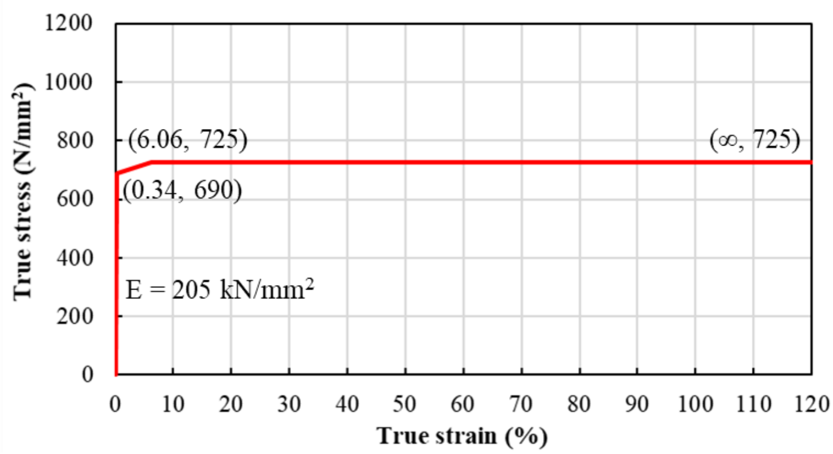

a) linear hardening

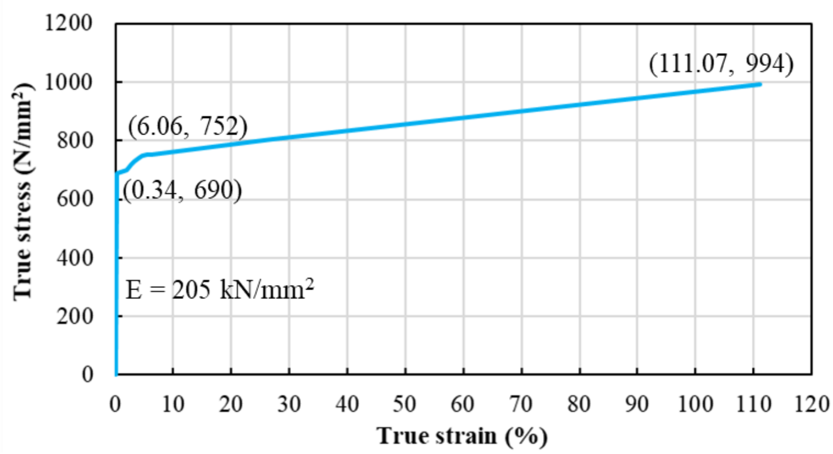

b) non-linear hardening
(Ho et al. 2020)

Fig. 7.30 Material models for parametric studies

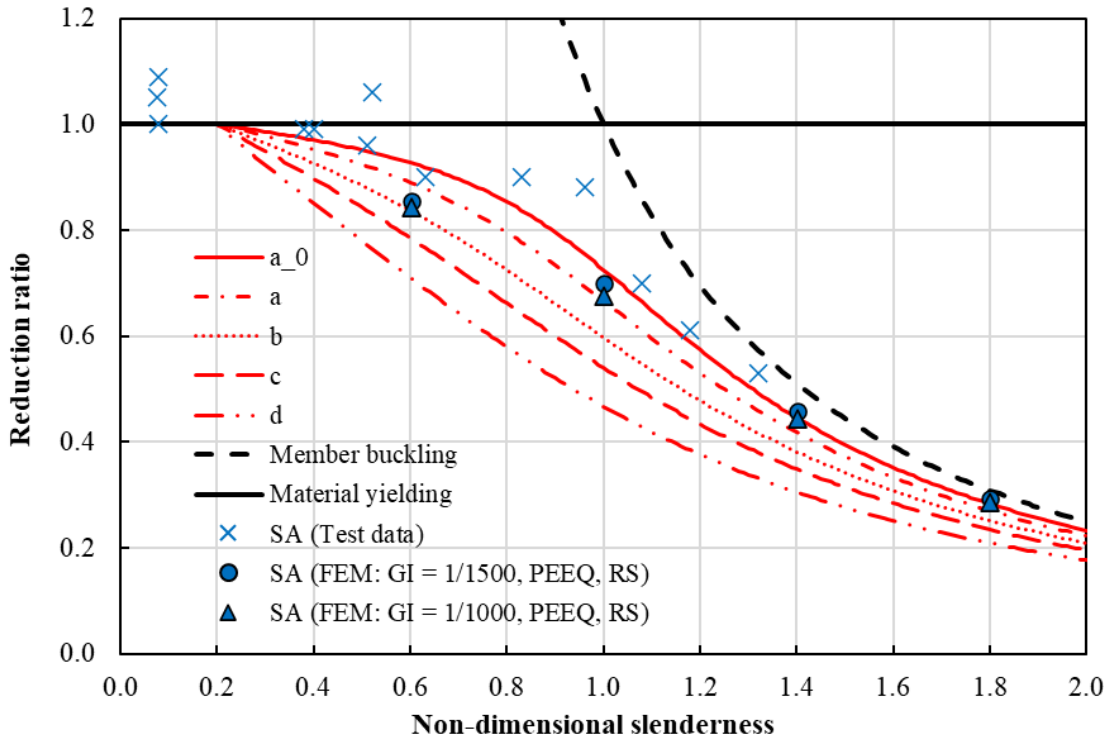

Fig. 7.31 Test data, parametric studies and design curves of Series SA sections

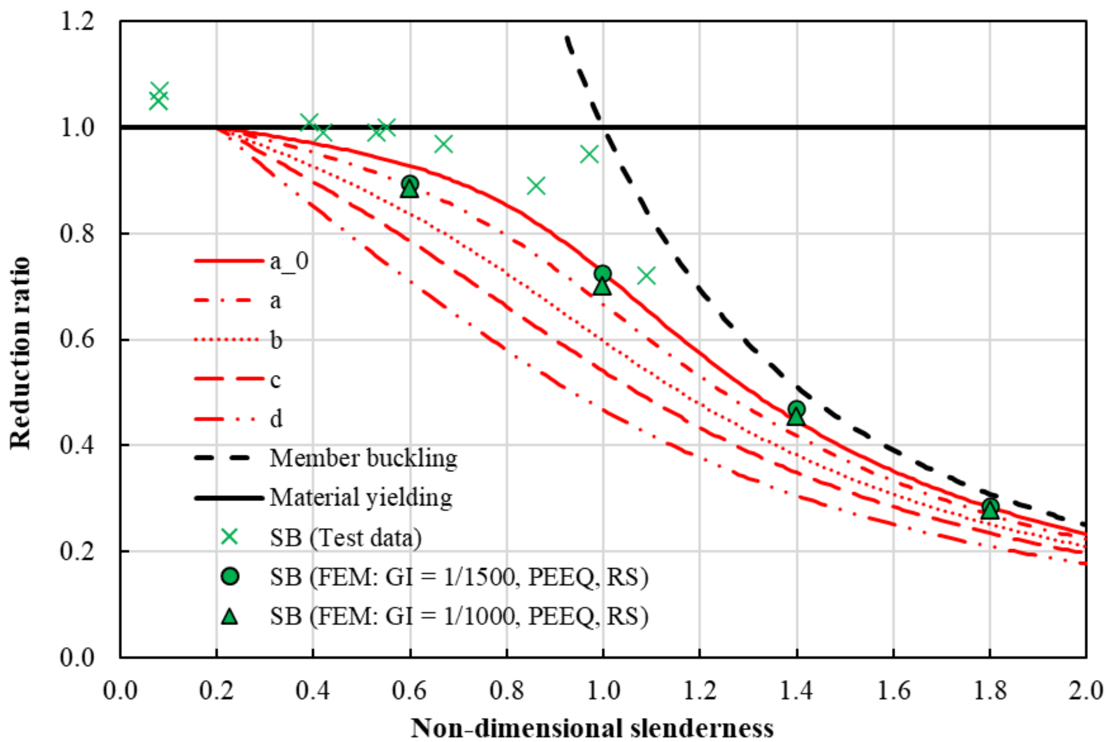

Fig. 7.32 Test data, parametric studies and design curves of Series SB sections

Table 7.1 Compatibility of solid elements in various numerical analyses

Type of analysis	Name of solid element	Purpose of analysis	Corresponding Chapter in the Thesis
(1) 3D transverse bending analysis	C3D8R	To analyse stresses and strains due to transverse bending and springback.	Chapter 5
(2) 3D heat transfer analysis	DC3D8	To analyse temperature fields and histories due to longitudinal welding.	Chapter 6
(3) 3D thermomechanical analysis	C3D8R	To analyse residual stresses due to longitudinal welding.	Chapter 6
(4) 3D column buckling analysis	C3D8R	To analyse stresses, strains, forces and displacements under compression.	Chapter 7

Note:
C3D8R is an 8-node linear, reduced integration and hourglass control solid element; and
DC3D8 is an 8-node linear heat transfer solid element.

Table 7.2 Investigation programme of model validation: stocky columns under concentric compression

Series	Designation	Section classification	Measured dimension of specimen (mm)					A_g (mm^2)	I_z (mm^4)	$\bar{\lambda}_z$
			B	H	t	R_{out}	L_m			
SA	(1) S1A-S	2	163.0	150.0	5.88	23.88	461	3355	1301 x10^4	0.08
	(2) S2A-S	4	207.7	204.5	5.88	23.88	608	4497	2955 x10^4	0.08
	(3) S3A-S	1	212.0	206.7	9.89	39.89	610	7297	4673 x10^4	0.08
	(4) S4A-S	1	252.0	260.0	9.89	39.89	759	9143	8652 x10^4	0.08
SB	(5) S1B-S	3	150.0	156.0	5.88	23.88	461	3355	1152 x10^4	0.08
	(6) S2B-S	4	200.0	207.0	5.88	23.88	609	4542	2841 x10^4	0.08
	(7) S3B-S	2	202.0	208.5	9.89	39.89	608	7432	4499 x10^4	0.08
	(8) S4B-S	3	250.0	257.0	9.89	39.89	758	9341	8873 x10^4	0.08

Table 7.3 Programme and results of mesh convergence study: Test S3A-S

Model	Global mesh size (mm)	Number of elements			Total number of elements	Computational time (min)	$N_{c,FEM}$ (kN)	$N_{c,Et}$ / $N_{c,FEM}$
		through thickness	at corner	along length				
(1) Mesh A@3-layer	3.33	3	15	92	59892	12	5862	1.023
(2) Mesh B@4-layer	2.50	4	22	122	142008	37	5878	1.021
(3) Mesh C@6-layer	1.67	6	33	184	490176	349	5882	1.020

Note: $N_{c,Et}$ = 5999 kN for Test S3A-S.

Table 7.4 Comparison between test data and numerical results: stocky columns under concentric compression

Series	Designation	Section classification	Measured dimension of specimen (mm)					A_g	$N_{c,Et}$	$N_{c,FEM}$	$N_{c,Et}$ / $N_{c,FEM}$
			B	H	t	R_{out}	L_m	(mm^2)	(kN)	(kN)	
SA	(1) S1A-S	2	163.0	150.0	5.88	23.88	461	3355	2450	2412	1.02
	(2) S2A-S	4	207.7	204.5	5.88	23.88	608	4497	2745	2752	1.00
	(3) S3A-S	1	212.0	206.7	9.89	39.89	610	7297	5999	5884	1.02
	(4) S4A-S	1	252.0	260.0	9.89	39.89	759	9143	6914	6842	1.01
SB	(5) S1B-S	3	150.0	156.0	5.88	23.88	461	3355	2517	2394	1.05
	(6) S2B-S	4	200.0	207.0	5.88	23.88	609	4542	2719	2699	1.01
	(7) S3B-S	2	202.0	208.5	9.89	39.89	608	7432	5891	5831	1.01
	(8) S4B-S	3	250.0	257.0	9.89	39.89	758	9341	7108	6896	1.03

Table 7.5 Comparison between test data and numerical results: stocky columns under eccentric compression

Series	Designation	Section classification	Measured dimension of specimen (mm)					A_g	e_0	$N_{c,Et}$	$N_{c,FEM}$	$N_{c,Et}$ / $N_{c,FEM}$
			B	H	t	R_{out}	L_m	(mm^2)	(mm)	(kN)	(kN)	
SA	(1) S2A-E	4	210.0	202.3	5.88	23.88	328	4499	99.5	1235	1286	0.96
	(2) S3A-E	1	214.0	203.5	9.89	39.89	329	7274	99.5	2772	2768	1.00
	(3) S4A-E	1	265.0	253.0	9.89	39.89	529	9261	100.5	3599	3482	1.03
SB	(4) S2B-E	4	198.0	206.7	5.88	23.88	329	4515	100.5	1246	1264	0.99
	(5) S3B-E	1	198.5	210.0	9.89	39.89	329	7392	101.0	2704	2646	1.02
	(6) S4B-E	3	250.0	260.3	9.89	39.89	529	9405	101.0	3713	3707	1.00

Table 7.6 Comparison between test data and numerical results: slender columns under concentric compression

Series	Designation	Section classification	Measured dimension of specimen (mm)					A_g	e_0	v_0	$\bar{\lambda}_z$	$N_{b,Et}$	$N_{b,FEM}$	$N_{b,Et}$ / $N_{b,FEM}$
			B	H	t	R_{out}	L_m	(mm^2)	(mm)	(mm)		(kN)	(kN)	
SA	(1) S1A-P	2	160.7	153.3	5.88	23.88	1280	3343	+1.0	--	0.52	2603	2296	1.13
	(2) S2A-P	4	209.0	203.0	5.88	23.88	1580	4495	+1.0	--	0.46	2981	2919	1.02
	(3) S3A-P	1	213.5	206.7	9.89	39.89	1278	7326	+1.5	+0.5	0.40	5448	5165	1.05
	(4) S4A-P	1	261.7	253.0	9.89	39.89	1579	9196	--	+1.5	0.38	6867	6640	1.03
	(5) S1A-Q	2	159.5	152.8	5.88	23.88	2281	3322	-1.5	+1.0	0.83	2187	2092	1.05
	(6) S2A-Q	4	209.8	202.5	5.88	23.88	1978	4498	+2.0	--	0.56	2913	2886	1.01
	(7) S3A-Q	1	220.5	196.6	9.89	39.89	2278	7266	+2.0	+2.0	0.63	4917	4783	1.03
	(8) S4A-Q	1	264.3	255.5	9.89	39.89	2279	9298	+1.0	+1.5	0.51	6698	6399	1.05
SB	(9) S1B-P	3	149.5	159.5	5.88	23.88	1279	3390	+2.0	+0.5	0.55	2477	2210	1.12
	(10) S2B-P	4	199.7	208.7	5.88	23.88	1580	4558	+1.5	--	0.48	2724	2667	1.02
	(11) S3B-P	1	199.8	210.4	9.89	39.89	1280	7425	+2.0	+0.5	0.42	5556	5284	1.05
	(12) S4B-P	3	250.0	261.0	9.89	39.89	1580	9420	-2.5	+0.5	0.39	7149	6779	1.05
	(13) S1B-Q	3	150.3	158.8	5.88	23.88	2281	3390	-1.0	+0.5	0.86	2213	2068	1.07
	(14) S2B-Q	4	199.5	209.0	5.88	23.88	1978	4560	+2.0	--	0.58	2852	2696	1.06
	(15) S3B-Q	1	200.4	210.2	9.89	39.89	2278	7433	-2.5	+0.5	0.67	5451	4886	1.12
	(16) S4B-Q	3	250.0	261.5	9.89	39.89	2279	9430	-1.0	+0.5	0.53	7027	6611	1.06

Note: "--" denotes that e_0 or v_0 is smaller than 0.5 mm, thus ignored in modelling.

Table 7.7 Investigation programme of parametric studies: Section S3A

(B) Material model	(C) Initial state			(D) Non-dimensional slenderness
	(C1) GI	(C2) PEEQ	(C3) RS	
(1) S690, linear hardening	(1) $L_{eff}/1500$	No	No	(1) 0.6
(2) S690, non-liner hardening	(2) $L_{eff}/1500$	No	Yes	(2) 1.0
	(3) $L_{eff}/1500$	Yes	Yes	(3) 1.4
	(4) $L_{eff}/1000$	Yes	Yes	(4) 1.8
	(5) $L_{eff}/500$	No	No	

Total number of models: 32

Table 7.8 Investigation programme of parametric studies: Section S3B

(B) Material model	(C) Initial state			(D) Non-dimensional slenderness
	(C1) GI	(C2) PEEQ	(C3) RS	
(1) S690, linear hardening	(1) $L_{eff}/1500$	No	No	(1) 0.6
	(2) $L_{eff}/1500$	No	Yes	(2) 1.0
	(3) $L_{eff}/1500$	Yes	Yes	(3) 1.4
	(4) $L_{eff}/1000$	Yes	Yes	(4) 1.8
	(5) $L_{eff}/500$	No	No	

Total number of models: 20

Table 7.9 Results of parametric studies for Section S3A (material: S690 linear hardening)

Case	Initial state (C1) GI	(C2) PEEQ	(C3) RS	$N_{b,FEM}$ / $N_{c,Rd}$ $\bar{\lambda}$ = 0.6	$\bar{\lambda}$ = 1.0	$\bar{\lambda}$ = 1.4	$\bar{\lambda}$ = 1.8
Case a	L_{eff}/1500	No	No	0.965	0.808	0.478	0.298
Case b	L_{eff}/1500	No	Yes	0.844	0.689	0.454	0.291
Case c	L_{eff}/1500	Yes	Yes	0.854	0.700	0.459	0.293
Case d	L_{eff}/1000	Yes	Yes	0.843	0.676	0.445	0.287
Case e	L_{eff}/500	No	No	0.904	0.695	0.434	0.279

Note: $N_{c,Rd}$ = 4829 kN for Section S3A.

Table 7.10 Comparison among parametric studies for Section S3A (material: S690 linear hardening)

Case	Initial state (C1) GI	(C2) PEEQ	(C3) RS	$N_{b,FEM}$ / $N_{c,Rd}$ $\bar{\lambda}$ = 0.6	$\bar{\lambda}$ = 1.0	$\bar{\lambda}$ = 1.4	$\bar{\lambda}$ = 1.8
Case a	L_{eff}/1500	No	No	0.965	0.808	0.478	0.298
Case b	L_{eff}/1500	No	Yes	0.844	0.689	0.454	0.291
		Case b / Case a:		***87.5%***	***85.3%***	***95.0%***	***97.7%***
Case b	L_{eff}/1500	No	Yes	0.844	0.689	0.454	0.291
Case c	L_{eff}/1500	Yes	Yes	0.854	0.700	0.459	0.293
		Case c / Case b:		***101.2%***	***101.6%***	***101.1%***	***100.7%***
Case c	L_{eff}/1500	Yes	Yes	0.854	0.700	0.459	0.293
Case d	L_{eff}/1000	Yes	Yes	0.843	0.676	0.445	0.287
		Case d / Case c:		***98.7%***	***96.6%***	***96.9%***	***98.0%***
Case c	L_{eff}/1500	Yes	Yes	0.854	0.700	0.459	0.293
Case e	L_{eff}/500	No	No	0.904	0.695	0.434	0.279
		Case e / Case c:		***105.9%***	***99.3%***	***94.6%***	***95.2%***

Table 7.11 Results of parametric studies: Section S3A (material: S690 non-linear hardening)

Case	Initial state			$N_{b,FEM}$ / $N_{c,Rd}$			
	(C1) GI	(C2) PEEQ	(C3) RS	$\bar{\lambda}$ = 0.6	$\bar{\lambda}$ = 1.0	$\bar{\lambda}$ = 1.4	$\bar{\lambda}$ = 1.8
Case c	L_{eff}/1500	Yes	Yes	0.866	0.715	0.465	0.294
Case d	L_{eff}/1000	Yes	Yes	0.855	0.689	0.450	0.288
Case e	L_{eff}/500	No	No	0.904	0.695	0.434	0.279

Note: $N_{c,Rd}$ = 4829 kN for Section S3A.

Table 7.12 Comparison among parametric studies: Section S3A (material: S690 non-linear hardening)

Case	Initial state			$N_{b,FEM}$ / $N_{c,Rd}$			
	(C1) GI	(C2) PEEQ	(C3) RS	$\bar{\lambda}$ = 0.6	$\bar{\lambda}$ = 1.0	$\bar{\lambda}$ = 1.4	$\bar{\lambda}$ = 1.8
Case c	L_{eff}/1500	Yes	Yes	0.866	0.715	0.465	0.294
Case d	L_{eff}/1000	Yes	Yes	0.855	0.689	0.450	0.288
		Case d / Case c:		***98.7%***	***96.4%***	***96.8%***	***98.0%***
Case c	L_{eff}/1500	Yes	Yes	0.866	0.715	0.465	0.294
Case e	L_{eff}/500	No	No	0.904	0.695	0.434	0.279
		Case e / Case c:		***104.4%***	***97.2%***	***93.3%***	***94.9%***

Table 7.13 Results of parametric studies: Section S3B (material: S690 linear hardening)

Case	Initial state			$N_{b,FEM}$ / $N_{c,Rd}$			
	(C1) GI	(C2) PEEQ	(C3) RS	$\bar{\lambda}$ = 0.6	$\bar{\lambda}$ = 1.0	$\bar{\lambda}$ = 1.4	$\bar{\lambda}$ = 1.8
Case a	L_{eff}/1500	No	No	0.962	0.811	0.480	0.298
Case b	L_{eff}/1500	No	Yes	0.890	0.722	0.469	0.286
Case c	L_{eff}/1500	Yes	Yes	0.895	0.725	0.471	0.286
Case d	L_{eff}/1000	Yes	Yes	0.885	0.701	0.456	0.280
Case e	L_{eff}/500	No	No	0.907	0.698	0.436	0.279

Note: $N_{c,Rd}$ = 5037 kN for Section S3B.

Table 7.14 Comparison among parametric studies: Section S3B (material: S690 linear hardening)

Case	Initial state			$N_{b,FEM}$ / $N_{c,Rd}$			
	(C1) GI	(C2) PEEQ	(C3) RS	$\bar{\lambda}$ = 0.6	$\bar{\lambda}$ = 1.0	$\bar{\lambda}$ = 1.4	$\bar{\lambda}$ = 1.8
Case a	L_{eff}/1500	No	No	0.962	0.811	0.480	0.298
Case b	L_{eff}/1500	No	Yes	0.890	0.722	0.469	0.286
		Case b / Case a:		***92.5%***	***89.0%***	***97.7%***	***96.0%***
Case b	L_{eff}/1500	No	Yes	0.890	0.722	0.469	0.286
Case c	L_{eff}/1500	Yes	Yes	0.895	0.725	0.471	0.286
		Case c / Case b:		***100.6%***	***100.4%***	***100.4%***	***100.0%***
Case c	L_{eff}/1500	Yes	Yes	0.895	0.725	0.471	0.286
Case d	L_{eff}/1000	Yes	Yes	0.885	0.701	0.456	0.280
		Case d / Case c:		***98.9%***	***96.7%***	***96.8%***	***97.9%***
Case c	L_{eff}/1500	Yes	Yes	0.895	0.725	0.471	0.286
Case e	L_{eff}/500	No	No	0.907	0.698	0.436	0.279
		Case e / Case c:		***101.3%***	***96.3%***	***92.6%***	***97.6%***

CHAPTER 8: CONCLUSIONS AND FUTURE WORK

8.1 Introduction

This research project presents a systematic experimental-numerical incorporated investigation into the structural behaviour of high strength S690 cold-formed square hollow sections (CFSHS) under compression. Effects of fabrication processes, namely, i) transverse bending, and ii) longitudinal welding, onto the structural behaviour of these sections are also examined. The key findings from Chapters 3 to 7 are summarized in following Sections, and the work to be done in the future is also recommended.

8.2 Experimental Investigation

A comprehensive experimental investigation was carried out to demonstrate the effects of fabrication processes in S690 CFSHS, including monotonic tensile coupon tests and measurements of residual strains. Moreover, large scale tests on stocky and slender columns under compression were also conducted. The key findings from all these experiments are summarized as follows:

8.2.1 Monotonic tensile tests on flat and curved coupons

In order to evaluate strength enhancements induced by transverse bending, a total of 19 flat and curved coupons extracted from four 10 mm thick S690 CFSHS with $R_{in}/t = 3.0$ were tested under uni-axial tension. An increase of 5 % in yield strength and an increase of 10 % in tensile strength were found in the curved coupons extracted from the corner regions, when compared with those extracted from the flat portions.

8.2.2 Measurements of residual strains

The temperature histories and the welding parameters of S690 CFSHS were measured during welding, and the residual strains of four typical S690 CFSHS were measured with the sectioning method. Two welded cold-formed sections and two cold-formed sections without welding were investigated. All those test results were used for calibrating the numerical models of predicting residual strains due to transverse bending and longitudinal welding.

8.2.3 Structural behaviour of columns under compression

A total of 12 CFSHS fabricated with different combinations of transverse bending and longitudinal welding were investigated. To examine structural behaviour of these sections under compression, a total of 38 S690 CFSHS column tests were conducted under three loading conditions, including 8 stocky columns under concentric compression, 6 stocky columns under eccentric compression, and 24 slender columns under concentric compression. Details of these tetes were summarized as follows:

- Stocky columns under concentric compression

A total of 8 stocky columns were tested under concentric compression. Except for those columns with Class 4 sections, all these stocky columns with Classes 1, 2 and 3 sections were demonstrated to have mobilized the full resistances of their gross sections. For those Class 4 sections, by considering local buckling in their plated elements, they were demonstrated to have attained the design resistances of their effective sections. Besides, both series of these sections were shown to have achieved their section resistances, but larger plastic deformations were mobilized in Series SA sections, when compared with those in Series SB sections. Hence, Series SA sections were demonstrated to possess a high degree of ductility under compression.

- Stocky columns under eccentric compression

A total of 6 stocky columns were tested under eccentric compression. Except for those columns with Class 4 sections, all these stocky columns with Classes 1, 2 and 3 sections were demonstrated to have mobilized the full resistances of their gross sections. For those Class 4 sections, by considering local buckling in their plated elements, they were demonstrated to have attained the design resistances of their effective sections. Besides, both series of these sections were shown to have achieved their section resistances while large plastic deformations were mobilized in Series SA sections, when compared with those of Series SB sections. Hence, Series SA sections were demonstrated to possess a high degree of ductility under combined compression and bending.

- Slender columns under concentric compression

A total of 24 slender columns were tested under concentric compression. Except for those columns with Class 4 sections, all these columns with Classes 1, 2 and 3 sections were demonstrated to have mobilized their member resistances against axial buckling. For those Class 4 sections, by adopting their effective sections, they were also demonstrated to have attained their member resistances against axial buckling. Based on a direct comparison between the measured and the design resistances of these slender columns, it was proposed to improve the design method so that a higher design curve with a smaller imperfection factor should be used, when compared with the current code of practice.

8.3 Analytical and Numerical Investigation

Analytical solutions and numerical models were developed to provide various efficient solutions to predict residual stresses in these CFSHS, and their effects on structural behaviour of slender columns of these S690 CFSHS.

8.3.1 Prediction on strength enhancement with various methods

Both the 3D and the 2D press-braking numerical methods were developed to obtain the stress-strain characteristics at the corner regions of the S690 CFSHS, and thus, to determine their strength enhancements at large deformations. The accurate results were obtained with the validated 3D models using certain computational resources. However, it was necessary to calibrate the models against the test data, which was a demanding process that required extensive modelling techniques. Considering the essence of the plane-strain problem, the simplified 2D transverse bending models were also established, which were able to provide accurate results using reduced computational resources. It was proposed to use these 2D models to predict the plastic strains and the corresponding residual stresses at the corner regions for all the S690 CFSHS. Both the strains and the stresses obtained from these 2D models were readily incorporated into finite elements models for both thermomechanical and structural analyses.

Moreover, a simplified method, which was developed based on the theory of sheet bending, did not have any specific requirement on either laboratory resources or modelling techniques. With only a small accuracy sacrificed, the results were determined in a highly efficient way. This approach was further developed to offer a hand calculation method. Hence, the predictions on the strength enhancements at the corner regions were readily achieved.

8.3.2 Numerical prediction on residual stresses with thermomechanical analyses

Both the analytical solution and the numerical model were developed based on the welding parameters, the temperature-dependent thermomechanical properties and the double-ellipsoidal heat source model. The analytical solution was shown to be effective to predict the dimensions of the fusion zones due to welding, which helped to determine the lengths of the semi-axes adopted in the double-ellipsoidal heat source model. The numerical predictions on the residual stresses of S690 CFSHS implemented with the sequentially-coupled thermomechanical analyses were shown to match well with the measurements of the sectioning method, and force equilibrium was well achieved in this numerical method.

The simplified patterns of the residual stresses of the S690 CFSHS were developed based on the numerical results of the sequentially-coupled thermomechanical analyses, and thus, these patterns were readily input as the initial states of the numerical models for subsequent structural analyses.

8.3.3 Model validation of S690 CFSHS columns under compression

A total of 30 numerical models were established and carefully validated against the test data presented in Chapter 4. All the numerical models were successfully validated, with consideration onto the effects of transverse bending and longitudinal welding. These initial plastic stains and the residual stresses, which were predicted in Chapters 5 and 6, were incorporated into the structural models of the S690 CFSHS as initial states. The influences on structural performance of member resistances caused by various effects were evaluated, including types of sections, material models, initial geometric imperfections, initial equivalent plastic strains, residual stresses and member slenderness. Material models, initial equivalent plastic strains and residual stresses were found to affect member resistances significantly when their non-dimensional slenderness ratios were small, but these effects were obviously reduced as the member became slender.

8.4 Design Recommendation for S690 CFSHS under Compression

8.4.1 Material properties and strength enhancements

An experimental investigation into S690 standard tensile coupons was presented. It was found that the measured mechanical properties of the S690 steels complied well with the requirements given in EN 1993-1-12 and EN 10025-6. The measured yield strengths of the S690 steels were used to predict section and member resistances of the S690 CFSHS columns after testing.

Strength enhancements at the corner regions were examined in this project, as they were introduced as plastic deformations due to cold-bending. Based on the results of the curved coupon tests extracted from S690 CFSHS, an enhancement in yield strength of 5 % was found when $R_{in}/t = 3.0$. However, as the corner regions took up only 20 ~ 30 % the gross section in area, the enhancement of the section resistances was typically smaller than 1.5 %, and thus, this enhancement may be ignored in the design of section and member resistances for these S690 CFSHS.

8.4.2 Section classification of CFSHS

Two sets of rules of section classification for CFSHS are proposed in EN 1993-1-1 and EN 1993-1-5. It was found that the sections classified by the modified rules given in EN 1993-1-5 matched well their anticipated mobilization in both strength and ductility. Therefore, it was proposed to adopt the modified rules to classify all CFSHS under compression. However, this modification was applicable to the design of stocky columns of S690 CFSHS only, because using this modification may further increase safety margin for member resistances under axial buckling, but their resistances have already underestimated based on the design curve “c”. It is therefore recommended that the modified c-values should not be adopted for the design of slender columns.

8.4.3 CFSHS slender columns under axial buckling

A total of 52 numerical analyses were performed using the validated numerical models to generate a set of numerical data on the members resistances of these S690 CFSHS. By comparing the test data, the numerical data and the design curves, it was found that the current design rules given in EN 1993-1-1 were conservative in adopting the design curve “c” for these CFSHS members under axial buckling. It was recommended to adopt a design curve with a smaller imperfection factor to improve the design efficiency. It was shown that the design curve “b” matched well with all the test data and all the numerical data. Therefore, it was proposed to adopt the design curve “b” for these S690 CFSHS columns under axial buckling.

8.5 Recommendations for Future Work

This Thesis presents the first systematic research to investigate the structural behaviour of S690 CFSHS, and the effects of fabrication on structural behaviour were also examined. However, in order to promote effective use of this type of high strength steel sections, more work should be done. It is proposed to further investigate various aspects of this research project and to provide an efficient solution to structural design with both theoretical and experimental evidences.

8.5.1 Effects of steel grades, plate thicknesses and R_{in}/t ratios with transverse bending

Effects of transverse bending were investigated in this project by using 6 and 10 mm S690 steel plates with $R_{in}/t = 3.0$. After reviewing the literature, bendability is significantly influenced by three key factors, namely i) plate thickness, ii) steel grade, and iii) R_{in}/t ratio. Therefore, it is reasonable to design a test programme to cover i) more plate thicknesses, i.e. from 3 mm to 16 mm, ii) more steel grades, i.e. from S355 to S960, and iii) more R_{in}/t ratios, i.e. from 1.0 to 12.0. It is believed that these test data will facilitate assessment on bendability of these steel plates in various conditions, and thus, to develop generalized analytical and numerical solutions to transverse bending effects at cold-bent corners.

8.5.2 Material properties of high strength steels at elevated temperatures

In this project, the material properties of S690 at elevated temperatures for the thermomechanical analyses were assigned to be the recommended values for the normal strength steels given in EN 1993-1-2. Errors may exist in the numerical results of the residual stresses due to inaccurate values of these material properties at elevated temperatures. Hence, it is recommended to carry out an experimental investigation into the high strength S690 steels at elevated temperatures, to quantify their mechanical properties from the ambient temperatures up to 1800 °C, and these include conductivity, expansion coefficient, specific heat, yield strength and Young's modulus.

8.5.3 Structural member tests in other cross-sectional shapes with S690 steels

The structural performance of S690 CFSHS stocky and slender columns under compression was examined experimentally and numerically in this project. The results proved that these types of structural members had high resistances under these specified loading conditions. However, members in other cold-formed structural hollow sections are equally important in engineering practice, such as CFRHS as well as CFCHS. It is recommended that those structural members should be designed, fabricated and tested accordingly, following the research methodology employed in this project. Moreover, the current design rules for these cold-formed structural hollow sections should be reviewed thoroughly, and thus, be improved with the upcoming experimental and numerical data.

REFERENCES

ABAQUS 6.13. (2013). ABAQUS Analysis User's Manual, version 6.13.

Arola, A. M., Kesti, V., & Ruoppa, R. (2015). The effect of punch radius on the deformation of ultra-high strength steel in bending. In Key engineering materials (Vol. 639, pp. 139-146). Trans Tech Publications Ltd.

Ban, H., & Shi, G. (2018). A review of research on high-strength steel structures. Proceedings of the Institution of Civil Engineers-Structures and Buildings, 171(8), 625-641.

Ban, H., Shi, G., Shi, Y., & Wang, Y. (2012a). Overall buckling behavior of 460 MPa high strength steel columns: Experimental investigation and design method. Journal of Constructional Steel Research, 74, 140-150.

Ban, H., Shi, G., Shi, Y., & Wang, Y. (2012b). Residual stress tests of high-strength steel equal angles. Journal of Structural Engineering, 138(12), 1446-1454.

Ban, H., Shi, G., Shi, Y., & Bradford, M. A. (2013a). Experimental investigation of the overall buckling behaviour of 960 MPa high strength steel columns. Journal of Constructional Steel Research, 88, 256-266.

Ban, H., Shi, G., Shi, Y., & Wang, Y. (2013b). Residual stress of 460 MPa high strength steel welded box section: Experimental investigation and modeling. Thin-Walled Structures, 64, 73-82.

Ban, H., Shi, G., Bai, Y., Shi, Y., & Wang, Y. (2013c). Residual stress of 460 MPa high strength steel welded I section: experimental investigation and modeling. International Journal of Steel Structures, 13(4), 691-705.

Bridgman, P. W. (1952). Studies in Large Plastic Flow and Fracture. Mc Grraw Hill, New York.

CEN. (2001). Welding - Recommendations for welding of metallic materials - Part 2: Arc welding of ferritic steels. BS EN 1011-2:2001, European Committee for Standardization (CEN), Brussels, Belgium.

CEN. (2005). Eurocode - Basis of structural design. BS EN 1990:2002+A1:2005, European Committee for Standardization (CEN), Brussels, Belgium.

CEN. (2007). Eurocode 3 - Design of steel structures - Part 1-12: Additional rules for the extension of EN 1993 up to steel grades S 700. BS EN 1993-1-12:2007, European Committee for Standardization (CEN), Brussels, Belgium.

CEN. (2008). Welding consumables - Gases and gas mixtures for fusion welding and allied processes. BS EN ISO 14175:2008, European Committee for Standardization (CEN), Brussels, Belgium.

CEN. (2009a). Welding - Recommendations for welding of metallic materials - Part 1: General guidance for arc welding. BS EN 1011-1:2009, European Committee for Standardization (CEN), Brussels, Belgium.

CEN. (2009b). Eurocode 3 - Design of steel structures - Part 1-2: General rules - Structural fire design. BS EN 1993-1-2:2005, European Committee for Standardization (CEN), Brussels, Belgium.

CEN. (2010). Eurocode 3 - Design of steel structures - Part 1-8: Design of joints. BS EN 1993-1-8:2005, European Committee for Standardization (CEN), Brussels, Belgium.

CEN. (2014). Eurocode 3 - Design of steel structures - Part 1-1: General rules and rules for buildings. BS EN 1993-1-1:2005+A1:2014, European Committee for Standardization (CEN), Brussels, Belgium.

CEN. (2016). Welding - Calibration, verification and validation of equipment used for welding, including ancillary activities. BS EN ISO 17662:2016, European Committee for Standardization (CEN), Brussels, Belgium.

CEN. (2017). Welding - Measurement of preheating temperature, interpass temperature and preheat maintenance temperature. BS EN ISO 13916:2017, European Committee for Standardization (CEN), Brussels, Belgium.

CEN. (2019a). Hot rolled products of structural steels - Part 2: Technical delivery conditions for non-alloy structural steels. BS EN 10025-2:2019, European Committee for Standardization (CEN), Brussels, Belgium.

CEN. (2019b). Hot rolled products of structural steels - Part 4: Technical delivery conditions for thermomechanical rolled weldable fine grain structural steels. BS EN 10025-4:2019, European Committee for Standardization (CEN), Brussels, Belgium.

CEN. (2019c). Hot rolled products of structural steels - Part 6: Technical delivery conditions for flat products of high yield strength structural steels in the quenched and tempered condition. BS EN 10025-6:2019, European Committee for Standardization (CEN), Brussels, Belgium.

CEN. (2019d). Cold formed welded steel structural hollow sections - Part 2: Tolerances, dimensions and sectional properties. BS EN 10219-2:2019, European Committee for Standardization (CEN), Brussels, Belgium.

CEN. (2019e). Eurocode 3 - Design of steel structures - Part 1-5: Plated structural elements. BS EN 1993-1-5:2006+A2:2019, European Committee for Standardization (CEN), Brussels, Belgium.

CEN. (2019f). Specification and qualification of welding procedures for metallic materials - Welding procedure specification - Part 2: Gas welding. BS EN ISO 15609-2, European Committee for Standardization (CEN), Brussels, Belgium.

CEN. (2019g). Metallic materials - Tensile testing - Part 1: Method of test at room temperature. BS EN ISO 6892-1:2009, European Committee for Standardization (CEN), Brussels, Belgium.

Chen, J., & Chan, T. M. (2020). Material properties and residual stresses of cold-formed high-strength-steel circular hollow sections. Journal of Constructional Steel Research, 170, 106099.

Chen, J., Zhu, J. Y., & Chan, T. M. (2020a). Experimental and numerical investigation on stub column behaviour of cold-formed octagonal hollow sections. Engineering Structures, 214, 110669.

Chen, J., Chan, T. M., & Varma, A. H. (2020b). Stub Column Behavior of Cold-Formed High-Strength Steel Circular Hollow Sections under Compression. Journal of Structural Engineering, 146(12), 04020277.

ECCS. (1986). Recommended testing procedure for assessing the behaviour of structural steel elements under cyclic loads. Brussels, Belgium: European Convention for Constructional Steelwork.

Fachinotti, V. D., Anca, A. A., & Cardona, A. (2011). Analytical solutions of the thermal field induced by moving double-ellipsoidal and double-elliptical heat sources in a semi-infinite body. International Journal for Numerical Methods in Biomedical Engineering, 27(4), 595-607.

Fang, H., Chan, T. M., & Young, B. (2019). Behavior of Octagonal High-Strength Steel Tubular Stub Columns. Journal of Structural Engineering, 145(12), 04019150.

Fang, H., Chan, T. M., & Young, B. (2020). Experimental and Numerical Investigations of Octagonal High-Strength Steel Tubular Stub Columns under Combined Compression and Bending. Journal of Structural Engineering, 147(1), 04020282.

Gardner, L., Saari, N., & Wang, F. (2010). Comparative experimental study of hot-rolled and cold-formed rectangular hollow sections. Thin-Walled Structures, 48(7), 495-507.

Gkantou, M., Theofanous, M., Wang, J., Baniotopoulos, C., & Gardner, L. (2017a). Behaviour and design of high-strength steel cross-sections under combined loading. Proceedings of the Institution of Civil Engineers-Structures and Buildings, 170(11), 841-854.

Gkantou, M., Theofanous, M., Antoniou, N., & Baniotopoulos, C. (2017b). Compressive behaviour of high-strength steel cross-sections. Proceedings of the Institution of Civil Engineers-Structures and Buildings, 170(11), 813-824.

Goldak, J., Chakravarti, A., & Bibby, M. (1984). A new finite element model for welding heat sources. Metallurgical transactions B, 15(2), 299-305.

Guo, Y. B., Ho, H. C., Chung, K. F., & Elghazouli, A. Y. (2020). Cyclic deformation characteristics of S355 and S690 steels under different loading protocols. Engineering Structures, 221, 111093.

Han, F., Wang, Y., Zhang, T., Li, Q., & Song, Y. (2020). Effect of different roll forming processes on material properties of square tubes. advanced steel construction, 16(2), 181-190.

Hill, R. (1950). The mathematical theory of plasticity (Oxford engineering science series). Oxford: Clarendon Press.

Ho, H. C., Liu, X., Chung, K. F., Elghazouli, A. Y., & Xiao, M. (2018). Hysteretic behaviour of high strength S690 steel materials under low cycle high strain tests. Engineering Structures, 165, 222-236.

Ho, H. C., Xiao, M., Hu, Y. F., Guo, Y. B., Chung, K. F., Yam, M. C. H., & Nethercot, D. A. (2020). Determination of a full range constitutive model for high strength S690 steels. Journal of Constructional Steel Research, 174, 106275.

Hosford, W. F., & Caddell, R. M. (2011). Metal forming: mechanics and metallurgy. Cambridge University Press.

Hu, Y. F., Chung, K. F., Ban, H., & Nethercot, D. A. (2020). Investigations into residual stresses in S690 cold-formed circular hollow sections due to transverse bending and longitudinal welding. Engineering Structures, 219, 110911.

Huang, Y., & Young, B. (2014). The art of coupon tests. Journal of Constructional Steel Research, 96, 159-175.
Huang, X., Liu, Z., & Xie, H. (2013). Recent progress in residual stress measurement techniques. Acta Mechanica Solida Sinica, 26(6), 570-583.

Jiang, J., Chiew, S. P., Lee, C. K., & Tiong, P. L. Y. (2017). A numerical study on residual stress of high strength steel box column. Journal of Constructional Steel Research, 128, 440-450.

Khan, M., Paradowska, A., Uy, B., Mashiri, F., & Tao, Z. (2016). Residual stresses in high strength steel welded box sections. Journal of Constructional Steel Research, 116, 55-64.

Lee, C. K., Chiew, S. P., & Jiang, J. (2012a). Residual stress study of welded high strength steel thin-walled plate-to-plate joints, Part 1: Experimental study. Thin-Walled Structures, 56, 103-112.

Lee, C. K., Chiew, S. P., & Jiang, J. (2012b). Residual stress study of welded high strength steel thin-walled plate-to-plate joints part 2: Numerical modeling. Thin-walled structures, 59, 120-131.

Lee, C. K., Chiew, S. P., & Jiang, J. (2014). Residual stress of high strength steel box T-joints Part 2: Numerical study. Journal of Constructional Steel Research, 98, 73-87.

Lee, C. K., Chiew, S. P., & Jiang, J. (2014). Residual stress of high strength steel box T-joints: Part 1: Experimental study. Journal of Constructional Steel Research, 93, 20-31.
Li, T. J., Li, G. Q., & Wang, Y. B. (2015). Residual stress tests of welded Q690 high-strength steel box-and H-sections. Journal of Constructional Steel Research, 115, 283-289.

Li, T. J., Li, G. Q., Chan, S. L., & Wang, Y. B. (2016). Behavior of Q690 high-strength steel columns: Part 1: Experimental investigation. Journal of Constructional Steel Research, 123, 18-30.

Ling, Y. (1996). Uniaxial true stress-strain after necking. AMP Journal of technology, 5(1), 37-48.

Liu, X., & Chung, K. F. (2018). Experimental and numerical investigation into temperature histories and residual stress distributions of high strength steel S690 welded H-sections. Engineering Structures, 165, 396-411.

Liu, X., Chung, K. F., Ho, H. C., Xiao, M., Hou, Z. X., & Nethercot, D. A. (2018). Mechanical behavior of high strength S690-QT steel welded sections with various heat input energy. Engineering Structures, 175, 245-256.

Liu, X., Chung, K. F., Huang, M., Wang, G., & Nethercot, D. A. (2019). Thermomechanical parametric studies on residual stresses in S355 and S690 welded H-sections. Journal of Constructional Steel Research, 160, 387-401.

Ma, J. L., Chan, T. M., & Young, B. (2015). Material properties and residual stresses of cold-formed high strength steel hollow sections. Journal of Constructional Steel Research, 109, 152-165.

Ma, J. L., Chan, T. M., & Young, B. (2016). Experimental investigation on stub-column behavior of cold-formed high-strength steel tubular sections. Journal of Structural Engineering, 142(5), 04015174.

Ma, J. L., Chan, T. M., & Young, B. (2019). Cold-Formed High-Strength Steel Rectangular and Square Hollow Sections under Combined Compression and Bending. Journal of Structural Engineering, 145(12), 04019154.

Ma, T. Y., Liu, X., Hu, Y. F., Chung, K. F., & Li, G. Q. (2018). Structural behaviour of slender columns of high strength S690 steel welded H-sections under compression. Engineering Structures, 157, 75-85.

Meng, X., & Gardner, L. (2020a). Behavior and Design of Normal-and High-Strength Steel SHS and RHS Columns. Journal of Structural Engineering, 146(11), 04020227.

Meng, X., & Gardner, L. (2020b). Cross-sectional behaviour of cold-formed high strength steel circular hollow sections. Thin-Walled Structures, 156, 106822.

Moen, C. D., Igusa, T., & Schafer, B. W. (2008). Prediction of residual stresses and strains in cold-formed steel members. Thin-walled structures, 46(11), 1274-1289.

Mutafi, A., Yidris, N., Loughlan, J., Zahari, R., & Ishak, M. R. (2019). Investigation into the distribution of residual stresses in pressed-braked thin-walled steel lipped channel sections using the 3D-FEM technique. Thin-Walled Structures, 135, 437-445.

Nseir, J. (2015). Development of a new design method for the cross-section capacity of steel hollow sections (Doctoral dissertation, Université de Liège, Liège, Belgique).

Nguyen, N. T., Ohta, A., Matsuoka, K., Suzuki, N., & Maeda, Y. (1999). Analytical solutions for transient temperature of semi-infinite body subjected to 3-D moving heat sources. WELDING JOURNAL-NEW YORK-, 78, 265-s.

Nishioka, K., & Ichikawa, K. (2012). Progress in thermomechanical control of steel plates and their commercialization. Science and Technology of Advanced Materials, 13(2), 023001.

Pournara, A. E., Karamanos, S. A., Mecozzi, E., & Lucci, A. (2017). Structural resistance of high-strength steel CHS members. Journal of Constructional Steel Research, 128, 152-165.

Quach, W. M., & Young, B. (2015). Material properties of cold-formed and hot-finished elliptical hollow sections. Advances in Structural Engineering, 18(7), 1101-1114.

Quach, W. M., Teng, J. G., & Chung, K. F. (2006). Finite element predictions of residual stresses in press-braked thin-walled steel sections. Engineering structures, 28(11), 1609-1619.

Rossi, B., Degée, H., & Boman, R. (2013). Numerical simulation of the roll forming of thin-walled sections and evaluation of corner strength enhancement. Finite Elements in Analysis and Design, 72, 13-20.

Rossini, N. S., Dassisti, M., Benyounis, K. Y., & Olabi, A. G. (2012). Methods of measuring residual stresses in components. Materials & Design, 35, 572-588.

Shi, G., Zhou, W., & Lin, C. (2015). Experimental investigation on the local buckling behavior of 960 MPa high strength steel welded section stub columns. Advances in Structural Engineering, 18(3), 423-437.

Somodi, B., & Kövesdi, B. (2017a). Flexural buckling resistance of cold-formed HSS hollow section members. Journal of Constructional Steel Research, 128, 179-192.

Somodi, B., & Kövesdi, B. (2017b). Residual stress measurements on cold-formed HSS hollow section columns. Journal of Constructional Steel Research, 128, 706-720.

Somodi, B., & Kövesdi, B. (2018). Residual stress measurements on welded square box sections using steel grades of S235–S960. Thin-Walled Structures, 123, 142-154.

SSAB. (2010). Welding handbook - A guide to better welding of Hardox and Weldox.

SSAB. (2017). Strenx, Hardox and Docol - Bending of high strength steel.

Tong, L., Hou, G., Chen, Y., Zhou, F., Shen, K., & Yang, A. (2012). Experimental investigation on longitudinal residual stresses for cold-formed thick-walled square hollow sections. Journal of Constructional Steel Research, 73, 105-116.

Vorkov, V., Aerens, R., Vandepitte, D., & Duflou, J. R. (2017). Experimental investigation of large radius air bending. The International Journal of Advanced Manufacturing Technology, 92(9-12), 3553-3569.

Wang, F., Zhao, O., & Young, B. (2019). Flexural behaviour and strengths of press-braked S960 ultra-high strength steel channel section beams. Engineering Structures, 200, 109735.

Wang, F., Liang, Y., & Zhao, O. (2020a). Experimental and numerical studies of pin-ended press-braked S960 ultra-high strength steel channel section columns. Engineering Structures, 215, 110629.

Wang, F., Zhao, O., & Young, B. (2020b). Testing and numerical modelling of S960 ultra-high strength steel angle and channel section stub columns. Engineering Structures, 204, 109902.

Wang, J., Afshan, S., Gkantou, M., Theofanous, M., Baniotopoulos, C., & Gardner, L. (2016). Flexural behaviour of hot-finished high strength steel square and rectangular hollow sections. Journal of Constructional Steel Research, 121, 97-109.

Wang, J., Afshan, S., Schillo, N., Theofanous, M., Feldmann, M., & Gardner, L. (2017). Material properties and compressive local buckling response of high strength steel square and rectangular hollow sections. Engineering Structures, 130, 297-315.

Wang, Y. B., Li, G. Q., & Chen, S. W. (2012). The assessment of residual stresses in welded high strength steel box sections. Journal of Constructional Steel Research, 76, 93-99.

Wang, Y. B., Li, G. Q., Chen, S. W., & Sun, F. F. (2014). Experimental and numerical study on the behavior of axially compressed high strength steel box-columns. Engineering Structures, 58, 79-91.

Weng, C. C., & Pekoz, T. (1990). Residual stresses in cold-formed steel members. Journal of Structural Engineering, 116(6), 1611-1625.

Weng, C. C., & White, R. N. (1990). Residual stresses in cold-bent thick steel plates. Journal of structural engineering, 116(1), 24-39.

Willms, R. (2009). High strength steel for steel constructions. In Nordic Steel Construction Conference, Malmo, Sweden.

Withers, P. J., & Bhadeshia, H. K. D. H. (2001). Residual stress. Part 1–measurement techniques. Materials science and Technology, 17(4), 355-365.

Yang, C., Yang, J., Su, M., & Li, Y. (2017). Residual stress in high-strength-steel welded circular tube. Proceedings of the Institution of Civil Engineers-Structures and Buildings, 170(9), 631-640.

Yao, Y., Quach, W. M., & Young, B. (2019). Finite element-based method for residual stresses and plastic strains in cold-formed steel hollow sections. Engineering Structures, 188, 24-42.

Yun, X., & Gardner, L. (2017). Stress-strain curves for hot-rolled steels. Journal of Constructional Steel Research, 133, 36-46.

Yun, X., Wang, Z., & Gardner, L. (2020). Structural performance and design of hot-rolled steel SHS and RHS under combined axial compression and bending. In Structures (Vol. 27, pp. 1289-1298). Elsevier.

Zhang, L., Tan, K. H., & Zhao, O. (2020a). Press-braked stainless steel channel section columns failing by flexural buckling: Testing, numerical simulation and design. Thin-Walled Structures, 157, 107066.

Zhang, L., Liang, Y., & Zhao, O. (2020b). Flexural-torsional buckling behaviour and resistances of fixed-ended press-braked S690 high strength steel angle section columns. Engineering Structures, 223, 111180.

Zhang, X. Z., Liu, S., Zhao, M. S., & Chiew, S. P. (2016). Comparative experimental study of hot-formed, hot-finished and cold-formed rectangular hollow sections. Case Studies in Structural Engineering, 6, 115-129.

Zhu, C., Hobbs, M. J., & Willmott, J. R. (2020). An accurate instrument for emissivity measurements by direct and indirect methods. Measurement Science and Technology, 31(4), 044007.